UC Berkeley
UC Berkeley Electronic Theses and Dissertations

Title
Performance-Based Robust Nonlinear Seismic Analysis with Application to Reinforced Concrete Bridge Systems

Permalink
https://escholarship.org/uc/item/8769z6k3

Author
Liang, Xiao

Publication Date
2016

Peer reviewed|Thesis/dissertation

eScholarship.org Powered by the California Digital Library
University of California

Performance-Based Robust Nonlinear Seismic Analysis with Application to Reinforced Concrete Bridge Systems

By

Xiao Liang

A dissertation submitted in partial satisfaction of the

requirements for the degree of

Doctor of Philosophy

in

Engineering – Civil and Environmental Engineering

in the

Graduate Division

of the

University of California, Berkeley

Committee in charge:

Professor Khalid M. Mosalam, Chair
Professor Stephen A. Mahin
Professor David R. Brillinger

Summer 2016

Performance-Based Robust Nonlinear Seismic Analysis with Application to Reinforced Concrete Bridge Systems

© Copyright 2016

by

Xiao Liang

ABSTRACT

Performance-Based Robust Nonlinear Seismic Analysis with Application to Reinforced Concrete Bridge Systems

by

Xiao Liang

Doctor of Philosophy in Engineering – Civil and Environmental Engineering

University of California, Berkeley

Professor Khalid M. Mosalam, Chair

The performance-based earthquake engineering (PBEE) approach, developed at the Pacific Earthquake Engineering Research (PEER) Center, aims to robustly decompose the performance assessment and design process into four logical stages that can be studied and resolved in a systematic and consistent manner. However, two key challenges are experienced in this approach, namely the accurate seismic structural analysis and the selection and modification of ground motions (GMs). This dissertation investigates these two challenges with application to reinforced concrete (RC) bridge systems.

In nonlinear structural dynamics, the most accurate analytical simulation method is the nonlinear time history analysis (NTHA). It involves the use of different types of direct integration algorithms and nonlinear equation solvers where their stability performance and convergence behaviors are of great significance. Lyapunov stability theory, the most complete framework for stability analysis of dynamical systems, is introduced in this study. Based on this theory, a new nonlinear equation solver is developed and its convergence performance was theoretically formulated and verified by several examples. Stability is one of the most important properties of direct integration algorithms that must be considered for efficient and reliable NTHA simulations. Two Lyapunov-based approaches are proposed to perform stability analysis for nonlinear structural systems. The first approach transforms the stability analysis to a problem of existence, that can be solved via convex optimization. The second approach is specifically applicable to explicit algorithms for nonlinear single-degree of freedom and multi-degree of freedom systems considering strictly positive real lemma. In this approach, the stability analysis of the formulated nonlinear system is transformed to investigating the strictly positive realness of its corresponding transfer function matrix.

Ground motion selection and modification (GMSM) procedures determine the necessary input excitations to the NTHA simulations of structures. Therefore, proper selection of the GMSM procedures is vital and an important prerequisite for the accurate and robust NTHA simulation and thus for the entire PBEE approach. Although many GMSM procedures are available, there is no consensus regarding a single accurate method and many studies focused on evaluating these

procedures. In this dissertation, a framework for probabilistic evaluation of the GMSM procedures is developed in the context of a selected large earthquake scenario with bidirectional GM excitations.

In urban societies, RC highway bridges, representing key components of the transportation infrastructure systems, play a significant role in transporting goods and people around natural terrains. Therefore, they are expected to sustain minor damage and maintain their functionality in the aftermath of major earthquakes, which commonly occur in California due to many active faults. Accurate seismic structural analysis of existing and newly designed RC highway bridges is fundamental to estimate their seismic demands. As such important lifeline structures, RC highway bridge systems are investigated as an application of the previously discussed theoretical developments proposed in this dissertation to address the two key challenges in the PEER PBEE approach.

TABLE OF CONTENTS

LIST OF FIGURES

LIST OF TABLES

ACKNOWLEDGMENTS

First I would like to express my utmost gratitude to my research adviser and the chair of my dissertation committee Prof. Khalid M. Mosalam for mentoring and supporting me during the course of my graduate study at Berkeley. His solid knowledge, inspiring ideas, and stimulating discussions, have been fundamental in my academic development and growth as a researcher and a person. He posed interesting questions, provided useful suggestions and comments, helped me to revise papers and encouraged me to do independent research. He has always been cordial, attentive, available, and supportive throughout all the peaks and valleys of my PhD course. I consider myself extremely fortunate to have been his student. He is not only my PhD advisor, but also my life advisor.

My grateful thanks are extended to Prof. Stephen Mahin and Prof. David Brillinger for valuable discussion and for sitting on my dissertation committees, and Prof. Jack Moehle for chairing my qualifying exam committee. The participation of Prof. Stephen Mahin, Prof. Shaofan Li and Prof. Cari Kaufman in my qualifying exam committee and the suggestions they gave me are also greatly appreciated. I am very grateful for the opportunity that Prof. Anil Chopra gave me to work as a graduate student instructor for his course. I am also thankful to all my Professors at UC Berkeley for the valuable knowledge and expertise that I gained in their courses. Their technical advices and informative classes truly inspired me and will always remain a cornerstone of my knowledge.

I would like to extend my greatest appreciation and special thanks to Dr. Selim Günay for his kindness and intellectual exchanges. He helped me like no anyone else since my first day of the PhD journey. His fruitful thoughts, endless patience and supports are greatly appreciated and helped me to pass through the adaptive phase of my PhD course. I am grateful for California Department of Transportation (Caltrans) for sponsoring this study, and the administrative support of Mr. Peter Lee of Caltrans is greatly appreciated. I would also like to thank Prof. Farzin Zareian at the University of California, Irvine, for providing the OpenSees models of the analyzed bridges.

Last but not least, I wish to extend my warmest and deepest gratitude and thankfulness to my family for their unconditional love and support. Thousands of words cannot express my gratitude to my great parents, Liang, Fang and Liu, Qi. They have been my role models since I was a kid and they are the best teachers and inspirations for me. My thanks are especially due for my grandparents for all their immeasurable care since I was born. In particular, I would like to express my big thanks to my beloved wife, Minghui Zheng, for all her love, care and sacrifice all these years. It is her who encourages me to pursue my dream and supports me without any reservation. I feel grateful and fortunate to have her in my life and she is a great blessing to me.

1 Introduction

1.1 MOTIVATION AND OBJECTIVE

The response of a structure to earthquake excitation and the consequences of this response involve various uncertainties at different stages including the definition of hazard, structural response, damage, and the corresponding loss determination. Performance-based Earthquake Engineering (PBEE) approach, developed at the Pacific Earthquake Engineering Research (PEER) Center, aims to robustly divide the performance assessment and design process into these logical stages that can be studied and resolved in a systematic and consistent manner [Moehle and Deierlein 2004]. Therefore, uncertainties in these stages can be explicitly taken into account to enable comprehensive understanding of the structural performance in a probabilistic manner and determine the most efficient decision about the seismic risk mitigation actions [Günay and Mosalam 2013]. In order to achieve this goal of the PBEE approach, considerable amount of structural simulations are required. Due to physical, economical, and time constraints, experimental testing is not feasible as the sole structural simulator in PBEE. Alternatively, analytical simulations, where the analytical models are calibrated using the results of the experimental tests, fit reasonably well within the PBEE framework.

One of the key challenges involved in the PBEE approach is the accurate and robust seismic structural analysis. In nonlinear structural dynamics, the most accurate analytical simulation method is accepted to be the nonlinear time history analysis (NTHA). Using this approach, direct integration algorithms in conjunction with nonlinear equation solvers are used to solve the temporally discretized equations of motion that govern the structural responses under dynamic loading. Therefore, the selection of direct integration and nonlinear solution algorithms is essential to ensure accurate and robust NTHA. The used integration algorithms are fundamentally categorized into either implicit or explicit. Explicit algorithms do not require iterations by adopting certain approximations related to the kinematics of the structural system. On the contrary, implicit algorithms involve iterations and need to be complemented by nonlinear equation solvers when applied to nonlinear structural systems. The most standard nonlinear equation solver is the regular Newton-Raphson (NR) algorithm where major drawbacks exist. In order to overcome these drawbacks, a new nonlinear equation solver is developed in this dissertation based on Lyapunov stability theory.

Stability is one of the most important properties of direct integration algorithms that must be considered for efficient and reliable simulations using NTHA. For linear structures, the stability analysis of direct integration algorithms is conducted using the *amplification operator* and its associated *spectral radius*. Such analysis provides useful insight for the selection of the suitable

integration algorithm with the proper time step size to solve a dynamic problem. Integration algorithms, however, are usually applied to multi-degree of freedom (MDOF) nonlinear dynamic problems. Therefore, the stability analysis of direct integration algorithms involving nonlinear dynamics is necessary and should be extended to MDOF structural systems. Two Lyapunov-based approaches are proposed to conduct the stability analysis of direct integration algorithms for nonlinear structural systems.

Another key challenge in the PBEE approach is the selection and modification of ground motions (GMs) to serve as input excitations for the simulations using NTHA of structures. The intricate nonlinear response of structures is highly sensitive to the ground motion selection and modification (GMSM) of the input records. Therefore, the GMSM of the input records are vital prerequisites for accurate seismic analysis. Numerous research efforts focused on developing different GMSM procedures, which are generally categorized into two approaches: (1) amplitude scaling and (2) spectrum shape matching procedures. The first approach selects and modifies the GM records based on scalar intensity measures (IMs). The second approach that takes the spectrum shape into account selects and scales a suite of GM records that has close matching to a target spectrum. Although many GMSM procedures are available, there is no consensus regarding a single accurate method and many studies focused on evaluating these procedures. The existing evaluation studies in the literature are primarily for building structures and considered unidirectional input ground motion. In general, bidirectional GM studies should be conducted, especially for the structures with very different behaviors in two directions, e.g., bridge structures. To fill in this knowledge gap, a framework based on the PBEE approach is proposed to evaluate different GMSM procedures conducting NTHA simulations under bidirectional GM excitations.

In urban societies, reinforced concrete (RC) highway bridges, key components of infrastructure systems, play a significant role in transportation and distribution of goods and commuting people. Therefore, they are expected to sustain minor damage and maintain their functionality in the aftermath of earthquakes, which commonly occur in California due to many active faults. In the last two decades, however, even bridges designed according to modern design codes were observed to experience poor performance or even collapse during earthquakes caused by inherent vulnerability of the bridge structural systems. Thus, accurate seismic structural analysis of existing and newly designed RC highway bridges is fundamental to estimate their seismic demands. As such important lifeline structures, RC highway bridge systems are investigated as an application of the previously discussed theoretical developments proposed in this dissertation to address the two key challenges in the PBEE approach.

In summary, the objective of this study is to enhance the PBEE approach in terms of accurate and robust NTHA simulations and probabilistic evaluation of GMSM procedures. In light of this objective, the major contributions of this study can be summarized as follows:

1. Development of a nonlinear equation solver that attempts to overcome the drawbacks of the NR algorithms.
2. Development of a Lyapunov-based approach that enables performing the stability analysis numerically.
3. Development of a Lyapunov-based approach to investigate the stability of explicit direct integration algorithms for nonlinear MDOF systems by means of the *strictly positive real lemma*.
4. Recommendations of accurate and robust NTHA simulations for RC highway bridge systems.

5. Development of a framework to probabilistically evaluate GMSM procedures with application to RC highway bridge systems.

1.2 ORGANIZATION OF THE DISSERTATION

This dissertation is organized into 10 chapters as schematically illustrated in Figure 1.1 and discussed in this section. After this introductory chapter, Chapter 2 reviews the direct integration algorithms and the nonlinear equation solvers investigated in this study. The theoretical developments are presented in Chapters 3 through 6. Chapter 3 starts with the introduction of continuous-time and discrete-time systems and the definitions of stability. It then introduces the Lyapunov stability theory for these two systems. Based on such theory for continuous-time systems, a new nonlinear equation solver is developed to overcome the drawbacks of the NR algorithms and its convergence performance is demonstrated by several numerical examples. Chapters 4 and 5 utilize the Lyapunov stability theory for discrete-time systems to investigate the stability of direct integration algorithms for nonlinear structural systems. Chapter 4 proposes a numerical approach to transform the problem of seeking a Lyapunov function to a convex optimization problem, i.e., an approach that enables performing the stability analysis numerically. In addition, the accuracy of the integration algorithms is examined using a geometrically nonlinear problem, which has a closed-form exact solution. Chapter 5 proposes another Lyapunov-based approach to investigate the stability of explicit direct integration algorithms for nonlinear MDOF systems by means of the *strictly positive real lemma*. This approach transforms the stability analysis to pursuing the strictly positive realness of the transfer function matrix for the formulated MDOF system. Several examples, including a bridge structure and a generic multi-story shear building, are presented in this chapter to demonstrate this proposed approach. Chapter 6 starts with the well-known PEER PBEE approach. By taking advantage of this approach, it presents a framework for probabilistic evaluation of GMSM procedures.

The application of the theoretical developments in Chapters 3 through 6 is presented in Chapters 7 to 9. Chapter 7 provides a brief introduction of RC highway bridge structures selected in this study and reviews the computational models of these bridges. Chapter 8 investigates solutions to the numerical problems of convergence experienced in the NTHA simulations of these RC highway bridge systems. Recommendations are given in Chapters 8 for the accurate and robust NTHA simulations. Chapter 9 probabilistically evaluates several GMSM procedures considering the distinct structural behaviors in the longitudinal and transverse directions of RC highway bridges under bidirectional GM excitations. A brief summary, the main conclusions and future extension based on this study are presented in Chapter 10. This dissertation also includes six appendices. Appendices A to E give some derivations and details used for the proposed two Lyapunov-based approaches of stability analysis. Appendices E and F document all the utilized GMs in this dissertation.

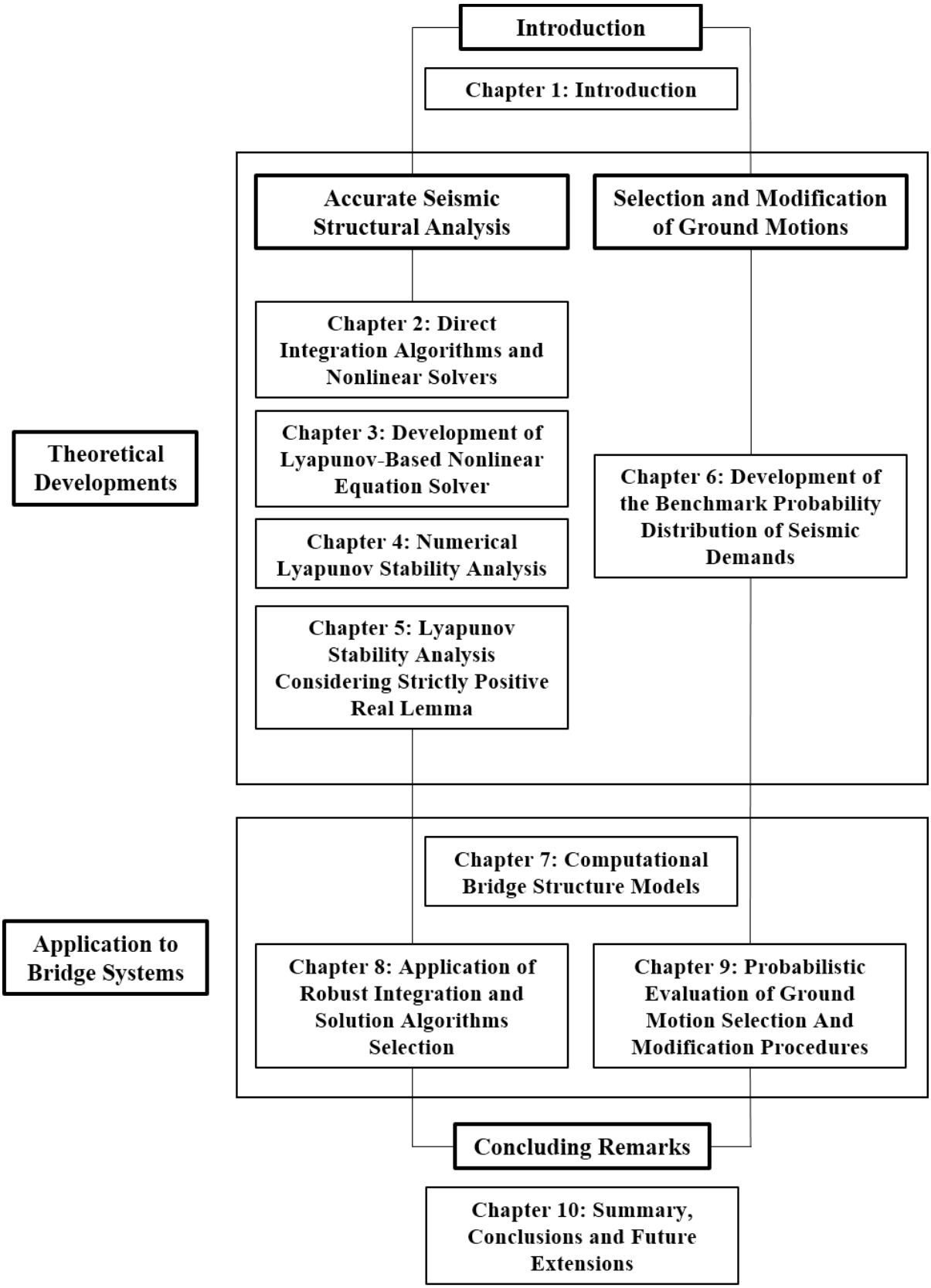

Figure 1.1 Classification of dissertation chapters.

2 Direct Integration Algorithms and Nonlinear Solvers

2.1 INTRODUCTION

The response of a structure to earthquake excitation and the consequences of this response involve various uncertainties at different stages including the definition of hazard, structural response, damage, and the corresponding loss determination. Performance-based Earthquake Engineering (PBEE) approach aims to consider all these uncertainties in order to determine the most efficient decision about the seismic risk mitigation actions [Günay and Mosalam 2013]. In order to achieve this goal of the PBEE approach, considerable amount of structural analytical simulations are required. Attributed to continuous improvement of computational power [Mosalam et al. 2013], nonlinear time history analysis (NTHA) method as the most suitable approach is becoming increasingly prevalent for analyzing large and complex structures.

The structural response under dynamic loading is governed by the differential equations of motion. In structural dynamics, direct integration algorithms are commonly used to solve these equations of motion after they are temporally time-discretized. Various implicit and explicit direct integration methods have been developed. Some examples of well-known methods are the Newmark family of algorithms [Newmark 1959], Hilber-Hughes-Taylor (HHT) algorithm [Hilber et al. 1977], the generalized-α algorithm [Chung and Hulbert 1993], the TRBDF2 algorithm [Bathe 2007], and the Operator-Splitting (OS) algorithms [Hughes et al. 1979], among many others.

Direct integration algorithms for solving a structural dynamics problem are fundamentally categorized into either implicit or explicit. An integration algorithm is explicit when the responses of the next time step depend on the responses of previous and current time steps only. On the other hand, implicit algorithms require iterations because the responses of the next time step depend on the responses of previous, current and also next time steps. Therefore, explicit algorithms do not require iterations by adopting certain approximations related to the kinematics of the structural system. On the contrary, implicit algorithms involve iterations and need to be complemented by nonlinear equation solvers when applied to nonlinear structural systems.

The most standard nonlinear equation solver is the Newton-Raphson (NR) algorithm where its local rate of convergence is quadratic [Bathe 2006]. It requires computing and inverting the Jacobian matrix explicitly at every iteration that can lead to excessive computations. The modified NR algorithm holds the Jacobian matrix constant as the one from the first iteration over the time step. It has a lower computational cost per iteration than the regular NR algorithm but possesses only linear local rate of convergence. For both modified and regular NR algorithms, the search

directions can be improved by line search techniques [Crisfield 1991] when a positive definite Jacobian matrix is obtained. Therefore, this improvement may not always be the case with degrading materials and analysis involving large displacements. Quasi-Newton methods seek a compromise between the modified and regular NR algorithms by modifying the Jacobian matrix with low-rank updates during the search for equilibrium, resulting in a superlinear rate of convergence. Some examples of Quasi-Newton algorithms are the Broyden algorithm [Broyden 1965] and the Broyden–Fletcher–Goldfarb–Shanno (BFGS) algorithm [Broyden 1970; Fletcher 1970; Goldfarb 1970; Shanno 1970]. Krylov-Newton algorithm also seeks a balance between the regular and modified NR algorithms by matrix-vector operations [Scott and Fenves 2010]. The subsequent sections introduce the direct integration algorithms and nonlinear equation solvers investigated in this study.

2.2 DIRECT INTEGRATION ALGORITHMS

The equations of motion of a multi-degree of freedom (MDOF) system under an external dynamic force excitation can be defined as follows:

$$\mathbf{m}\ddot{\mathbf{u}} + \mathbf{c}\dot{\mathbf{u}} + \mathbf{f} = \mathbf{p} \tag{2.1}$$

where $\mathbf{m}$ is the mass matrix, $\mathbf{c}$ is the damping matrix, and $\ddot{\mathbf{u}}$, $\dot{\mathbf{u}}$, $\mathbf{f}$, and $\mathbf{p}$ are the acceleration, velocity, restoring force, and external force vectors, respectively. The restoring force can generally be defined as a function of displacement. Due to several factors, such as the random variation of the external force with time, e.g. due to earthquake shaking, and the nonlinear variation of the restoring force vector with displacement, closed form solution of Eq. (2.1) is not possible [Chopra 2006]. Therefore, numerical integration methods are used for the sought solution.

Differences between direct integration methods are mainly introduced by the way they handle Eqs. (2.2)-(2.4), arranged as the Newmark difference equations for displacement and velocity and the discretized dynamic equilibrium equation, respectively.

$$\mathbf{u}_{i+1} = \mathbf{u}_i + (\Delta t)\dot{\mathbf{u}}_i + \frac{(\Delta t)^2}{2}\left[(1-2\beta)\ddot{\mathbf{u}}_i + 2\beta\,\ddot{\mathbf{u}}_{i+1}\right] \tag{2.2}$$

$$\dot{\mathbf{u}}_{i+1} = \dot{\mathbf{u}}_i + (\Delta t)\left[(1-\gamma)\ddot{\mathbf{u}}_i + \gamma\,\ddot{\mathbf{u}}_{i+1}\right] \tag{2.3}$$

$$\mathbf{m}\ddot{\mathbf{u}}_{i+1} + \mathbf{c}\dot{\mathbf{u}}_{i+1} + \mathbf{f}_{i+1} = \mathbf{p}_{i+1} \tag{2.4}$$

In the above equations, γ and β parameters define the variation of accelerations over a time step, Δt. For example, $\gamma = 1/2$ and $\beta = 1/4$ represent constant average acceleration over the time step, while $\gamma = 1/2$ and $\beta = 1/6$ define linear variation of acceleration during the time step.

The following sub-sections describe the alternative integration methods and their corresponding algorithms, namely the Explicit Newmark, Operator-Splitting, and TRBDF2 integrators and the commonly utilized Implicit Newmark integration method, and the corresponding algorithms. This description starts from the basic three Eqs. (2.2)-(2.4) and emphasizes departure points and differences between these methods.

2.2.1 Explicit Newmark Algorithm

Explicit Newmark (EN) integration [Newmark, 1959] is defined by setting $\beta = 0.0$. In this way, the implicit nature of Eq. (2.2) is eliminated, making the method an explicit one, by removal of the $\ddot{\mathbf{u}}_{i+1}$ term. Accordingly, Eq. (2.2) becomes

$$\mathbf{u}_{i+1} = \mathbf{u}_i + (\Delta t)\dot{\mathbf{u}}_i + \frac{(\Delta t)^2}{2}\ddot{\mathbf{u}}_i \tag{2.5}$$

Substituting Eqs. (2.3) and (2.5) in Eq. (2.4), the linear system of equations defined by Eqs. (2.6) is obtained, which can be solved to determine the acceleration. Subsequently, Eq. (2.3) is used to determine the velocity.

$$\begin{aligned} \mathbf{m}_{\text{eff}}\ddot{\mathbf{u}}_{i+1} &= \mathbf{p}_{\text{eff}} \\ \mathbf{m}_{\text{eff}} &= \mathbf{m} + (\Delta t)\gamma\,\mathbf{c} \\ \mathbf{p}_{\text{eff}} &= \mathbf{p}_{i+1} - \mathbf{f}_{i+1} - \mathbf{c}\left[\dot{\mathbf{u}}_i + (\Delta t)(1-\gamma)\ddot{\mathbf{u}}_i\right] \end{aligned} \tag{2.6}$$

The algorithm for an integration time step of the EN method is summarized as follows:

1. Compute the displacement using Eq. (2.2);
2. Obtain the restoring force, $\mathbf{f}$, corresponding to the computed displacement from the constitutive relationships of the defined materials and elements using a state determination method [Spacone et al. 1996];
3. Calculate the acceleration by solving the linear system of equations defined by Eqs. (2.6);
4. Determine the velocity using Eq. (2.3);
5. Increment *i* and proceed with the next integration time step.

2.2.2 Operator-Splitting Algorithm

Similar to the EN method, the Operator-Splitting (OS) method [Hughes et al. 1979] eliminates the implicit nature of the solution algorithm. However, instead of the direct elimination adopted by the EN, OS uses a prediction-correction technique. The predicted displacement, $\tilde{\mathbf{u}}_{i+1}$, is obtained by neglecting the $\ddot{\mathbf{u}}_{i+1}$ term in the bracketed part of Eq. (2.2), i.e.,

$$\tilde{\mathbf{u}}_{i+1} = \mathbf{u}_i + (\Delta t)\dot{\mathbf{u}}_i + \frac{(\Delta t)^2}{2}\left[(1-2\beta)\ddot{\mathbf{u}}_i\right] \tag{2.7}$$

After the prediction of the displacement, the method is defined by setting the restoring force of the integration time step as the sum of the restoring force corresponding to the predicted displacement, $\tilde{\mathbf{f}}_{i+1}$, and the difference between the corrected and predicted displacements multiplied by the tangential stiffness matrix, $\mathbf{k}_T$, i.e.,

$$\mathbf{f}_{i+1} = \tilde{\mathbf{f}}_{i+1} + \mathbf{k}_T\left(\mathbf{u}_{i+1} - \tilde{\mathbf{u}}_{i+1}\right) \tag{2.8}$$

The difference between the corrected and predicted displacements is defined as follows:

$$\Delta\mathbf{u}_{i+1} = \mathbf{u}_{i+1} - \tilde{\mathbf{u}}_{i+1} \tag{2.9}$$

Substituting Eq. (2.9) in Eq. (2.8) gives,

$$\mathbf{f}_{i+1} = \tilde{\mathbf{f}}_{i+1} + \mathbf{k}_T\left(\Delta\mathbf{u}_{i+1}\right) \tag{2.10}$$

Subtracting Eq. (2.7) from Eq. (2.2) leads to the relationship between $\Delta\mathbf{u}_{i+1}$ and $\ddot{\mathbf{u}}_{i+1}$, i.e.,

$$\ddot{\mathbf{u}}_{i+1} = \frac{\Delta\mathbf{u}_{i+1}}{\left(\Delta t\right)^2\beta} \tag{2.11}$$

Substituting Eq. (2.11) in the Newmark difference equation for velocity, i.e., Eq. (2.3), gives,

$$\dot{\mathbf{u}}_{i+1} = \dot{\mathbf{u}}_i + \left(\Delta t\right)\left(1-\gamma\right)\ddot{\mathbf{u}}_i + \frac{\gamma}{\left(\Delta t\right)\beta}\left(\Delta\mathbf{u}_{i+1}\right) \tag{2.12}$$

The linear system of Eqs. (2.13) is obtained by substitution of Eqs. (2.10), (2.11) and (2.12) in Eq. (2.4), which can be solved to determine the displacement along with Eq. (2.14).

$$\begin{aligned} \mathbf{k}_{\mathbf{eff}}\,\Delta\mathbf{u}_{i+1} &= \mathbf{p}_{\mathrm{eff}} \\ \mathbf{k}_{\mathbf{eff}} &= \frac{1}{\left(\Delta t\right)^2\beta}\mathbf{m} + \frac{\gamma}{\Delta t\,\beta}\,\mathbf{c} + \mathbf{k}_T \\ \mathbf{p}_{\mathbf{eff}} &= \mathbf{p}_{i+1} - \tilde{\mathbf{f}}_{i+1} - \mathbf{c}\left[\dot{\mathbf{u}}_i + \Delta t\left(1-\gamma\right)\ddot{\mathbf{u}}_i\right] \end{aligned} \tag{2.13}$$

$$\mathbf{u}_{i+1} = \tilde{\mathbf{u}}_{i+1} + \Delta\mathbf{u}_{i+1} \tag{2.14}$$

The algorithm for an integration time step of the OS method is summarized as follows:

1. Compute the predicted displacement using Eq. (2.7);
2. Obtain the restoring force, $\tilde{\mathbf{f}}$, corresponding to the predicted displacement from the constitutive relationships of the defined materials and elements using a state determination method [Spacone et al. 1996];
3. Determine the difference between the corrected and the predicted displacements by solving the linear system of equations defined by Eqs. (2.13);
4. Determine the acceleration using Eq. (2.11);
5. Calculate the corrected displacement using Eq. (2.14);
6. Obtain the restoring force corresponding to the corrected displacement following the procedure outlined in step 2 above;
7. Determine the velocity using Eq. (2.12);
8. Increment *i* and proceed with the next integration time step.

It is noted that the initial stiffness matrix, $\mathbf{k}_I$, was used instead of $\mathbf{k}_T$ in some of the studies in literature. For example, [Combescure and Pegon 1997] used $\mathbf{k}_I$ in hybrid simulations involving physical and computational substructures due to the difficulties in obtaining the tangent stiffness matrices of the test specimens.

2.2.3 Implicit Newmark Algorithm

The implicit nature of the solution algorithm is eliminated in the EN and OS methods. In contrast to these methods, the Implicit Newmark (IN) integrator [Newmark 1959] treats the governing equations (difference and dynamic equilibrium equations) directly without altering their implicit nature. Rearranging the time-discrete equilibrium equations, i.e., Eq. (2.4), one obtains

$$\mathbf{p}_{i+1} - \mathbf{m}\ddot{\mathbf{u}}_{i+1} - \mathbf{c}\dot{\mathbf{u}}_{i+1} - \mathbf{f}_{i+1} = \mathbf{0} \tag{2.15}$$

where $\mathbf{u}_{i+1}$ and $\dot{\mathbf{u}}_{i+1}$ are functions of $\ddot{\mathbf{u}}_{i+1}$ through Eqs. (2.2) and (2.3). Morover, $\mathbf{f}_{i+1}$ is a function of $\mathbf{u}_{i+1}$. Therefore, Eq. (2.15) represents a nonlinear system of equations in terms of $\ddot{\mathbf{u}}_{i+1}$. The implicit nature of this equation is eliminated in the EN and OS methods as previously discussed, which is not the case for the IN integration algorithm [Newmark 1959] considering Eq. (2.15).

Using a nonlinear equation solver, Eq. (2.15) can be solved for either the acceleration $\ddot{\mathbf{u}}_{i+1}$ or the displacement increment, $\delta\mathbf{u}_{i+1}$ as defined below, referred to as the acceleration and displacement formulations, respectively. The displacement formulation is presented herein because it leads to fewer convergence problems than the acceleration formulation [Schellenberg et al. 2009]. Moreover, OpenSees [McKenna et al. 2010], the computational platform used to conduct the analyses presented in the following sections, uses the displacement formulation.

In order to solve for the displacement increments, the difference Eqs. (2.2) and (2.3) are redefined such that the velocities and accelerations are expressed in terms of displacements as follows:

$$\ddot{\mathbf{u}}_{i+1} = \frac{\delta \mathbf{u}_{i+1}}{(\Delta t)^2 \beta} - \frac{1}{(\Delta t)\beta}\dot{\mathbf{u}}_i - \left(\frac{1}{2\beta} - 1\right)\ddot{\mathbf{u}}_i \tag{2.16}$$

$$\delta \mathbf{u}_{i+1} = \mathbf{u}_{i+1} - \mathbf{u}_i \tag{2.17}$$

$$\dot{\mathbf{u}}_{i+1} = \frac{\gamma}{(\Delta t)\beta}\delta \mathbf{u}_{i+1} - \left(\frac{\gamma}{\beta} - 1\right)\dot{\mathbf{u}}_i - (\Delta t)\left(\frac{\gamma}{2\beta} - 1\right)\ddot{\mathbf{u}}_i \tag{2.18}$$

As a result of the redefined difference equations, $\dot{\mathbf{u}}_{i+1}$, $\ddot{\mathbf{u}}_{i+1}$ and also $\mathbf{f}_{i+1}$ are represented as functions of $\mathbf{u}_{i+1}$. The most common nonlinear equation solver that can be used to solve the nonlinear system of equations, defined in terms of $\mathbf{u}_{i+1}$ shown in Eq. (2.15), is the regular NR method, which seeks the roots of a function as follows:

$$g'\left(x^k\right)\delta x^k = -g\left(x^k\right) \tag{2.19}$$

where g and g' represent the function and its derivative with respect to x, respectively, x is the root of the function, k is the iteration number and δx^k is the difference between the value of x in the current and previous iterations. If the left-hand side of Eq. (2.15) is considered as the function g in Eq. (2.19), one can write the following in terms of displacement,

$$g'\left(\mathbf{u}_{i+1}^k\right)\delta \mathbf{u}_{i+1}^k = -g\left(\mathbf{u}_{i+1}^k\right) \tag{2.20}$$

$$g\left(\ddot{\mathbf{u}}_{i+1}^k\right) = \mathbf{m}\ddot{\mathbf{u}}_{i+1}^k + \mathbf{c}\dot{\mathbf{u}}_{i+1}^k + \mathbf{f}_{i+1}^k - \mathbf{p}_{i+1} \tag{2.21}$$

$$g'\left(\mathbf{u}_{i+1}^k\right) = \frac{1}{(\Delta t)^2 \beta}\mathbf{m} + \frac{\gamma}{(\Delta t)\beta}\mathbf{c} + \mathbf{k}_T \tag{2.22}$$

where $\mathbf{k}_T$ is the tangential stiffness matrix corresponding to the displacement vector $\mathbf{u}_{i+1}^k$, which can be obtained as a result of a state determination method [Spacone et al. 1996]. Substitution of Eqs. (2.21) and (2.22) in Eq. (2.20) leads to the linear system of Eqs. (2.23) in the same format as the other methods explained earlier.

$$\begin{aligned} \mathbf{k}_{\text{eff}}\,\delta \mathbf{u}_{i+1}^k &= \mathbf{p}_{\text{eff}} \\ \mathbf{k}_{\text{eff}} &= \frac{1}{(\Delta t)^2 \beta}\mathbf{m} + \frac{\gamma}{(\Delta t)\beta}\mathbf{c} + \mathbf{k}_T \\ \mathbf{p}_{\text{eff}} &= \mathbf{p}_{i+1} - \mathbf{m}\ddot{\mathbf{u}}_{i+1}^k - \mathbf{c}\dot{\mathbf{u}}_{i+1}^k - \mathbf{f}_{i+1}^k \end{aligned} \tag{2.23}$$

At this point, it is beneficial to state that all three methods discussed above reduce the nonlinear differential equations of motion to a system of linear algebraic equations. However, depending on the way each method treats the three basic Eqs. (2.2)-(2.4), the resulting coefficient matrix (or the Jacobian matrix), $\mathbf{m}_{\text{eff}}$ for EN, and $\mathbf{k}_{\text{eff}}$ for OS and IN, and the effective load vector,

$\mathbf{p}_{\text{eff}}$, differ from one method to the other. Accordingly, these differences determine the adequacy and ease of application of each method as explained later.

After the determination of the displacement increment for iteration k from Eqs. (2.23), the method continues by the calculation of the displacement, velocity and acceleration for iteration $k+1$ using Eqs. (2.24)-(2.26), respectively.

$$\mathbf{u}_{i+1}^{k+1} = \mathbf{u}_{i+1}^{k} + \delta \mathbf{u}_{i+1}^{k} \tag{2.24}$$

$$\dot{\mathbf{u}}_{i+1}^{k+1} = \frac{\gamma}{\Delta t \beta}\left(\mathbf{u}_{i+1}^{k+1} - \mathbf{u}_i\right) - \left(\frac{\gamma}{\beta} - 1\right)\dot{\mathbf{u}}_i - \Delta t\left(\frac{\gamma}{2\beta} - 1\right)\ddot{\mathbf{u}}_i \tag{2.25}$$

$$\ddot{\mathbf{u}}_{i+1}^{k+1} = \frac{1}{(\Delta t)^2 \beta}\left(\mathbf{u}_{i+1}^{k+1} - \mathbf{u}_i\right) - \frac{1}{\Delta t\, \beta}\dot{\mathbf{u}}_i - \left(\frac{1}{2\beta} - 1\right)\ddot{\mathbf{u}}_i \tag{2.26}$$

An iterative method requires an initial guess for the sought value, i.e., for $\ddot{\mathbf{u}}_{i+1}^{k=1}$. For the regular NR method, displacement of the previous iteration can be used as the initial guess as defined in Eq. (2.27). Subsequent substitution of this equation into Eqs. (2.2) and (2.3) leads to the corresponding velocity and acceleration, i.e., $\dot{\mathbf{u}}_{i+1}^{k=1}$ and $\ddot{\mathbf{u}}_{i+1}^{k=1}$ vectors as follows

$$\mathbf{u}_{i+1}^{k=1} = \mathbf{u}_i \tag{2.27}$$

$$\dot{\mathbf{u}}_{i+1}^{k=1} = -\left(\frac{\gamma}{\beta} - 1\right)\dot{\mathbf{u}}_i - (\Delta t)\left(\frac{\gamma}{2\beta} - 1\right)\ddot{\mathbf{u}}_i \tag{2.28}$$

$$\ddot{\mathbf{u}}_{i+1}^{k=1} = -\frac{1}{(\Delta t)\beta}\dot{\mathbf{u}}_i - \left(\frac{1}{2\beta} - 1\right)\ddot{\mathbf{u}}_i \tag{2.29}$$

The algorithm for an integration time step of the IN method is summarized as follows:

1. Determine the initial guess, $k = 1$, for displacement from Eq. (2.27) and the corresponding velocity and acceleration from Eqs. (2.28) and (2.29), respectively;

For each iteration k =1: N, where N is the total number of iterations:

2. Obtain the restoring force, $\mathbf{f}$, corresponding to the computed displacement from the constitutive relationships of the defined materials and elements using a state determination method [Spacone et al. 1996];
3. Determine the displacement increment by solving the linear system of equations defined by Eqs. (2.23).
4. Compute the displacement, velocity and acceleration using Eqs. (2.24)-(2.26);
5. Check convergence by comparing a calculated norm with a defined tolerance value. If the norm is smaller than the tolerance, set $N = k$, increment i and proceed to the next time integration step; otherwise, increment k and go to step 2.

Regarding the above algorithm, two remarks are stated as follows:

- The presence of the convergence check requires at least two iterations. Therefore, unless a solution is separately coded for a linear case, a general nonlinear analysis software requires at least two iterations for the IN integration, even for the case of a linear problem.
- Different norms can be used for the convergence check in step 5. Examples of these norms are the displacement increment, unbalanced force and energy norms.

2.2.4 TRBDF2 Algorithm

TRBDF2 method [Bank et al. 1985; Bathe and Baig 2005; Bathe 2007] is a composite integration method, that uses IN and three point backward Euler scheme, alternately in consecutive integration time steps. The first step uses the IN method with constant average acceleration, i.e. with $\gamma = 1/2$ and $\beta = 1/4$ in the difference Eqs. (2.2) and (2.3). The consequent step uses the equations of the three-point Euler backward method, i.e., Eqs. (2.30) and (2.31) for the relationship between the displacement, velocity and acceleration, instead of the Newmark difference Eqs. (2.2) and (2.3).

$$\dot{\mathbf{u}}_{i+1} = \frac{\mathbf{u}_{i+1} - 4\mathbf{u}_i + 3\mathbf{u}_{i-1}}{\Delta t} \tag{2.30}$$

$$\ddot{\mathbf{u}}_{i+1} = \frac{\dot{\mathbf{u}}_{i+1} - 4\dot{\mathbf{u}}_i + 3\dot{\mathbf{u}}_{i-1}}{\Delta t} \tag{2.31}$$

Following the regular NR method as demonstrated for IN, the following linear system of Eqs. (2.32) is obtained:

$$\mathbf{k}_{\text{eff}}\,\delta\mathbf{u}_{i+1}^{k}=\mathbf{p}_{\text{eff}}$$
$$\mathbf{k}_{\text{eff}}=\frac{9}{(\Delta t)^2}\mathbf{m}+\frac{3}{\Delta t}\mathbf{c}+\mathbf{k}_T \tag{2.32}$$
$$\mathbf{p}_{\text{eff}}=\mathbf{p}_{i+1}-\mathbf{m}\left(\frac{9\mathbf{u}_{i+1}^{k}-12\mathbf{u}_i+3\mathbf{u}_{i-1}}{(\Delta t)^2}-\frac{4\dot{\mathbf{u}}_i-\dot{\mathbf{u}}_{i-1}}{\Delta t}\right)-\mathbf{c}\left(\frac{3\mathbf{u}_{i+1}^{k}-4\mathbf{u}_i+\mathbf{u}_{i-1}}{\Delta t}\right)-\mathbf{f}_{i+1}^{k}$$

After the determination of the displacement increment for iteration k from Eqs. (2.32), the method continues by the calculation of the displacement, velocity and acceleration for iteration $k+1$ using Eqs. (2.33)-(2.35), respectively.

$$\mathbf{u}_{i+1}^{k+1}=\mathbf{u}_{i+1}^{k}+\delta\mathbf{u}_{i+1}^{k} \tag{2.33}$$

$$\dot{\mathbf{u}}_{i+1}^{k+1}=\frac{\mathbf{u}_{i+1}^{k+1}-4\mathbf{u}_i+3\mathbf{u}_{i\text{-}1}}{\Delta t} \tag{2.34}$$

$$\ddot{\mathbf{u}}_{i+1}^{k+1}=\frac{\dot{\mathbf{u}}_{i+1}^{k+1}-4\dot{\mathbf{u}}_i+3\dot{\mathbf{u}}_{i\text{-}1}}{\Delta t} \tag{2.35}$$

It is noted that the consecutive steps are considered as the sub-steps of a one step in [Bathe and Baig 2005; Bathe 2007], rather than considering them as consecutive steps, which is exactly the same as the formulation presented above, but with a time step $\Delta t/2$. [Bathe and Baig 2005] and [Bathe 2007] used the method in structural dynamics to conserve energy and momentum at large deformations (not necessarily involving material nonlinearity) where the IN method may fail to do so and become unstable. Herein, it is considered not because of its superior stability performance than that of IN, but because of its better convergence behavior, due to the numerical damping provided by the Euler backward method, as discussed in the next chapter.

2.3 NONLINEAR EQUATION SOLVERS

Eq. (2.4) can be written in a residual form as follows:

$$\mathbf{r}(\mathbf{u})=\mathbf{p}-\mathbf{m}\ddot{\mathbf{u}}-\mathbf{c}\dot{\mathbf{u}}-\mathbf{f} \tag{2.36}$$

The statement of equilibrium requires that the residual forces to be zeros, i.e.,

$$\mathbf{r}(\mathbf{u})=\mathbf{0} \tag{2.37}$$

The following sub-sections describe how each of the discussed nonlinear solvers attempt to satisfy Eq. (2.37). It is noted that the subscript *i* representing the number of the integration time step is dropped to simplify the expressions in the following sub-sections.

2.3.1 Regular Newton-Raphson Algorithm

The regular NR algorithm is based on linear approximation of the residual vector as follows:

$$\mathbf{r}\left(\mathbf{u}^k + \Delta\mathbf{u}^{k+1}\right) \approx \mathbf{r}\left(\mathbf{u}^k\right) + \frac{\partial \mathbf{r}\left(\mathbf{u}^k\right)}{\partial \mathbf{u}}\left(\Delta\mathbf{u}^{k+1}\right) \tag{2.38}$$

The superscript k denotes the iteration number within one time step and the matrix $\frac{\partial \mathbf{r}\left(\mathbf{u}^k\right)}{\partial \mathbf{u}}$ is called the system Jacobian matrix, which can be denoted as follows,

$$\mathbf{J}_k = \frac{\partial \mathbf{r}\left(\mathbf{u}^k\right)}{\partial \mathbf{u}} = -\mathbf{k}_T \tag{2.39}$$

where $\mathbf{k}_T$ is the tangential stiffness matrix. The algorithm starts with an initial guess and iterates with the following equations until a certain convergence criterion is met.

$$\begin{aligned} \Delta\mathbf{u}^{k+1} &= -\mathbf{J}_k^{-1}\,\mathbf{r}\left(\mathbf{u}^k\right) = \mathbf{k}_T^{-1}\,\mathbf{r}\left(\mathbf{u}^k\right) \\ \mathbf{u}^{k+1} &= \mathbf{u}^k + \Delta\mathbf{u}^{k+1} \end{aligned} \tag{2.40}$$

2.3.2 Broyden Algorithm

In regular NR algorithm, the Jacobian matrix is computed at every iteration, which is a complicated and expensive operation. The idea behind Broyden method is to compute the whole Jacobian only at the first iteration, and to do a *rank-one update* at the other iterations [Broyden 1965], i.e.,

$$\mathbf{J}_k = \mathbf{J}_{k\text{-}1} + \frac{\Delta\mathbf{r}^k - \mathbf{J}_{k\text{-}1}\Delta\mathbf{u}^k}{\left\|\Delta\mathbf{u}^k\right\|^2}\left(\Delta\mathbf{u}^k\right)^T \tag{2.41}$$

where $\|\bullet\|$ indicates the discrete L_2-norm[1] and superscript T indicates transpose.

$$\begin{aligned} \Delta\mathbf{u}^k &= \mathbf{u}^k - \mathbf{u}^{k\text{-}1} \\ \Delta\mathbf{r}^k &= \mathbf{r}^k - \mathbf{r}^{k\text{-}1} \end{aligned} \tag{2.42}$$

Subsequently, the algorithm proceeds with Eqs. (2.40) as in the regular NR algorithm. It is to be noted that the modified NR is a special case where the rank-one update is ignored.

[1] $\|\mathbf{u}\| = \sqrt{\sum_{i=1}^{n} u_i^2}$ where n in the number of components of the vector $\mathbf{u}$

2.3.3 Newton-Raphson with Line Search Algorithm

The direction of $\Delta\mathbf{u}$ determined by the regular NR method is often correct. However, the same is not always true for the step size $\|\Delta\mathbf{u}\|$. Furthermore, it is computationally less expensive to compute the residual for several points along $\Delta\mathbf{u}$ rather than forming and factorizing a new Jacobian matrix [Crisfield 1991].

In the Newton-Raphson with Line Search (NRLS) algorithm, the regular NR method is used to compute $\Delta\mathbf{u}$. However, only a certain portion of the calculated $\Delta\mathbf{u}$ is used to determine the displacement in the next iteration as follows:

$$\begin{aligned} \Delta\mathbf{u}^{k+1} &= -\mathbf{J}_k^{-1}\,\mathbf{r}\left(\mathbf{u}^k\right) = \mathbf{k}_T^{-1}\,\mathbf{r}\left(\mathbf{u}^k\right) \\ \mathbf{u}^{k+1} &= \mathbf{u}^k + \eta\,\Delta\mathbf{u}^{k+1} \end{aligned} \tag{2.43}$$

Four types of line search algorithm are available in OpenSees [McKenna *et al.* 2010]: *Bisection*, *Secant*, *RegulaFalsi* and *Interpolated*. The different line search algorithms embrace different root finding methods to determine the factor η. A root of the function $s(\eta)$ is defined as follows:

$$s(\eta) = \Delta\mathbf{u}^{k+1}\,\mathbf{r}\left(\mathbf{u}^k + \eta\,\Delta\mathbf{u}^{k+1}\right) \tag{2.44}$$

with the following initial guess

$$s_0 = \Delta\mathbf{u}^{k+1}\mathbf{r}\left(\mathbf{u}^k\right) \tag{2.45}$$

2.3.4 Broyden–Fletcher–Goldfarb–Shanno Algorithm

From an initial guess $\mathbf{u}_0$ and an approximate Hessian matrix[2] $\mathbf{B}_0$, the following steps in the Broyden–Fletcher–Goldfarb–Shanno (BFGS) algorithm are repeated until convergence [Bathe and Cimento 1980]:

1) A direction $\Delta\mathbf{u}^k$ is obtained by solving the following equation:

$$\mathbf{B}_k\left(\Delta\mathbf{u}^k\right) = -\nabla\mathbf{r}\left(\mathbf{u}^k\right) \tag{2.46}$$

where $\mathbf{B}_k$ is an approximation of the Hessian matrix, which is updated at each iteration, and $\nabla\mathbf{r}\left(\mathbf{u}^k\right)$ is the gradient[3] of the function evaluated at $\mathbf{u}^k$.

2) A line search is performed to find the step size η^k for the *k-th* iteration and update the displacement as follows:

---

[2]Hessian matrix is a square matrix of second-order partial derivatives of a function.

[3] $\nabla f = \dfrac{\partial f}{\partial x}\mathbf{i} + \dfrac{\partial f}{\partial y}\mathbf{j} + \dfrac{\partial f}{\partial z}\mathbf{k}$ where $\mathbf{i}, \mathbf{j}$ and $\mathbf{k}$ are unit vectors in the directions x, y and z, respectively.

$$\mathbf{u}^{k+1} = \mathbf{u}^k + \eta^k \Delta\mathbf{u}^k \tag{2.47}$$

3) Set the Hessian matrix, which is updated for the next iteration as follows:

$$\mathbf{B}_{k+1} = \mathbf{B}_k + \frac{\mathbf{y}^k \left(\mathbf{y}^k\right)^T}{\left(\mathbf{y}^k\right)^T \mathbf{s}^k} - \frac{\mathbf{B}_k \mathbf{s}^k \left(\mathbf{s}^k\right)^T \mathbf{B}_k}{\left(\mathbf{s}^k\right)^T \mathbf{B}_k \mathbf{s}^k} \tag{2.48}$$

where

$$\mathbf{s}^k = \eta^k \Delta\mathbf{u}^k \tag{2.49}$$

$$\mathbf{y}^k = \nabla\mathbf{r}\left(\mathbf{u}^{k+1}\right) - \nabla\mathbf{r}\left(\mathbf{u}^k\right) \tag{2.50}$$

2.3.5 Krylov-Newton Algorithm

At each time step, instead of Eq. (2.37), the Krylov-Newton algorithm seeks the solution to the system of the following preconditioned residual equations [Scott and Fenves 2010]:

$$\mathbf{R}(\mathbf{u}) = \mathbf{k}_0^{-1}\mathbf{r}(\mathbf{u}) = \mathbf{0} \tag{2.51}$$

where $\mathbf{k}_0$ is the tangential stiffness at the first iteration of the time step. The solution to Eq. (2.51) is equivalent to that of Eq. (2.37) as long as $\mathbf{k}_0$ is nonsingular. Thus, Eq. (2.38) becomes

$$\mathbf{R}\left(\mathbf{u}^{k+1}\right) = \mathbf{R}\left(\mathbf{u}^k\right) - \mathbf{A}\,\Delta\mathbf{u}^{k+1} = \mathbf{0} \tag{2.52}$$

where $\mathbf{A}$ is the identity matrix when modified NR algorithm is used, while $\mathbf{A} = \mathbf{k}_0^{-1}\mathbf{k}_T$ when using the regular NR algorithm. The tangent at the initial guess, instead of the current tangent, is used for the modified NR algorithm in the iterations.

The Krylov-Newton algorithm decomposes $\Delta\mathbf{u}^{k+1}$ into two components as follows:

$$\Delta\mathbf{u}^{k+1} = \mathbf{w}^{k+1} + \mathbf{q}^{k+1} \tag{2.53}$$

where $\mathbf{w}^{k+1}$ is the acceleration component and $\mathbf{q}^{k+1}$ is the standard modified Newton component. $\mathbf{w}^{k+1}$ is further represented as a linear combination of the vectors from the subspace of displacement increments with size *m*, i.e.,

$$\mathbf{w}^{k+1} = c_1\Delta\mathbf{u}^1 + \cdots + c_m\Delta\mathbf{u}^m \tag{2.54}$$

To satisfy Eq. (2.52), the first step is to minimize the norm of vector $\mathbf{R}\left(\mathbf{u}^k\right) - \mathbf{A}\mathbf{w}^{k+1}$, which represents an over-determined system of equations for the unknown coefficients $c_1, \ldots c_m$ in Eq. (2.54), by least-squares analysis [Golub and Van Loan 1996]. The second step for satisfying Eq. (2.52) is to solve the following equations:

$$\mathbf{R}\left(\mathbf{u}^{k+1}\right) = \mathbf{g}_k - \mathbf{A}\mathbf{q}^{k+1} = \mathbf{0} \tag{2.55}$$

where $\mathbf{g}_k = \mathbf{R}(\mathbf{u}^k) - \mathbf{A}\mathbf{w}^{k+1}$, and $\mathbf{A}$ is the identity matrix using the modified NR algorithm. Thus,

$$\mathbf{q}^{k+1} = \mathbf{g}_k \tag{2.56}$$

The displacement increment is then calculated by summing the two components determined from Eqs. (2.54) and (2.56).

3 Development of Lyapunov-Based Nonlinear Equation Solver

3.1 INTRODUCTION

The regular Newton-Raphson (NR) algorithm reviewed in Chapter 2 is the most standard and commonly used nonlinear equation solver in nonlinear structural analysis subjected to static and/or dynamic loading. However, major drawbacks exist in this algorithm:

1. The Jacobian matrix is required to be computed explicitly, which maybe computationally expensive and difficult;
2. The Jacobian matrix is required to be invertible;
3. The convergence of this algorithm is not guaranteed, i.e., the initial guess is important and needs to be within the region of attraction of the solution point.

Lyapunov stability theory [Khalil 2002; Haddad and Chellaboina 2008], developed by the Russian mathematician Aleksandr Lyapunov in [Lyapunov 1892], is the most complete framework of stability analysis for dynamical systems. It is based on constructing a function of the system state coordinates (usually considered as the energy function of the system) that serves as a generalized norm of the solution of the dynamical system. The appeal of Lyapunov stability theory resides in the fact that conclusions about the stability behavior of the dynamical system can be obtained without actually computing the system solution trajectories. As a consequence, Lyapunov stability theory has become one of the most fundamental and standard tools of dynamical systems and control theory.

This chapter proposes a nonlinear equation solver for nonlinear structural analysis for problems involving static and/or dynamic loads based on Lyapunov stability theory. Several recent works that are similar in spirit to this development are [Milano 2009; Xie et al. 2013] that are applied to power flow problems. The main idea is to reformulate the equations of motions into a hypothetical dynamical system characterized by a set of ordinary differential equations, whose equilibrium points represent the solutions of the nonlinear structural problems. Starting from the Lyapunov stability theory, it is demonstrated that this hypothetical dynamical system is characterized by a globally asymptotic stability, i.e., convergence, to the equilibrium points for structural dynamics. This feature overcomes the inherent limitations of the traditional iterative minimization algorithms and has no restriction on the selection of the initial guess for various structural nonlinear behaviors. Comparisons between the proposed algorithm and regular NR algorithm are presented using several numerical examples from structural statics and dynamics.

3.2 STABILITY OF NONLINEAR SYSTEMS

The stability of two categories, continuous-time and discrete-time nonlinear systems, is presented in this section.

3.2.1 Continuous-Time Systems

Consider a continuous-time nonlinear system [Khalil 2002]:

$$\dot{\boldsymbol{x}} = \mathbf{g}(\boldsymbol{x}) \tag{3.1}$$

and assume its equilibrium point is at $\boldsymbol{x} = \mathbf{0}$, i.e., $\mathbf{g}(\mathbf{0}) = \mathbf{0}$. If the equilibrium of interest is $\boldsymbol{x}^*$ that is other than zero, i.e., $\boldsymbol{x}^* \neq \mathbf{0}$, let

$$\tilde{\boldsymbol{x}} = \boldsymbol{x} - \boldsymbol{x}^* \tag{3.2}$$

and therefore

$$\dot{\tilde{\boldsymbol{x}}} = \boldsymbol{g}(\boldsymbol{x}) = \boldsymbol{g}(\tilde{\boldsymbol{x}} + \boldsymbol{x}^*) = \tilde{\boldsymbol{g}}(\tilde{\boldsymbol{x}}) \tag{3.3}$$

which leads to

$$\tilde{\mathbf{g}}(\mathbf{0}) = \mathbf{0} \tag{3.4}$$

3.2.2 Discrete-Time Systems

Similarly, consider a nonlinear discrete-time system [Khalil 2002]:

$$\boldsymbol{x}_{k+1} = \mathbf{g}(\boldsymbol{x}_k) \tag{3.5}$$

and assume that the system has an equilibrium point at the origin, i.e., $\mathbf{g}(\mathbf{0}) = \mathbf{0}$. If the equilibrium of interest is $\boldsymbol{x}^*$ that is other than zero, i.e., $\boldsymbol{x}^* \neq \mathbf{0}$, let

$$\tilde{\boldsymbol{x}}_k = \boldsymbol{x}_k - \boldsymbol{x}^* \tag{3.6}$$

and therefore

$$\tilde{\boldsymbol{x}}_{k+1} + \boldsymbol{x}^* = \mathbf{g}(\boldsymbol{x}_k) = \mathbf{g}(\tilde{\boldsymbol{x}}_k + \boldsymbol{x}^*) \tag{3.7}$$

$$\tilde{\boldsymbol{x}}_{k+1} = \mathbf{g}(\tilde{\boldsymbol{x}}_k + \boldsymbol{x}^*) - \boldsymbol{x}^* = \tilde{\mathbf{g}}(\tilde{\boldsymbol{x}}_k) \tag{3.8}$$

which also leads to Eq. (3.4).

3.2.3 Stability Definitions

Stability: The equilibrium $\boldsymbol{x} = \mathbf{0}$ is stable if for each $\varepsilon > 0$, there exists $\delta > 0$ such that:

$$|\boldsymbol{x}(0)| \le \delta \Rightarrow |\boldsymbol{x}(t)| \le \varepsilon \tag{3.9}$$

for all $t \ge 0$ [Khalil 2002]. The equilibrium point is unstable if it is not stable.

Asymptotic stability: The equilibrium $\boldsymbol{x} = \mathbf{0}$ is asymptotically stable if it is stable and $\boldsymbol{x}(0) \to 0$ for all $\boldsymbol{x}(0)$ in a neighborhood of $\boldsymbol{x} = \mathbf{0}$.

Global asymptotic stability: The equilibrium $\boldsymbol{x} = \mathbf{0}$ is globally asymptotically stable if it is stable and $\boldsymbol{x}(0) \to 0$ for all $\boldsymbol{x}(0)$. It is noted that $\boldsymbol{x}(0) \to 0$ does not necessarily guarantee stability. For example, trajectories may converge to the origin only after a large detour that violates the stability definition in Eq. (3.9).

3.3 LYAPUNOV STABILITY THEORY

The Lyapunov stability theory is discussed in this section. This discussion focus on the previously discussed continuous-time and discrete-time nonlinear systems.

3.3.1 Continuous-Time Systems

Let v be a continuously differentiable scalar function defined on the domain $D \in R^n$ that contains the origin. The equilibrium point $\boldsymbol{x} = \mathbf{0}$ is stable if the following conditions are satisfied [Khalil 2002]:

$$v(\mathbf{0}) = 0 \text{ and } v(\boldsymbol{x}) > 0 \quad \forall \boldsymbol{x} \in D - \{\mathbf{0}\} \tag{3.10}$$

and

$$\dot{v}(\boldsymbol{x}) = \frac{d}{dt} v(\boldsymbol{x}) = \nabla v(\boldsymbol{x})^T \cdot \mathbf{g}(\boldsymbol{x}) \le 0 \quad \forall \boldsymbol{x} \in D \tag{3.11}$$

Moreover, $\boldsymbol{x} = \mathbf{0}$ is asymptotically stable if

$$\dot{v}(\boldsymbol{x}) < 0 \quad \forall \boldsymbol{x} \in D - \{\mathbf{0}\} \tag{3.12}$$

If, in addition, $D = R^n$ and the Lyapunov function v is radially unbounded, i.e.,

$$|\boldsymbol{x}| \to \infty \Rightarrow v(\boldsymbol{x}) \to \infty \tag{3.13}$$

then $\boldsymbol{x} = \mathbf{0}$ is globally asymptotically stable.

3.3.2 Discrete-Time Systems

Analogously to the continuous-time systems case, the discrete-time Lyapunov stability theory is discussed herein. let v be a continuously scalar function defined on the domain D that contains the origin. The equilibrium point $\boldsymbol{x} = \mathbf{0}$ is stable if [Khalil 2002] Eqs. (3.10) and (3.14) are satisfied.

$$\Delta v_{k+1} = v(\boldsymbol{x}_{k+1}) - v(\boldsymbol{x}_k) \leq 0 \quad \forall \boldsymbol{x} \in D \tag{3.14}$$

Moreover, $\boldsymbol{x} = \mathbf{0}$ is asymptotically stable if

$$\Delta v(\boldsymbol{x}_{k+1}) < 0 \quad \forall x \in D - \{\mathbf{0}\} \tag{3.15}$$

If, in addition, $D = R^n$ and the Lyapunov function v is radially unbounded as defined in Eq. (3.13), then $\boldsymbol{x} = \mathbf{0}$ is globally asymptotically stable.

For continuous time systems, it is required that the derivative of the Lyapunov function is negative along the trajectories. For discrete-time systems, it is required that the difference in the Lyapunov function is negative along the trajectories. Also, quite importantly we do not require that v is continuously differentiable, but to be only continuous.

3.4 LYAPUNOV-BASED NONLINEAR EQUATION SOLVER

As stated in Eq. (2.37), the general formulation of nonlinear set of equation is as follows:

$$\mathbf{g}(\boldsymbol{x}) = \mathbf{0} \tag{3.16}$$

Consider a hypothetical dynamical system characterized by the following first order differential equation

$$\dot{\boldsymbol{x}} = -\mathbf{K}\left[\frac{\partial}{\partial \boldsymbol{x}} \boldsymbol{g}(\boldsymbol{x})\right]^T \mathbf{g}(\boldsymbol{x}) = -\mathbf{K}\mathbf{J}(\boldsymbol{x})^T \mathbf{g}(\boldsymbol{x}) \tag{3.17}$$

where $\mathbf{K}$ is positive definite, i.e., $\mathbf{K} = \mathbf{K}^T \succ \mathbf{0}$ and the Jacobian matrix

$$\mathbf{J}(\boldsymbol{x}) = \frac{\partial}{\partial \boldsymbol{x}} \mathbf{g}(\boldsymbol{x}) \tag{3.18}$$

For this system, the Lyapunov function is chosen as follows:

$$v(\boldsymbol{x}) = \frac{1}{2} \mathbf{g}(\boldsymbol{x})^T \mathbf{g}(\boldsymbol{x}) \tag{3.19}$$

A sufficient condition for the system, and thus the direct integration algorithm, to be stable is as follows:

$$\begin{aligned}\dot{v}(\boldsymbol{x}) &= \frac{1}{2}\left[\frac{\partial}{\partial \boldsymbol{x}}\mathbf{g}(\boldsymbol{x})\dot{\boldsymbol{x}}\right]^T \mathbf{g}(\boldsymbol{x}) + \frac{1}{2}\mathbf{g}(\boldsymbol{x})^T\left[\frac{\partial}{\partial \boldsymbol{x}}\mathbf{g}(\boldsymbol{x})\dot{\boldsymbol{x}}\right] \\ &= -\frac{1}{2}\left[\mathbf{J}(\boldsymbol{x})\mathbf{K}\mathbf{J}(\boldsymbol{x})^T\mathbf{g}(\boldsymbol{x})\right]^T\mathbf{g}(\boldsymbol{x}) - \frac{1}{2}\mathbf{g}(\boldsymbol{x})^T\left[\mathbf{J}(\boldsymbol{x})\mathbf{K}\mathbf{J}(\boldsymbol{x})^T\mathbf{g}(\boldsymbol{x})\right] \\ &= -\mathbf{g}(\boldsymbol{x})^T\mathbf{J}(\boldsymbol{x})\mathbf{K}\mathbf{J}(\boldsymbol{x})^T\mathbf{g}(\boldsymbol{x})\end{aligned} \tag{3.20}$$

Considering the Jacobian matrix $\mathbf{J}(\boldsymbol{x})$ is well-defined, i.e., $\mathbf{J}(\boldsymbol{x}) \neq \mathbf{0}$, $\mathbf{J}(\boldsymbol{x})\mathbf{K}\mathbf{J}(\boldsymbol{x})^T$ is positive definite and therefore $\dot{v}(\boldsymbol{x}) < 0$ where the asymptotical stability condition of the hypothetical dynamical system in Eq. (3.17) is guaranteed. Then any differential equation solver can be used to solve Eq. (3.17), starting from the initial condition (or guess) $\boldsymbol{x}(t=0) = \boldsymbol{x}^0$. To reduce the computational expense of calculating $\mathbf{J}(\boldsymbol{x})$, a special case of Eq. (3.17) is to replace $\mathbf{J}(\boldsymbol{x})$ with the constant $\mathbf{J}(\boldsymbol{x}^0)$.

3.4.1 Static Problems

For static structural problems, Eqs. (3.16) and (3.17) become

$$\mathbf{g} = \mathbf{f}(\mathbf{u}) = \mathbf{0} \tag{3.21}$$

$$\dot{\mathbf{u}} = -\mathbf{K}\left[\frac{\partial}{\partial \mathbf{u}}\mathbf{f}(\mathbf{u})\right]^T \mathbf{f}(\mathbf{u}) = -\mathbf{K}\mathbf{J}(\mathbf{u})^T\mathbf{f}(\mathbf{u}) = -\mathbf{K}\mathbf{k}_T^T\mathbf{f}(\mathbf{u}) \tag{3.22}$$

and the corresponding Jacobian matrix is

$$\mathbf{J}(\mathbf{u}) = \frac{\partial}{\partial \mathbf{u}}\mathbf{f}(\mathbf{u}) = \mathbf{k}_T \tag{3.23}$$

where $\mathbf{k}_T$ is the tangent stiffness of the structural system. The Lyapunov function corresponding to Eq. (3.19) becomes

$$v(\mathbf{u}) = \frac{1}{2}\mathbf{f}(\mathbf{u})^T\mathbf{f}(\mathbf{u}) \tag{3.24}$$

Therefore, as proved previously, the hypothetical dynamical system in Eq. (3.22) is asymptotically stable. Moreover, if the restoring force is radially unbounded, i.e.,

$$|\mathbf{u}| \to \infty \Rightarrow \mathbf{f}(\mathbf{u}) \to \infty \Rightarrow v(\mathbf{u}) \to \infty \tag{3.25}$$

Then, the hypothetical system in Eq. (3.22) is globally asymptotically stable and converges to the equilibrium corresponding to $v(\mathbf{u}) = 0$ and thus $\mathbf{f}(\mathbf{u}) = \mathbf{0}$. It is to be noted that the tangent stiffness matrix $\mathbf{k}_T$ can be replaced by the constant stiffness matrix at the initial guess at $\mathbf{u}^0$.

3.4.2 Dynamic Problems

For a structural system subjected to dynamic loadings, e.g., earthquake excitations, the discretized equations of nodal equilibrium for the nonlinear dynamic response of the structural system can be written in the following residual form

$$\mathbf{g}(\mathbf{u}_{i+1}) = \mathbf{m}\ddot{\mathbf{u}}_{i+1} + \mathbf{c}\dot{\mathbf{u}}_{i+1} + \mathbf{f}_{i+1} - \mathbf{p}_{i+1} \tag{3.26}$$

Consider using the implicit Newmark integration algorithm and reorder the Newmark difference equations Eqs. (2.2) and (2.3) as follows:

$$\dot{\mathbf{u}}_{i+1} = \frac{\gamma}{(\Delta t)\beta}(\mathbf{u}_{i+1} - \mathbf{u}_i) - \left(\frac{\gamma}{\beta} - 1\right)\dot{\mathbf{u}}_i - (\Delta t)\left(\frac{\gamma}{2\beta} - 1\right)\ddot{\mathbf{u}}_i \tag{3.27}$$

$$\ddot{\mathbf{u}}_{i+1} = \frac{1}{(\Delta t)^2\beta}(\mathbf{u}_{i+1} - \mathbf{u}_i) - \frac{1}{(\Delta t)\beta}\dot{\mathbf{u}}_i - \left(\frac{1}{2\beta} - 1\right)\ddot{\mathbf{u}}_i \tag{3.28}$$

Substituting Eqs. (3.27) and (3.28) into Eq. (3.26) leads to the following

$$\begin{aligned} \boldsymbol{g}(\mathbf{u}_{i+1}) &= \mathbf{m}\ddot{\mathbf{u}}_{i+1} + \mathbf{c}\dot{\mathbf{u}}_{i+1} + \mathbf{f}_{i+1} - \mathbf{p}_{i+1} \\ &= \mathbf{m}\left[\frac{1}{(\Delta t)^2\beta}(\mathbf{u}_{i+1} - \mathbf{u}_i) - \frac{1}{(\Delta t)\beta}\dot{\mathbf{u}}_i - \left(\frac{1}{2\beta} - 1\right)\ddot{\mathbf{u}}_i\right] \\ &\quad + \mathbf{c}\left[\frac{\gamma}{(\Delta t)\beta}(\mathbf{u}_{i+1} - \mathbf{u}_i) - \left(\frac{\gamma}{\beta} - 1\right)\dot{\mathbf{u}}_i - (\Delta t)\left(\frac{\gamma}{2\beta} - 1\right)\ddot{\mathbf{u}}_i\right] + \mathbf{f}_{i+1} - \mathbf{p}_{i+1} \end{aligned} \tag{3.29}$$

For the i+1 step, the responses of the previous step, i.e., *i-th* step, are constants. Therefore, Eq. (3.29) can be further simplified as follows:

$$\boldsymbol{g}(\mathbf{u}_{i+1}) = \left[\frac{\mathbf{m}}{(\Delta t)^2\beta} + \frac{\mathbf{c}\gamma}{(\Delta t)\beta}\right]\mathbf{u}_{i+1} + \mathbf{f}(\mathbf{u}_{i+1}) + \text{constants} \tag{3.30}$$

and the corresponding Jacobian matrix is as follows:

$$\begin{aligned} \mathbf{J}(\mathbf{u}_{i+1}) = \frac{\partial}{\partial \mathbf{u}_{i+1}}\mathbf{g}(\mathbf{u}_{i+1}) &= \frac{1}{(\Delta t)^2\beta}\mathbf{m} + \frac{\gamma}{(\Delta t)\beta}\mathbf{c} + \frac{\partial}{\partial \mathbf{u}_{i+1}}\mathbf{f}(\mathbf{u}_{i+1}) \\ &= \frac{1}{(\Delta t)^2\beta}\mathbf{m} + \frac{\gamma}{(\Delta t)\beta}\mathbf{c} + \mathbf{k}_{T_{i+1}} \end{aligned} \tag{3.31}$$

where $\mathbf{k}_{T_{i+1}}$ is the tangent stiffness matrix at the i+1 step. Therefore, according to Eq. (3.17), the hypothetical dynamical system and corresponding Lyapunov function are as follows:

$$\dot{\mathbf{u}}_{i+1} = -\mathbf{K}\left[\frac{\partial}{\partial \mathbf{u}_{i+1}}\mathbf{g}(\mathbf{u}_{i+1})\right]^T \mathbf{g}(\mathbf{u}_{i+1}) = -\mathbf{K}\mathbf{J}(\mathbf{u}_{i+1})^T \mathbf{g}(\mathbf{u}_{i+1})$$
$$= -\mathbf{K}\left(\frac{1}{(\Delta t)^2 \beta}\mathbf{m} + \frac{\gamma}{(\Delta t)\beta}\mathbf{c} + \mathbf{k}_{T_{i+1}}\right)^T \mathbf{g}(\mathbf{u}_{i+1}) \tag{3.32}$$

$$v(\mathbf{u}_{i+1}) = \frac{1}{2}\mathbf{g}(\mathbf{u}_{i+1})^T \mathbf{g}(\mathbf{u}_{i+1}) \tag{3.33}$$

It is clear from Eq. (3.30) that $\mathbf{g}(\mathbf{u}_{i+1})$ is radially unbounded which is independent of the radially unboundedness of $\mathbf{f}(\mathbf{u}_{i+1})$. Therefore, the equilibrium point of the dynamical system in Eq. (3.32) is globally asymptotically stable. In other words, it converges to the solution of Eq. (3.32) for all initial values or guesses of $\mathbf{u}_{i+1}$. Moreover, similar to the formulation for the static problems, the tangent stiffness matrix $\mathbf{k}_{T_{i+1}}$ can be replaced by the constant stiffness at $\mathbf{u}_{i+1}^0$.

The general procedures for the proposed Lyapunov-based nonlinear solver are summarized as follows:

1. Compute the Jacobian matrix using Eq. (3.23) and (3.31) for static and dynamical systems, respectively;
2. Form the hypothetical dynamical system represented by Eq. (3.22) and (3.32) for static and dynamical systems, respectively;
3. Solve the set of equation for the hypothetical dynamical system using numerical integration scheme starting from the initial condition (or guess).

3.5 NUMERICAL EXAMPLES

Several numerical examples are presented in this section to compare the convergence behaviors of the regular NR algorithm and that of the proposed algorithm. The first example is a single-degree of freedom (SDOF) nonlinear static system characterized by a single parameter. The second example is a two-DOF static system with bilinear force-deformation relationships. The third example is a two-DOF dynamical system used to compare the convergence behavior of these two nonlinear equation solvers with a single time step integrator. The second and third examples are performed using the inconsistent Jacobian matrix as discussed below. In this section, the hypothetical dynamical system of all the numerical examples is solved by the Dormand–Prince method [Dormand and Prince 1980] that is implemented as the differential equation solver *ode45* in MATLAB [Mathworks Inc. 2015]. For convenience, all units are omitted in this section, where use of consistent units is taken into account.

3.5.1 SDOF Nonlinear Static System

Consider the restoring force of the nonlinear SDOF system, as shown in Figure. 3.1, has the following form

$$f(u) = sign(u)|u|^r \tag{3.35}$$

where $sign(u) = 1$ if $u \geq 1$, otherwise $sign(u) = -1$.

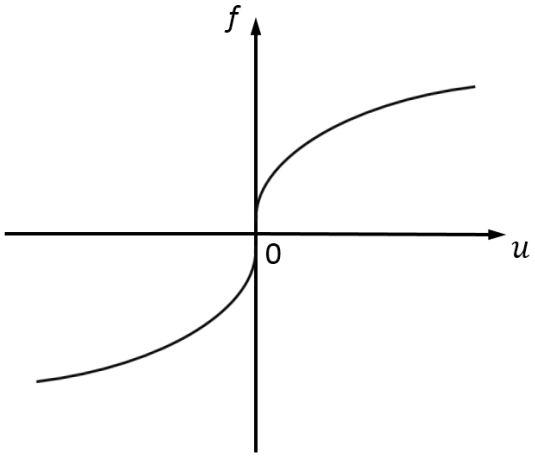

Figure 3.1 The sketch of the restoring force for the SDOF nonlinear static system.

Based on the regular NR algorithm,

$$\begin{aligned} u^{i+1} &= u^i - J(u^i)^{-1} f(u^i) = u^i - sign(u^i)\frac{1}{r}|u^i| \\ &= \left(1 - \frac{1}{r}\right)u^i \end{aligned} \tag{3.36}$$

From Eq. (3.36), it can be seen that the regular NR algorithm is reduced to a linear system where the eigenvalue is $(r-1)/r$. Its convergence is guaranteed if $(r-1)/r \in (-1,1)$, i.e., $r > 1/2$. For example, if $r = 2$, the regular NR algorithm converges to the solution, i.e., $u = 0$, as shown in Figure 3.2a. However, if $r < 1/2$, e.g., $r = 1/3$ and $r = 1/4$, the algorithm diverges as shown in Figures 3.2b and 3.2c. It is noted that the algorithm oscillates or flip-flops indefinitely between u^0 and $-u^0$ if $r = 1/2$ as shown in Figure 3.2d.

Considering the formulation in the previous section and Eq. (3.35), the first order ordinary differential equation for the hypothetical dynamical system and the corresponding Lyapunov function are as follows:

$$\dot{u} = -K\left[\frac{\partial}{\partial u} f(u)\right]^T f(u) = -Krsign(u)|u|^{2r-1} \tag{3.37}$$

$$v(u) = \frac{1}{2}|u|^{2r} \tag{3.38}$$

Figure 3.3 presents the traces of equilibrium search for the same SDOF examples with different values of r using the proposed nonlinear equation solver. It is clear that the proposed algorithm is

globally asymptotically stable for this example. Figure 3.3 is obtained by solving the hypothetical dynamical system is Eq. (3.37), therefore the x-axis of Figure 3.3 is labeled as the number of time steps.

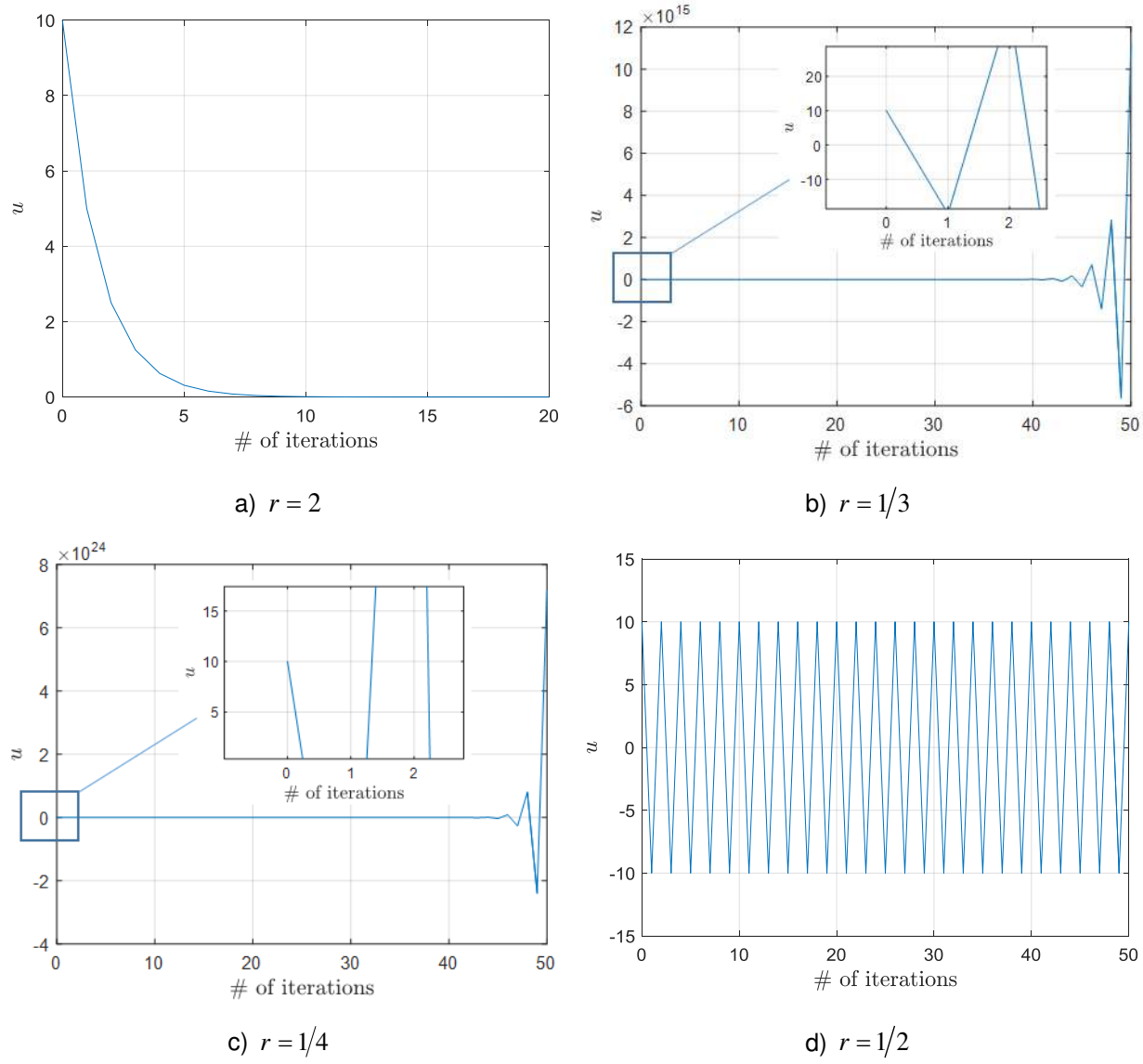

a) $r = 2$

b) $r = 1/3$

c) $r = 1/4$

d) $r = 1/2$

Figure 3.2 Traces of equilibrium search for the SDOF example using the regular NR algorithm.

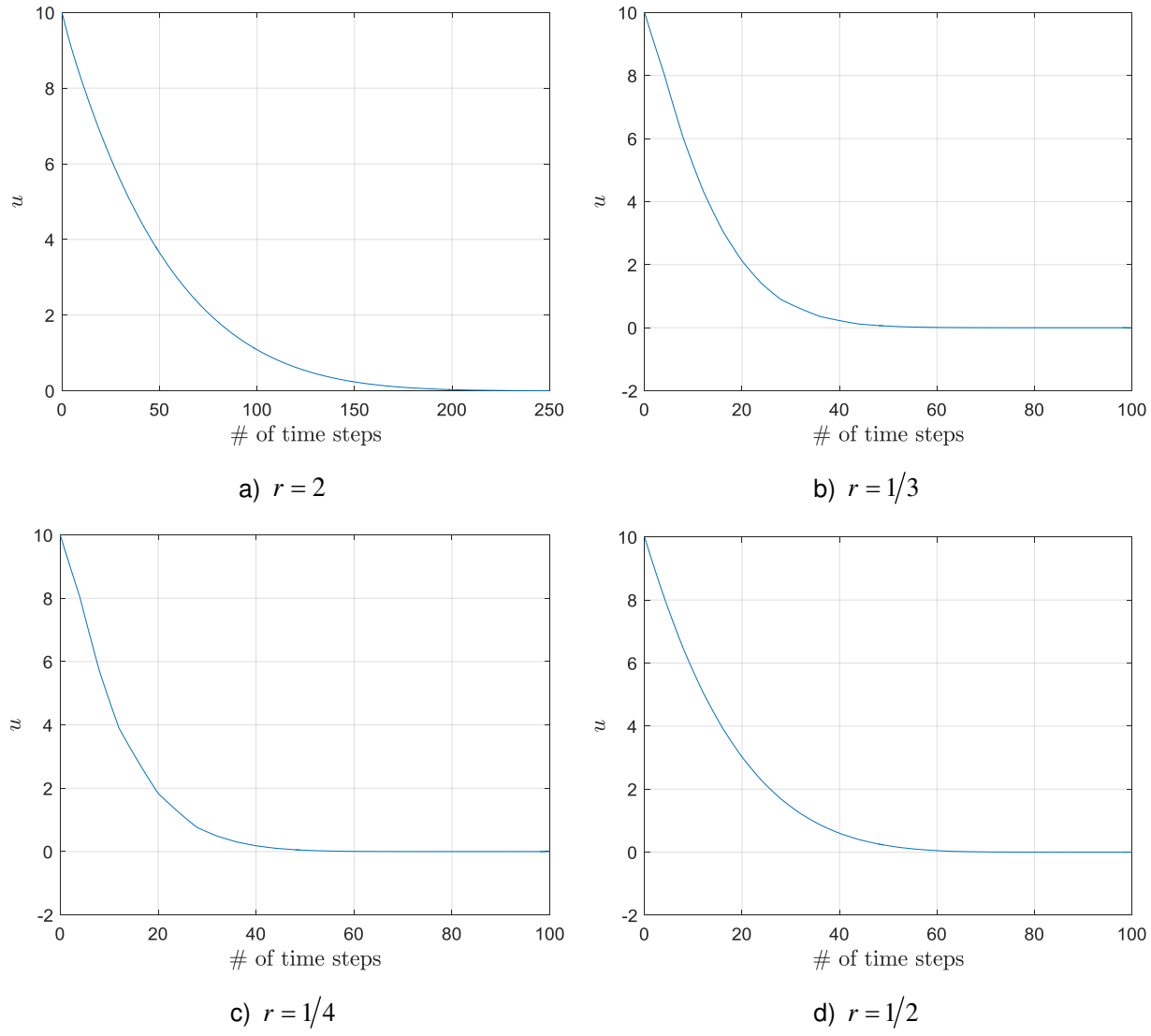

Figure 3.3 Traces of equilibrium search for the SDOF example using the proposed Lyapunov-based algorithm.

3.5.2 Two-DOF Nonlinear Static System

A two-story shear building is modeled as the system shown in Figure 3.4. It consists of two uniaxial springs with bilinear force-deformation relationships shown in Figure 3.5. A load vector of $\mathbf{P} = [10 \quad 20]^T$ is applied to the system. Taking advantage of the compatibility matrix $\mathbf{A}$, shown in Figure 3.4, the consistent Jacobian stiffness matrix is obtained as follows:

$$\mathbf{k}_b = \begin{bmatrix} k_1 & 0 \\ 0 & k_2 \end{bmatrix} \rightarrow \mathbf{J} = \mathbf{A}^T \mathbf{k}_b \mathbf{A} = \begin{bmatrix} k_1 + k_2 & -k_2 \\ -k_2 & k_2 \end{bmatrix} \tag{3.39}$$

The restoring vector $\mathbf{f}$, that is radially unbounded, is as follows (q's are defined in Figure 3.5):

$$\mathbf{f} = \begin{bmatrix} f_1 \\ f_2 \end{bmatrix} = \begin{bmatrix} q_1 - q_2 \\ q_2 \end{bmatrix} \tag{3.40}$$

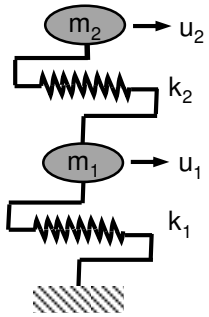

$$\mathbf{m} = \begin{bmatrix} 1/2500 & 0 \\ 0 & 1/2500 \end{bmatrix}, \quad \mathbf{A} = \begin{bmatrix} 1 & 0 \\ -1 & 1 \end{bmatrix}$$

Figure 3.4 Two-DOF nonlinear system.

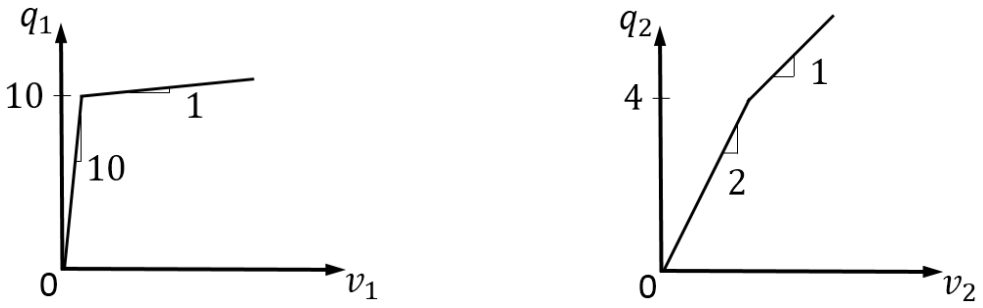

a) Spring 1 **b) Spring 2**

Figure 3.5 Force-deformation relationships of the two springs.

The efficiency of the regular NR algorithm relies heavily on the computation of a numerically consistent Jacobian matrix. For complex constitutive models, a consistent Jacobian matrix can be difficult to develop and implement. Utilization of an inconsistent Jacobian matrix or the one with approximation errors is likely to lead to the non-convergence of the regular NR algorithm [Scott and Fenves 2010], as demonstrated in this example. To mimic an error in the Jacobian calculations of the element state determination, an artificial coupling of the two springs is introduced as assumed in [Scott and Fenves 2010], leading to the following Jacobian matrix:

$$\mathbf{k}_b = \begin{bmatrix} k_1 & 0.5 \\ 0.5 & k_2 \end{bmatrix} \rightarrow \mathbf{J} = \mathbf{A}^T \mathbf{k}_b \mathbf{A} = \begin{bmatrix} k_1 + k_2 - 1 & -k_2 + 0.5 \\ -k_2 + 0.5 & k_2 \end{bmatrix} \tag{3.41}$$

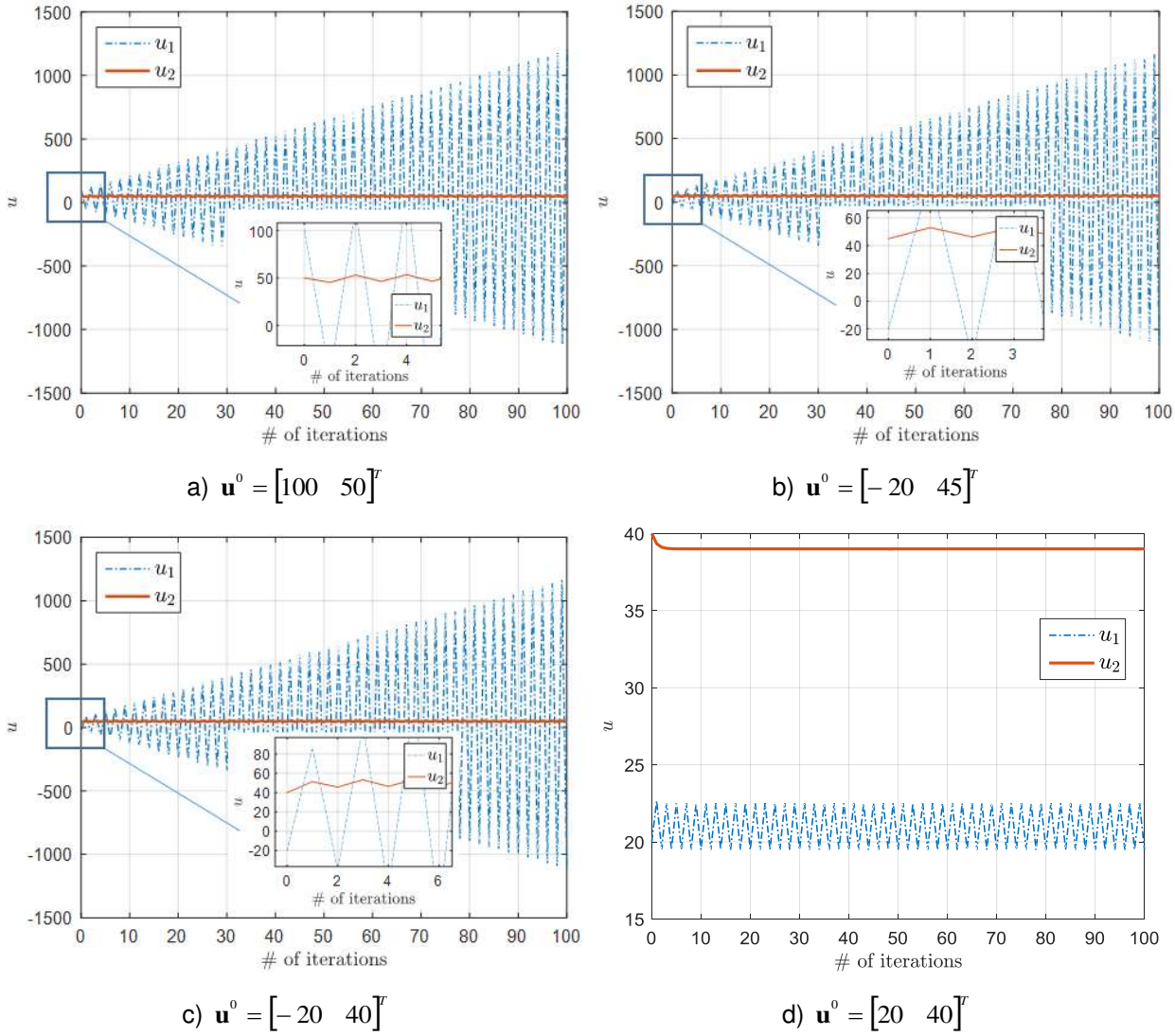

a) $\mathbf{u}^0 = [100 \quad 50]^T$

b) $\mathbf{u}^0 = [-20 \quad 45]^T$

c) $\mathbf{u}^0 = [-20 \quad 40]^T$

d) $\mathbf{u}^0 = [20 \quad 40]^T$

Figure 3.6 Traces of equilibrium search for the two-DOF static example using the regular NR algorithm.

The equilibrium point of this system is predetermined as $\mathbf{u} = [39 \quad 21]^T$. Figures 3.6 and 3.7 show respectively the convergence behavior of the regular NR and that of the proposed Lyapunov-based algorithms with different initial guesses. As shown in Figure 3.6, the regular NR algorithm either diverges or oscillates around the true solution. It is noted from Figure 3.6d that even though the initial guess is just around the equilibrium point, the regular NR algorithm fails to converge to the true solution. In contrast, the proposed Lyapunov-based algorithm converges for all the initial guesses. This is expected as this proposed algorithm is globally asymptotically stable for this system with the property of radially unboundedness shown in Eq. (3.40).

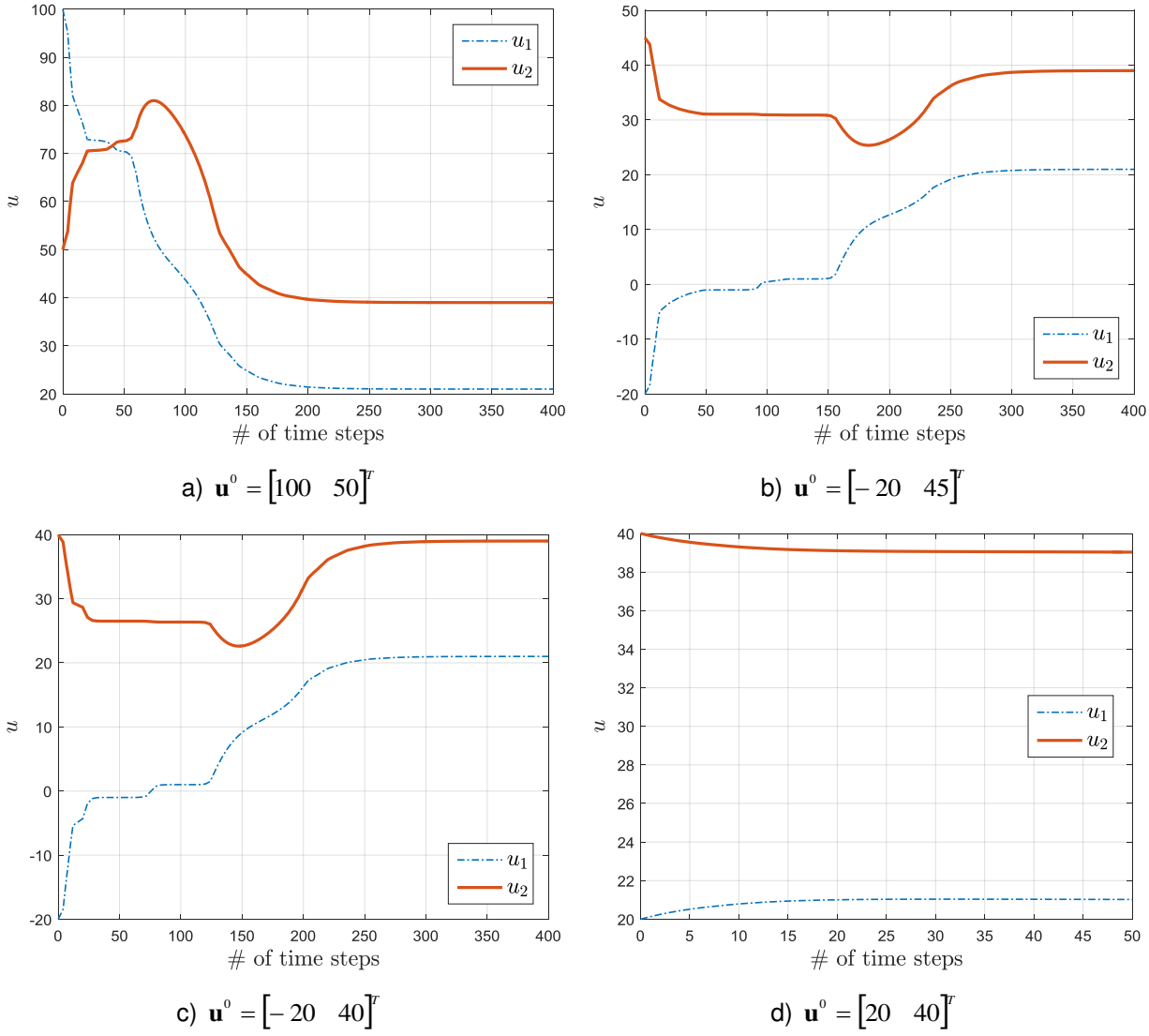

Figure 3.7 Traces of equilibrium search for the two-DOF static example using the proposed Lyapunov-based algorithm.

3.5.3 Two-DOF Nonlinear Dynamical System

The same two-DOF system as in the previous example is simulated to demonstrate the convergence behavior of the two nonlinear equation solvers in the i+1 time step after time discretizing the governing equations by the implicit Newmark algorithm with constant acceleration, i.e., $\gamma = 1/2$ and $\beta = 1/4$. The simulations are based on the following numerical conditions:

$$\Delta t = 0.1, \quad \dot{\mathbf{u}}_i = [200 \quad 100]^T, \quad \ddot{\mathbf{u}}_i = [-100 \quad 50]^T, \quad \mathbf{p}_{i+1} = [1 \quad 2]^T \tag{3.42}$$

The initial guess of the displacement vector at the time step i+1 is set to equal the obtained one at the time step i, i.e., $\mathbf{u}_{i+1}^0 = \mathbf{u}_i$, and the same inconsistent Jacobian matrix as in Eq. (3.41) is used.

Figure 3.8 presents the traces of the displacement vector by the regular NR algorithm where u_1 ends with oscillation indefinitely for all four displacement vectors at the time step i, leading to the commonly experienced convergence problems. In contrast, as shown in Figure 3.9, the proposed algorithm is able to accurately find the solution for all four situations.

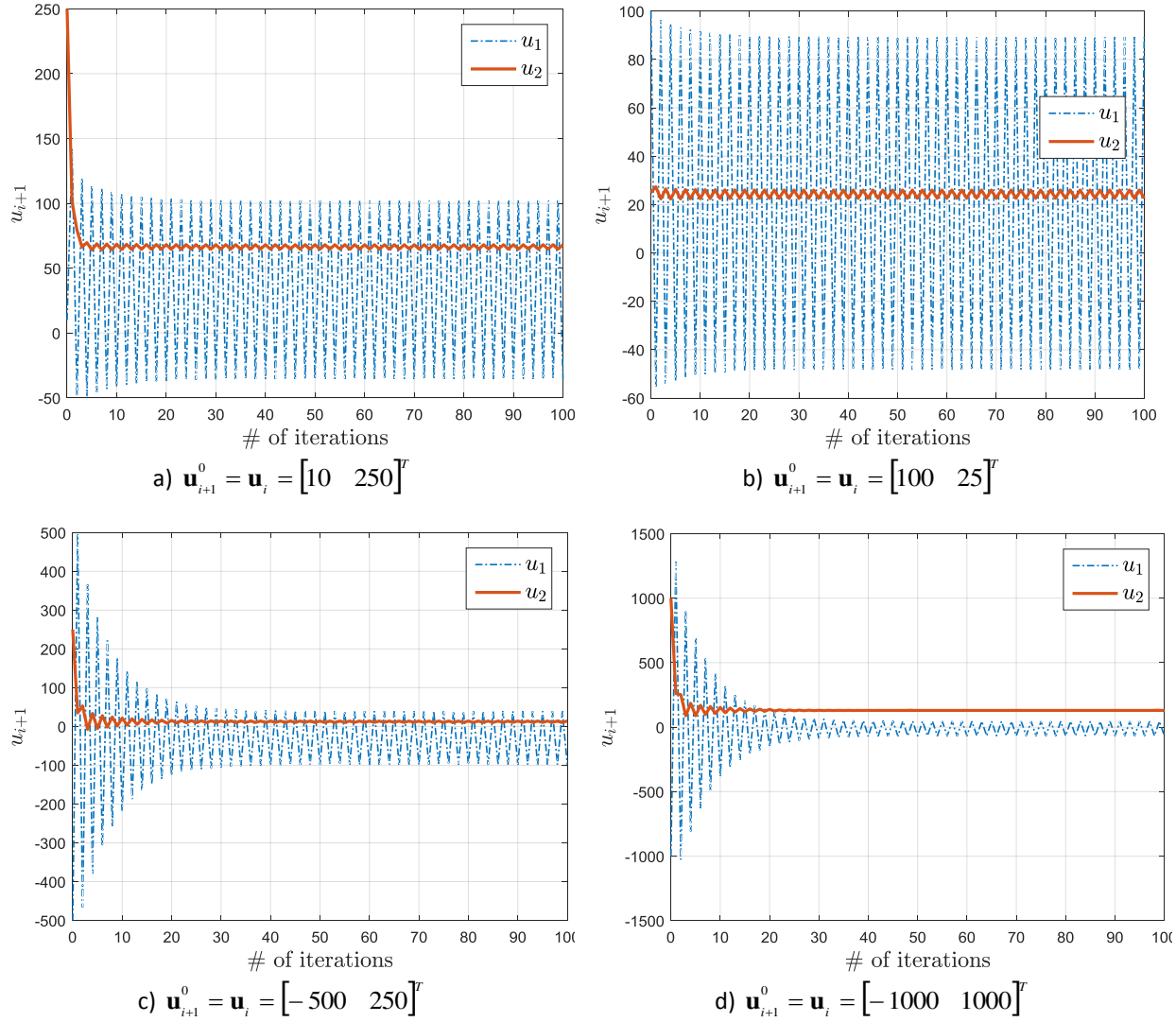

Figure 3.8 Traces of equilibrium search for the two-DOF dynamic example using the regular NR algorithm.

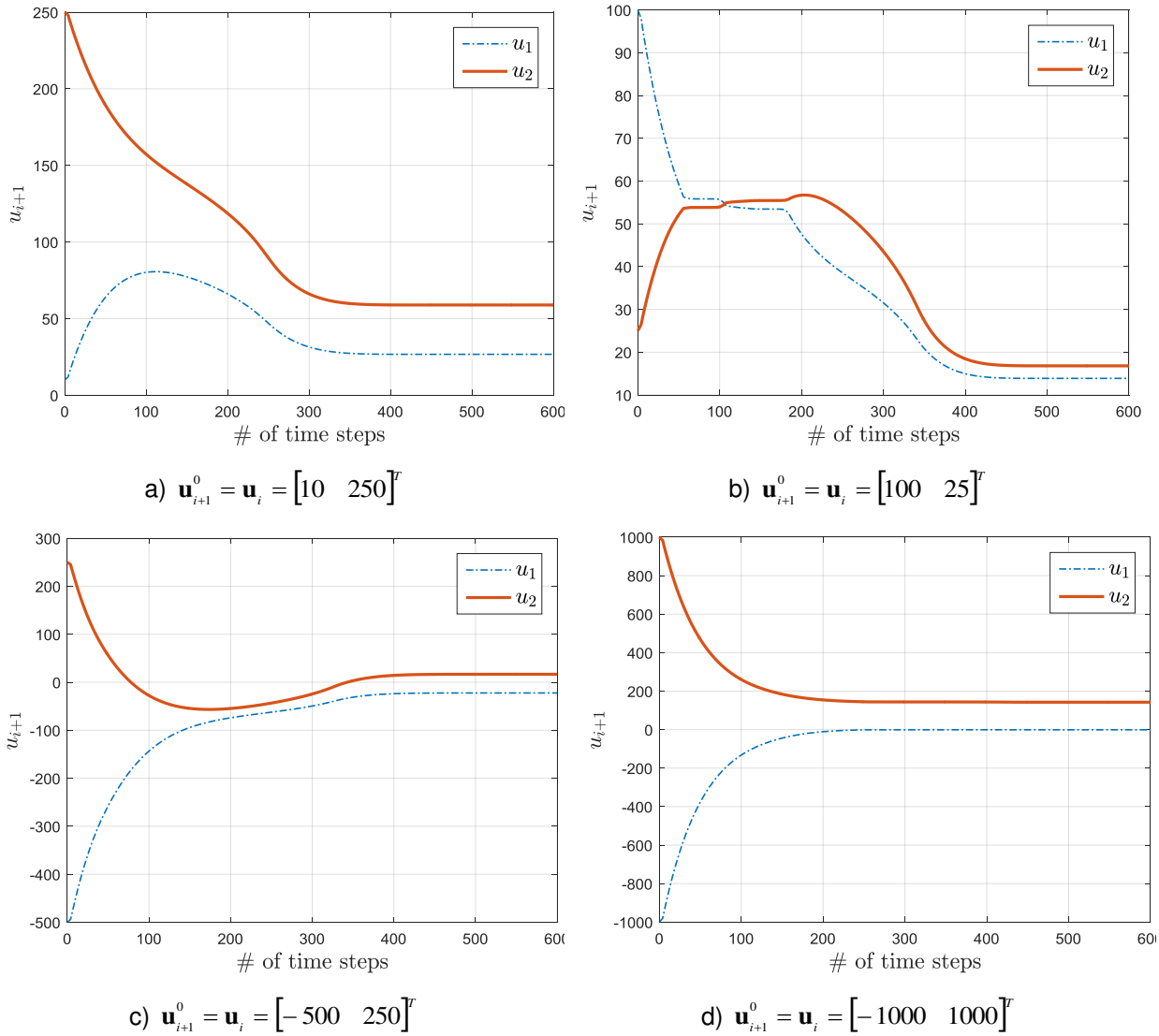

a) $\mathbf{u}_{i+1}^0 = \mathbf{u}_i = \begin{bmatrix} 10 & 250 \end{bmatrix}^T$

b) $\mathbf{u}_{i+1}^0 = \mathbf{u}_i = \begin{bmatrix} 100 & 25 \end{bmatrix}^T$

c) $\mathbf{u}_{i+1}^0 = \mathbf{u}_i = \begin{bmatrix} -500 & 250 \end{bmatrix}^T$

d) $\mathbf{u}_{i+1}^0 = \mathbf{u}_i = \begin{bmatrix} -1000 & 1000 \end{bmatrix}^T$

Figure 3.9 Traces of equilibrium search for the two-DOF dynamic example using the proposed Lyapunov-based algorithm.

4 Numerical Lyapunov Stability Analysis

4.1 INTRODUCTION

Stability is one of the most important properties of direct integration algorithms that must be considered for efficient and reliable simulations. Most of the past studies conducted the stability analysis of direct integration algorithms for linear elastic structures (e.g., Bathe and Wilson 1972; Hilber et al. 1977; Hughes 1987; Tamma et al. 2000) using the amplification operator and its associated spectral radius. These research efforts provide useful insight for the selection of the suitable integration algorithm with the proper time step size to solve a dynamic problem. Integration algorithms, however, are usually applied to nonlinear dynamic problems. Studies involving nonlinear dynamics are therefore necessary but relatively limited in the past literature. Hughes (1976) investigated the stability of the Newmark algorithm with constant acceleration applied to problems involving nonlinear dynamics. Zhong and Crisfield (1998) developed an energy conserving corotational procedure for the dynamics of shell structures. Kuhl and Crisfield (1999) developed a generalized formulation of the energy-momentum method within the framework of the generalized-α algorithm. Chen and Ricles (2008) explored the stability of several direct integration algorithms for nonlinear SDOF systems by utilizing discrete control theory.

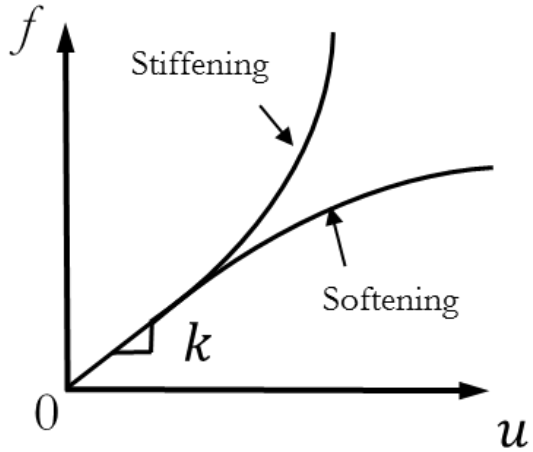

Figure 4.1 Definition of stiffening and softening systems.

In this chapter, two general classes of nonlinear SDOF structural systems, stiffening and non-degrading softening systems, are considered. The idealized backbone curves (force-displacement relationship) of these two systems are illustrated in Figure 4.1. Systematic Lyapunov

stability and accuracy analyses of several implicit and explicit direct integration algorithms for these two nonlinear structural systems are presented [Liang and Mosalam 2015, 2016a]. The stability analysis of nonlinear systems, unlike linear ones, is rather complicated and challenging. This is attributed to specific properties possessed by nonlinear systems. For example, the stability of nonlinear systems is dependent on initial conditions and the principle of superposition does not hold in general.

Lyapunov stability theory that introduced in Chapter 3 is taken advantage of to study the stability of nonlinear systems. Generally speaking, constructing the previously mentioned energy function for the nonlinear system, which is the basis of Lyapunov stability theory, is not readily available. To handle this difficulty, this chapter proposes a numerical approach to transform the problem of seeking a Lyapunov function to a convex optimization problem, which can solve the problem in a simpler and clearer way. However, this proposed approach may involve extensive computations. Accordingly, this chapter proposes an approach that enables performing the stability analysis numerically. Convex optimization considers the problem of minimizing convex functions over convex sets where a wide range of problems can be formulated in this way. In this optimization, any local minimum must be a global minimum, which is an important property leading to reliable and efficient solutions using, e.g. interior-point methods, which are suitable for computer-aided design or analysis tools [Boyd and Vandenberge 2004]. It is shown that the proposed approach is generally applicable to direct integration algorithms for various nonlinear behaviors. Moreover, based on Lyapunov stability theory, some arguments of stability regarding these direct integration algorithms from past studies are found to be groundless and these findings are discussed in this chapter. The chapter also investigates the OS algorithm that uses tangent stiffness in the formulation, which has not been previously studied. It is shown that this algorithm possesses similar stability properties to those of the implicit Newmark integration. Finally, the accuracy of the integration methods is examined using a geometrically nonlinear problem, which has a closed-form exact solution.

4.2 DIRECT INTEGRATION ALGORITHMS

The discretized equation of motion of a SDOF system under an external dynamic force excitation is expressed as:

$$m\ddot{u}_{i+1} + c\dot{u}_{i+1} + f_{i+1} = p_{i+1} \tag{4.1}$$

where m and c are the mass and viscous damping, and $\ddot{u}_{i+1}$, $\dot{u}_{i+1}$, f_{i+1}, and p_{i+1} are the acceleration, velocity, restoring force, and external force at the time step $i+1$, respectively. The restoring force, $f(u)$, is generally defined as a function of displacement, u.

Usually, single-step direct integration algorithms are defined by the following difference equations:

$$u_{i+1} = u_i + \eta_0(\Delta t)\dot{u}_i + \eta_1(\Delta t)^2\ddot{u}_i + \eta_2(\Delta t)^2\ddot{u}_{i+1} + \eta_3 \tag{4.2}$$

$$\dot{u}_{i+1} = \eta_4\dot{u}_i + \eta_5(\Delta t)\ddot{u}_i + \eta_6(\Delta t)\ddot{u}_{i+1} + \eta_7 \tag{4.3}$$

In general, Eqs. (4.1)-(4.3) require an iterative solution, which forms the basis of implicit algorithms. On the other hand, these algorithms become explicit when $\eta_2 = 0$. Coefficients of the Newmark integration family (Newmark 1959) and the explicit OS algorithms (Hughes et al. 1979) are summarized in Table 1 where $\kappa = m/\left(\beta(\Delta t)^2\right) + c\gamma/\left(\beta(\Delta t)\right) + k_{i+1}$ and k_{i+1} is defined below.

Table 4.1 Coefficients for the Newmark and the OS Integration Algorithms.

Coefficient	Newmark	OS
κ_0	1	$1 - c/\left(\kappa(\Delta t)\right)$
κ_1	$(1-2\beta)/2$	$(1-2\beta)/2 - c(1-\gamma)/\left(\kappa(\Delta t)\right)$
κ_2	β	0
κ_3	0	$\left(p_{i+1} - \tilde{f}_{i+1}\right)/\kappa$
κ_4	1	$1 - c\gamma/\left(\beta\kappa(\Delta t)\right)$
κ_5	$1-\gamma$	$1 - \gamma - c\gamma(1-\gamma)/\left(\beta\kappa(\Delta t)\right)$
κ_6	γ	0
κ_7	0	$\gamma\left(p_{i+1} - \tilde{f}_{i+1}\right)/\left(\beta\kappa(\Delta t)\right)$

4.3 LYAPUNOV STABILITY ANALYSIS

For each direct integration algorithm, the relationship between the kinematic quantities at time steps $i+1$ and i can be established as follows:

$$\boldsymbol{x}_{i+1} = \mathbf{A}_i \boldsymbol{x}_i + \mathbf{L}_i \tag{4.4}$$

where $\boldsymbol{x}_i = \left[(\Delta t)^2 \ddot{u}_i \;\; (\Delta t)\dot{u}_i \;\; u_i\right]^T$, $\mathbf{A}_i$ and $\mathbf{L}_i$ are the approximation operator and the loading vector at the time step i, respectively. The loading vector, $\mathbf{L}$, is generally independent of the vector of kinematic quantities, $\boldsymbol{x}$. Eq. (4.4) can be further extended as:

$$\boldsymbol{x}_{i+1} = \left(\prod_{j=i}^{1} \mathbf{A}_j\right)\boldsymbol{x}_1 + \sum_{l=1}^{i-1}\left(\left(\prod_{k=i}^{l+1} \mathbf{A}_k\right)\mathbf{L}_l\right) + \mathbf{L}_i \tag{4.5}$$

where $\prod_{j=i}^{1} \mathbf{A}_j = \mathbf{A}_i \mathbf{A}_{i-1} \cdots \mathbf{A}_2 \mathbf{A}_1$. In order to investigate the stability of the system in Eq. (4.4), a Lyapunov artificial energy function v_{i+1} [Franklin et al. 2015] at the time step $i+1$, can be chosen as:

$$v_{i+1} = \boldsymbol{x}_{i+1}^T \mathbf{M} \boldsymbol{x}_{i+1} \tag{4.6}$$

where $\mathbf{M}$ is positive definite, i.e. $\mathbf{M}=\mathbf{M}^T \succ \mathbf{0}$ and $\mathbf{0}$ is the null matrix of the same dimension as $\mathbf{M}$. The system in Eq. (4.4) is stable if the Lyapunov function in Eq. (4.6) is bounded for $i \to \infty$. Substituting Eq. (4.5) into Eq. (4.6) with some manipulations leads to the following:

$$\begin{aligned} v_{i+1} = \boldsymbol{x}_1^T \left(\prod_{k=i}^{1} \mathbf{A}_k^T \right) \mathbf{M} \left(\prod_{j=i}^{1} \mathbf{A}_j \right) \boldsymbol{x}_1 + \sum_{l=1}^{i-1} \sum_{m=1}^{i-1} \left(\mathbf{L}_l^T \left(\prod_{k=i}^{l+1} \mathbf{A}_k^T \right) \mathbf{M} \left(\prod_{n=i}^{m+1} \mathbf{A}_n \right) \mathbf{L}_m \right) + \mathbf{L}_i^T \mathbf{M} \mathbf{L}_i + \\ 2\boldsymbol{x}_1^T \left(\prod_{k=i}^{1} \mathbf{A}_k^T \right) \mathbf{M} \mathbf{L}_i + 2 \left(\sum_{l=1}^{i-1} \mathbf{L}_l^T \left(\prod_{k=i}^{l+1} \mathbf{A}_k^T \right) \right) \mathbf{M} \mathbf{L}_i + \\ 2\boldsymbol{x}_1^T \left(\prod_{k=i}^{1} \mathbf{A}_k^T \right) \mathbf{M} \left(\sum_{m=1}^{i-1} \left(\prod_{n=i}^{m+1} \mathbf{A}_n \right) \mathbf{L}_m \right) \end{aligned} \tag{4.7}$$

The loading vector, $\mathbf{L}$, is generally a function of external force, p. Therefore, it is bounded. Therefore, based on Eq. (4.7), the boundedness of the Lyapunov function v_{i+1} for $i \to \infty$ leads to the boundedness of $\prod_{j=i}^{1} \mathbf{A}_j$ for $i \to \infty$. For linear behavior of structures, the approximation operator, $\mathbf{A}$, remains constant, thus $\prod_{j=i}^{1} \mathbf{A}_j$ becomes $\mathbf{A}^i$ that can be decomposed as follows:

$$\mathbf{A}^i = \mathbf{V}\mathbf{D}^i\mathbf{V}^{-1} \tag{4.8}$$

where $\mathbf{D}$ and $\mathbf{V}$ are matrices of eigenvalues and eigenvectors of $\mathbf{A}$, respectively. The boundedness of $\mathbf{A}^i$ for $i \to \infty$ leads to the well-known stability criterion for linear systems, namely the spectral radius of the approximation operator $\rho(\mathbf{A})$ must be less than or equal to 1.0.

For nonlinear structures, $\prod_{j=i}^{1} \mathbf{A}_j$ is more involved due to the continuous variation of the approximation operator $\mathbf{A}_i$. Therefore, the stability of a nonlinear system cannot be solely determined using the spectral radius of its approximation operator $\mathbf{A}_i$. However, the investigation of the eigen properties of $\mathbf{A}_i$ is still necessary in nonlinear problems. For small values of Δt, e.g. Δt required for accuracy as discussed later in the section "Accuracy Analysis," the increment of restoring force can be approximated [Chopra 2006] as:

$$f_{i+1}^* - f_i = k_{T_{i+1}}^* \left(u_{i+1}^* - u_i \right) \tag{4.9}$$

where $\left(f_{i+1}^*, k_{T_{i+1}}^*, u_{i+1}^* \right) = \left(f_{i+1}, k_{T_{i+1}}, u_{i+1} \right)$ for the Newmark family of algorithms and $\left(f_{i+1}^*, k_{T_{i+1}}^*, u_{i+1}^* \right) = \left(\tilde{f}_{i+1}, \tilde{k}_{T_{i+1}}, \tilde{u}_{i+1} \right)$ for the OS algorithms. It should be noted that $k_{T_{i+1}}$ is the tangent stiffness at the time step $i+1$, and other parameters are defined before. The tangent stiffness is generally a function of the displacement, thus Eq. (4.4) represents a nonlinear system of equations. With the approximation in Eq. (4.9), the approximation operator $\mathbf{A}_i$ for the Newmark and the OS algorithms is derived as follows:

$$\mathbf{A}_i = \begin{bmatrix} \dfrac{1-\frac{1-2\beta}{2}\omega_0^2(\Delta t)^2 - 2\zeta\omega_n(1-\gamma)(\Delta t)}{1+2\zeta\omega_n\gamma(\Delta t)+\beta\omega_1^2(\Delta t)^2} & -\dfrac{\omega_0^2(\Delta t)^2}{1+2\zeta\omega_n\gamma(\Delta t)+\beta\omega_1^2(\Delta t)^2} & 0 \\ \dfrac{\gamma\left(1-\frac{1-2\beta}{2}\omega_0^2(\Delta t)^2 - 2\zeta\omega_n(1-\gamma)(\Delta t)\right)}{1+2\zeta\omega_n\gamma(\Delta t)+\beta\omega_1^2(\Delta t)^2}+(1-\gamma) & 1-\dfrac{\gamma\omega_0^2(\Delta t)^2}{1+2\zeta\omega_n\gamma(\Delta t)+\beta\omega_1^2(\Delta t)^2} & 0 \\ \dfrac{\beta\left(1-\frac{1-2\beta}{2}\omega_0^2(\Delta t)^2 - 2\zeta\omega_n(1-\gamma)(\Delta t)\right)}{1+2\zeta\omega_n\gamma(\Delta t)+\beta\omega_1^2(\Delta t)^2}+\dfrac{1-2\beta}{2} & 1-\dfrac{\beta\omega_0^2(\Delta t)^2}{1+2\zeta\omega_n\gamma(\Delta t)+\beta\omega_1^2(\Delta t)^2} & 1 \end{bmatrix} \tag{4.10}$$

where $\zeta = c/(2m\omega_n)$, $\omega_n^2 = k_I/m$. Coefficients ω_0 and ω_1 for the Newmark integration family and the OS algorithms are listed in Table 4.2.

Table 4.2 Coefficients of approximation operators for the Newmark and the OS Integration Algorithms.

Coefficient	Newmark	$OS_{initial}$	$OS_{tangent}$
ω_0	$\omega_{T_{i+1}}$	$\tilde{\omega}_{T_{i+1}}$	$\tilde{\omega}_{T_{i+1}}$
ω_1	$\omega_{T_{i+1}}$	ω_n	$\tilde{\omega}_{T_{i+1}}$

where $\omega_{T_{i+1}}^2 = k_{T_{i+1}}/m, \tilde{\omega}_{T_{i+1}}^2 = \tilde{k}_{T_{i+1}}/m$. It is obvious that one of the eigenvalues of $\mathbf{A}_i$ in Eq. (4.10) is 1. For the Newmark and OS algorithms with $(\beta,\gamma) = (1/4, 1/2)$, the other two eigenvalues are obtained as:

$$\lambda_{1,2} = \frac{1-\frac{3}{8}\omega_0^2(\Delta t)^2 + \frac{1}{8}\omega_1^2(\Delta t)^2 \pm \Delta t\sqrt{\omega_n^2\zeta^2 + \frac{1}{4}\omega_n\zeta\Delta t\left(\omega_1^2-\omega_0^2\right)+(\Delta t)^2\left(9\omega_0^4 - 10\omega_0^2\omega_1^2+\omega_1^4\right)-\omega_0^2}}{1+\omega_n\zeta\Delta t + \frac{1}{4}\omega_1^2(\Delta t)^2} \tag{4.11}$$

On the other hand, for the explicit Newmark algorithm, i.e., $(\beta,\gamma) = (0, 1/2)$,

$$\lambda_{1,2} = \frac{1-\frac{1}{2}\omega_{T_{i+1}}^2(\Delta t)^2 \pm \Delta t\sqrt{\omega_n^2\zeta^2 + \frac{1}{4}\omega_{T_{i+1}}^4(\Delta t)^2 - \omega_{T_{i+1}}^2}}{1+\omega_n\zeta\Delta t} \tag{4.12}$$

Different from the integration algorithms above, the TRBDF2 is a multi-step algorithm with numerical damping introduced by the Euler backward scheme. Its approximation operator in Eq. (4.14) is obtained for the case of zero viscous damping ($\zeta = 0$) by similar linearization approximation for the tangent stiffness as before and given as follows:

$$k_{T_{i+1}} = (f_{i+1} - f_{i+0.5})/(u_{i+1} - u_{i+0.5}) = (f_{i+0.5} - f_i)/(u_{i+0.5} - u_i) \tag{4.13}$$

$$\mathbf{A}_i = \frac{1}{B}\begin{bmatrix} 9-\frac{47}{16}\omega_{T_{i+1}}^2(\Delta t)^2 & \frac{5}{16}\omega_{T_{i+1}}^4(\Delta t)^4 - 9\omega_{T_{i+1}}^2(\Delta t)^2 & 0 \\ 9-\frac{5}{16}\omega_{T_{i+1}}^2(\Delta t)^2 & 9-\frac{47}{16}\omega_{T_{i+1}}^2(\Delta t)^2 & 0 \\ \frac{9}{2}+\frac{1}{16}\omega_{T_{i+1}}^2(\Delta t)^2 & 9-\frac{5}{16}\omega_{T_{i+1}}^2(\Delta t)^2 & \left(\omega_{T_{i+1}}^2(\Delta t)^2+9\right)\left(\frac{1}{16}\omega_{T_{i+1}}^2(\Delta t)^2+1\right) \end{bmatrix} \tag{4.14}$$

where $B = \left(\omega_{T_{i+1}}^2(\Delta t)^2+9\right)\left(\frac{1}{16}\omega_{T_{i+1}}^2(\Delta t)^2+1\right)$. Thus, besides the one obvious eigenvalue of 1, the other two are as follows:

$$\lambda_{1.2} = \frac{9-\frac{47}{16}\omega_{T_{i+1}}^2(\Delta t)^2 \pm \left(9-\frac{5}{16}\omega_{T_{i+1}}^2(\Delta t)^2\right)\sqrt{-\omega_{T_{i+1}}^2(\Delta t)^2}}{\frac{1}{16}\omega_{T_{i+1}}^4(\Delta t)^4+\frac{25}{16}\omega_{T_{i+1}}^2(\Delta t)^2+9} \tag{4.15}$$

It can be shown that for $k_{T_{i+1}} \geq 0$, magnitudes of the eigenvalues in Eq. (4.15) are always less than 1 because of introduced numerical damping.

The conditions for $\rho(\mathbf{A}_i) \leq 1$ are summarized in Table 4.3 for the case of zero viscous damping ($\zeta = 0$), which is the most critical case for the stability analysis of direct integration algorithms. In Table 4.3, $T_{T_{i+1}} = 2\pi/\omega_{T_{i+1}} = 2\pi\sqrt{m/k_{T_{i+1}}}$ and $(\beta,\gamma) = (1/4, 1/2)$ are used for implicit Newmark, $OS_{initial}$ and $OS_{tangent}$ and thereafter in this chapter. A noteworthy observation is that the approximation operator of the explicit $OS_{tangent}$ algorithm is the same as that of the implicit Newmark algorithm with $\omega_{T_{i+1}}$ replaced by $\tilde{\omega}_{T_{i+1}}$ (refer to Table 4.2). This indicates that they possess similar stability properties, as indicated in Table 4.3.

Table 4.3 Conditions for $\rho(\mathbf{A}_i) \leq 1$.

Integration Algorithms	Limits
Implicit Newmark	$k_{T_{i+1}} \geq 0$
Explicit Newmark	$\Delta t/T_{T_{i+1}} \leq 1/\pi$
$OS_{initial}$	$0 \leq \tilde{k}_{T_{i+1}} \leq k_I$
$OS_{tangent}$	$\tilde{k}_{T_{i+1}} \geq 0$
TRBDF2	$k_{T_{i+1}} \geq 0$

The conditions in Table 4.3 are *not* stability criteria of the listed direct integration algorithms used in nonlinear systems. They are *only* the conditions for $\rho(\mathbf{A}_i) \leq 1$. Some past studies, however, determined the stability of direct integration algorithms based solely on the spectral radius. Combescure and Pegon (1997) claimed that the $OS_{initial}$ algorithm is unconditionally stable as long as the tangent stiffness is smaller than or equal to the initial stiffness; otherwise, the algorithm is unstable. They directly applied the stability criterion that only works for linear structures, i.e. $\rho(\mathbf{A}) \leq 1$, to nonlinear ones. As previously discussed, the boundedness of

$\prod_{j=i}^{1}\mathbf{A}_j$ for $i\to\infty$ is the stability criterion for both linear and nonlinear structures. For a nonlinear structure, with the continuous variation of the approximation operator, it is obvious that the boundedness of $\prod_{j=i}^{1}\mathbf{A}_j$ for $i\to\infty$ cannot be guaranteed by $\rho(\mathbf{A}_i)\le 1$. Moreover, the unboundedness of $\prod_{j=i}^{1}\mathbf{A}_j$ for $i\to\infty$ cannot be simply equivalent to $\rho(\mathbf{A}_i)>1$.

The example below is presented to illustrate that the system can still go unstable with $\rho(\mathbf{A}_i)\le 1$ for every time step, i.e., the stability cannot be strictly guaranteed by $\rho(\mathbf{A}_i)\le 1$ only. The implicit Newmark method with constant average acceleration is used in this example considering the following numerical conditions where all units are assumed consistent and omitted for convenience:

$$\zeta = 0.01 \quad \Delta t = 0.01T_n = 0.01(2\pi/\omega_n) \quad k_I = 100 \quad m = 1 \tag{4.16}$$

The response of the *i-th* time step, $\boldsymbol{x}_i$, with the loading vector $\mathbf{L}=\mathbf{0}$, is as follows:

$$\boldsymbol{x}_i = \left[(\Delta t)^2\ddot{u}_i \;\; (\Delta t)\dot{u}_i \;\; u_i\right]^T = \left(\prod_{j=i}^{1}\mathbf{A}_j\right)\boldsymbol{x}_0 \tag{4.17}$$

The total number of simulated time steps is 10,000 with initial conditions $\boldsymbol{x}_0 = \left[(\Delta t)^2\ddot{u}_0 \;\; (\Delta t)\dot{u}_0 \;\; u_0\right]^T = [1\;\;0\;\;0]^T$. In this example, 10,000 values of tangent stiffness are selected randomly under the condition that all of them are larger than the value of initial stiffness $k_I = 100$, i.e. $k_{T_i} > k_I$, $i:1\to 10{,}000$, i.e. assuming a stiffening behavior. Therefore, according to Table 4.3, $\rho(\mathbf{A}_i)=1$, $i:1\to 10{,}000$.

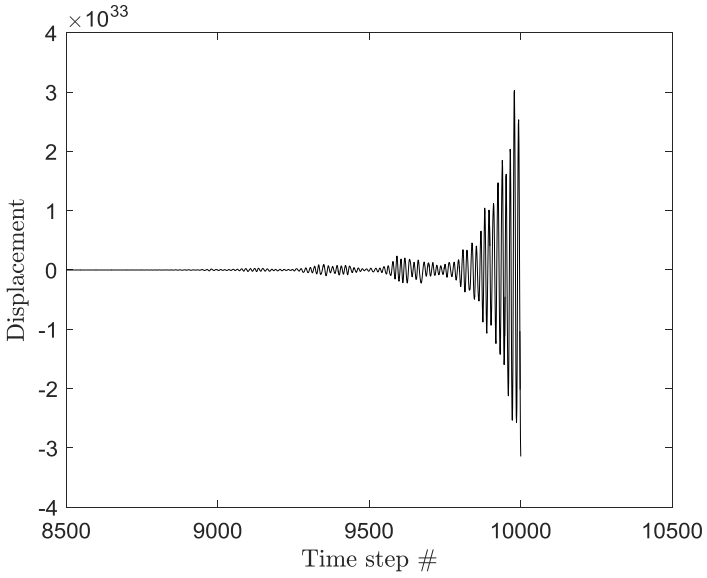

Figure 4.2 Time history plot of the displacement of an unstable example with $\rho(\mathbf{A}_i)=1$.

Figure 4.2 shows the time history plot of displacement u_i, $i:1\rightarrow 10{,}000$ where clearly the algorithm is unstable even with $\rho(\mathbf{A}_i)\leq 1$, $i:1\rightarrow 10{,}000$. Moreover, the numerical example used in the section "Accuracy Analysis" also shows that the stability criterion based on investigating the conditions of the spectral radius fails to identify the stability of the $OS_{initial}$ algorithm. Chen and Ricles (2008) demonstrated using discrete control theory that the Newmark method with constant average acceleration and explicit Newmak method are unconditionally stable if the stability limits listed in Table 4.3 are satisfied; otherwise, these methods are unstable. However, the root locus method presented in [Chen and Ricles 2008] is a frequency domain equivalence of investigating the conditions of the spectral radius for the approximation operator. This root locus method is only applicable to linear time-invariant systems [Franklin et al. 2015], i.e., linear structures, and that is the reason why the obtained results and stability limits are the same as those expressed by Eqs. (4.11) and (4.12) and listed in Table 4.3. Accordingly, these published arguments of stability, i.e. those by Combescure and Pegon (1997) and Chen and Ricles (2008), are incorrect and theoretically groundless and thus, in general, not applicable to nonlinear problems.

4.4 NUMERICAL LYAPUNOV ANALYSIS

In this section, a numerical approach is presented to enable investigating the stability discussed in the previous sections. This approach is based on transforming the stability analysis to a problem of convex optimization, which is applicable to direct integration algorithms applied to nonlinear problems.

As previously discussed, a system is stable if its $\prod_{j=i}^{1}\mathbf{A}_j$ is bounded for $i\rightarrow\infty$. This is equivalent to investigating the system in Eq. (7) with the loading vector $\mathbf{L}=\mathbf{0}$, i.e.,

$$\boldsymbol{x}_{i+1}=\mathbf{A}_i\boldsymbol{x}_i \tag{4.18}$$

$\mathbf{A}_i$ can be rewritten non-dimensionally, e.g., in the implicit Newmark algorithm:

$$\mathbf{A}_i=\begin{bmatrix} \dfrac{1-2\pi\zeta\mu-\pi^2\delta_{i+1}^2\mu^2}{1+2\pi\zeta\mu+\pi^2\delta_{i+1}^2\mu^2} & -\dfrac{\omega_0^2(\Delta t)^2}{1+2\pi\zeta\mu+\pi^2\delta_{i+1}^2\mu^2} & 0 \\ \dfrac{1}{1+2\pi\zeta\mu+\pi^2\delta_{i+1}^2\mu^2} & \dfrac{1+2\pi\zeta\mu-\pi^2\delta_{i+1}^2\mu^2}{1+2\pi\zeta\mu+\pi^2\delta_{i+1}^2\mu^2} & 0 \\ \dfrac{\frac{1}{2}}{1+2\pi\zeta\mu+\pi^2\delta_{i+1}^2\mu^2} & \dfrac{1+2\pi\zeta\mu}{1+2\pi\zeta\mu+\pi^2\delta_{i+1}^2\mu^2} & 1 \end{bmatrix} \tag{4.19}$$

where $\delta_{i+1}=\omega_{T_{i+1}}/\omega_n$, $\mu=\Delta t/T_n$, $T_n=2\pi/\omega_n=2\pi\sqrt{m/k_I}$. Therefore, $\mathbf{A}_i$ is a function of δ_{i+1}. Similar to Eq. (4.6), the Lyapunov function v_{i+1} at the time step $i+1$ can be selected as:

$$v_{i+1}=\boldsymbol{x}_{i+1}^T\mathbf{M}_{i+1}\boldsymbol{x}_{i+1} \tag{4.20}$$

where the positive definite matrix $\mathbf{M}_{i+1} = \mathbf{M}_{i+1}^T$ is a function of δ_{i+1}. A sufficient condition for the system and thus the direct integration algorithm to be stable is as follows:

$$\begin{aligned} \Delta v_{i+1} &= v_{i+1} - r_t v_i \\ &= \boldsymbol{x}_{i+1}^T \mathbf{M}_{i+1} \boldsymbol{x}_{i+1} - r_t \boldsymbol{x}_i^T \mathbf{M}_i \boldsymbol{x}_i \\ &= \boldsymbol{x}_i^T \left(\mathbf{A}_i^T \mathbf{M}_{i+1} \mathbf{A}_i - r_t \mathbf{M}_i \right) \boldsymbol{x}_i \\ &= \boldsymbol{x}_i^T \mathbf{P}_{i+1} \boldsymbol{x}_i \le 0 \end{aligned} \tag{4.21}$$

where $0 < r_t \le 1$ controls the rate of convergence, i.e. the smaller the r_t, the faster the convergence. Eq. (4.21) leads to the negative semi-definiteness of $\mathbf{P}_{i+1}$, i.e. $\mathbf{P}_{i+1} \preccurlyeq \mathbf{0}$. For a direct integration algorithm, $\mathbf{M}_{i+1}$ can be expressed as:

$$\mathbf{M}_{i+1} = \sum_{j=1}^{N} \alpha_j \boldsymbol{\Phi}(\delta_{i+1})_j \tag{4.22}$$

where α_j and $\boldsymbol{\Phi}(\delta_{i+1})_j$ are the j–th constant coefficient and base function, respectively, and N is the total number of base functions. One example set of base functions is given in the Appendix. The set of base functions of only $\boldsymbol{\Phi}_1$ to $\boldsymbol{\Phi}_6$ represent constant $\mathbf{M}_{i+1}$. $\boldsymbol{\Phi}_7$ to $\boldsymbol{\Phi}_{12}$ constitute the set of base functions that treats $\mathbf{M}_{i+1}$ as a linear function of δ_{i+1}. Nonlinear relationship between $\mathbf{M}_{i+1}$ and δ_{i+1} can be considered by additional base functions $\boldsymbol{\Phi}_{13}$ to $\boldsymbol{\Phi}_{18}$.

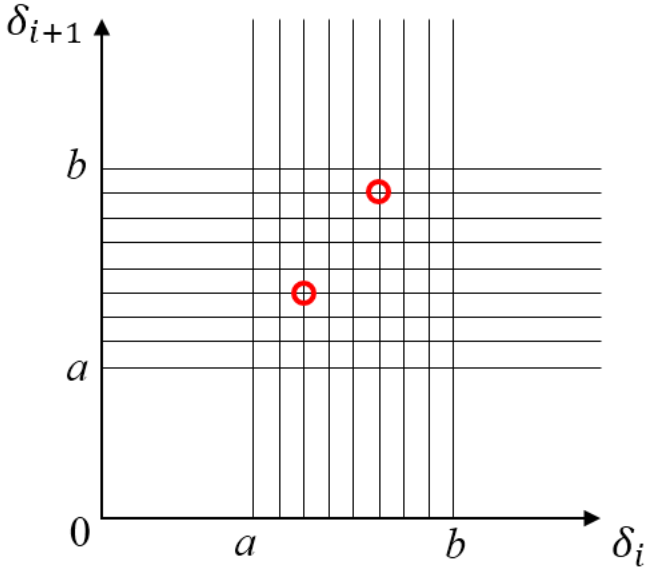

Figure 4.3 Schematic illustration of discretization process.

With the range of δ_i and δ_{i+1} given, e.g. $\delta_i, \delta_{i+1} \in [a,b]$, points can be sampled within this range (Figure 4.3), e.g., sampling $n+1$ points in $[a,b]$ with interval $\Delta\delta = (b-a)/n$. This yields

$(n+1)^2$ possible pairs of (δ_i, δ_{i+1}). Accordingly, the stability analysis becomes a problem of convex optimization that seeks the determination of the coefficients α_j by minimizing their norm for the selected base functions $\mathbf{\Phi}(\delta_{i+1})_j$ where $j:1\to N$, subjected to the following conditions on the $(n+1)^2$ possible pairs of (δ_i, δ_{i+1}):

$$\begin{aligned}
&\delta_i, \delta_{i+1} \in [a,b], \quad \Delta\delta = (b-a)/n \\
&\mathbf{A}_i^T \mathbf{M}_{i+1} \mathbf{A}_i - r_t \mathbf{M}_i = \mathbf{A}_i(\delta_{i+1})^T \left(\sum_{j=1}^{N} \alpha_j \mathbf{\Phi}(\delta_{i+1})_j \right) \mathbf{A}_i(\delta_{i+1}) - r_t \sum_{j=1}^{N} \alpha_j \mathbf{\Phi}(\delta_i)_j \prec= \mathbf{0} \\
&\mathbf{M}_i = \sum_{j=1}^{N} \alpha_j \mathbf{\Phi}(\delta_i)_j \succ \mathbf{0}, \quad \mathbf{M}_{i+1} = \sum_{j=1}^{N} \alpha_j \mathbf{\Phi}(\delta_{i+1})_j \succ \mathbf{0}
\end{aligned} \tag{4.23}$$

Moreover, with prior knowledge about the variation of δ_{i+1}, the range of $|\delta_{i+1} - \delta_i|$ can be specified, e.g. $|\delta_{i+1} - \delta_i| < \varepsilon$, where ε is an optional parameter that is not necessarily small. For example, suppose we are interested in investigating the stability of a certain algorithm in the range of $\delta_i, \delta_{i+1} \in [1,2]$, and $\delta_i = 1.5$ at *i-th* time step. If prior knowledge is known such that $\varepsilon = 0.3$, i.e. $\delta_{i+1} \in (1.2, 1.8)$, fewer possible pairs of (δ_i, δ_{i+1}) that require less computational effort can be considered.

The problem of convex optimization can be solved numerically by CVX, a software package for specifying and solving convex programs (CVX Research Inc. 2011). Two examples, the softening and the stiffening cases, for the implicit Newmark algorithm are considered based on the following conditions:

$$\zeta = 0.05 \quad \mu = 0.05/(2\pi) \quad n = 20 \quad \varepsilon = 0.05 \quad r_t = 1.0 \tag{4.24}$$

The set of base functions $\mathbf{\Phi}_1$ to $\mathbf{\Phi}_{12}$ in the Appendix is used.

4.4.1 Softening Example

Suppose we are interested in investigating the stability of the implicit Newmark algorithm in the range of $\delta_i, \delta_{i+1} \in [0.9, 1.0]$, therefore $\Delta\delta = (b-a)/n = 0.005$. The coefficients α_j, $j:1\to 12$, obtained by minimizing the 2-norm of α, i.e. $\min \sqrt{\left(\sum_{j=1}^{12} |\alpha_j|^2 \right)}$, are as follows:

$$\begin{aligned}
&\alpha_1 = 1.90\times10^{-8}, \quad \alpha_2 = 2.46\times10^{-9}, \quad \alpha_3 = 1.70\times10^{-10}, \quad \alpha_4 = -2.25\times10^{-9}, \\
&\alpha_5 = -2.70\times10^{-10}, \quad \alpha_6 = -4.60\times10^{-10}, \quad \alpha_7 = 1.76\times10^{-8}, \quad \alpha_8 = 1.05\times10^{-9}, \\
&\alpha_9 = 6.00\times10^{-11}, \quad \alpha_{10} = -3.35\times10^{-9}, \quad \alpha_{11} = 4.30\times10^{-10}, \quad \alpha_{12} = -2.00\times10^{-10}
\end{aligned} \tag{4.25}$$

The existence of such set of α_j implies the existence of $\mathbf{M}_{i+1}$ in Eq. (4.22) that satisfies the inequality in Eq. (4.21), which indicates that the implicit Newmark algorithm is stable for the conditions in Eq. (4.24) in the range of $\delta_i, \delta_{i+1} \in [0.9, 1.0]$.

4.4.2 Stiffening Example

Following similar procedure to the previous softening example, in the stiffening case with range of interest $\delta_i, \delta_{i+1} \in [1.0, 1.1]$, the obtained coefficients α_j, $j: 1 \to 12$, are as follows:

$$\begin{aligned} &\alpha_1 = 9.81\times10^{-7}, \quad \alpha_2 = 2.28\times10^{-10}, \quad \alpha_3 = 1.93\times10^{-8}, \quad \alpha_4 = -2.25\times10^{-8}, \\ &\alpha_5 = -2.30\times10^{-9}, \quad \alpha_6 = -1.53\times10^{-9}, \quad \alpha_7 = 1.01\times10^{-6}, \quad \alpha_8 = 3.39\times10^{-11}, \\ &\alpha_9 = 7.03\times10^{-9}, \quad \alpha_{10} = -8.94\times10^{-8}, \quad \alpha_{11} = 7.20\times10^{-9}, \quad \alpha_{12} = -5.01\times10^{-10} \end{aligned} \tag{4.26}$$

The set of α_j in Eqs. (4.25) and (26) from many determined sets has the minimum 2-norm explaining the listed small values of α_j. The existence of such set of α_j implies that the implicit Newmark algorithm is stable for the conditions in Eq. (4.24) in the range of $\delta_i, \delta_{i+1} \in [1.0, 1.1]$. The accuracy of the proposed numerical stability analysis approach depends on the selection of the interval $\Delta\delta$. Similar to the time step Δt used in nonlinear time history analysis, smaller $\Delta\delta$, that requires higher computational effort, leads to more accurate and reliable stability analysis. For example, if n+1=41 points (denoted as set A) are sampled ($\Delta\delta = 0.0025$) for the softening example, $41^2 - 21^2 = 1240$ additional pairs of (δ_i, δ_{i+1}), which require more computational effort, need to be considered than that for the case with n+1=21 sampled points (denoted as set B). The stability analysis based on set A is closer to that of the continuous interval of $[0.9, 1.0]$ than that based on set B. Furthermore, it is to be noted that the set of coefficients α that satisfies the inequality of Eq. (4.21) for set A, also fulfils the same inequality for set B because the set of the possible pairs of (δ_i, δ_{i+1}) for set B is a subset of that for set A. Therefore, the stability of the set of larger number of sampled points implies the stability of smaller number of sampled points. It should be emphasized that Eq. (4.21) is a sufficient condition for the direct integration algorithm to be stable. Therefore, the existence of the coefficients corresponding to the selected base functions obtained by the numerical approach proposed in this chapterr that satisfies Eq. (4.21) implies that the range of interest for δ_{i+1} is a sufficient range for the direct integration algorithm to be stable. However, inexistence of such coefficients does not indicate the instability of the direct integration algorithm within the range of interest for δ_{i+1}.

The proposed approach in this section can be applied to investigating the stability of other direct integration algorithms, including the other four methods considered in this chapter. Also, various nonlinear problems, including stiffening ($\delta_{i+1} > 1$) and softening ($\delta_{i+1} < 1$) behaviors in Fig. 1, can be taken into account. Accordingly, the proposed approach is generally applicable to direct integration algorithms as long as they can be expressed as given by Eq. (4.18). Moreover, this approach can potentially be extended to MDOF systems. For m-DOF systems, the $3m \times 3m$ approximation operator is a function of δ_{i+1}^j, where $j: 1 \to m$ denotes the *j-th* DOF, and thus

$(m+1)(9m^2+3m)/2$ selected base functions and corresponding coefficients are needed if $\mathbf{M}_{i+1}$ is expressed as an affine function of δ_{i+1}^j, $j:1\to m$. For example, for each possible pair of $(\delta_i^1, \delta_{i+1}^1, \ldots, \delta_i^m, \delta_{i+1}^m)$, the computational effort for 10-DOF systems is $[(10+1)(9\times10^2+3\times10)/2]/[(1+1)(9\times1^2+3\times1)/2]=426.25$ times that for SDOF systems. Therefore, the proposed approach may involve extensive computations for MDOF systems.

4.5 ACCURACY ANALYSIS

The accuracy of the numerical integration algorithms depends on several factors, e.g., the loading, the time-step size, and the physical parameters of the system. In order to develop an understanding of this accuracy, a nonlinear test problem with an available closed-form exact solution is analyzed in this section.

Consider a simple pendulum (Figure 4.4) of length l, forming a time-dependent angle $\theta(t)$ with the vertical axis and undergoing time-dependent angular acceleration $\ddot{\theta}(t)$. The governing equation, initial conditions, exact solution, and period of vibration are summarized in Table 4.4 where g is the gravitational acceleration, $\tilde{n}=K(r)-\kappa_0 t$, $\kappa_0=\sqrt{g/l}$, $K(r)$ is the complete elliptical integral of the first kind, and $sn(n;r)$ is the Jacobi elliptic function [Abramowitz and Stegun 1972].

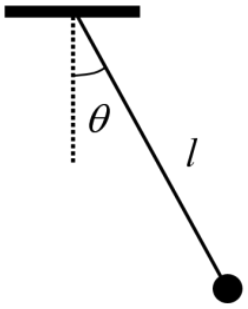

Figure 4.4 Schematic illustration of the nonlinear pendulum in a general deformed state.

Table 4.4 Nonlinear pendulum.

Property	Expression
Governing equation	$\ddot{\theta}+(g/l)\sin\theta=0$
Initial conditions	$\theta(0)=\theta_0, \dot{\theta}(0)=0$
Exact solution (Beléndez et al. 2007)	$\theta(t)=2\arcsin\{\sin(\theta_0/2)sn(\tilde{n};r)\}, r=\sin^2(\theta_0/2)$
Period	$T=4K(r)/\kappa_0$

Figures 4.5 and 4.6 present the period elongation and the amplitude decay of the investigated integration algorithms for $\theta_0=0.10\pi$ and $\theta_0=0.50\pi$, respectively. The period is

shortened using explicit Newmark [Chopra 2006], and elongated by the other algorithms. It is observed that $OS_{tangent}$ and implicit Newmark present similar period elongations. The TRBDF2 has the smallest period change while it is about twice computationally expensive compared to the other algorithms. Considering roughly the same computational efforts, e.g. $\Delta t/T = 0.08$ for TRBDF2 and $\Delta t/T = 0.04$ for the others, the accuracy becomes comparable. Moreover, the accuracy of all algorithms is indifferent for the integration time steps required for accuracy, i.e. $\Delta t/T < 0.01$ [Bathe 2006]. All algorithms do not result in any significant amplitude decay except TRBDF2, which presents some amplitude decay due to introduced numerical damping. Up to $\Delta t/T = 0.1$, period elongation (< ±3%) and amplitude decay (< 1%) are acceptable.

The nonlinear pendulum problem is also used to demonstrate the incorrectness of the stability criterion of the $OS_{initial}$ algorithm from past studies and the suitability of the proposed numerical stability analysis approach in this chapter. The tangent stiffness of this nonlinear pendulum is obtained as:

$$k_T = (g/l)\cos\theta \tag{4.27}$$

This tangent stiffness k_T is always positive if $\theta \in (-\pi/2, \pi/2)$. The $OS_{initial}$ algorithm with initial condition $\theta_0 = 0.10\pi$ results in the fact that all the values of tangent stiffness are larger than that of the initial stiffness, which is $(g/l)\cos(0.10\pi)$. Recall that the stability criterion by Combescure and Pegon (1997), refer to Table 3, implies that the $OS_{initial}$ algorithm should be unstable for $\theta_0 = 0.10\pi$. The numerical problem is analyzed using the proposed numerical stability analysis approach for the following conditions:

$$\zeta = 0 \quad \mu = 0.05/(2\pi) \quad n = 20 \quad r_t = 1.0 \tag{4.28}$$

The set of base functions $\mathbf{\Phi}_1$ to $\mathbf{\Phi}_6$ as in the Appendix is used, which represents constant $\mathbf{M}_{i+1}$. Same procedure as in section "Numerical Stability Analysis" is performed for $\theta_0 = 0.10\pi$ in this example. Therefore, for the range of interest $\delta_i, \delta_{i+1} \in [1.0, 1/\cos\theta_0]$, the coefficients α_j, $j: 1 \to 6$ obtained by minimizing the 2-norm of α, i.e. $\min \sqrt{(\sum_{j=1}^{6} |\alpha_j|^2)}$, are as follows:

$$\begin{aligned} &\alpha_1 = 7.91\times10^{-7}, \quad \alpha_2 = 2.59\times10^{-10}, \quad \alpha_3 = 1.60\times10^{-8}, \\ &\alpha_4 = -5.96\times10^{-8}, \quad \alpha_5 = 3.35\times10^{-9}, \quad \alpha_6 = -1.58\times10^{-9} \end{aligned} \tag{4.29}$$

The existence of such set of α_j implies that the $OS_{initial}$ algorithm is stable for $\theta_0 = 0.10\pi$. The results by the proposed approach is consistent with the fact that the $OS_{initial}$ algorithm is stable as reflected in Figure 4.5, which demonstrates the incorrectness of the stability criterion by Combescure and Pegon (1997).

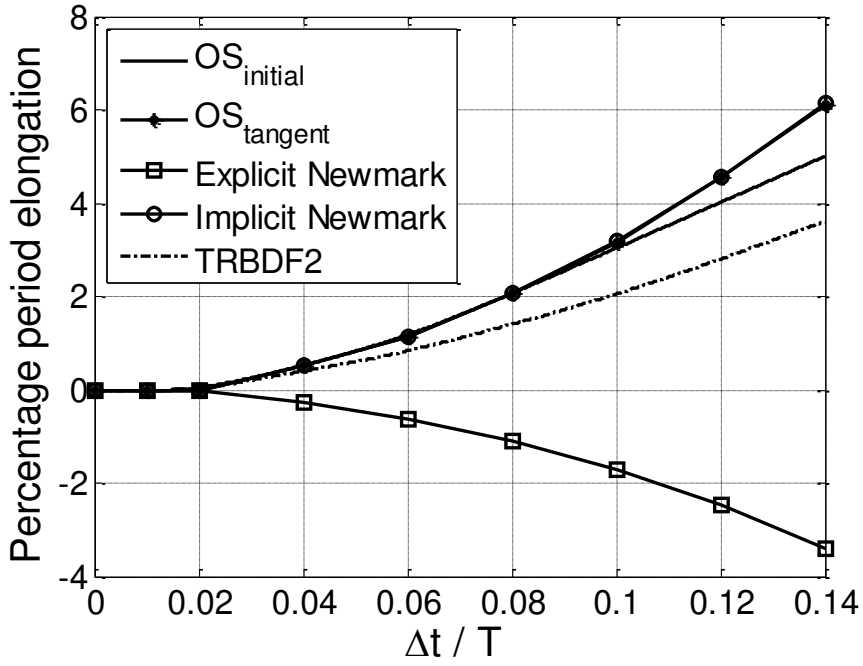

a) Period elongation

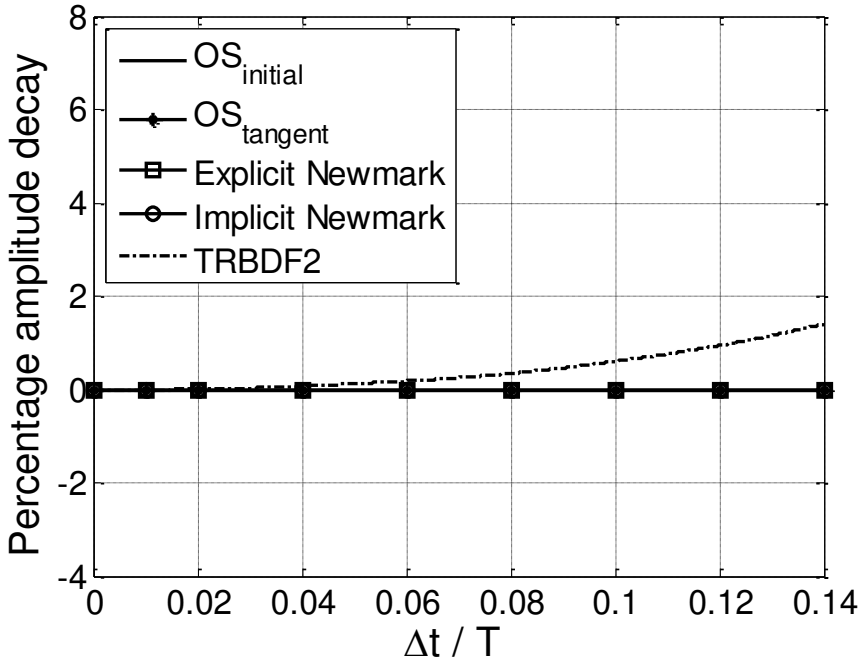

b) Amplitude decay

Figure 4.5 Period elongation and amplitude decay for the pendulum problem with $\theta_0 = 0.10\pi$.

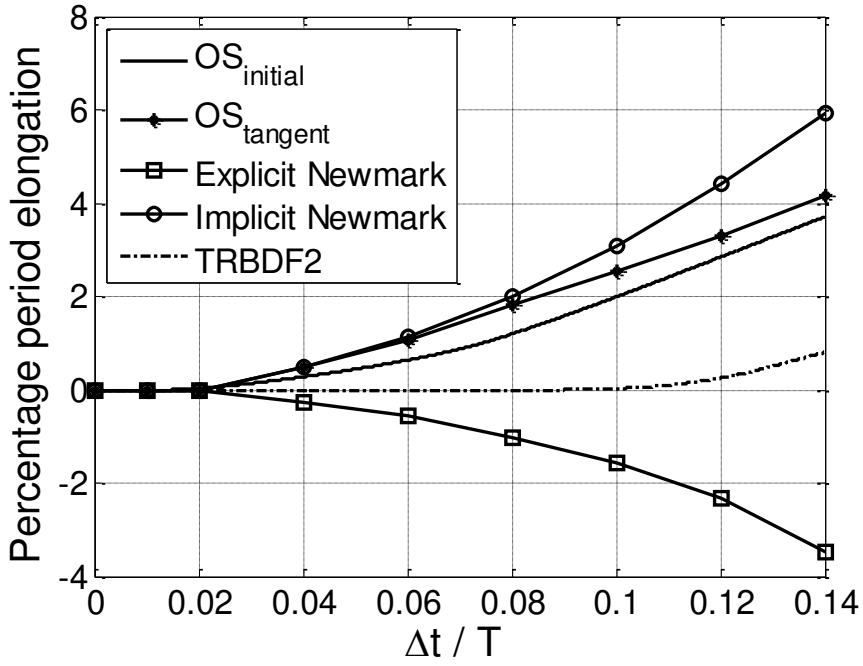

a) Period elongation

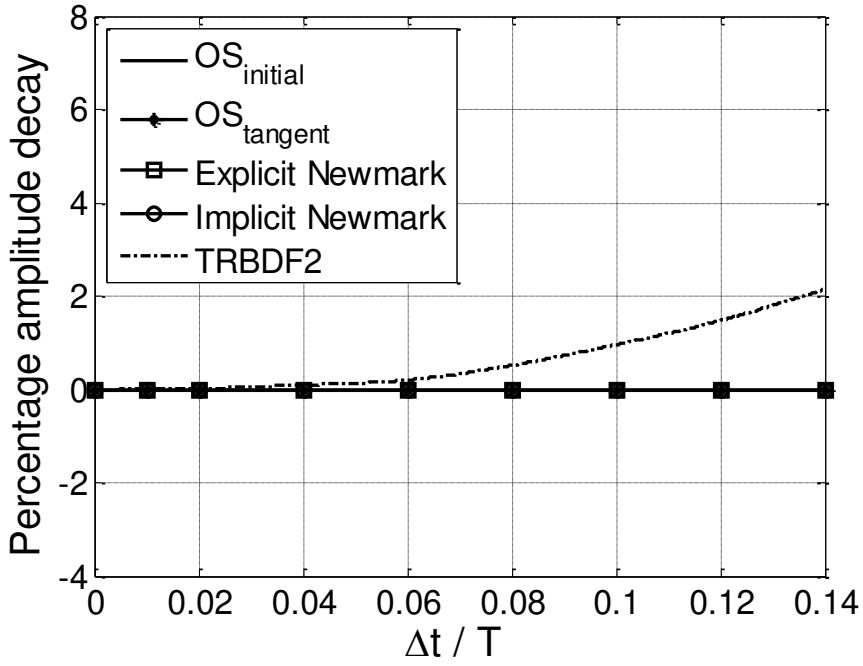

b) Amplitude decay

Figure 4.6 Period elongation and amplitude decay for the pendulum problem with $\theta_0 = 0.50\pi$.

5 Lyapunov Stability Considering Strictly Positive Real Lemma

5.1 INTRODUCTION

In Chapter 4, a numerical approach is proposed to conduct Lyapunov stability analysis of various implicit and explicit direct integration algorithms for SDOF nonlinear systems. Implicit algorithms may encounter numerical convergence problems when applied to nonlinear structural systems, especially those with large number of degrees of freedom (DOFs) or complex sources of nonlinearity. On the contrary, explicit algorithms do not require iterations by adopting certain approximations related to the kinematics of the structural system, making them appealing for use in solving nonlinear dynamic problems. Various explicit direct integration algorithms have been developed, including the explicit Newmark algorithm [Newmark 1959], the Operator-Splitting algorithm [Hughes et al. 1979] and the generalized- α predictor-corrector explicit (PCE) algorithm [Chung and Hulbert 1993; Hulbert and Chung 1996]. Liang et al. (2014b, 2016b) investigated the suitability of the latter for efficient nonlinear seismic response of multi-degree of freedom (MDOF) reinforced concrete highway bridge systems and promising results in terms of accuracy and numerical stability were obtained.

In this chapter, another Lyapunov-based approach is proposed to investigate Lyapunov stability of explicit direct integration algorithms for MDOF nonlinear systems [Liang and Mosalam 2015, 2016b-d]. Two general classes of MDOF nonlinear responses of structural systems are considered. They are stiffening systems, e.g., in situations where gaps between components of the system are closed, and softening systems, e.g., due to initiation and propagation of damage which is common in modeling reinforced concrete structures when subjected to extreme loads. The idealized backbone curves (force-displacement relationships) of these two systems are discussed later in the chapter. In this study, the explicit algorithm is formulated for a generic MDOF nonlinear system that has responses governed by nonlinear functions of the restoring forces. Based on this formulation, a systematic approach is proposed to investigate the Lyapunov stability of explicit algorithms for MDOF nonlinear systems by means of the strictly positive real lemma [Cains 1989]. This approach transforms the stability analysis to pursuing the strictly positive realness of the transfer function matrix for the formulated MDOF system. Furthermore, this is equivalent to a problem of convex optimization that can be solved graphically for SDOF systems, e.g., by Nyquist plot [Franklin et al. 2015], or numerically for MDOF systems, e.g., by CVX [CVX Research Inc. 2011]. Using the proposed approach, *a sufficient condition* in terms of bounds for each basic resisting force in this study, where the explicit algorithm is stable in the sense of Lyapunov, can be obtained. Specifically, the maximum and minimum bounds for each basic

resisting force for stable (in the sense of Lyapunov) MDOF stiffening and softening systems, respectively, are determined. Finally, this proposed Lyapunov stability analysis is demonstrated by a SDOF system, a bridge structure, and a generic multi-story shear building with nonlinear stiffening or softening behavior to study the stability performance of two types of commonly used explicit direct integration algorithms.

5.2 MATHEMATICAL PRELIMINARIES

In this section, definitions, notations, the generalized strictly positive real lemma and the corresponding corollary are introduced. Here, $(\bullet)^T$ and $(\bullet)^*$ denote transpose and complex conjugate transpose, respectively; $(\bullet) \succ \mathbf{0}$ and $(\bullet) \prec \mathbf{0}$ denote positive and negative definiteness, respectively. Denote

$$\mathbf{G}(z) \sim \left[\begin{array}{c|c} \overline{\mathbf{A}} & \overline{\mathbf{B}} \\ \hline \overline{\mathbf{C}} & \overline{\mathbf{D}} \end{array}\right] \tag{5.1}$$

as a state-space realization [Cains 1989] of a transfer function matrix $\mathbf{G}(z)$ expressed as follows:

$$\mathbf{G}(z) = \overline{\mathbf{D}} + \overline{\mathbf{C}}\left(\mathbf{I}z - \overline{\mathbf{A}}\right)^{-1}\overline{\mathbf{B}} \tag{5.2}$$

where $z = e^{j\theta}$ is a complex variable with $j = \sqrt{-1}$ and $\theta \in [0,\ 2\pi]$, $\overline{\mathbf{A}}$, $\overline{\mathbf{B}}$, $\overline{\mathbf{C}}$ and $\overline{\mathbf{D}}$ are real constant matrices and $\mathbf{I}$ is the identity matrix with proper dimensions.

A square transfer function matrix $\mathbf{G}(z)$ is called strictly positive real (Kapila and Haddad 1996) if: (i) $\mathbf{G}(z)$ is asymptotically stable, which is stronger than Lyapunov stability as it guarantees convergence to a specific value as "time" approaches infinity, and (ii) $\mathbf{G}(e^{j\theta}) + \mathbf{G}^*(e^{j\theta})$ is positive definite $\forall\, \theta \in [0,\ 2\pi]$. Condition (i) can be guaranteed by the condition that the spectral radius of $\overline{\mathbf{A}}$ must be less than 1.0, i.e. $\rho(\overline{\mathbf{A}}) < 1.0$. Let $\mathbf{Z}$ be the corresponding controllability matrix defined as follows:

$$\mathbf{Z} = [\overline{\mathbf{B}} \quad \overline{\mathbf{A}}\overline{\mathbf{B}} \quad \overline{\mathbf{A}}^2\overline{\mathbf{B}} \quad \cdots \quad \overline{\mathbf{A}}^{\overline{n}-1}\overline{\mathbf{B}}] \tag{5.3}$$

where $\overline{n}$ is the dimension of the square matrix $\overline{\mathbf{A}}$.

With controllability of $(\overline{\mathbf{A}}, \overline{\mathbf{B}})$, i.e. $\text{rank}(\mathbf{Z}) = \overline{n}$ and $\rho(\overline{\mathbf{A}}) < 1.0$, based on the *generalized discrete-time strictly positive real lemma* [Kunimatsu et al. 2008; Xiao and Hill 1999], if $\mathbf{G}(z)$ is strictly positive real, then there exist matrices $\overline{\mathbf{M}} = \overline{\mathbf{M}}^T \succ \mathbf{0}$, $\overline{\mathbf{L}}$ and $\overline{\mathbf{W}}$ where the following conditions are satisfied:

$$\overline{\mathbf{M}} = \overline{\mathbf{A}}^T\overline{\mathbf{M}}\,\overline{\mathbf{A}} + \overline{\mathbf{L}}^T\overline{\mathbf{L}} \tag{5.4a}$$

$$\mathbf{0} = \overline{\mathbf{B}}^T\overline{\mathbf{M}}\,\overline{\mathbf{A}} - \overline{\mathbf{C}} + \overline{\mathbf{W}}^T\overline{\mathbf{L}} \tag{5.4b}$$

$$\mathbf{0} = \overline{\mathbf{D}} + \overline{\mathbf{D}}^T - \overline{\mathbf{B}}^T \overline{\mathbf{M}}\, \overline{\mathbf{B}} - \overline{\mathbf{W}}^T \overline{\mathbf{W}} \tag{5.4c}$$

Moreover, based on a corollary [Kottenstette and Antsaklis 2010; Lee and Chen 2003], the square transfer function matrix $\mathbf{G}(z)$ in Eq. (5.2) is strictly positive real and matrix $\overline{\mathbf{A}}$ is asymptotically stable if and only if there exists a matrix $\mathbf{P} = \mathbf{P}^T \succ \mathbf{0}$ such that Eq. (5.5) is satisfied.

$$\begin{bmatrix} \overline{\mathbf{A}}^T \mathbf{P} \overline{\mathbf{A}} - \mathbf{P} & \overline{\mathbf{A}}^T \mathbf{P} \overline{\mathbf{B}} - \overline{\mathbf{C}}^T \\ \left(\overline{\mathbf{A}}^T \mathbf{P} \overline{\mathbf{B}} - \overline{\mathbf{C}}^T\right)^T & -\left(\overline{\mathbf{D}}^T + \overline{\mathbf{D}}\right) + \overline{\mathbf{B}}^T \mathbf{P} \overline{\mathbf{B}} \end{bmatrix} \prec \mathbf{0} \tag{5.5}$$

5.3 EXPLICIT INTEGRATION ALGORITHMS

The discretized equations of motion of a MDOF system under an external dynamic force excitation is expressed as follows:

$$\mathbf{m}\ddot{\mathbf{u}}_{i+1} + \mathbf{c}\dot{\mathbf{u}}_{i+1} + \mathbf{f}_{i+1} = \mathbf{p}_{i+1} \tag{5.6}$$

where $\mathbf{m}$ and $\mathbf{c}$ are the mass and viscous damping matrices, and $\ddot{\mathbf{u}}_{i+1}$, $\dot{\mathbf{u}}_{i+1}$, $\mathbf{f}_{i+1}$ and $\mathbf{p}_{i+1}$ are the vectors of acceleration, velocity, restoring force and external force at the time step $i+1$, respectively. Due to several factors, such as the random variation of the external force with time, e.g. earthquake shaking, and the nonlinear variation of the restoring force vector with deformation due to material and/or geometrical nonlinearities, closed form solution of Eq. (5.6) is not always possible [Chopra 2006]. Therefore, direct integration algorithms are used for the sought solution. Two categories of explicit integration algorithms are considered in this chapter: standard single-step and predictor-corrector explicit algorithms.

5.3.1 Standard Single-step Explicit Algorithms

Standard single-step explicit (SSE) direct integration algorithms considered in this chapter are defined by the following difference equations:

$$\mathbf{u}_{i+1} = \mathbf{u}_i + \eta_0(\Delta t)\dot{\mathbf{u}}_i + \eta_1(\Delta t)^2 \ddot{\mathbf{u}}_i \tag{5.7a}$$

$$\dot{\mathbf{u}}_{i+1} = \dot{\mathbf{u}}_i + \eta_2(\Delta t)\ddot{\mathbf{u}}_i + \eta_3(\Delta t)\ddot{\mathbf{u}}_{i+1} \tag{5.7b}$$

For example, $\boldsymbol{\eta} = [\eta_0 \quad \eta_1 \quad \eta_2 \quad \eta_3] = [1 \quad 1/2 \quad 1/2 \quad 1/2]$ leads to the explicit Newmark algorithm [Newmark 1959]. Substituting Eq. (5.7b) in Eq. (5.6), the following linear system of equations is readily obtained.

$$\mathbf{m}_{eff}\ddot{\mathbf{u}}_{i+1} = \mathbf{p}_{eff} \tag{5.8a}$$

$$\mathbf{m}_{eff} = \mathbf{m} + \eta_3(\Delta t)\,\mathbf{c} \tag{5.8b}$$

$$\mathbf{p}_{eff} = \mathbf{p}_{i+1} - \mathbf{f}_{i+1} - \mathbf{c}\left[\dot{\mathbf{u}}_i + \eta_2(\Delta t)\ddot{\mathbf{u}}_i\right] \tag{5.8c}$$

The acceleration can be determined by solving Eqs. (5.8) and then substituting in Eq. (5.7b) to determine the velocity.

5.3.2 Predictor-corrector Explicit Algorithms

Generalized-α predictor-corrector explicit (PCE) algorithm [Chung and Hulbert 1993; Hulbert and Chung 1996] is considered in this section. The predicted displacement and velocity are:

$$\tilde{\mathbf{u}}_{i+1} = \mathbf{u}_i + (\Delta t)(1-\gamma)\dot{\mathbf{u}}_i + (0.5-\beta)(\Delta t)^2 \ddot{\mathbf{u}}_i \tag{5.9a}$$

$$\dot{\tilde{\mathbf{u}}}_{i+1} = \dot{\mathbf{u}}_i + (1-\gamma)(\Delta t)\ddot{\mathbf{u}}_i \tag{5.9b}$$

where parameters γ and β are defined in Eq. (5.12). The balance equation of this method is:

$$\mathbf{m}\ddot{\mathbf{u}}_{i+1-\alpha_m} + \mathbf{c}\dot{\tilde{\mathbf{u}}}_{i+1-\alpha_f} + \tilde{\mathbf{f}}_{i+1-\alpha_f} = \mathbf{p}_{i+1-\alpha_f} \tag{5.10}$$

where $\tilde{\mathbf{f}}_{i+1-\alpha_f}$ is the restoring force vector corresponding to $\tilde{\mathbf{u}}_{i+1-\alpha_f}$ and $\mathbf{p}_{i+1-\alpha_f}$ is the external force vector at time step $i+1-\alpha_f$ with other parameters defined as follows:

$$\ddot{\mathbf{u}}_{i+1-\alpha_m} = (1-\alpha_m)\ddot{\mathbf{u}}_{i+1} + \alpha_m \ddot{\mathbf{u}}_i \tag{5.11a}$$

$$\dot{\tilde{\mathbf{u}}}_{i+1-\alpha_f} = (1-\alpha_f)\dot{\tilde{\mathbf{u}}}_{i+1} + \alpha_f \dot{\mathbf{u}}_i \tag{5.11b}$$

$$\tilde{\mathbf{u}}_{i+1-\alpha_f} = (1-\alpha_f)\tilde{\mathbf{u}}_{i+1} + \alpha_f \mathbf{u}_i \tag{5.11c}$$

$$t_{i+1-\alpha_f} = (1-\alpha_f)t_{i+1} + \alpha_f t_i \tag{5.11d}$$

The algorithmic parameters are given by

$$\alpha_m = \frac{2\rho_\infty - 1}{\rho_\infty + 1}, \quad \alpha_f = \frac{\rho_\infty}{\rho_\infty + 1}, \quad \gamma = \frac{1}{2} - \alpha_m + \alpha_f, \quad \beta = \frac{1}{4}\left(\frac{1}{2} + \gamma\right)^2 \tag{5.12}$$

where ρ_∞ is the desired high-frequency dissipation. The acceleration at time step $i+1$, $\ddot{\mathbf{u}}_{i+1}$, can be calculated using Eqs. (5.10) and (5.11a). Subsequently, the displacement and velocity at time step $i+1$ can be determined by the following correctors:

$$\mathbf{u}_{i+1} = \tilde{\mathbf{u}}_{i+1} + \beta(\Delta t)^2 \ddot{\mathbf{u}}_{i+1} \tag{5.13a}$$

$$\dot{\mathbf{u}}_{i+1} = \dot{\tilde{\mathbf{u}}}_{i+1} + \gamma(\Delta t)\ddot{\mathbf{u}}_{i+1} \tag{5.13b}$$

5.4 MDOF NONLINEAR SYSTEMS

For a MDOF system with n DOFs, the *j*–th term of the restoring force vector, $f^j, j \in [1,n]$, can be expressed as a linear combination of N basic resisting forces of the system, $q^l, l \in [1,N]$, i.e.

$$f^j = \sum_{l=1}^{N} \alpha_l^j q^l = \boldsymbol{\alpha}^j \mathbf{q} \tag{5.14}$$

where $\mathbf{q}^T = [q^1, q^2, \ldots, q^N]$ and $\boldsymbol{\alpha}^j = [\alpha_1^j, \alpha_2^j, \ldots, \alpha_N^j]$. Therefore,

$$\mathbf{f} = [f^1, f^2, \ldots, f^n]^T = \boldsymbol{\alpha}\mathbf{q} \tag{5.15}$$

where $\boldsymbol{\alpha} = [\boldsymbol{\alpha}^1, \boldsymbol{\alpha}^2, \ldots, \boldsymbol{\alpha}^n]^T$ is a $n \times N$ matrix. In general, N is the summation of the number of the basic resisting forces from each element that contribute to the n DOFs of the system. For the special case of a shear building, $N = n$ because of its assumed shear mode behavior. The *l*–th basic resisting force, q^l, is here defined as a function of $\bar{u}^l$, which is in itself a linear combination of the displacement of each DOF, $u^j, j \in [1,n]$, i.e.

$$\bar{u}^l = \sum_{j=1}^{n} \beta_j^l u^j = \boldsymbol{\beta}^l \mathbf{u} \tag{5.16}$$

where $\mathbf{u} = [u^1, u^2, \ldots, u^n]$ and $\boldsymbol{\beta}^l = [\beta_1^l, \beta_2^l, \ldots, \beta_n^l]$. Therefore,

$$\bar{\mathbf{u}} = [\bar{u}^1, \bar{u}^2, \ldots, \bar{u}^N]^T = \boldsymbol{\beta}\mathbf{u} \tag{5.17}$$

where $\boldsymbol{\beta} = [\boldsymbol{\beta}^1, \boldsymbol{\beta}^2, \ldots, \boldsymbol{\beta}^N]^T$ is a $N \times n$ matrix. Detailed explanation of N defining the number of columns and rows of the matrices $\boldsymbol{\alpha}$ and $\boldsymbol{\beta}$, respectively, for the bridge and shear building examples are discussed in Appendices B and C, respectively. Moreover, the *l*–th basic resisting force, q^l, is restricted to the following range (to be determined in this chapter according to the outcome of the conducted Lyapunov stability analysis):

$$\bar{k}_{Min}^l \left(\bar{u}^l\right)^2 \le q^l \bar{u}^l \le \bar{k}_{Max}^l \left(\bar{u}^l\right)^2 \tag{5.18}$$

where $\bar{k}_{Min}^l$ and $\bar{k}_{Max}^l$ are the minimum and maximum bounds of q^l, respectively. Therefore, summing up all basic resisting forces from 1 to N gives

$$\sum_{l=1}^{N} \left[\bar{k}_{Min}^l \left(\bar{u}^l\right)^2\right] \le \sum_{l=1}^{N} \left(q^l \bar{u}^l\right) \le \sum_{l=1}^{N} \left[\bar{k}_{Max}^l \left(\bar{u}^l\right)^2\right] \tag{5.19}$$

Eq. (5.19) is equivalent to the following:

$$\bar{\mathbf{u}}^T \bar{\mathbf{k}}_{Min} \bar{\mathbf{u}} \le \bar{\mathbf{u}}^T \mathbf{q} \le \bar{\mathbf{u}}^T \bar{\mathbf{k}}_{Max} \bar{\mathbf{u}} \tag{5.20}$$

where

$$\bar{\mathbf{k}}_{Min} = \text{diag}[\,\bar{k}^1_{Min},\, \bar{k}^2_{Min}, \ldots,\, \bar{k}^N_{Min}\,] \tag{5.21a}$$

$$\bar{\mathbf{k}}_{Max} = \text{diag}[\,\bar{k}^1_{Max},\, \bar{k}^2_{Max}, \ldots,\, \bar{k}^N_{Max}\,] \tag{5.21b}$$

Defining $\bar{k}^l_I$ as the initial bound of q^l, Fig. 1 shows the schematic illustrations of the l–th resisting force bounded in the sector between $\bar{k}^l_{Min}\left(\bar{u}^l\right)$ and $\bar{k}^l_{Max}\left(\bar{u}^l\right)$ for stiffening (Figure 5.1a) and softening (Figure 5.1b) systems. As mentioned before, the maximum, $\bar{k}^l_{Max}$ and minimum, $\bar{k}^l_{Min}$, bounds of q^l, where $l : 1 \to N$, for stable (in the sense of Lyapunov) stiffening and softening MDOF systems, respectively, are to be determined in this chapter. In the next two subsections, the explicit integration algorithms introduced in the previous section are formulated for MDOF (n DOFs) nonlinear systems with stiffening and softening behavior (Figure 5.1).

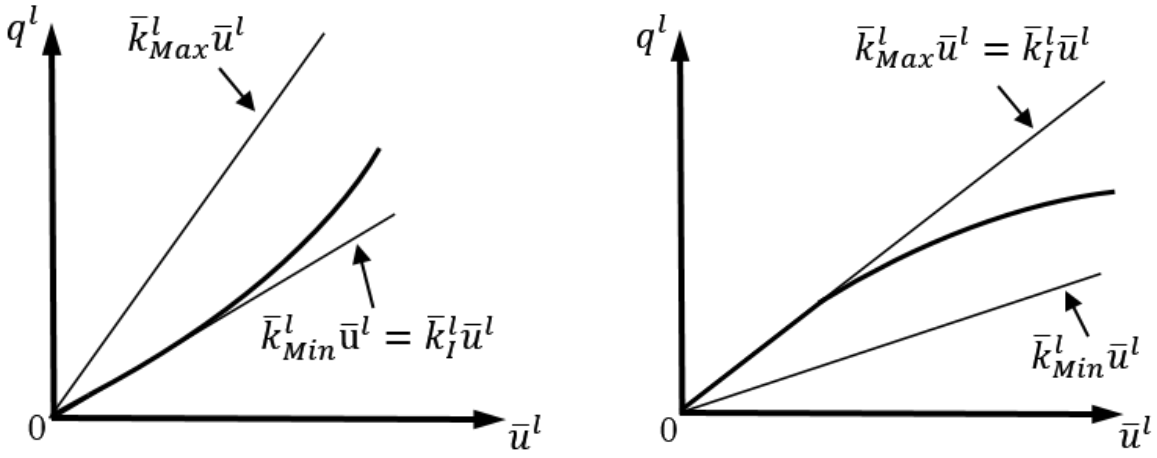

a) Stiffening system **b) Softening system**

Figure 5.1 Schematic illustrations of two nonlinear systems with sector-bounded basic resisting forces.

5.4.1 MDOF Stiffening Systems

For the two categories of explicit direct integration algorithms, the relationship between the kinematic quantities at time steps $i+1$ and i can be established as follows:

$$\boldsymbol{x}_{i+1} = \mathbf{A}\boldsymbol{x}_i - \mathbf{B}_1 \bar{\mathbf{f}}_{i+1} + \mathbf{D}\bar{\mathbf{p}}_{i+1} = \mathbf{A}\boldsymbol{x}_i - \mathbf{B}_1 \boldsymbol{\alpha} \bar{\mathbf{q}}_{i+1} + \mathbf{D}\bar{\mathbf{p}}_{i+1} \tag{5.22}$$

where $\boldsymbol{x}_i = \left[(\Delta t)^2 \ddot{\mathbf{u}}_i^T \quad (\Delta t)\dot{\mathbf{u}}_i^T \quad \mathbf{u}_i^T\right]^T$. For the SSE algorithms, $\mathbf{A}$, $\mathbf{B}_1$ and $\mathbf{D}$ are as follows with $\bar{\mathbf{f}}_{i+1} = \mathbf{f}_{i+1}$, $\bar{\mathbf{p}}_{i+1} = \mathbf{p}_{i+1}$ and $\bar{\mathbf{q}}_{i+1} = \mathbf{q}_{i+1}$:

$$\mathbf{A}=\begin{bmatrix} -\eta_2(\Delta t)\mathbf{m}_{eff}^{-1}\mathbf{c} & -(\Delta t)\mathbf{m}_{eff}^{-1}\mathbf{c} & \mathbf{0} \\ \eta_2\mathbf{I}-\eta_2\eta_3(\Delta t)\mathbf{m}_{eff}^{-1}\mathbf{c} & \mathbf{I}-\eta_3(\Delta t)\mathbf{m}_{eff}^{-1}\mathbf{c} & \mathbf{0} \\ \eta_1\mathbf{I} & \eta_0\mathbf{I} & \mathbf{I} \end{bmatrix} \tag{5.23a}$$

$$\mathbf{B}_1=\mathbf{D}=\begin{bmatrix}(\Delta t)^2\mathbf{m}_{eff}^{-1} & \eta_3(\Delta t)^2\mathbf{m}_{eff}^{-1} & \mathbf{0}\end{bmatrix}^T \tag{5.23b}$$

where $\mathbf{0}$ and $\mathbf{I}$ are $n\times n$ null and identity matrices, respectively. The external force vector, $\mathbf{p}$, is generally independent of the kinematic quantities, $\boldsymbol{x}$, and does not affect the Lyapunov stability of the direct integration algorithms (Liang and Mosalam 2015, 2016a). Therefore, $\overline{\mathbf{p}}_{i+1}$ in Eq. (5.22) is set to zero in the subsequent parts of this chapter. For the PCE algorithms, $\mathbf{A}$ is listed in Table 5.1 and considering $\overline{\mathbf{f}}_{i+1}=\widetilde{\mathbf{f}}_{i+1-\alpha_f}$, $\overline{\mathbf{p}}_{i+1}=\mathbf{p}_{i+1-\alpha_f}$ and $\overline{\mathbf{q}}_{i+1}=\widetilde{\mathbf{q}}_{i+1-\alpha_f}$, we have:

$$\mathbf{B}_1=\mathbf{D}=\begin{bmatrix}\dfrac{(\Delta t)^2\mathbf{m}^{-1}}{1-\alpha_m} & \dfrac{\gamma(\Delta t)^2\mathbf{m}^{-1}}{1-\alpha_m} & \dfrac{\beta(\Delta t)^2\mathbf{m}^{-1}}{1-\alpha_m}\end{bmatrix}^T \tag{5.24}$$

Table 5.1 Elements of $\mathbf{A}$ matrix for PCE algorithms.

Element	Expression	Element	Expression
$\mathbf{A}_{11}$	$-\left(\mathbf{m}^{-1}\mathbf{c}(1-\alpha_f)(1-\gamma)(\Delta t)-\alpha_m\mathbf{I}\right)/(1-\alpha_m)$	$\mathbf{A}_{22}$	$\mathbf{I}+\gamma\mathbf{A}_{12}$
$\mathbf{A}_{21}$	$(1-\gamma)\mathbf{I}+\gamma\mathbf{A}_{11}$	$\mathbf{A}_{32}$	$\mathbf{I}+\beta\mathbf{A}_{12}$
$\mathbf{A}_{31}$	$(0.5-\beta)\mathbf{I}+\beta(\Delta t)^2\mathbf{A}_{11}$	$\mathbf{A}_{13}=\mathbf{A}_{23}$	$\mathbf{0}$
$\mathbf{A}_{12}$	$-\mathbf{m}^{-1}\mathbf{c}(\Delta t)/(1-\alpha_m)$	$\mathbf{A}_{33}$	$\mathbf{I}$

It is obvious that n of the eigenvalues of $\mathbf{A}$ are 1.0's leading to failure to guarantee the previously mentioned first condition (i) of the strictly positive realness of the transfer function matrix. Therefore, Eq. (5.22) (after setting $\overline{\mathbf{p}}_{i+1}=\mathbf{0}$) is further manipulated as follows:

$$\begin{aligned}\boldsymbol{x}_{i+1}&=\mathbf{A}\boldsymbol{x}_i-\mathbf{B}_1\boldsymbol{\alpha}\overline{\mathbf{k}}_{Min}\mathbf{C}\boldsymbol{x}_i+\mathbf{B}_1\boldsymbol{\alpha}\overline{\mathbf{k}}_{Min}\mathbf{C}\boldsymbol{x}_i-\mathbf{B}_1\boldsymbol{\alpha}\overline{\mathbf{q}}_{i+1}\\&=\left(\mathbf{A}-\mathbf{B}_1\boldsymbol{\alpha}\overline{\mathbf{k}}_{Min}\mathbf{C}\right)\boldsymbol{x}_i-\mathbf{B}_1\boldsymbol{\alpha}\left(\overline{\mathbf{q}}_{i+1}-\overline{\mathbf{k}}_{Min}\mathbf{C}\boldsymbol{x}_i\right)\\&=\left(\mathbf{A}-\mathbf{B}_1\boldsymbol{\alpha}\overline{\mathbf{k}}_{Min}\mathbf{C}\right)\boldsymbol{x}_i-\mathbf{B}_1\boldsymbol{\alpha}\left(\overline{\mathbf{q}}_{i+1}-\overline{\mathbf{k}}_{Min}\overline{\mathbf{u}}_{i+1}\right)\\&=\mathbf{A}_{e1}\boldsymbol{x}_i-\mathbf{B}_1\boldsymbol{\alpha}\mathbf{q}_{e1}\end{aligned} \tag{5.25}$$

where

$$\mathbf{C}=\boldsymbol{\beta}\widetilde{\mathbf{C}} \tag{5.26a}$$

$$\tilde{\mathbf{C}} = \begin{cases} \begin{bmatrix} \eta_1\mathbf{I} & \eta_0\mathbf{I} & \mathbf{I} \end{bmatrix} & \text{SSE algorithms} \\ \begin{bmatrix} (1-\alpha_f)(0.5-\beta)\mathbf{I} & (1-\alpha_f)\mathbf{I} & \mathbf{I} \end{bmatrix} & \text{PCE algorithms} \end{cases} \tag{5.26b}$$

$$\bar{\mathbf{u}}_{i+1} = \mathbf{C}\boldsymbol{x}_i \tag{5.26c}$$

$$\mathbf{A}_{e1} = \mathbf{A} - \mathbf{B}_1\boldsymbol{\alpha}\bar{\mathbf{k}}_{Min}\mathbf{C} \tag{5.26d}$$

$$\mathbf{q}_{e1} = \bar{\mathbf{q}}_{i+1} - \bar{\mathbf{k}}_{Min}\bar{\mathbf{u}}_{i+1} \tag{5.26e}$$

5.4.2 MDOF Softening Systems

For softening systems, similar to Eq. (5.22), with $\mathbf{B}_2 = -\mathbf{B}_1$ and also setting $\bar{\mathbf{p}}_{i+1} = \mathbf{0}$, as mentioned above:

$$\begin{aligned} \boldsymbol{x}_{i+1} &= \mathbf{A}\boldsymbol{x}_i + \mathbf{B}_2\boldsymbol{\alpha}\bar{\mathbf{q}}_{i+1} \\ &= \mathbf{A}\boldsymbol{x}_i + \mathbf{B}_2\boldsymbol{\alpha}\bar{\mathbf{k}}_{Max}\mathbf{C}\boldsymbol{x}_i - \mathbf{B}_2\boldsymbol{\alpha}\bar{\mathbf{k}}_{Max}\mathbf{C}\boldsymbol{x}_i + \mathbf{B}_2\boldsymbol{\alpha}\bar{\mathbf{q}}_{i+1} \\ &= \left(\mathbf{A} + \mathbf{B}_2\boldsymbol{\alpha}\bar{\mathbf{k}}_{Max}\mathbf{C}\right)\boldsymbol{x}_i - \mathbf{B}_2\boldsymbol{\alpha}\left(\bar{\mathbf{k}}_{Max}\mathbf{C}\boldsymbol{x}_i - \bar{\mathbf{q}}_{i+1}\right) \\ &= \left(\mathbf{A} + \mathbf{B}_2\boldsymbol{\alpha}\bar{\mathbf{k}}_{Max}\mathbf{C}\right)\boldsymbol{x}_i - \mathbf{B}_2\boldsymbol{\alpha}\left(\bar{\mathbf{k}}_{Max}\bar{\mathbf{u}}_{i+1} - \bar{\mathbf{q}}_{i+1}\right) \\ &= \mathbf{A}_{e2}\boldsymbol{x}_i - \mathbf{B}_2\boldsymbol{\alpha}\mathbf{q}_{e2} \end{aligned} \tag{5.27}$$

where

$$\mathbf{A}_{e2} = \mathbf{A} + \mathbf{B}_2\boldsymbol{\alpha}\bar{\mathbf{k}}_{Max}\mathbf{C} \tag{5.28a}$$

$$\mathbf{q}_{e2} = \bar{\mathbf{k}}_{Max}\bar{\mathbf{u}}_{i+1} - \bar{\mathbf{q}}_{i+1} \tag{5.28b}$$

Accordingly, both stiffening and softening systems can be expressed in Eq. (5.29) with coefficients $\mathbf{A}_e, \mathbf{B}_e$ and $\mathbf{q}_e$ summarized in Table 5.2.

$$\boldsymbol{x}_{i+1} = \mathbf{A}_e\boldsymbol{x}_i - \mathbf{B}_e\mathbf{q}_e \tag{5.29}$$

Table 5.2 Coefficients of MDOF stiffening and softening systems.

Matrix	Stiffening Systems	Softening Systems
$\mathbf{A}_e$	$\mathbf{A}_{e1} = \mathbf{A} - \mathbf{B}_1\boldsymbol{\alpha}\bar{\mathbf{k}}_{Min}\mathbf{C}$	$\mathbf{A}_{e2} = \mathbf{A} + \mathbf{B}_2\boldsymbol{\alpha}\bar{\mathbf{k}}_{Max}\mathbf{C}$
$\mathbf{B}_e$	$\mathbf{B}_1\boldsymbol{\alpha}$	$\mathbf{B}_2\boldsymbol{\alpha}$
$\mathbf{q}_e$	$\mathbf{q}_{e1} = \bar{\mathbf{q}}_{i+1} - \bar{\mathbf{k}}_{Min}\mathbf{C}\boldsymbol{x}_i$	$\mathbf{q}_{e2} = \bar{\mathbf{k}}_{Max}\mathbf{C}\boldsymbol{x}_i - \bar{\mathbf{q}}_{i+1}$

5.5 LYAPUNOV STABILITY ANALYSIS AS A PROBLEM OF CONVEX OPTIMIZATION

Based on Eq. (5.18) and Table 5.2, the *l*–th effective basic resisting force, q_e^l, expressed as a function of $\bar{\mathrm{u}}_{i+1}^l$, has the following range:

$$0 \le q_e^l \bar{\mathrm{u}}_{i+1}^l \le \bar{k}^l \left(\bar{\mathrm{u}}_{i+1}^l\right)^2 \tag{5.30}$$

where $\bar{k}^l = \bar{k}_{Max}^l - \bar{k}_{Min}^l$. Summing up all effective basic resisting forces from 1 to N gives

$$0 \le \sum_{l=1}^{N} \left(q_e^l \bar{\mathrm{u}}_{i+1}^l\right) \le \sum_{l=1}^{N} \left[\bar{k}^l \left(\bar{\mathrm{u}}_{i+1}^l\right)^2\right] \tag{5.31}$$

Therefore, $\mathbf{q}_e$, expressed as a function of $\bar{\mathbf{u}}$, has the following range:

$$0 \le \bar{\mathbf{u}}_{i+1}^T \mathbf{q}_e \le \bar{\mathbf{u}}_{i+1}^T \bar{\mathbf{k}} \bar{\mathbf{u}}_{i+1} \tag{5.32}$$

where

$$\bar{\mathbf{k}} = \bar{\mathbf{k}}_{Max} - \bar{\mathbf{k}}_{Min} = \mathrm{diag}[\bar{k}^1, \bar{k}^2, \ldots, \bar{k}^N] \tag{5.33}$$

For the system in Eq. (5.29), based on the Lyapunov stability theory introduced in Chapter 3, a Lyapunov artificial energy function candidate v_{i+1} [Franklin et al. 2015] at the time step $i+1$ can be chosen as follows:

$$v_{i+1} = \boldsymbol{x}_{i+1}^T \mathbf{M} \boldsymbol{x}_{i+1} \tag{5.34}$$

where $\mathbf{M} = \mathbf{M}^T \succ \mathbf{0}$. *A sufficient condition* for the system, and thus the explicit direct integration algorithm, to be stable in the sense of Lyapunov is as follows:

$$\begin{aligned} \Delta v_{i+1} &= v_{i+1} - v_i = \boldsymbol{x}_{i+1}^T \mathbf{M} \boldsymbol{x}_{i+1} - \boldsymbol{x}_i^T \mathbf{M} \boldsymbol{x}_i \\ &= \left(\mathbf{A}_e \boldsymbol{x}_i - \mathbf{B}_e \mathbf{q}_e\right)^T \mathbf{M} \left(\mathbf{A}_e \boldsymbol{x}_i - \mathbf{B}_e \mathbf{q}_e\right) - \boldsymbol{x}_i^T \mathbf{M} \boldsymbol{x} \\ &= \boldsymbol{x}_i^T \left(\mathbf{A}_e^T \mathbf{M} \mathbf{A}_e - \mathbf{M}\right) \boldsymbol{x}_i - 2 \mathbf{q}_e^T \mathbf{B}_e^T \mathbf{M} \mathbf{A}_e \boldsymbol{x}_i + \mathbf{q}_e^T \mathbf{B}_e^T \mathbf{M} \mathbf{B}_e \mathbf{q}_e \le 0 \end{aligned} \tag{5.35}$$

Defining the weight coefficient of the constraint in Eq. (5.30) as $\lambda_l > 0$ with $\sum_{l=1}^{N} \lambda_l = 1$, multiplying Eq. (5.30) by $\lambda_l \, q_e^l / \bar{\mathrm{u}}_{i+1}^l, \left|\bar{\mathrm{u}}_{i+1}^l\right| > 0$, which is always positive, and rearranging, one obtains:

$$\lambda_l q_e^l \left(q_e^l - \bar{k}^l \bar{u}_{i+1}^l\right) \le 0 \tag{5.36}$$

Summing up all effective basic resisting forces from 1 to N gives the following:

$$\sum_{l=1}^{N}\left[\lambda_l q_e^l\left(q_e^l-\bar{k}^l\bar{u}_{i+1}^l\right)\right]=\mathbf{q}_e^T\boldsymbol{\lambda}\left(\mathbf{q}_e-\bar{\mathbf{k}}\bar{\mathbf{u}}_{i+1}\right)=\mathbf{q}_e^T\boldsymbol{\lambda}\left(\mathbf{q}_e-\bar{\mathbf{k}}\mathbf{C}\boldsymbol{x}_i\right)\le 0 \tag{5.37}$$

where the coefficient matrix $\boldsymbol{\lambda}=\text{diag}[\,\lambda_1,\,\lambda_2,\ldots,\,\lambda_N\,]$. Defining $\Delta\bar{v}_{i+1}$ as an upper bound of Δv_{i+1} that incorporates the constraints in Eq. (5.37), Eq. (5.35) becomes

$$\begin{aligned}\Delta v_{i+1}\le\Delta\bar{v}_{i+1}&=\boldsymbol{x}_i^T\left(\mathbf{A}_e^T\mathbf{M}\mathbf{A}_e-\mathbf{M}\right)\boldsymbol{x}_i-2\mathbf{q}_e^T\mathbf{B}_e^T\mathbf{M}\mathbf{A}_e\boldsymbol{x}_i+\mathbf{q}_e^T\mathbf{B}_e^T\mathbf{M}\mathbf{B}_e\mathbf{q}_e-2\mathbf{q}_e^T\boldsymbol{\lambda}\left(\mathbf{q}_e-\bar{\mathbf{k}}\mathbf{C}\boldsymbol{x}_i\right)\\&=\boldsymbol{x}_i^T\left(\mathbf{A}_e^T\mathbf{M}\mathbf{A}_e-\mathbf{M}\right)\boldsymbol{x}_i+\mathbf{q}_e^T\left(\mathbf{B}_e^T\mathbf{M}\mathbf{B}_e-2\boldsymbol{\lambda}\right)\mathbf{q}_e-2\mathbf{q}_e^T\left(\mathbf{B}_e^T\mathbf{M}\mathbf{A}_e-\boldsymbol{\lambda}\bar{\mathbf{k}}\mathbf{C}\right)\boldsymbol{x}_i\end{aligned} \tag{5.38}$$

where $\Delta\bar{v}_{i+1}$ can be further transformed as follows:

$$\begin{aligned}\Delta\bar{v}_{i+1}&=\Delta\bar{v}_{i+1}+\boldsymbol{x}_i^T\mathbf{L}^T\mathbf{L}\boldsymbol{x}_i-\boldsymbol{x}_i^T\mathbf{L}^T\mathbf{L}\boldsymbol{x}_i\\&=\boldsymbol{x}_i^T\left(\mathbf{A}_e^T\mathbf{M}\mathbf{A}_e-\mathbf{M}+\mathbf{L}^T\mathbf{L}\right)\boldsymbol{x}_i-\\&\quad\left[\mathbf{q}_e^T\left(2\boldsymbol{\lambda}-\mathbf{B}_e^T\mathbf{M}\mathbf{B}_e\right)\mathbf{q}_e-2\mathbf{q}_e^T\left(\boldsymbol{\lambda}\bar{\mathbf{k}}\mathbf{C}-\mathbf{B}_e^T\mathbf{M}\mathbf{A}_e\right)\boldsymbol{x}_i+\boldsymbol{x}_i^T\mathbf{L}^T\mathbf{L}\boldsymbol{x}_i\right]\end{aligned} \tag{5.39}$$

where $\mathbf{L}$ is a $3n\times 3n$ matrix. *A sufficient condition* for $\Delta\bar{v}_{i+1}\le 0$ and thus $\Delta v_{i+1}\le 0$ is as follows:

$$\mathbf{M}=\mathbf{A}_e^T\mathbf{M}\mathbf{A}_e+\mathbf{L}^T\mathbf{L} \tag{5.40a}$$

$$\mathbf{0}=\mathbf{B}_e^T\mathbf{M}\mathbf{A}_e-\boldsymbol{\lambda}\bar{\mathbf{k}}\mathbf{C}+\mathbf{W}^T\mathbf{L} \tag{5.40b}$$

$$\mathbf{0}=\boldsymbol{\lambda}+\boldsymbol{\lambda}^T-\mathbf{B}_e^T\mathbf{M}\mathbf{B}_e-\mathbf{W}^T\mathbf{W} \tag{5.40c}$$

where $\mathbf{W}$ is a $3n\times N$ matrix. With Eqs. (5.40), Eq. (5.35) becomes

$$\begin{aligned}\Delta v_{i+1}\le\Delta\bar{v}_{i+1}&=\boldsymbol{x}_i^T\mathbf{0}\boldsymbol{x}_i-\left(\mathbf{q}_e^T\mathbf{W}^T\mathbf{W}\mathbf{q}_e-2\mathbf{q}_e^T\mathbf{W}^T\mathbf{L}\boldsymbol{x}_i+\boldsymbol{x}_i^T\mathbf{L}^T\mathbf{L}\boldsymbol{x}_i\right)\\&=-\left(\mathbf{W}\mathbf{q}_e-\mathbf{L}\boldsymbol{x}_i\right)^T\left(\mathbf{W}\mathbf{q}_e-\mathbf{L}\boldsymbol{x}_i\right)\le 0\end{aligned} \tag{5.41}$$

Therefore, the Lyapunov stability of the explicit integration algorithm depends solely on the existence of $\mathbf{M}$, $\mathbf{L}$ and $\mathbf{W}$ such that Eqs. (5.40) are satisfied. Recall the generalized discrete-time strictly positive real lemma presented before, i.e. Eqs. (5.4), the comparison between Eqs. (5.4) and (5.40) gives

$$\bar{\mathbf{A}}=\mathbf{A}_e,\quad\bar{\mathbf{B}}=\mathbf{B}_e,\quad\bar{\mathbf{C}}=\boldsymbol{\lambda}\bar{\mathbf{k}}\mathbf{C},\quad\bar{\mathbf{D}}=\boldsymbol{\lambda},\quad\bar{\mathbf{M}}=\mathbf{M},\quad\bar{\mathbf{L}}=\mathbf{L},\quad\bar{\mathbf{W}}=\mathbf{W} \tag{5.42}$$

Accordingly, the stability analysis reduces to seeking $\bar{\mathbf{k}}$ such that the transfer function matrix $\mathbf{G}(z)$ in Eq. (5.43) is strictly positive real.

$$\mathbf{G}(z)=\boldsymbol{\lambda}+\boldsymbol{\lambda}\bar{\mathbf{k}}\mathbf{C}\left(\mathbf{I}z-\mathbf{A}_e\right)^{-1}\mathbf{B}_e \tag{5.43}$$

For SDOF systems, the matrices $\boldsymbol{\alpha}$, $\boldsymbol{\beta}$, and $\boldsymbol{\lambda}$ become 1, Eq. (5.43) reduces to

$$G(z) = 1 + \bar{k}\mathbf{C}(\mathbf{I}z - \mathbf{A}_e)^{-1}\mathbf{B}_e \tag{5.44}$$

The strictly positive realness of $G(z)$ can be guaranteed by the asymptotical stability of $\mathbf{A}_e$ and

$$\mathrm{Re}[G(z)] > 0 \tag{5.45}$$

which leads to

$$\mathrm{Re}[H(z)] > -1/\bar{k} \tag{5.46}$$

where

$$H(z) = \mathbf{C}(\mathbf{I}z - \mathbf{A}_e)^{-1}\mathbf{B}_e \tag{5.47}$$

The Nyquist plot [Franklin et al. 2015] can be used to plot $H(e^{j\theta})\ \forall\ \theta \in [0, 2\pi]$. From this plot, the minimum value of $\mathrm{Re}[H(z)]$ that is corresponding to the $-1/\bar{k}$ can be obtained.

For MDOF systems, recall the corollary in Eq. (5.5), the strictly positive realness of $\mathbf{G}(z)$ in Eq. (5.43) becomes equivalent to Eq. (5.48) with $\mathbf{P} = \mathbf{P}^T \succ \mathbf{0}$:

$$\begin{bmatrix} \mathbf{A}_e^T\mathbf{P}\mathbf{A}_e - \mathbf{P} & \mathbf{A}_e^T\mathbf{P}\mathbf{B}_e - (\boldsymbol{\lambda}\bar{\mathbf{k}}\mathbf{C})^T \\ \left[\mathbf{A}_e^T\mathbf{P}\mathbf{B}_e - (\boldsymbol{\lambda}\bar{\mathbf{k}}\mathbf{C})^T\right]^T & -(\boldsymbol{\lambda}^T + \boldsymbol{\lambda}) + \mathbf{B}_e^T\mathbf{P}\mathbf{B}_e \end{bmatrix} \prec \mathbf{0} \tag{5.48}$$

Eq. (5.48) is a linear matrix inequality (LMI) over variables $\mathbf{P}$ and $\bar{\mathbf{k}}$ [Boyd et al. 1994]. Accordingly, the stability analysis becomes a problem of convex optimization, which addresses the problem of minimizing convex functions over convex sets, by which a wide range of problems can be formulated. In convex optimization, any local minimum must be a global minimum. This important property leads to reliable and efficient solutions, e.g. interior-point methods, which are suitable for computer-aided design or analysis tools [Boyd and Vandenberge 2004]. This problem of convex optimization in Eq. (5.48), which seeks $\bar{\mathbf{k}}$ and the corresponding $\mathbf{P}$ by minimizing certain convex cost function, e.g. $\min\left(\sum_{l=1}^{N} \bar{k}^l\right)$, subjected to the constraints of $\mathbf{P} = \mathbf{P}^T \succ \mathbf{0}$ and $\bar{\mathbf{k}} \succ \mathbf{0}$, can be solved numerically by CVX, a package for specifying and solving convex problems [CVX Research Inc. 2011]. It should be noted that a poorly chosen cost function or coefficient matrix may lead to reduced sufficient condition, i.e., the difference between the upper and lower bounds of the basic resisting force of the system ($\bar{\mathbf{k}}$). In general, a smaller value of the weight coefficient for the constraint λ_l leads to a larger value of $\bar{k}^l$. For example, in a two-DOF system, $\min\left(-\bar{k}^2\right)$ and $\lambda_2 = 0.1$ (5. $\lambda_1 = 1 - \lambda_2 = 0.9$) may not be a good cost function and weight coefficient if the basic force q^1 is of primary interest since this cost function may result in small $\bar{k}^1$. In this case, $\min\left(-\bar{k}^1\right)$ and $\lambda_1 = 0.1$ would be an appropriate selection. Therefore, the selection of the cost function and coefficient matrix is important and should take all the basic resisting forces of interest into account.

It is noteworthy that if $\mathbf{q}$ in Eq. (5.20) is strictly within the following range:

$$\bar{\mathbf{u}}^T\bar{\mathbf{k}}_{Min}\bar{\mathbf{u}} < \bar{\mathbf{u}}^T\mathbf{q} < \bar{\mathbf{u}}^T\bar{\mathbf{k}}_{Max}\bar{\mathbf{u}} \tag{5.49}$$

Therefore, Eqs. (5.32), (5.37) and (5.41) become

$$0 < \bar{\mathbf{u}}_{i+1}^T\mathbf{q}_e < \bar{\mathbf{u}}_{i+1}^T\bar{\mathbf{k}}\bar{\mathbf{u}}_{i+1} \tag{5.50a}$$

$$\mathbf{q}_e^T\boldsymbol{\lambda}\left(\mathbf{q}_e - \bar{\mathbf{k}}\bar{\mathbf{u}}_{i+1}\right) = \mathbf{q}_e^T\boldsymbol{\lambda}\left(\mathbf{q}_e - \bar{\mathbf{k}}\mathbf{C}\boldsymbol{x}_i\right) < 0 \tag{5.50b}$$

$$\Delta v_{i+1} < \Delta\bar{v}_{i+1} \le 0 \tag{5.50c}$$

Accordingly, the explicit direct integration algorithm is asymptotically stable in this case, i.e. $\bar{\mathbf{u}}^T\mathbf{q} \in \left(\bar{\mathbf{u}}^T\bar{\mathbf{k}}_{Min}\bar{\mathbf{u}}, \bar{\mathbf{u}}^T\bar{\mathbf{k}}_{Max}\bar{\mathbf{u}}\right)$. It should be emphasized that Eq. (5.41) is *a sufficient condition* for the direct explicit integration algorithm to be stable. Therefore, the matrix $\bar{\mathbf{k}}$ obtained by the approach proposed in this chapter that satisfies Eq. (5.48) implies that $\bar{\mathbf{u}}^T\mathbf{q} \in [\bar{\mathbf{u}}^T\bar{\mathbf{k}}_{Min}\bar{\mathbf{u}}, \bar{\mathbf{u}}^T\bar{\mathbf{k}}_{Max}\bar{\mathbf{u}}]$, where $\bar{\mathbf{k}}_{Max} = \bar{\mathbf{k}}_{Min} + \bar{\mathbf{k}}$, is *a sufficient range* for the direct explicit integration algorithm to be stable. However, having some basic resisting force vector $\mathbf{q}$ that may fall outside this range does not indicate the instability of the direct explicit integration algorithm.

5.6 NUMERICAL EXAMPLES FOR SDOF SYSTEMS

In this section, the two categories of explicit direct integration algorithms previously discussed are used to demonstrate the approach proposed in the previous sections based on the following numerical conditions:

$$m = 1, \quad k_I = 1, \quad \omega_n = 2\pi/T_n = \sqrt{k_I/m}, \quad \zeta = c/\left(2m\omega_n\right) = 0.05, \quad \mu = \left(\Delta t\right)/T_n = 0.01 \tag{5.51}$$

For convenience, all units in this and subsequent sections are omitted.

Based on Eq. (5.51), $\mathbf{A}_e$, $\mathbf{C}$ and $\rho\left(\mathbf{A}_e\right)$ for the explicit Newmark algorithm, i.e., $\boldsymbol{\eta} = \begin{bmatrix}1 & 1/2 & 1/2 & 1/2\end{bmatrix}$, are as follows:

$$\mathbf{A}_e = \begin{bmatrix} -0.0051 & -0.0102 & -0.0039 \\ 0.4975 & 0.9949 & -0.0020 \\ 0.5000 & 1.0000 & 1.0000 \end{bmatrix} \tag{5.52a}$$

$$\mathbf{C} = \begin{bmatrix}0.5000 & 1.0000 & 1.0000\end{bmatrix} \tag{5.52b}$$

$$\rho\left(\mathbf{A}_e\right) = 0.9969 \tag{5.52c}$$

$\rho(\mathbf{A}_e)<1$ implies that $\mathbf{A}_e$ is asymptotically stable and thus the first condition of the strictly positive realness of $G(z)$ in Eq. (5.44) is satisfied.

5.6.1 Stiffening Systems

For stiffening systems, $\mathbf{B}_e = \mathbf{B}_1$ is as follows:

$$\mathbf{B}_e = [0.0039 \quad 0.0020 \quad 0]^T \tag{5.53}$$

The row ranks of the Kalman's controllability matrix:

$$\mathbf{Z} = [\mathbf{B}_e \quad \mathbf{A}_e\mathbf{B}_e \quad \mathbf{A}_e^2\mathbf{B}_e] \tag{5.54}$$

is equal to 3, i.e., $\text{rank}(\mathbf{Z}) = 3$. Therefore, $(\mathbf{A}_e, \mathbf{B}_e)$ is controllable.

The Nyquist plot of $H(z)$ in Eq. (5.46) corresponding to $\mathbf{A}_e$, $\mathbf{C}$ and $\mathbf{B}_e$ in Eqs. (5.52) and (5.53) is shown in Figure 5.2, where $\min\{\text{Re}[H(z)]\} = -4.7642$ is obtained. Based on Eq. (5.45), one obtains:

$$-1/k < \min\{\text{Re}[H(z)]\} \tag{5.55a}$$

$$k < -1/\min\{\text{Re}[H(z)]\} = 0.2099 \tag{5.55b}$$

Accordingly, for stiffening systems, the explicit Newmark algorithm is stable in the sense of Lyapunov in the range that $f/u \in [k_I, k_I + k) = [1, 1.2099), |u| > 0$ for the numerical conditions in Eq. (5.51).

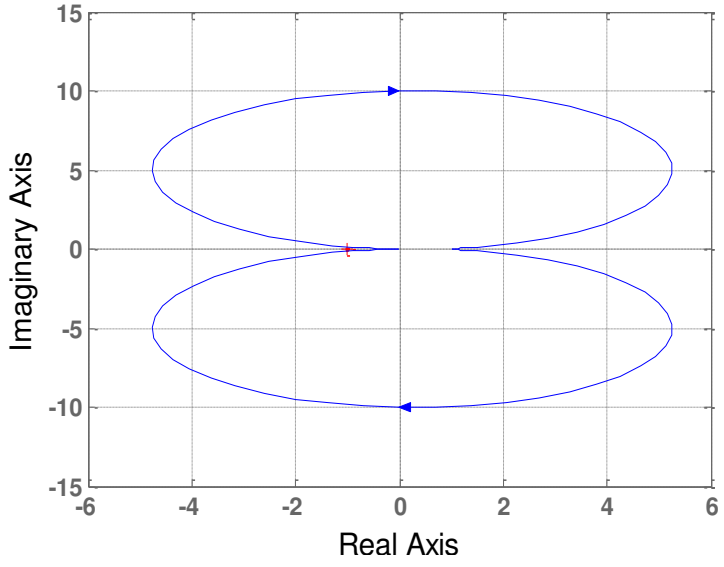

Figure 5.2 Nyquist plot of $H(z)$ for a stiffening system of the explicit Newmark algorithm.

5.6.2 Softening Systems

For softening systems, $\mathbf{B}_e = \mathbf{B}_2$ is as follows:

$$\mathbf{B}_e = -\begin{bmatrix} 0.0039 & 0.0020 & 0 \end{bmatrix}^T \tag{5.56}$$

Figure 5.3 shows the Nyquist plot of $H(z)$ in Eq. (5.45) corresponding to $\mathbf{A}_e$, $\mathbf{C}$ and $\mathbf{B}_e$ in Eqs. (5.52) and (5.56). Similar to Eqs. (5.40), with $\min\{\mathrm{Re}[H(z)]\} = -5.2586$ obtained from Figure 5.3, one obtains:

$$k < -1/\min\{\mathrm{Re}[H(z)]\} = 0.1902 \tag{5.57}$$

Therefore, for softening systems, the explicit Newmark algorithm is stable in the sense of Lyapunov in the range that $f/u \in (k_I - k, k_I] = (0.8098, 1]$, $|u| > 0$ for the numerical conditions in Eq. (5.51).

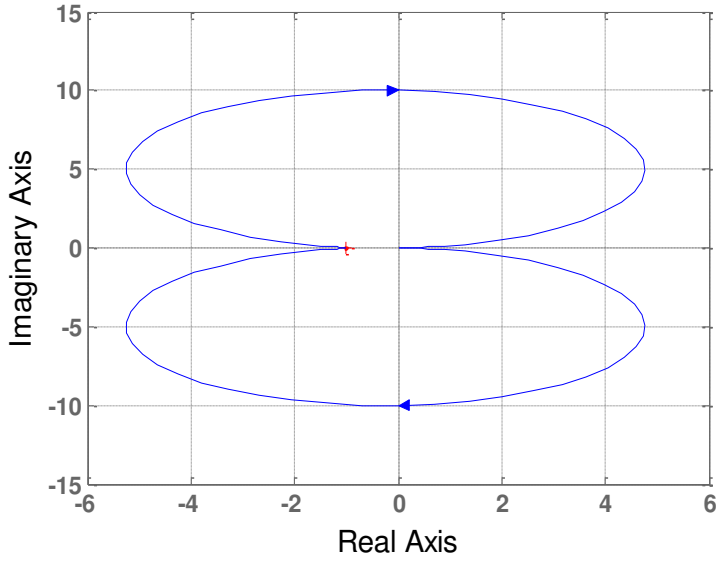

Figure 5.3 Nyquist plot of $H(z)$ for a softening system of the explicit Newmark algorithm.

Table 5.3 The k values of different SSE algorithms for stiffening and softening systems.

$\boldsymbol{\eta}$	$\rho(\mathbf{A}_e)$	Stiffening Systems	Softening Systems
$\begin{bmatrix} 1 & 1/2 & 1/4 & 3/4 \end{bmatrix}$	0.9964	0.3333	0.2853
$\begin{bmatrix} 1 & 1/2 & 3/4 & 1/4 \end{bmatrix}$	0.9974	0.1387	0.1308
$\begin{bmatrix} 1 & 1/4 & 1/2 & 1/2 \end{bmatrix}$	0.9974	0.1727	0.1639

Table 5.4 The k values of different generalized-α PCE algorithms for stiffening and softening systems.

ρ_∞	$\rho(\mathbf{A}_e)$	Stiffening systems	Softening systems
0.1	0.9969	0.2096	0.1901
0.3	0.9969	0.2101	0.1904
0.5	0.9969	0.2103	0.1905
0.7	0.9969	0.2103	0.1905
0.9	0.9969	0.2103	0.1905

The proposed approach can be applied to investigate the stability of other explicit direct integration algorithms. The results of other SSE algorithms defined by the vector $\boldsymbol{\eta}$ and the generalized-α PCE algorithms defined by ρ_∞ are listed in Tables 5.3 and 5.4, respectively.

5.7 NUMERICAL EXAMPLES FOR MDOF SYSTEMS

Several numerical examples for MDOF systems are presented in this section.

5.7.1 MDOF Bridge Structures

The MDOF bridge structure investigated in this section is depicted in Figure 5.4 with mass per unit length and the flexural rigidity (EI) given for each member. This bridge structure has the six DOFs shown where axial deformation neglected in all members.

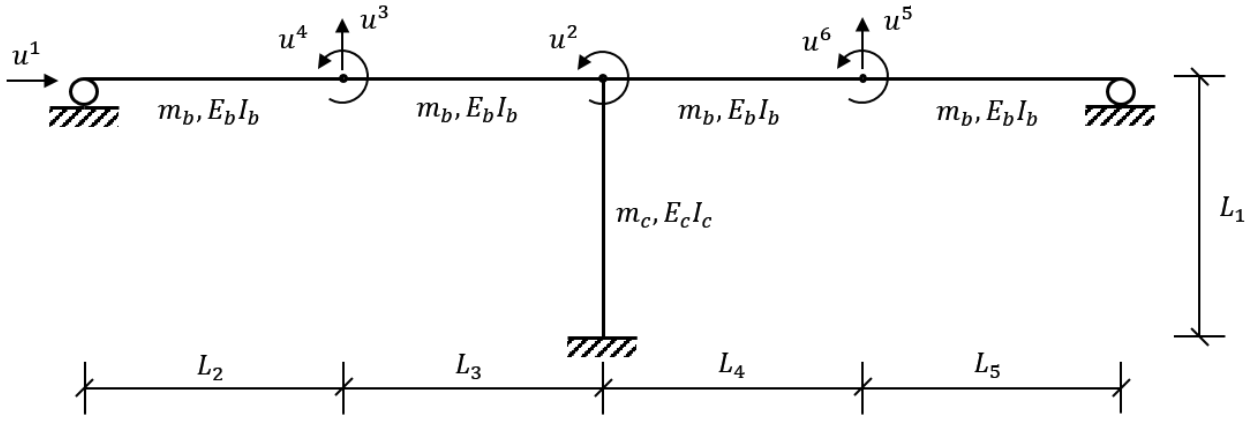

Figure 5.4 A MDOF bridge structure.

The derivation of the N basic resisting forces ($\mathbf{q}$ in terms of $\overline{\mathbf{u}}$) and the corresponding matrices $\boldsymbol{\alpha}$ and $\boldsymbol{\beta}$ for this bridge structure is given in Appendix I. The row rank of the controllability matrix:

$$\mathbf{Z} = [\mathbf{B}_e \quad \mathbf{A}_e\mathbf{B}_e \quad \mathbf{A}_e^2\mathbf{B}_e \quad \cdots \quad \mathbf{A}_e^{17}\mathbf{B}_e] \tag{5.58}$$

is such that $\text{rank}(\mathbf{Z}) = 18$. Therefore, $(\mathbf{A}_e, \mathbf{B}_e)$ is controllable and $\rho(\mathbf{A}_e) = 0.9999 < 1$.

In this section, the generalized-α PCE algorithm with $\rho_\infty = 0.6$ is used to demonstrate the approach proposed in the previous sections on MDOF structural systems with nonlinear stiffening or softening behavior. The Lyapunov stability analysis is conducted for the bridge in Figure 5.4 assuming the following numerical values:

$$m_b = m_c = 1.0, \quad L_i = 100.0, i = 1, 2, \cdots, 5, \quad E_bI_b = E_cI_c = 1.0 \times 10^8 \tag{5.59a}$$

$$\lambda_l = l \Big/ \sum_{l=1}^{N} l, \quad \mu = (\Delta t)/T_n = 0.01 \tag{5.59b}$$

where λ_l is the weight coefficient of the l-th constraint, refer to Eq. (5.36), $l : 1 \to N$, T_n is the period of the n–th mode of vibration, which is $T_n = T_6 = 0.19\,\text{sec}$ for the analyzed bridge. Rayleigh damping is assigned to the bridge [Chopra 2006], i.e.,

$$\mathbf{c} = a_0\mathbf{m} + a_1\mathbf{k} \tag{5.60}$$

where $\mathbf{m}$, $\mathbf{c}$ and $\mathbf{k}$ are the mass, viscous damping and linear elastic stiffness matrices, respectively. The constants a_0 and a_1 are determined from specified damping ratio ζ_i and ζ_j for the *i*–th and *j*–th modes, respectively. With both modes are assumed to possess the same damping ratio, i.e. $\zeta = 0.05$, the constants a_0 and a_1 are determined as follows [Chopra 2006]:

$$a_0 = \frac{2\omega_i\omega_j\zeta}{\omega_i + \omega_j}, \quad a_1 = \frac{2\zeta}{\omega_i + \omega_j} \tag{5.61}$$

where ω_i and ω_j are the natural frequencies of the *i*–th and *j*–th modes. Therefore, the damping ratio for the *k*–th mode is [Chopra 2006]:

$$\zeta_k = \frac{a_0}{2\omega_k} + \frac{a_1\omega_k}{2} \tag{5.62}$$

In this example, $i = 1$ and $j = 4$ are selected such that the mean value of the damping ratio of all modes, i.e. $\text{mean}(\zeta_1, \zeta_2, \ldots, \zeta_6)$, has the closest value to the assigned damping ratio $\zeta = 0.05$. The determination of the damping matrices for the other examples in this chapter follows the same procedure presented above.

Table 5.5 The $\bar{k}$ of each basic resisting force for the bridge structure.

Resisting force Number	Stiffening systems	Softening systems
1	11234.1	10084.7
2	3470.2	3478.0
3	836.4	707.1
4	725.9	612.7
5	769.1	723.8
6	1132.8	1015.1
7	691.7	644.9
8	437.6	413.0
9	908.3	857.2
10	550.0	528.6
11	372.8	353.9
12	527.7	494.7

Table 5.6 The $\bar{k}$ of each basic resisting force for the bridge structure for different λ and cost function.

Resisting force Number	Stiffening systems	Softening systems
1	5791.6	5680.6
2	430.0	419.8
3	897.9	890.5
4	897.9	890.5
5	802.7	753.3
6	1144.5	1086.5
7	834.4	824.0
8	575.9	564.0
9	1144.5	1086.5
10	802.7	753.3
11	575.9	564.0
12	834.4	824.0

Under earthquake excitation, nonlinearity usually occurs in the columns of bridge structure only where the bridge deck can be modeled using linear elastic elements. Therefore, the basic resisting forces associated with the column are of primary interest. Based on Appendix B, only the first two basic resisting forces are associated with the horizontal translation DOF of the column, u^1. Hence, the weight coefficients in Eq. (5.59b) are chosen such that the two smallest weight coefficients are assigned to the constraints corresponding to the first two basic resisting forces. Moreover, the cost function for this bridge structure is selected as $\min[-(\bar{k}^1+\bar{k}^2)]$, which is equivalent to maximizing $(\bar{k}^1+\bar{k}^2)$. Accordingly, we perform convex optimization over all possible $\bar{\mathbf{k}}$ that has the largest value of $(\bar{k}^1+\bar{k}^2)$ and the obtained result is the $\bar{\mathbf{k}}$ for all the basic resisting forces. In this cost function, $\bar{k}^1=\bar{k}^1_{Max}-\bar{k}^1_{Min}$ and $\bar{k}^2=\bar{k}^2_{Max}-\bar{k}^2_{Min}$ are the differences of the upper and lower bounds of the basic resisting forces q^1 and q^2 associated with the column element. With the initial bounds and corresponding matrix $\bar{\mathbf{k}}_I$ presented in Appendix I, the difference of the upper and lower bounds, $\bar{k}=\bar{k}_{Max}-\bar{k}_{Min}$, of each resisting force are listed in Table 5.5 for both stiffening, $\bar{\mathbf{u}}^T\mathbf{q}\in[\bar{\mathbf{u}}^T\bar{\mathbf{k}}_I\bar{\mathbf{u}},\bar{\mathbf{u}}^T(\bar{\mathbf{k}}_I+\bar{\mathbf{k}})\bar{\mathbf{u}}]$, and softening systems,

$\bar{\mathbf{u}}^T\mathbf{q} \in [\bar{\mathbf{u}}^T(\bar{\mathbf{k}}_I - \bar{\mathbf{k}})\bar{\mathbf{u}}, \bar{\mathbf{u}}^T\bar{\mathbf{k}}_I\bar{\mathbf{u}}]$. It is to be noted that the obtained $\bar{\mathbf{k}}$ depends on the selection of the coefficient matrix $\boldsymbol{\lambda}$ and the cost function. For example, different coefficient matrix $\boldsymbol{\lambda}$, e.g., $\lambda_l = 1/N$, or alternative cost function chosen to be minimized, e.g. $\min(-\bar{k}^1)$, will yield different $\bar{\mathbf{k}}$ as shown in Table 5.6.

5.7 MULTI-STORY SHEAR BUILDING STRUCTURES

The structures investigated in this section are multi-story shear buildings with stiffening or softening structural behavior. A general multi-story shear building structure is depicted in Figure 5.5. The detailed derivation of $\mathbf{q}$ and $\bar{\mathbf{u}}$ as well as corresponding matrices $\boldsymbol{\alpha}$ and $\boldsymbol{\beta}$ for this shear building is given in Appendix C. Accordingly, the maximum, $\bar{k}^j_{Max}$, and minimum, $\bar{k}^j_{Min}$, stiffness values of the *j*–th story, where $j:1\rightarrow n$, for stable (in the sense of Lyapunov) stiffening and softening multi-story shear building systems, respectively, are to be determined for the explicit Newmark algorithm, i.e. $\boldsymbol{\eta} = [1 \quad 1/2 \quad 1/2 \quad 1/2]$.

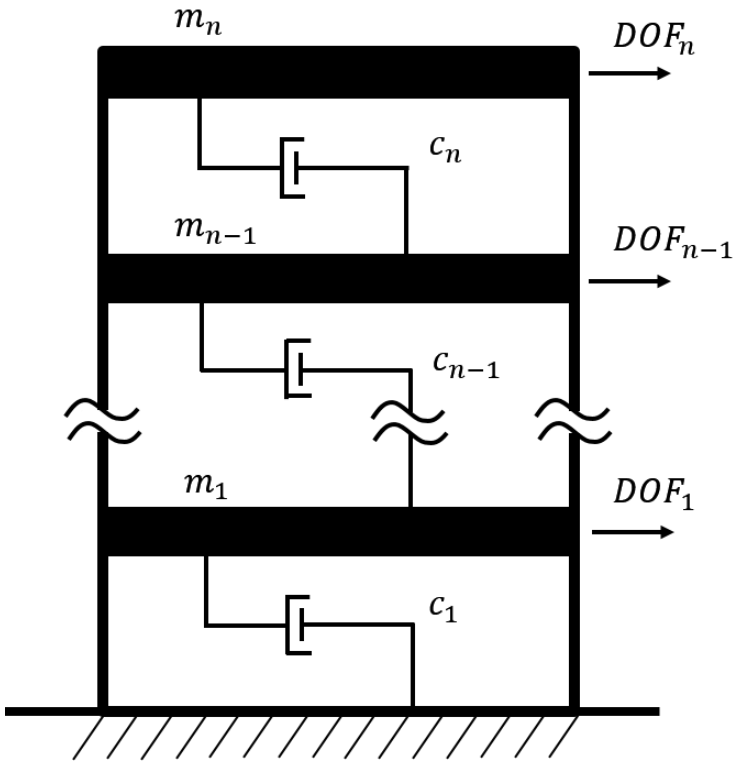

Figure 5.5 General multi-story shear building structure.

The Lyapunov stability analysis is conducted for the following numerical values:

$$m_j = 0.5, \quad \zeta = 0.05, \quad \bar{k}^j_I = 1000.0 \tag{5.63a}$$

$$\lambda_j = \omega_j^2 \Big/ \left(\sum_{j=1}^{n} \omega_j^2 \right), \quad \omega_j = 2\pi / T_j, \quad \mu = (\Delta t)/T_n = 0.01 \tag{5.63b}$$

where $j : 1 \to n$, T_j is the period of the j–th mode of vibration of the analyzed structure, and T_n is the period of the n–th mode of vibration, which depends on the number of stories, n, of the analyzed shear building. As in the previous example, the initial bound matrix $\bar{\mathbf{k}}_I = \text{diag}[\bar{k}_I^1, \bar{k}_I^2, \ldots, \bar{k}_I^n]$.

5.7.1 A Two-Story Shear Building

The Lyapunov stability analysis of the explicit Newmark integrator applied to a 2-story (Figure 5.5 with $n = 2$) shear building is conducted. The two periods of this building are $T_1 = 0.23\,\text{sec}$ and $T_2 = 0.09\,\text{sec}$. Based on Eqs. (5.63a) and (5.63b), $\mathbf{A}_e$ and $\mathbf{C}$ are given in Appendix D, and $\rho(\mathbf{A}_e) = 0.9988 \ < 1$.

5.7.1.1 Stiffening Systems

For stiffening systems, $\bar{\mathbf{k}}_{Min} = \bar{\mathbf{k}}_I$, $\mathbf{B}_e = \mathbf{B}_1 \boldsymbol{\alpha}$ is given in Appendix III. The row rank of the controllability matrix:

$$\mathbf{Z} = [\mathbf{B}_e \quad \mathbf{A}_e\mathbf{B}_e \quad \mathbf{A}_e^2\mathbf{B}_e \quad \cdots \quad \mathbf{A}_e^5\mathbf{B}_e] \tag{5.64}$$

is such that $\text{rank}(\mathbf{Z}) = 6$. Therefore, $(\mathbf{A}_e, \mathbf{B}_e)$ is controllable and the following $\bar{\mathbf{k}} = \bar{\mathbf{k}}_{Max} - \bar{\mathbf{k}}_I$:

$$\bar{\mathbf{k}} = \begin{bmatrix} 205 & 0 \\ 0 & 174 \end{bmatrix} \tag{5.65}$$

is obtained numerically using CVX [CVX Research Inc. 2011] as follows:

$$\underset{\mathbf{P}, \bar{\mathbf{k}}}{\textit{Minimize}} \ \ -\left(\bar{k}^1 + \bar{k}^2\right) \tag{5.66}$$

subjected to

$$\begin{bmatrix} \mathbf{A}_e^T\mathbf{P}\mathbf{A}_e - \mathbf{P} & \mathbf{A}_e^T\mathbf{P}\mathbf{B}_e - (\bar{\mathbf{k}}\mathbf{C})^T \\ \left[\mathbf{A}_e^T\mathbf{P}\mathbf{B}_e - (\bar{\mathbf{k}}\mathbf{C})^T\right]^T & -(\mathbf{I}^T + \mathbf{I}) + \mathbf{B}_e^T\mathbf{P}\mathbf{B}_e \end{bmatrix} \prec \mathbf{0}, \ \mathbf{P} = \mathbf{P}^T \succ \mathbf{0}, \ \bar{\mathbf{k}} \succ \mathbf{0} \tag{5.67}$$

where $\mathbf{P}$, given in Appendix D, is a 6×6 matrix. Accordingly, for the two-story shear building with stiffening behavior, the explicit Newmark algorithm is stable in the sense of Lyapunov for the numerical values in Eqs. (5.63) in the following range:

$$\bar{\mathbf{u}}^T\bar{\mathbf{k}}_{Min}\bar{\mathbf{u}} \le \bar{\mathbf{u}}^T\mathbf{q} \le \bar{\mathbf{u}}^T\bar{\mathbf{k}}_{Max}\bar{\mathbf{u}} \tag{5.68}$$

where

$$\bar{\mathbf{k}}_{Min} = \bar{\mathbf{k}}_I = \begin{bmatrix} 1000 & 0 \\ 0 & 1000 \end{bmatrix} \tag{5.69a}$$

$$\bar{\mathbf{k}}_{Max} = \bar{\mathbf{k}}_{Min} + \bar{\mathbf{k}} = \begin{bmatrix} 1205 & 0 \\ 0 & 1174 \end{bmatrix} \tag{5.69b}$$

5.7.1.2 Softening Systems

For softening systems, $\bar{\mathbf{k}}_{Max} = \bar{\mathbf{k}}_I$, $\mathbf{B}_e = \mathbf{B}_2\boldsymbol{\alpha} = -\mathbf{B}_1\boldsymbol{\alpha}$ as given in Appendix III, and the following $\bar{\mathbf{k}} = \bar{\mathbf{k}}_I - \bar{\mathbf{k}}_{Min}$:

$$\bar{\mathbf{k}} = \begin{bmatrix} 184 & 0 \\ 0 & 159 \end{bmatrix} \tag{5.70}$$

is obtained using similar procedure to Eqs. (5.66) and (5.67). The corresponding $\mathbf{P}$ is also given in Appendix D. Therefore, for the two-story shear building with softening behavior, the explicit Newmark algorithm is stable in the sense of Lyapunov for the numerical values in Eqs. (5.63) in the range of Eq. (5.68) with

$$\bar{\mathbf{k}}_{Max} = \bar{\mathbf{k}}_I = \begin{bmatrix} 1000 & 0 \\ 0 & 1000 \end{bmatrix} \tag{5.71a}$$

$$\bar{\mathbf{k}}_{Min} = \bar{\mathbf{k}}_{Max} - \bar{\mathbf{k}} = \begin{bmatrix} 816 & 0 \\ 0 & 841 \end{bmatrix} \tag{5.71b}$$

5.7.2 A 20-Story Shear Building

A 20-story (Figure 5.5 with $n = 20$) shear building is used to investigate the Lyapunov stability analysis of the explicit Newmark algorithm. The fundamental and 20th periods of this building are $T_1 = 1.83\,\text{sec}$ and $T_{20} = 0.07\,\text{sec}$, which are within the practical range for the 20-story shear building. Same Lyapunov stability analysis as in previous sections is conducted for the analyzed 20-story shear building with stiffening or softening behavior. The cost function for this bridge structure is selected as $\min\left(-\sum_{j=1}^{20} \bar{k}^j\right)$, which is equivalent to maximizing $\sum_{j=1}^{20} \bar{k}^j$. In this cost function, $\bar{k}^j = \bar{k}^j_{Max} - \bar{k}^j_{Min}$ is the difference of the upper and lower bounds of the basic resisting force q^j associated with the *j*–th story, where $j : 1 \to n$. Table 4 shows that the difference of the upper and lower bounds, $\bar{k} = \bar{k}_{Max} - \bar{k}_{Min}$, of each resisting force for the explicit Newmark algorithm to be stable (5.in the sense of Lyapunov) for both stiffening, $\bar{\mathbf{u}}^T\mathbf{q} \in [\bar{\mathbf{u}}^T\bar{\mathbf{k}}_I\bar{\mathbf{u}}, \bar{\mathbf{u}}^T\left(\bar{\mathbf{k}}_I + \bar{\mathbf{k}}\right)\bar{\mathbf{u}}]$, and softening, $\bar{\mathbf{u}}^T\mathbf{q} \in [\bar{\mathbf{u}}^T\left(\bar{\mathbf{k}}_I - \bar{\mathbf{k}}\right)\bar{\mathbf{u}}, \bar{\mathbf{u}}^T\bar{\mathbf{k}}_I\bar{\mathbf{u}}]$, systems.

Table 5.7 The $\bar{k}$ of each basic resisting force for the 20-story shear building.

Story Number	Stiffening systems	Softening systems	Story Number	Stiffening systems	Softening systems
1	716.1	203.7	11	31.3	35.9
2	125.1	149.6	12	25.3	30.8
3	98.8	150.4	13	21.8	28.5
4	133.0	166.5	14	19.6	26.7
5	163.4	140.0	15	17.3	24.0
6	119.7	97.7	16	15.0	21.2
7	76.9	74.8	17	14.2	20.4
8	56.5	64.1	18	16.9	23.7
9	46.7	55.3	19	29.6	37.3
10	39.0	44.8	20	116.1	106.7

From Table 5.7, it is observed that the largest difference of upper and lower bounds is obtained for the first story for both stiffening and softening systems. Define δ^j as the difference between the upper and lower bounds of the stiffness of the *j*–th story normalized by the corresponding initial stiffness, i.e.,

$$\delta^j = \bar{k}^j / \bar{k}_I^j \tag{5.72}$$

For shear buildings, usually the first story is the most critical one where high levels of nonlinearity may occur. Fig. 4 presents the effects of the total number of stories and damping values (2%, 5% and 10%) on δ^1 for stiffening (Figure 5.6a) and softening (Figure 5.6b) systems. The number of stories is investigated up to 25, i.e. $n:1\to 25$. It can be observed from Fig. 4 that δ^1 increases with the increase of the damping values. For the stiffening system (Figure 5.6a), δ^1 also increases in general with the increase of the number of stories; while for the softening system (Figure 5.6b), δ^1 increases or decreases with the increase of the number of stories for low (2%) or high (10%) damping ratios, respectively, while no change is observed for moderate (5%) damping ratio.

5.7.3 Discussion of Broader Scope

The proposed approach can be applied to investigate the stability of other explicit direct integration algorithms defined by the vector $\boldsymbol{\eta}$ or ρ_∞ for any MDOF nonlinear system defined by the matrices $\boldsymbol{\alpha}$ and $\boldsymbol{\beta}$. Moreover, it is also noted that neither $\bar{k}_{Min}^l$ nor $\bar{k}_{Max}^l$ is necessarily equal to $\bar{k}_I^l$, where $l:1\to N$, for the stiffening or the softening systems, respectively. These bounds values can take any other value along the loading path. Furthermore, besides strictly stiffening and softening systems as in Fig. 1, other nonlinear problems can be treated using the proposed stability analysis approach. This is true as long as Eq. (5.18) is satisfied and thus the nonlinear force is sector-bounded, e.g., those shown in Figure 5.7 with both stiffening and softening behavior including *occasionally tangent negative stiffness* values. Thus, the proposed approach is generally applicable to explicit direct integration algorithms for various MDOF nonlinear systems.

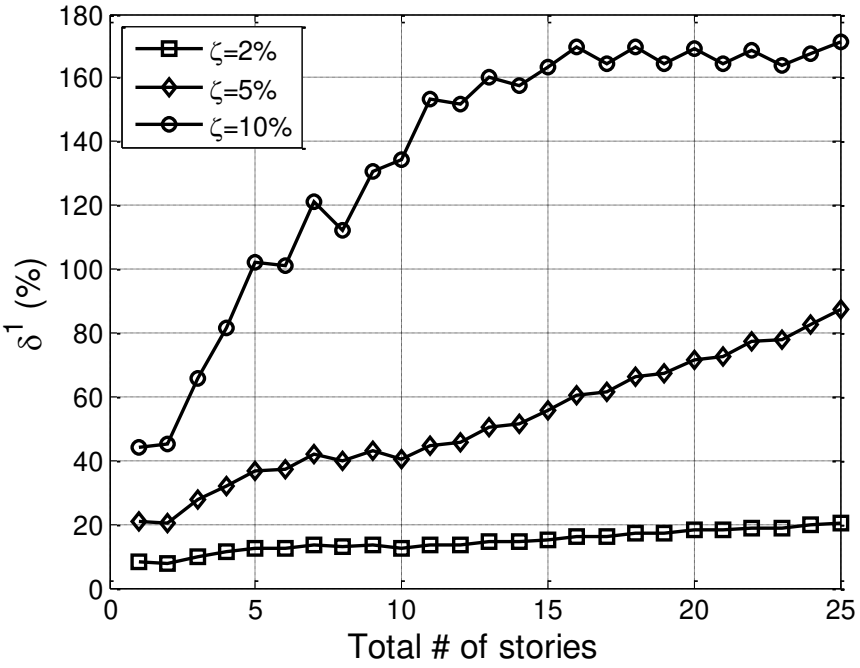

a) Stiffening systems

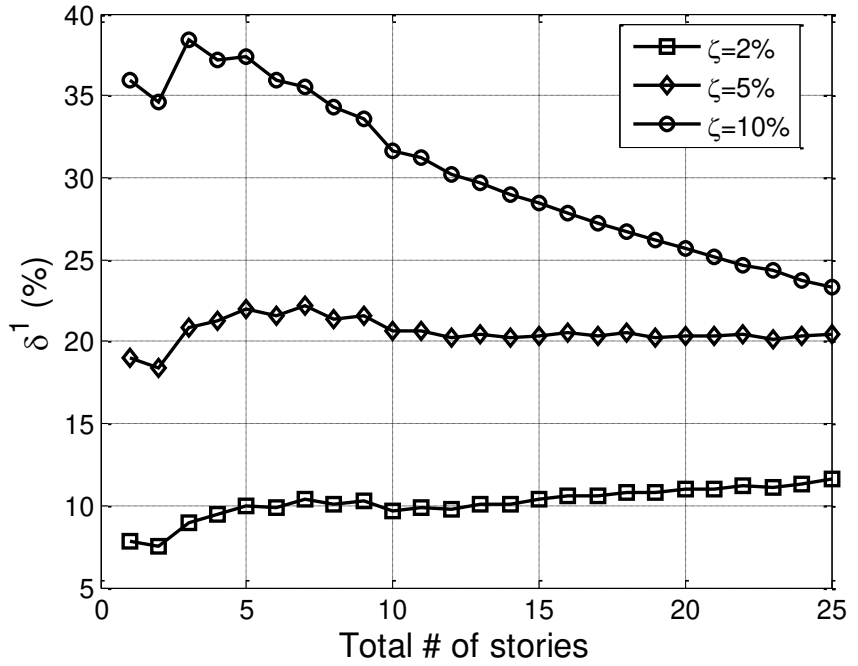

b) Softening systems

Figure 5.6 δ^1 of different number of stories and damping values.

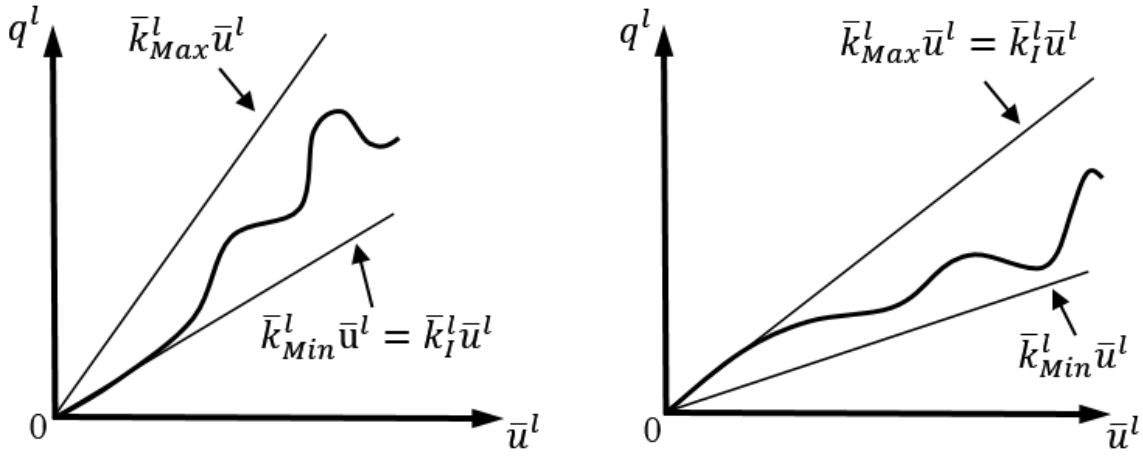

a) Stiffening system **b) Softening system**

Figure 5.7 Schematic illustrations of sector-bounded basic resisting forces not strictly stiffening or softening.

6 Development of the Benchmark Probability Distribution of Seismic Demands

6.1 INTRODUCTION

Besides accurate seismic structural analysis of structures that is fundamental to estimate their seismic demands [Liang et al. 2016b], another key challenge in the PBEE approach is the selection and modification of ground motions (GMs) to serve as input excitations for NTHA simulations of structures. The intricate nonlinear response of structures is highly sensitive to the ground motion selection and modification (GMSM) of the input records. Therefore, the GMSM of the input records is a vital prerequisite for accurate seismic analysis.

The GMSM procedures determine the necessary input GM records for the simulations of structures using NTHA. Numerous research efforts focused on developing different GMSM procedures, which are generally categorized into two approaches: (1) amplitude scaling and (2) spectrum shape matching procedures. The first approach selects and modifies the GM records based on scalar intensity measures (IMs). Some example choices of these scalar IMs include the spectral acceleration at a specific (e.g., fundamental) period of the structure [Watson-Lamprey and Abrahamson 2006; Shome et al. 1998], and certain peak response of inelastic single-degree of freedom systems [Tothong and Luco 2007; Luco and Cornell 2007; Kalkan and Chopra 2011] to account for nonlinear effects. The second approach that takes the spectrum shape into account selects and scales a suite of GM records that has close matching to a target spectrum [Naeim et al. 2004; Kottke and Rathje 2008; Baker 2011]. A comprehensive review of various GMSM procedures is given in [Haselton et al. 2009 and Katsanos et al. 2010]. Moreover, many simulated GM procedures were developed [e.g., Rezaeian and Der Kiureghian 2011], which are especially useful for design scenarios corresponding to scarce recorded GMs in existing databases. In this study, the two approaches of GMSM based on real GM records are of interest.

Although many GMSM procedures are available, there is no consensus regarding a single accurate method and many studies focused on evaluating these procedures. Hancock et al. (2008), Haselton et al. (2009), and Heo et al. (2010) compared different GMSM procedures in predicting median responses of seismic demands against developed reference benchmarks. Recently, Kwong et al. (2015) developed a framework for the evaluation of GMSM procedures by determining a benchmark seismic demand hazard curve. Later, Kwong and Chopra (2016) applied this framework to evaluate two GMSM procedures: (1) exact conditional spectrum [Lin et al. 2013] and (2) generalized conditional intensity measures [Bradley 2010]. These evaluation studies were primarily focused on building structures and considered unidirectional input ground motion. In

general, bridge structures exhibit distinct behaviors in the longitudinal and transverse directions. Hence, bidirectional GM studies focused on highway bridges are needed as conducted in this study.

In order to effectively evaluate the GMSM procedures, a reference benchmark *PDSD* should be established. A framework of performance-based earthquake engineering (PBEE) was developed at the Pacific Earthquake Engineering Research (PEER) Center, which explicitly takes into account uncertainties in earthquake hazard, structural response, damage and loss estimation [Günay and Mosalam 2013]. PEER PBEE enables comprehensive understanding of the structural performance in a probabilistic manner. This study takes advantage of the PEER PBEE to develop the reference benchmark *PDSD* for the structures.

6.2 BENCHMARK PROBABILITY DISTRIBUTION OF SEISMIC DEMANDS

The PEER PBEE methodology aims to robustly divide the performance assessment and design process into logical stages that can be studied and resolved in a systematic and consistent manner [Moehle and Deierlein 2004]. These stages of the process contain the definition, description, and quantification of earthquake intensity measure, structural response, damage and loss. Accordingly, uncertainties in these stages can be explicitly taken into account (Günay and Mosalam 2013), which enable comprehensive understanding of the structural performance in a probabilistic manner. The well-known PEER PBEE formula originally presented in (Cornell and Krawinkler 2000) is restated as follows

$$\lambda(dv) = \int_{dm}\int_{edp}\int_{im} G(dv \mid dm)\,dG(dm \mid edp)\,dG(edp \mid im)\,d\lambda(im) \tag{6.1}$$

where *im*, *edp*, *dm*, and *dv* are the intensity measure, engineering demand parameter, damage measure, and decision variable, respectively, $\lambda(x)$ is the mean annual rate of events exceeding a given level for a given variable x, $G(x)$ is the complementary cumulative distribution function (CCDF) for random variable X, i.e., $G(x) = \Pr(X > x)$, and the corresponding conditional CCDF is $G(x \mid y) = \Pr(X > x \mid Y = y)$. Moreover, the variables *im*, *edp*, and *dm* can be expressed in a vector form (e.g., Bradley 2012), i.e., multiple folds are implied in the integrals.

In this study, a reference benchmark *PDSD* is developed based on the PEER PBEE framework considering the first two sources of uncertainties, i.e., the earthquake intensity measure and the structural response. In addition, this study is extended to account for structural collapse of a certain damage group corresponding to a group of structural components affected by the same *EDP* (e.g., Cornell 1999, Baker and Cornell 2005, Lin et al. 2013). This study makes use of Eq. (6.2), which presents the general formula for the *PDSD*.

$$G(edp) = \Pr(EDP > edp) = \int_{\boldsymbol{im}} G(edp \mid \boldsymbol{im})\, f_{\mathbf{IM}}(\boldsymbol{im})\, d\boldsymbol{im} \tag{6.2}$$

where $\boldsymbol{im} = (im_1, im_2, \ldots, im_{n_{im}})$ are values of the intensity measures represented as random variables $\mathbf{IM} = (IM_1, IM_2, \ldots, IM_{n_{im}})$, n_{im} is the number of intensity measures considered, $\int_{\boldsymbol{im}}(\cdot)\,d\boldsymbol{im}$ is an abbreviated form of $\int_{im_1}\int_{im_2}\cdots\int_{im_{n_{im}}}(\cdot)\,dim_1 dim_2 \cdots dim_{n_{im}}$ and will be used thereafter

in this chapter, $G(edp \mid \boldsymbol{im}) = \Pr(EDP > edp \mid \mathbf{IM} = \boldsymbol{im})$ is the conditional probability of *EDP* exceeding the demand level *edp* given the vector of intensity measures $\boldsymbol{im}$, and $f_{\mathbf{IM}}(\boldsymbol{im})$ is the joint probability density function (PDF) of the intensity measures, i.e., $\mathbf{IM}$.

6.2.1 Intensity Measures

A non-parametric statistical inference, multivariate kernel density estimation (Härdle et al. 2004) is used to estimate $f_{\mathbf{IM}}(\boldsymbol{im})$. For this purpose, we consider an m-dimensional random vector $\boldsymbol{X} = (X_1, \ldots, X_m)^T$, where $X_1, \ldots, X_m$ are one-dimensional random variables. Drawing a random sample of size n in this setting means that we have n observations for each of the m random variables, $X_1, \ldots, X_m$. In this case, our goal is to estimate the probability density of $\boldsymbol{X} = (X_1, \ldots, X_m)^T$, which is the joint PDF of the random variables $X_1, \ldots, X_m$ as follows:

$$f_{\boldsymbol{X}}(\boldsymbol{x}) = f_{X_1, \ldots, X_m}(x_1, \ldots, x_m) \tag{6.3}$$

Considering adapting the kernel density estimator to m-dimensional cases, we have

$$\hat{f}_{\mathbf{X}}(\boldsymbol{x}) = \frac{1}{n}\sum_{i=1}^{n} \frac{1}{h_1 \ldots h_m} K\left(\frac{x_1 - X_{i1}}{h_1}, \ldots, \frac{x_m - X_{im}}{h_m}\right) \tag{6.4}$$

where $h_j, j = 1, 2, \cdots, m$, is the bandwidth for X_j, K is a multivariate kernel function with m arguments, X_{ij} is the *i*-th observation of the random variable X_j. The symbol "^" in Eq. (6.4) denotes the estimation, i.e., $\hat{g}(x)$ is an estimate of $g(x)$. In this study, Eq. (6.4) becomes

$$\hat{f}_{\mathbf{IM}}(\boldsymbol{im}) = \frac{1}{n}\sum_{i=1}^{n} \frac{1}{h_1 \ldots h_m} K\left(\frac{im_1 - IM_{i1}}{h_1}, \ldots, \frac{im_m - IM_{im}}{h_m}\right) \tag{6.5}$$

In order for this joint PDF estimate to equally weight each intensity measure, a whitening transformation [Krizhevsky and Hinton 2009] can be applied to the n groups of m intensity measures, i.e., $m \times n$ matrix $\mathbf{IM}_0$, as follows:

$$\begin{aligned} \mathbf{IM}_{\mu} &= \mathbf{IM}_0 - \boldsymbol{\mu} \\ \mathbf{IM}_{white} &= \mathbf{IM}_{\mu} \boldsymbol{\Sigma}^{-1/2} \end{aligned} \tag{6.6}$$

where $\boldsymbol{\mu}$ is a $m \times n$ matrix with all entries of the *j*-th column are equal to the mean of the *j*-th intensity measure, $j = 1, 2, \cdots, m$, respectively, and $\boldsymbol{\Sigma}$ is the $m \times m$ covariance matrix of the m columns of $\mathbf{IM}_{\mu}$. After this whitening transformation, each column of $\mathbf{IM}_{white}$ has zero mean and identity covariance matrix. A kernel density estimator for K and a bandwidth selection method for $h_j, j = 1, 2, \cdots, m$, proposed by Botev et al. (2010), are adopted to estimate the joint PDF $f_{\mathbf{IM}}(\boldsymbol{im})$. After such estimation, $\mathbf{IM}_{white}$ is transformed back to $\mathbf{IM}_0$, i.e.,

$$\mathbf{IM}_0 = \mathbf{IM}_{white}\boldsymbol{\Sigma}^{1/2} + \boldsymbol{\mu} \tag{6.7}$$

The procedures of density estimation discussed above can be readily applied to the investigated structures.

6.2.2 Collapse Consideration

When developing the *PDSD* of the investigated structures, it is necessary to account for the possibility that some GM records, whose $\mathbf{IM}$ are at high levels, may cause collapse of the structure. From Eq. (6.2), the conditional probability of exceedance $G(edp\,|\,\boldsymbol{im})$ is computed by the summation of probabilities of such occurrences conditioned on the two mutually exclusive categories of the bridge collapse (C) and non-collapse (NC), i.e.,

$$G(edp\,|\,\boldsymbol{im}) = G(edp\,|\,\boldsymbol{im},\mathrm{C})\times \Pr(\mathrm{C}\,|\,\boldsymbol{im}) + G(edp\,|\,\boldsymbol{im},\mathrm{NC})\times \Pr(\mathrm{NC}\,|\,\boldsymbol{im}) \tag{6.8}$$

Intuitively, we can set $G(edp\,|\,\boldsymbol{im},\mathrm{C}) = 1.0$. Thus, Eq. (9) leads to the following:

$$G(edp\,|\,\boldsymbol{im}) = \Pr(\mathrm{C}\,|\,\boldsymbol{im}) + G(edp\,|\,\boldsymbol{im},\mathrm{NC})\times\left[1-\Pr(\mathrm{C}\,|\,\boldsymbol{im})\right] \tag{6.9}$$

From the prescribed collapse criteria, Eq. (6.9) is further manipulated as follows:

$$G(edp\,|\,\boldsymbol{im}) = \int_{\boldsymbol{fc}} \left\{\Pr(\mathrm{C}\,|\,\boldsymbol{im}) + G(edp\,|\,\boldsymbol{im},\mathrm{NC})\times\left[1-\Pr(\mathrm{C}\,|\,\boldsymbol{im})\right]\right\} f_{\mathbf{FC}}(\boldsymbol{fc})\,d\boldsymbol{fc} \tag{6.10}$$

where $\boldsymbol{fc} = (fc_1, fc_2, \ldots, fc_{n_{fc}})$ are values of the failure criteria represented as random variables $\mathbf{FC} = (FC_1, FC_2, \ldots, FC_{n_{fc}})$, n_{fc} is the number of failure criteria considered, $\int_{\boldsymbol{fc}}(\cdot)\,d\boldsymbol{fc}$ is an abbreviated form of $\int_{fc_1}\int_{fc_2}\cdots\int_{fc_{n_{fc}}}(\cdot)\,dfc_1 dfc_2\cdots dfc_{n_{fc}}$, and $f_{\mathbf{FC}}(\boldsymbol{fc})$ is the joint PDF of failure criteria, i.e., $\mathbf{FC}$. The fragility surface or conditional probability of collapse, i.e., $\Pr(\mathrm{C}\,|\,\boldsymbol{im})$, is evaluated using multivariate binary logistic regression [Wasserman 2010] by fitting a binomial distribution to the observed collapsed (1: C; 0: NC) versus $\mathbf{IM}$, i.e.,

$$\hat{\Pr}(\mathrm{C}\,|\,\boldsymbol{im}) = \frac{\exp\left(\hat{\alpha}_0 + \sum_{i=1}^{m}\hat{\alpha}_i im_i\right)}{1+\exp\left(\hat{\alpha}_0 + \sum_{i=1}^{m}\hat{\alpha}_i im_i\right)} \tag{6.11}$$

where the coefficients $\hat{\alpha}_0 \ldots \hat{\alpha}_m$ can be obtained by the reweighted least squares algorithm [Wasserman 2010].

6.2.3 Non-Collapse Structural Responses

In Eq. (6.10), the only term that has not been determined is the probability of *EDP* exceeding the demand level *edp* given the intensity measures for the non-collapse scenario, i.e., $G(edp \mid \boldsymbol{im}, \mathrm{NC})$. In this study, the distribution of *EDP*s conditioned on the intensity measures is assumed to be lognormal (e.g., Kunnath 2006 and Kunnath et al. 2006). Multivariate linear regression (Wasserman 2010) can be used to estimate this distribution. From regression, for a given set of im_i, $i = 1, 2, \cdots, m$, under non-collapse scenario, the mean value of $\ln(EDP)$ is as follows:

$$\hat{\mu}_{\ln(edp)|\boldsymbol{im}} = \hat{\beta}_0 + \sum_{i=1}^{m} \hat{\beta}_i im_i \tag{6.12}$$

where coefficients $\hat{\beta}_i$, $i = 1, 2, \cdots, m$, are determined from the least square estimate [Wasserman 2010]. An unbiased estimate of the variance of the distribution is given as follows:

$$\hat{\sigma}^2_{\ln(edp)|\boldsymbol{im}} = \left[1/(N-k)\right] \sum_{i=1}^{N} \hat{\varepsilon}_i^2 \tag{6.13}$$

$$\hat{\varepsilon}_i = \hat{\beta}_0 + \sum_{j=1}^{m} \hat{\beta}_i IM_i^j - \ln(EDP_i) \tag{6.14}$$

where IM_i^j and EDP_i are the *i*-th sampling point of IM^j, $j = 1, 2, \cdots, m$, and *EDP*, respectively. N is the total number of sampling points that correspond to the NC and k is the number of the free parameters, i.e,, $k = m + 1$ for this case. The probability that the *EDP* exceeds the demand level of *edp* given $\boldsymbol{im}$ and for the NC scenario can now be calculated using the normal CCDF:

$$\hat{G}(edp \mid \boldsymbol{im}, \mathrm{NC}) = 1 - \Phi\left\{\left[\ln(edp) - \hat{\mu}_{\ln(edp)|\boldsymbol{im}}\right] / \hat{\sigma}_{\ln(edp)|\boldsymbol{im}}\right\} \tag{6.15}$$

where $\Phi(\cdot)$ denotes the standard normal CDF.

6.2.4 Integration of Intensity Measures and Structural Responses

Combination of the intensity measures from the kernel density estimator and the structural responses, including C and NC cases, i.e., substituting Eq. (6.10) and required estimates of its different terms, as discussed above, into Eq. (6.2), leads to the following

$$\hat{G}(edp) = \int_{\boldsymbol{im}} \int_{\boldsymbol{fc}} \left\{\hat{\Pr}(\mathrm{C} \mid \boldsymbol{im}) + \hat{G}(edp \mid \boldsymbol{im}, \mathrm{NC}) \times \left[1 - \hat{\Pr}(\mathrm{C} \mid \boldsymbol{im})\right]\right\} \hat{f}_{\mathbf{DR}}(\boldsymbol{fc}) \hat{f}_{\mathbf{IM}}(\boldsymbol{im}) d\boldsymbol{fc} d\boldsymbol{im} \tag{6.16}$$

The procedures of the benchmark *PDSD* development is readily extended to the case of multiple earthquake scenarios as follows:

$$\hat{G}_m(edp) \cong \sum_{l=1}^{N_{eqs}} \nu_l \cdot \left\{ \int_{\boldsymbol{im}} \int_{\boldsymbol{fc}} \left\{ \hat{\Pr}(\mathrm{C} \mid \boldsymbol{im}) + \hat{G}(edp \mid \boldsymbol{im}, \mathrm{NC}) \times \left[1 - \hat{\Pr}(\mathrm{C} \mid \boldsymbol{im}) \right] \right\} \hat{f}_{\mathbf{DR}}(\boldsymbol{fc}) \hat{f}_{\mathbf{IM}}(\boldsymbol{im}) d\boldsymbol{fc} d\boldsymbol{im} \right\}_l \tag{6.17}$$

where $\hat{G}_m(edp)$ is the *PDSD* for multiple earthquake scenarios with number N_{eqs} and ν_l [Bradley 2013] is the activity rate for the *l*-th earthquake scenario.

6.3 EVALUATION OF THE GMSM PROCEDURES

Similar to the development of the reference benchmark *PDSD*, the *PDSD* estimates by the GM records selected from each GMSM procedure are developed. Analogous to Eqs. (6.8) and (6.9), $G(edp)$ is divided into two mutually exclusive categories of C and NC, i.e.,

$$\begin{aligned} G(edp) &= G(edp \mid \mathrm{C}) \times \Pr(\mathrm{C}) + G(edp \mid \mathrm{NC}) \times \Pr(\mathrm{NC}) \\ &= \Pr(\mathrm{C}) + G(edp \mid \mathrm{NC}) \times \left[1 - \Pr(\mathrm{C}) \right] \end{aligned} \tag{6.18}$$

where it is assumed that $G(edp \mid \mathrm{C}) = 1.0$ and $\Pr(\mathrm{C})$ is the probability of collapse estimated as follows:

$$\hat{\Pr}(\mathrm{C}) = \frac{\#\text{ of records causing collapse}}{\text{total }\#\text{ of records}} \tag{6.19}$$

The probability of exceedance for the NC cases, i.e., $G(edp \mid \mathrm{NC})$, can be estimated by a non-parametric inference using the following empirical CCDF [Baker 2007; Vamvatsikos and Cornell 2004]

$$\hat{G}(edp \mid \mathrm{NC}) = \frac{1}{\overline{m}} \sum_{l=1}^{\overline{m}} I(EDP_l > edp) \tag{6.20}$$

where $\overline{m}$ is the number of GM records that produce NC, EDP_l is the value of *EDP* for the *l*-th record, and $I(\cdot)$ represents the indicator function, i.e., $I(EDP_l > edp) = 1.0$ if $EDP_l > edp$; otherwise, $I(EDP_l > edp) = 0.0$. Recall the previously discussed collapse criteria, along with the estimates in Eqs. (6.19) and (6.20), the *PDSD* estimate, i.e., $\hat{G}(edp)$, is obtained as follows:

$$\hat{G}(edp) = \int_{\boldsymbol{fc}} \left\{ \hat{\Pr}(\mathrm{C}) + \hat{G}(edp \mid \mathrm{NC}) \times \left[1 - \hat{\Pr}(\mathrm{C}) \right] \right\} \hat{f}_{\mathbf{FC}}(\boldsymbol{fc}) d\boldsymbol{fc} \tag{6.21}$$

7 Computational Bridge Structure Models

7.1 INTRODUCTION

In any urban transportation system, ordinary standard reinforced concrete (RC) highway bridges are essential lifeline structures for transporting goods and people around natural terrains. In California where numerous active faults exist, earthquakes occur frequently and therefore bridges should sustain minimal damage and remain operational in the aftermath of an earthquake. This requirement is essential for recovery and emergency management purposes. RC highway bridges were observed to have substandard performance during earthquakes due to the inherent lack of high redundancy of the structural system [Benzoti et al. 1996]. Even bridges designed according to modern codes were severely damaged or collapsed in different parts of the world during earthquakes in the last two decades. Accordingly, determination of the seismic response of existing and newly designed RC highway bridges, using techniques of structural analysis, is essential to ensure their seismic safety.

For a bridge to be considered as an ordinary standard bridge, it should satisfy the following conditions [Caltrans SDC 2010]: (1) the span length should be less than 300 feet; (2) the bridge should be constructed with normal-weight concrete; (3) foundations must be supported on spread footings, pile caps with piles, or pile shafts; (4) the soil is not susceptible to liquefaction, lateral spreading or scour; and (5) the fundamental period of the transverse and longitudinal directions of the bridge should be greater than or equal to 0.7 seconds. This chapter provides a brief description of selected ordinary standard RC highway bridge structures and reviews the related OpenSees [McKenna et al. 2010] computational bridge structure models by [Kaviani et al. 2014].

7.2 BRIDGE STRUCTURES

Three representative RC highway bridge structures are selected for this study. The selected bridges, designed after 2000, reflect common bridge engineering practice in California. The first selected bridge is the *Jack Tone Road Overcrossing* (Bridge A), with two spans supported on a single column. The second bridge is the *La Veta Avenue Overcrossing* (Bridge B), with two spans supported on a two-column bridge bent. The third bridge is the *Jack Tone Road Overhead* (Bridge C), with three spans and two three-column bridge bents. The characteristics and configurations of the selected bridges are summarized in Table 7.1 and Figure 7.1.

Table 7.1 Characteristics of the selected bridges.

Bridge	A	B	C
Name	Jack Tone Road Overcrossing	La Veta Avenue Overcrossing	Jack Tone Road Overhead
of spans	2	2	3
Column bent	Single-column	Two-column	Three-column
Column radius	33.1 in.	33.5 in.	33.1 in.
Column height	22.0 ft.	22.0 ft.	24.6 ft.
Abutment	Seat type	Seat type	Seat type
Seat length	33.85 in.	33.85 in.	33.85 in.
Superstructure concrete	$f_c^{'} = 5\,ksi, E_c = 4030.5\,ksi$	$f_c^{'} = 5\,ksi, E_c = 4030.5\,ksi$	$f_c^{'} = 5\,ksi, E_c = 4030.5\,ksi$
Column bent concrete and reinforcing materials	Concrete: $5\,ksi$ Steel: ASTM A706	Concrete: $5\,ksi$ Steel: ASTM A706	Concrete: $5\,ksi$ Steel: ASTM A706
Reinforcement details of column bent cross-section	Long.: 44#11 (bundles of 2) $\rho_l = 2.00\%$ Trans.: Spiral, #6 @ 3.34 in.	Long.: 44#11 (bundles of 2) $\rho_l = 1.95\%$ Trans.: Spiral, #4 @ 6.00 in.	Long.: 44#11 (bundles of 2) $\rho_l = 2.20\%$ Trans.: Spiral, #6 @ 3.34 in.

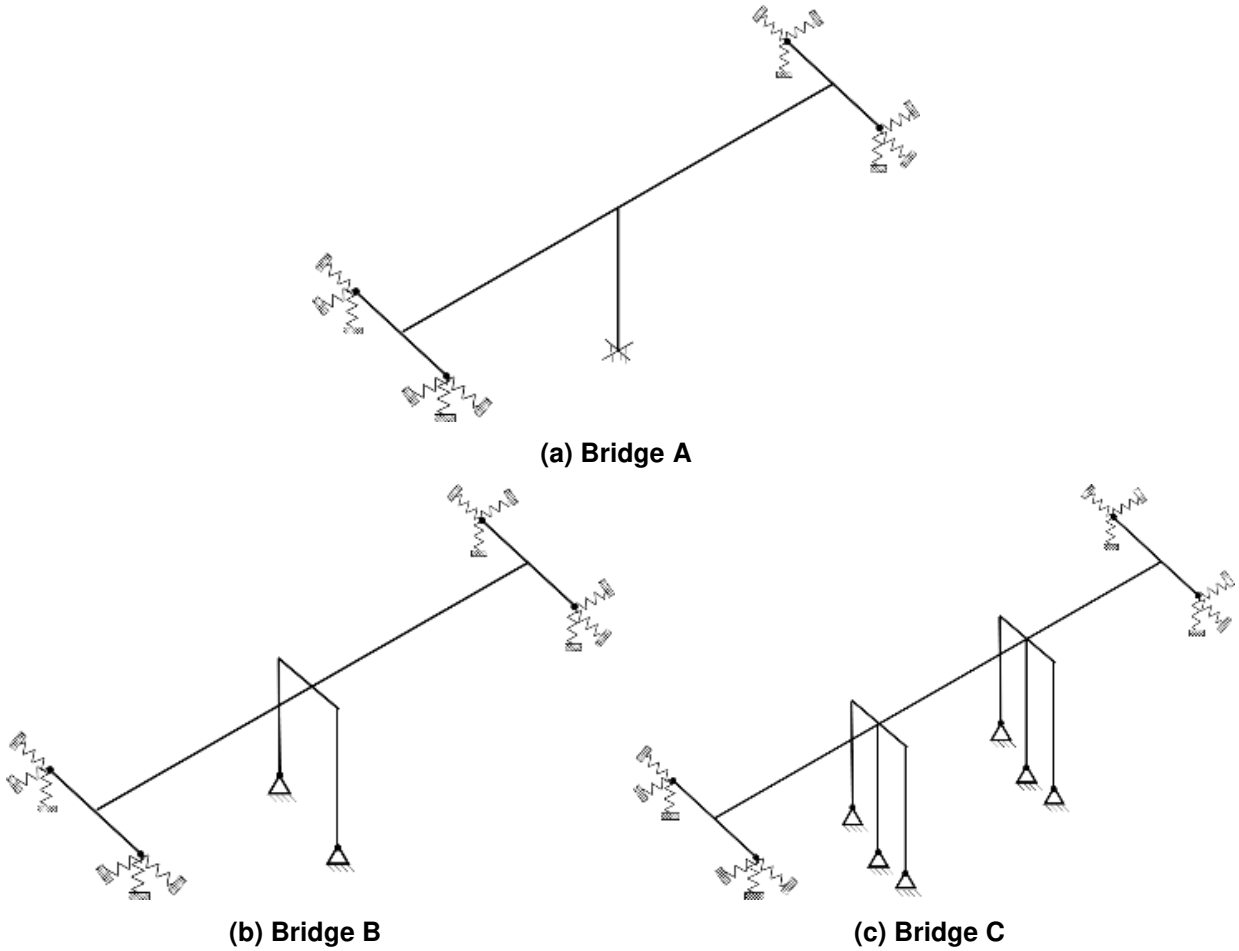

(a) Bridge A

(b) Bridge B

(c) Bridge C

Figure 7.1 Configurations of the selected bridges.

7.3 COMPUTATIONAL MODELS

Extensive analytical simulations were conducted on these three bridges [Kaviani et al. 2012] using OpenSees [McKenna et al. 2010], on which the modeling assumptions adopted were partly based on [Aviram et al. 2008]. OpenSees has a sufficient element and material response library and empowers scripted execution of repetitive nonlinear time history analyses (NTHA) through which the model parameters and input ground motions can be systematically varied. A representative bridge model (Bridge B) used in the simulations is depicted in Figure 7.2. Seat-type abutments, shear keys, expansion joints, column-bents, and the superstructure are included in the model. The adopted modeling is reviewed in this chapter for completeness and a more detailed explanation of the modeling assumptions can be found in [Kaviani et al. 2014].

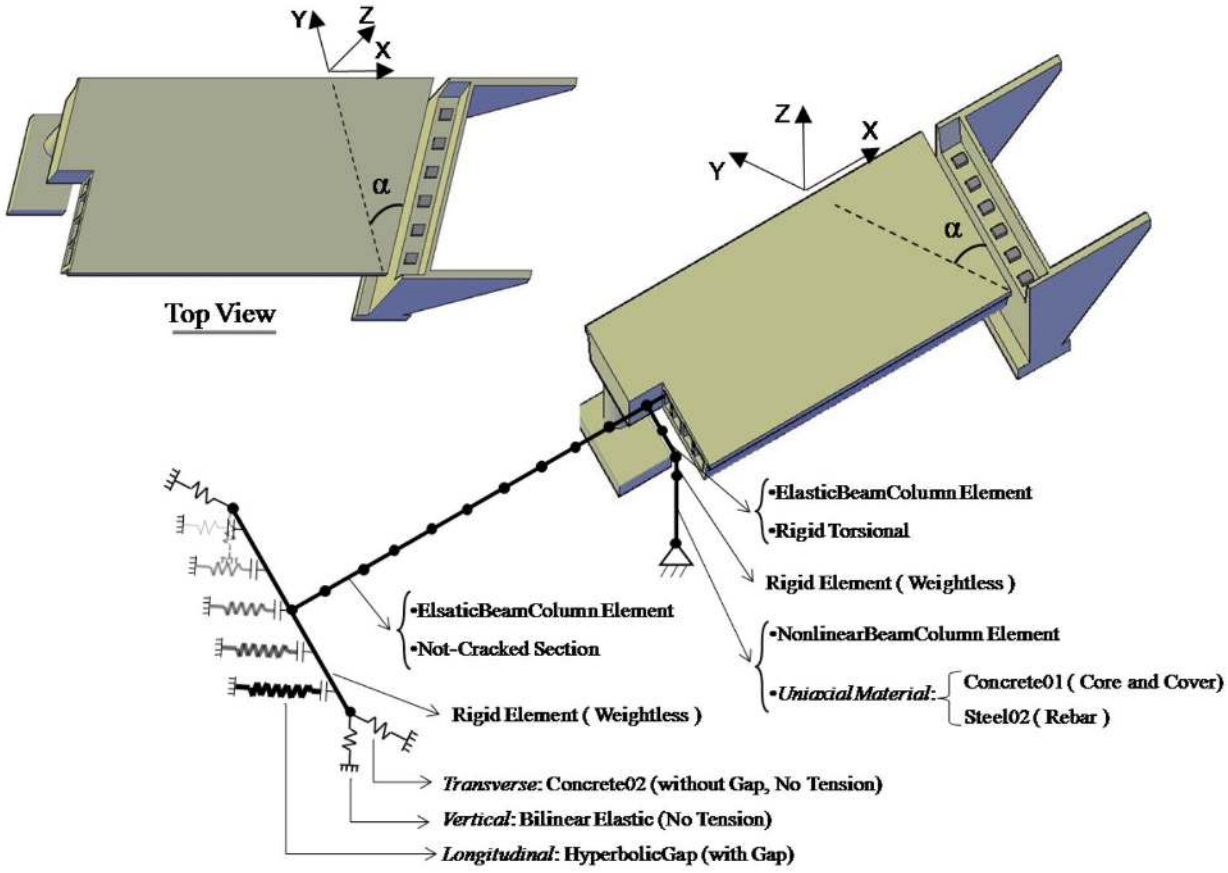

Figure 7.2 Modeling of Bridge B [Kaviani et al. 2014].

7.3.1 Material Properties

Material properties assigned to the models were on the basis of Caltrans SDC [2010]. The model developed by Mander et al. [1988] was used for the RC column of the selected bridges. It is recommended by Caltrans SDC [2010] that confined as well as unconfined concrete should be taken into account to determine the local capacity of ductile concrete member.

In this study, for the unconfined concrete, the compressive strain at the maximum compressive stress, $f_{ce}^{'} = 5\ ksi$, and the ultimate compression (spalling) strain were chosen as $\varepsilon_{c0} = 0.0028$ and $\varepsilon_{cp} = 0.005$, respectively. For the confined concrete, the compressive strain at the maximum compressive stress, $f_{cc}^{'} = 6.6\ ksi$, and the ultimate compression strain were employed as $\varepsilon_{cc} = 0.008$ and $\varepsilon_{cu} = 0.025$, respectively. The modulus of elasticity specified by Caltrans SDC [2010] is

$$E_c = 33 \times w^{1.5} \times \sqrt{f_c^{'}}\ \ (psi) \tag{7.1}$$

where $w = 143.96$ lb/ft^3 and $f_c^{'} = 5\ ksi$ are respectively the unit weight of concrete and the compressive strength of the unconfined concrete. Reinforcing steel A706/A706M (Grade 60/Grade 400) was used in this model with the steel modulus of elasticity and the expected yield strength were set as $E_s = 29{,}000\ ksi$ and $f_{ye} = 68\ ksi$ in accordance with Caltrans SDC [2010].

7.3.2 Superstructure Modeling

Caltrans SDC [2010] requires the superstructure of a bridge to be capacity protected and accordingly to remain elastic. Considering that the bridge is designed according to the code regulations, the bridge deck and the cap-beam that form the bridge superstructure are modeled with elastic beam-column elements using uncracked section properties (typical for prestressed concrete). The three-dimensional spine-line models for the bridge superstructures, with a series of elastic beam-column line elements located at the centroids of the cross-sections following the bridge alignment, were used to strike a good balance between computational efficiency and accuracy. The width of the deck is incorporated in the model at the two extreme nodes of the spine model, and by including a transverse rigid bar whose lengths is the same as the width of the deck. This approach allows accounting for the passive resistance of backfill soil distributed along the width of the deck. The orientation of the rigid bars and their widths are decided according to the abutment skew angle. Zero-length elements with uniaxial behavior—whose properties are discussed later below—are distributed along the width of the rigid boundary elements to model the passive backfill reaction normal to the backwall as well as the transverse reactions by the shear-keys. At each abutment, the deck is resting on several elastomeric (polytetrafluoroethylene) bearings through which the vertical loads from the superstructure are transferred to the stem wall. The two-phase (compressible and incompressible) vertical response of the bearing pads and the stem wall is represented with a bilinear force-deformation backbone curve [Kaviani et. al. 2012]. Horizontal resistance due to sliding friction between deck and bearing pads has been neglected, considering the relatively small value of the friction coefficient between the pads and their mating surface [Caltrans SDC 2010]. The integral cap beam is modeled with elastic beam-column elements—with very large torsional and bending (out-of-plane of bent) rigidities—and is rigidly connected at its central node to the deck spine model.

Each bridge span was divided into ten segments in the OpenSees model to achieve an accurate distribution of mass along the length of the superstructure. Also, the assignment of rotational mass (mass moment of inertia) was considered to achieve greater accuracy in the predicted dynamic responses and fundamental modes of the bridge, particularly for those modes

associated with the torsional and transverse motions. The rotational moment of inertia of a segment of superstructure was calculated as follows

$$M_{XX} = \frac{Md_w^2}{12} = \frac{(m/L)L_{trib}d_w^2}{12} \tag{7.2}$$

where M_{XX} is the rotational mass of the superstructure, m is the total mass of the superstructure, M is the total mass of the superstructure segment, tributary to the node, L_{trib} is the tributary length, d_w is the superstructure width, and L is the length of the superstructure. The rotational mass, M_{ZZ}, of the column was calculated as follows

$$M_{ZZ} = \frac{M_c R_{col}^2}{2} = \frac{(m_c/L_c)L_{trib}^c D_{col}^2}{8} \tag{7.3}$$

where m_c is the total mass of the column, M_c is the total mass of the column segment, tributary to the node, L_{trib}^c is the tributary length, R_{col} and D_{col} are the radius and diameter of the column, and L_c is the height of the column.

7.3.3 Column-bent Modeling

To model the columns (Figure 7.3), nonlinear force-based beam-column elements were utilized with fiber-discretized sections considering 10 integration points along the height. This is usually deemed to control the numerical integration errors and provide adequate accuracy [Kaviani et al. 2012], to consider the progression of column yielding and damage expected under strong ground motions.

Three different constitutive rules are used simultaneously within a fiber-discretized cross-section: (i) confined concrete for the core concrete, (ii) unconfined concrete for the cover concrete, and (iii) steel rebar for the reinforcing bars (Figure 7.3). OpenSees *Concrete01* constitutive model is a uniaxial Kent-Scott-Park concrete material object with degraded linear unloading/reloading stiffness according to the work of Karsan-Jirsa and no tensile strength [OpenSees Wiki 2010]. It was used for both the cover and core concrete. The steel rebar is modeled by *Steel02* material, a uniaxial Giuffre-Menegotto-Pinto steel material object with isotropic strain hardening [OpenSees Wiki 2010]. A rigid element is attached to the top of the nonlinear beam-column element to model the portion of the column-bent embedded in the superstructure. The boundary condition of the column base proves to introduce significant impact on the seismic responses obtained from NLTA [Kaviani et al. 2012]. In current models, the single-column bridge (Bridge A) is modeled with a fixed base connection, while both pinned and fixed base connection is assigned to the multi-column bridge (Bridge B and C).

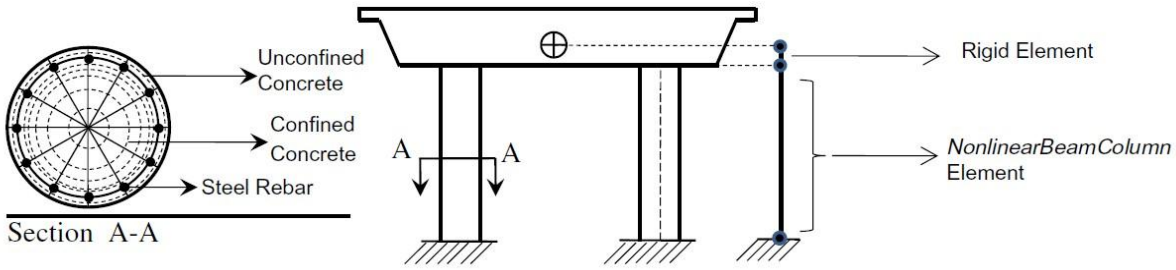

Figure 7.3 Column modeling scheme for Bridge B [Kaviani et al. 2014].

7.3.4 Abutment Modeling

The study focused on seat-type abutment modeling. A representative seat-type abutment is illustrated in Figure 7.4. Two modeling approaches, namely Type I and Type II, were considered for the abutment (Figure 7.5). In both approaches, the longitudinal responses of the backfill and the expansion joint, the transverse responses of the shear keys, and the vertical responses of the bearing pads and the stemwall were all explicitly considered. In the Type I modeling approach (Figure 7.5a), two nonlinear springs, one at each end, connected in series to gap elements, were used to model the passive backfill response and the expansion joint [Aviram et al. 2008], respectively. The shear key response was modeled using an elastic-perfectly-plastic backbone relationship. The vertical response of the bearing pads and stemwall was modeled by two parallel springs, one at each end (note that only one side is labelled in Figure 1), to represent the stiffness values. The backfill passive pressure was produced by the abutment backwall. The strength and initial stiffness of the soil springs were determined according to Caltrans SDC [Caltrans 2010]. In the Type II modeling approach, the number of nonlinear springs connected in series to the gap elements was increased to five as shown in Figure 7.5b, and the shear key response was modeled using a nonlinear spring with a tri-linear backbone relationship (Figure 7.6).

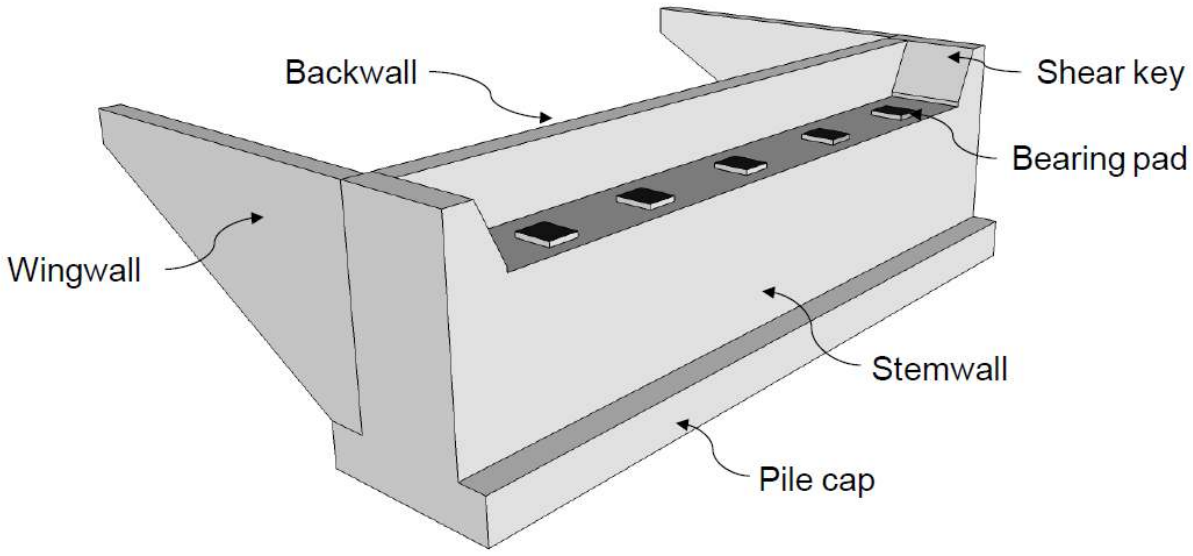

Figure 7.4 Configuration of a typical seat-type abutment [Kaviani et al. 2014].

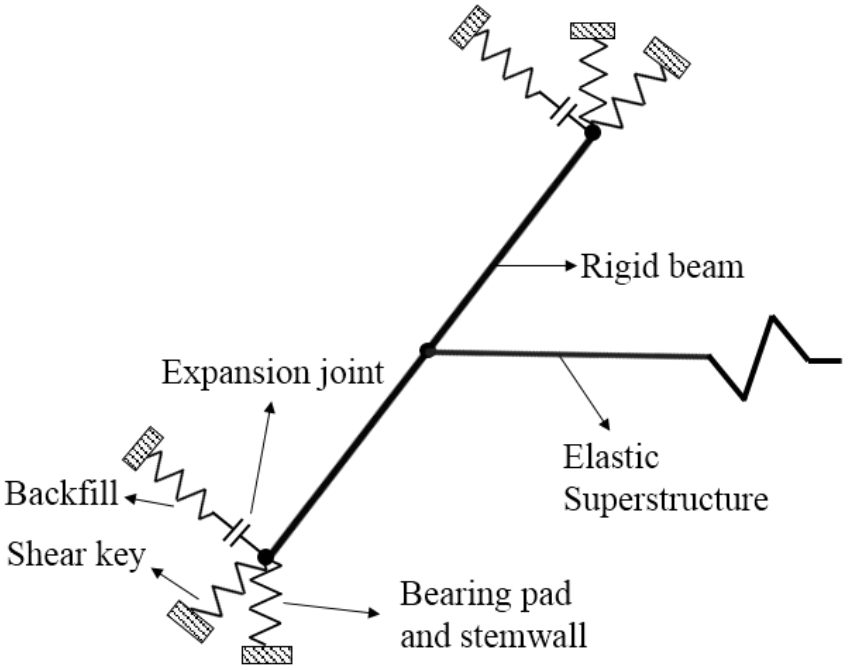

a) Type I abutment modeling

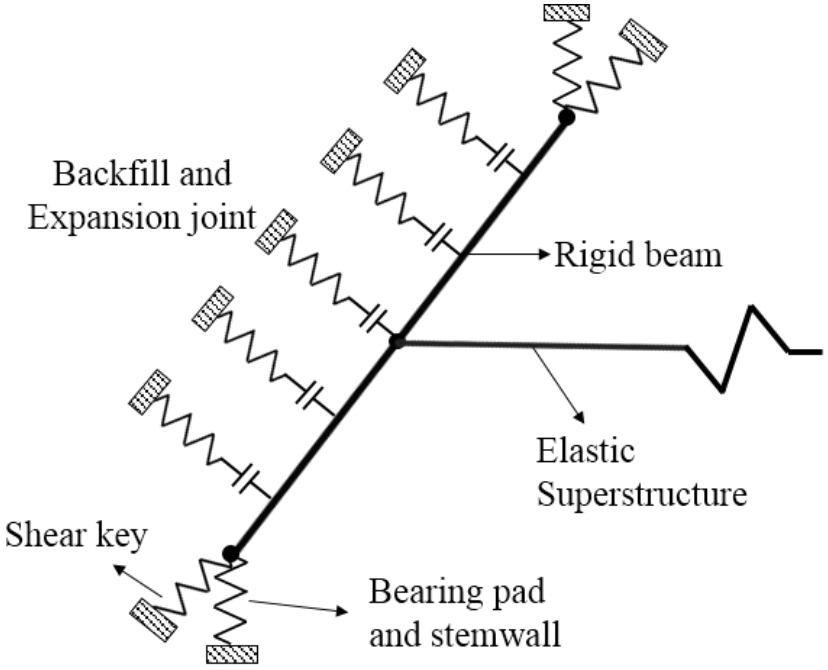

b) Type II abutment modeling

Figure 7.5 Abutment modeling with springs and gap elements.

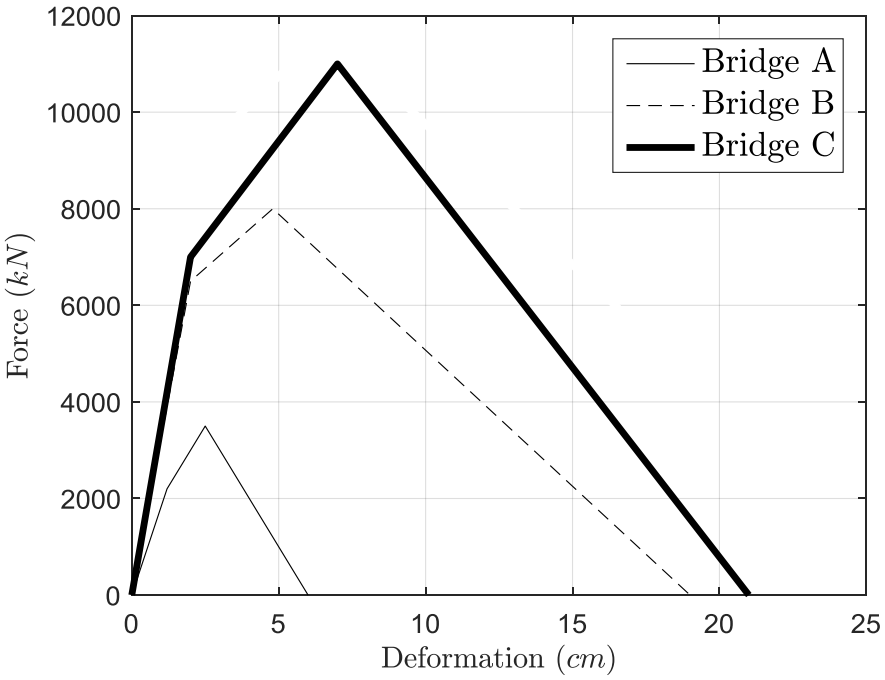

Figure 7.6 Shear key force-deformation backbone curves [Kaviani et al. 2014].

8 Application of Robust Integration and Solution Algorithms Selection

8.1 INTRODUCTION

As stated in Chapter 7, determination of the seismic response of existing and newly designed RC highway bridges is essential to ensure their seismic safety. The most suitable analysis method that can be used for this purpose is nonlinear time history analysis (NTHA). However, one of the factors that introduce a challenge to conduct NTHA is the problems of convergence. In general, these problems are attributed to three reasons: (1) various forms of nonlinear modeling required for accurate representation of the major bridge components (e.g., distributed plasticity models with discretized fiber sections for columns, stiffening gap elements used for the abutments, and combination of various nonlinear springs required for modeling shear keys); (2) complexity introduced by the interaction of the responses in longitudinal, transverse, and sometimes vertical directions; (3) dynamic complexity due to the mass distribution along the deck.

This chapter investigates solutions to the numerical problems of convergence through the use of efficient direct integration algorithms. Two of the explicit integration algorithms are the Explicit Newmark (EN) and the Operator-Splitting (OS) algorithms, which do not require iterations nor convergence checks. The TRBDF2 is an implicit integration algorithm developed to rectify potential stability problems of the Implicit Newmark (IN) for problems involving large deformations. The formulations of these algorithms are already introduced in Chapter 2. Applicability of these integration algorithms to NTHA of RC highway bridges is explored herein by using three representative RC highway bridges described in Chapter 7 where modeling of these three bridges includes the above-mentioned three sources of possible NTHA convergence issues.

The considered three integration algorithms can be used individually during the complete course of NTHA or selectively during the time steps where the commonly used IN fails to converge. Applicability of such adaptive switching of the considered integration algorithms is demonstrated in the chapter. Methods of convergence improvement are also investigated for the IN integrator. Finally, the efficacy of the proposed solutions is presented for a challenging subject in the context of PBEE [Günay and Mosalam 2013] that requires a significant number of NTHA. This subject is the identification of predominantly first-mode engineering demand parameters (*EDP*s) under earthquake excitation by making use of different ground motion selection and modification methods.

8.2 APPLICABILITY OF INTEGRATION ALGORITHMS

The applicability of the discussed explicit and implicit integration algorithms introduced in Chapter 2 for NTHA is discussed in this section. This discussion focuses on the three described RC highway bridges. Table 8.1 presents coefficients for the Newmark and the OS integration algorithms, i.e., the MDOF version of Table 4.1, where $\boldsymbol{\eta} = \mathbf{m}/\left((\Delta t)^2 \beta\right) + \mathbf{k}_{i+1} + \mathbf{c}\gamma/(\Delta t \beta)$.

Table 8.1 MDOF Coefficients for the Newmark and the OS Integration Algorithms.

Coefficient	Newmark	OS
$\boldsymbol{\eta}_0$	$\mathbf{I}$	$\mathbf{I} - [1/\Delta t]\boldsymbol{\eta}^{-1}\mathbf{c}$
$\boldsymbol{\eta}_1$	$[(1-2\beta)/2]\mathbf{I}$	$[(1-2\beta)/2]\mathbf{I} - [(1-\gamma)/\Delta t]\boldsymbol{\eta}^{-1}\mathbf{c}$
$\boldsymbol{\eta}_2$	$\beta\mathbf{I}$	$\mathbf{0}$
$\boldsymbol{\eta}_3$	$\mathbf{0}$	$\boldsymbol{\eta}^{-1}(\mathbf{p}_{i+1} - \tilde{\mathbf{f}}_{i+1})$
$\boldsymbol{\eta}_4$	$\mathbf{I}$	$\mathbf{I} - [\gamma/(\beta\Delta t)]\boldsymbol{\eta}^{-1}\mathbf{c}$
$\boldsymbol{\eta}_5$	$(1-\gamma)\mathbf{I}$	$(1-\gamma)\mathbf{I} - [\gamma(1-\gamma)/(\beta\Delta t)]\boldsymbol{\eta}^{-1}\mathbf{c}$
$\boldsymbol{\eta}_6$	$\gamma\mathbf{I}$	$\mathbf{0}$
$\boldsymbol{\eta}_7$	$\mathbf{0}$	$[\gamma/(\beta\Delta t)]\boldsymbol{\eta}^{-1}(\mathbf{p}_{i+1} - \tilde{\mathbf{f}}_{i+1})$

8.2.1 Explicit Newmark (EN) Algorithm

The EN integration algorithm, providing a straightforward application and accordingly being computationally efficient, is conditionally stable with the following stability limit for linear strutures

$$\frac{\Delta t}{T_n} \leq \frac{1}{\pi} \tag{8.1}$$

where T_n is the period of the highest mode of vibration of the analyzed structure. Eq. (8.1) restricts the use of the EN method for structures with massless DOF, since the presence of such DOF results in a singular mass matrix that yields zero-period modes. Accordingly, the EN method is not applicable to building and bridge structures which are modeled with massless rotational DOF, unless these DOF are condensed out. It is within the future objectives of this study to implement a condensation algorithm in OpenSees [McKenna et al. 2010] to facilitate broader use of the EN algorithm. Therefore, the EN algorithm is not pursued further for the NTHA of the investigated bridge systems in this chapter.

8.2.2 Operator-Splitting (OS) Algorithm

As mentioned in Chapter 4, the version of the OS algorithm considered herein (i.e., the one using the tangential stiffness matrix), possesses similar stability properties and accuracies to those of the

IN integration [Liang and Mosalam 2015, 2016a]. Moreover, the TRBDF2 algorithm is considered because of its superior stability and better convergence behavior due to numerical damping.

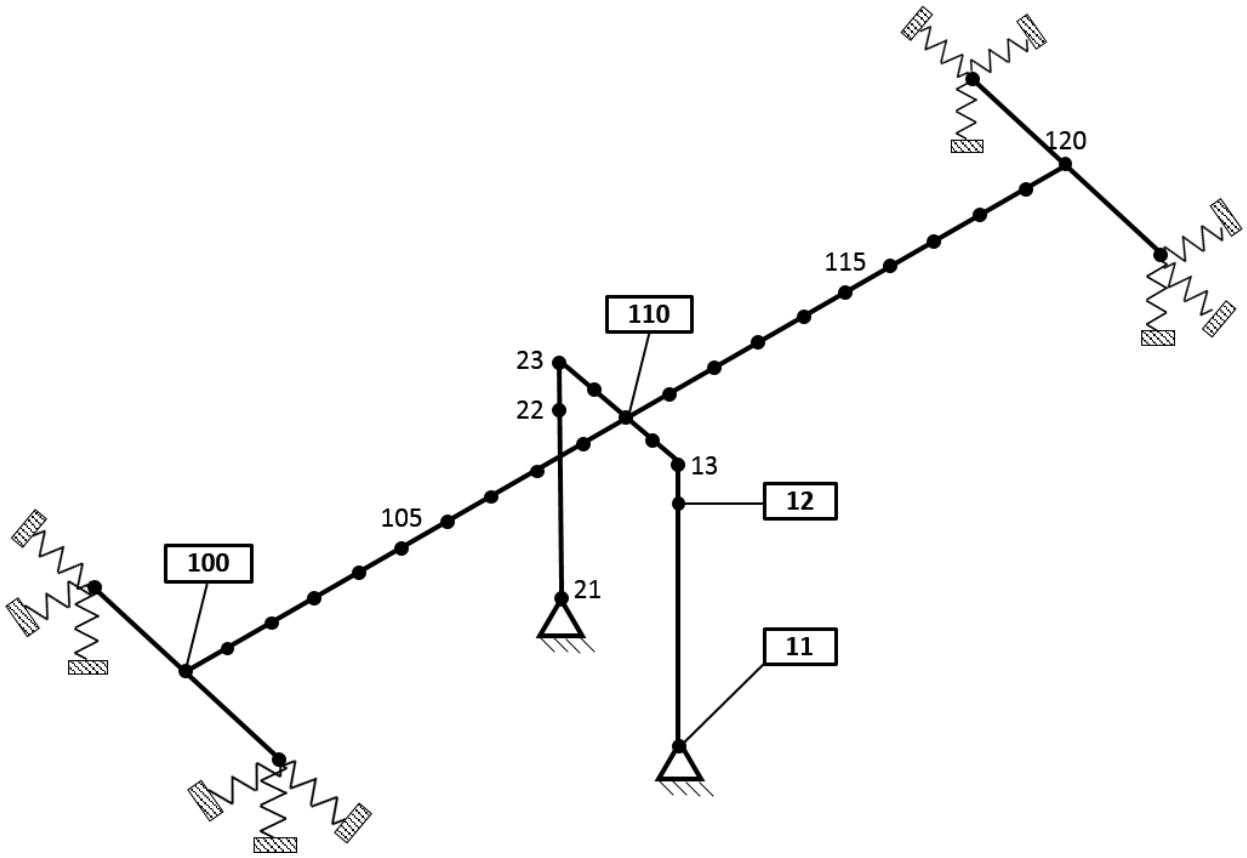

Figure 8.1 Superstructure and the column bent of Bridge B.

The NTHA is conducted for both abutment modeling approaches I and II of Bridges A, B, and C using the IN, OS, and TRBDF2 algorithms under 40 pulse-like three-component ground motions described in [Jayaram et al. 2010] and documented in the Appendix E. The pulse-like ground motions tend to introduce highly nonlinear responses. Therefore, they are selected in this study to assess the validity of the discussed integration algorithms for NTHA of bridges. The results from the IN algorithm, which is considered as the common algorithm used for NTHA, are considered as the reference results. It is to be noted that the use of a numerical solution as the reference is attributed to the lack of an available closed-form exact solution or reliable experimental data for the analyzed bridges under the selected earthquake excitations.

For comparison of the results, three *EDP*s are selected, namely the peak response value of abutment unseating displacement, column drift ratio, and column base shear. As identified in Figure 8.1 for Bridge B, these three *EDP*s correspond to the longitudinal displacement of Node 100, column drift ratio of Node 12, and column base shear of Node 11. Similar nodes are also utilized for Bridges A and C to investigate the NTHA results. The comparison is conducted quantitatively by using the error measure Max_{error}, defined as follows:

$$Max_{error} = \left| \frac{Max_{alt} - Max_{ref}}{Max_{ref}} \right| \tag{8.2}$$

where Max_{ref} and Max_{alt} are the maximum absolute response of the considered *EDP*s provided by the IN and by the other algorithms, respectively. The NTHA is conducted for all three bridges with detailed results presented for Bridge B and brief ones given for Bridges A and C. Figure 8.2 and 8.4 show the Max_{error} of the OS and TRBDF2 algorithms for the three selected *EDP*s of Bridge B, which were analyzed with both abutment modeling approaches I and II (Figure 7.5), from all 40 ground motions.

It is observed that all obtained errors are insignificant (< 0.2%). The abutment unseating displacement from IN and OS with Type I modeling is plotted in Figure 8.3a for ground motion #21 (Earthquake: Northridge – 01; Station: Sylmar – Olive View Med FF), which yields the largest Max_{error} as shown in Figure 8.2a. Figure 8.3b represents the corresponding moment-curvature plot ($M - \phi$) from the IN to reflect the obtained high level of nonlinearity in this case.

The good match of the time history responses for the highly nonlinear case in Fig. 8.3a and the small values of the error measure in Figure 8.2 indicate that the explicit OS algorithm is suitable for the intended objective of overcoming problems of convergence in the NTHA of RC highway bridges, while maintaining the accuracy of the results provided by the IN method. Similar good match and small error levels are also obtained for Bridges A and C as discussed in the section 8.4.

8.2.3 TRBDF2 Algorithm

Figure 8.4 shows the Max_{error} of the TRBDF2 algorithm for the three selected EDPs of Bridge B, analyzed with both abutment modeling approaches I and II (Figure 7.5), from all 40 ground motions. Analogous to the OS results in Figure 8.2, small errors in Figure 8.4 imply that the accuracy of the implicit TRBDF2 and IN algorithms are comparable. Furthermore, the TRBDF2 algorithm exhibits superior convergence features as discussed in the section 8.4.

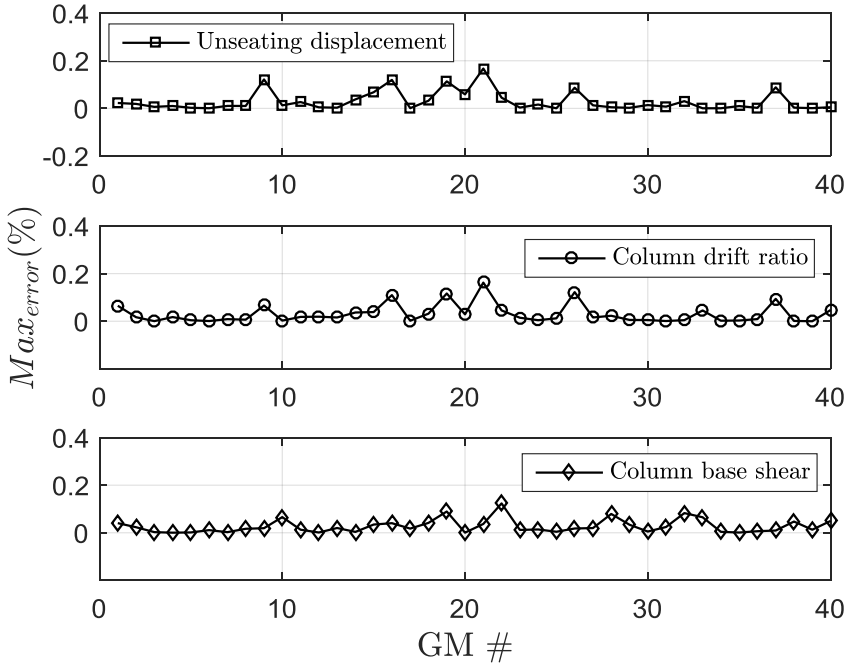

a) Type I abutment modeling

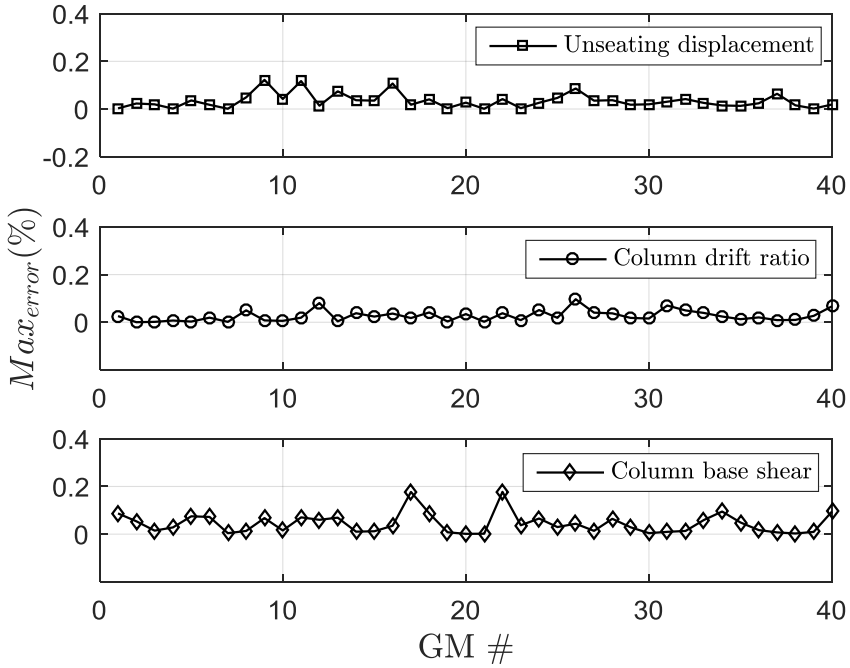

b) Type II abutment modeling

Figure 8.2 *Max*$_{error}$ of the OS algorithm for the three selected EDPs of Bridge B.

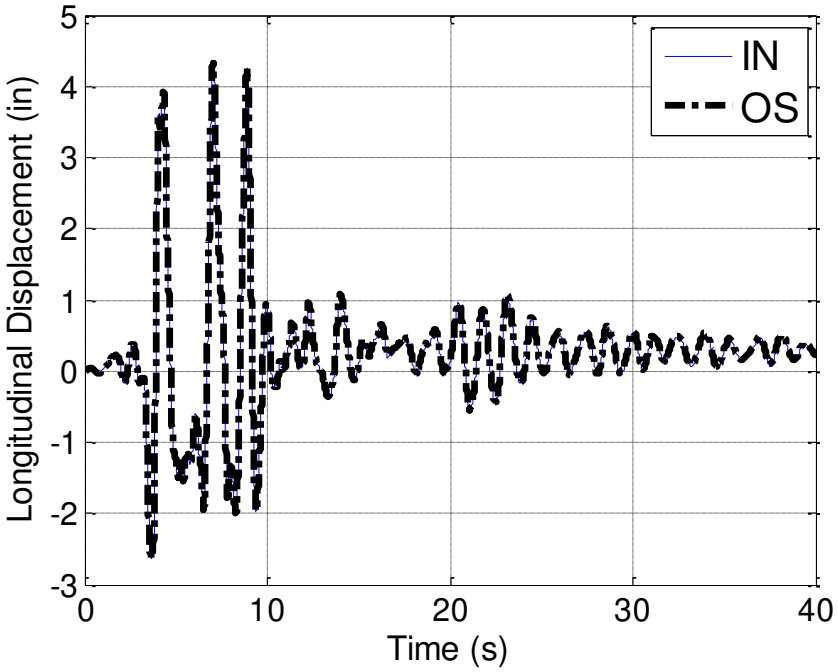

a) Abutment unseating displacement

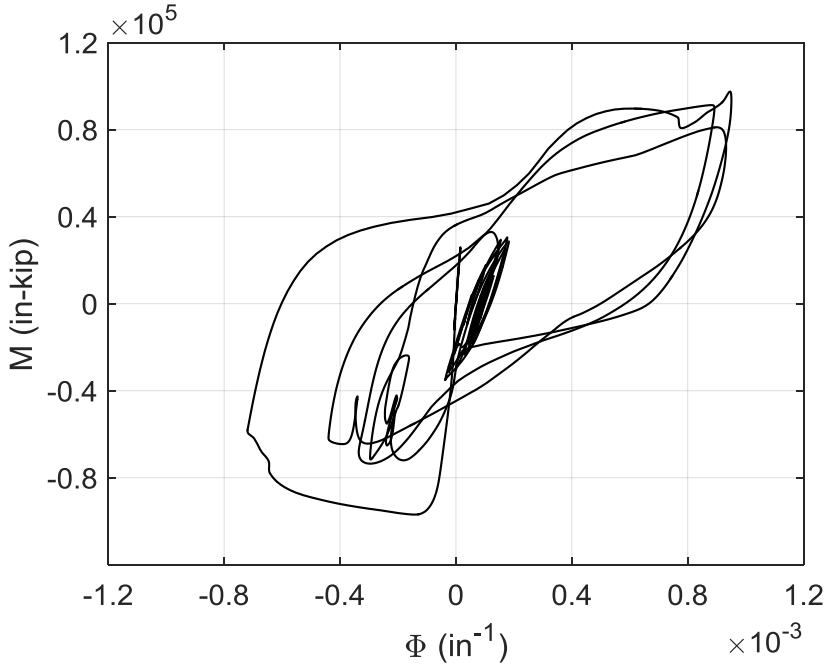

b) Moment-curvature response

Figure 8.3 Comparison of the IN and OS algorithm results for NTHA of Bridge B with Type I abutment modeling (Ground motion #21 as an example).

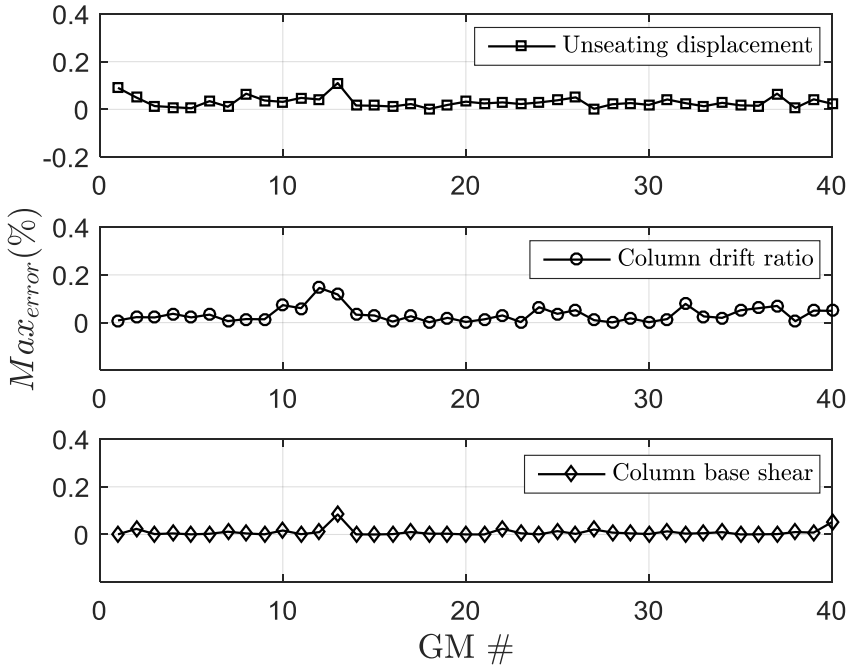

a) Type I abutment modeling

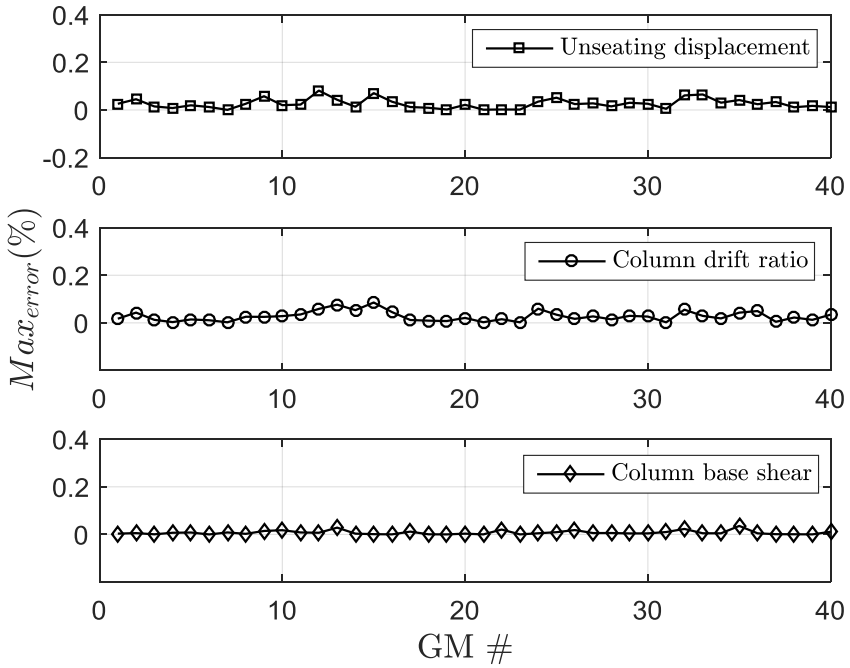

b) Type II abutment modeling

Figure 8.4 *Max*$_{error}$ of the OS algorithm for the three selected EDPs of Bridge B.

8.3 PARAMETRIC STUDY TO ASSESS CONVERGENCE PROPERTIES OF IN

As demonstrated in the previous section, the explicit algorithms are suitable alternatives of the IN method to avoid convergence problems. However, there exist some conditions where these explicit

algorithms are not applicable, e.g., the case of significant stiffening response due to closing of the gap elements in the above mentioned bridge models. Moreover, aside from the chosen integration method, formulation of some of the elements, e.g., the force-based beam-column elements or the materials, e.g., Bouc-Wen type, in OpenSees [McKenna et al. 2010] are iterative. Accordingly, the implicit algorithm, such as IN method, may be the only option for NTHA of models containing such elements and materials if the convergence problems at the element and material levels cannot be eliminated while using the alternative integrators.

The following sections investigate the effect of different parameters in improving the convergence properties of the IN method while preserving its accuracy for the bridge models described in Chapter 7. It is noted that this investigation is based on the displacement formulation of the method, which is observed to result in an improved convergence performance compared to the acceleration formulation. The considered parameters are categorized in five groups as follows:

1. Type and sequence of nonlinear equation solvers
2. Convergence test type
3. Convergence tolerance
4. Integration time step
5. Adaptive switching of integration algorithms

8.3.1 Type and Sequence of Nonlinear Equation Solvers

In order to achieve convergence, OpenSees [McKenna et al. 2010] allows trying various nonlinear solvers consecutively for any iteration of an integration time step. Therefore, one of the potential items that can be considered to improve convergence is the type and sequence of the nonlinear equation solvers. This investigation is further divided into two sub-groups, namely, (a) determination of the most suitable initial solver and (b) sequence of other solvers after the initial one. Nonlinear equation solvers considered are the ones introduced in Chapter 2, i.e., the regular Newton Raphson (NR), Broyden, Newton-Raphson with line search (NRLS), Broyden–Fletcher–Goldfarb–Shanno (BFGS), and Krylov-Newton algorithms.

Based on the convergence situations from the simulations with several relatively strong ground motions (GM1, GM11, GM18, GM19, GM28, and GM31) with scale factors ranging from 1.0 to 2.0, NRLS proves to be the most suitable initial solver. Table 8.2 shows the convergence condition for different scales of GM31 for Bridge A with Type II abutment modeling as an example, where it can be observed that all the simulations which used the NRLS solver as the initial solver are completed, whereas the simulations with other initial solvers fail to converge for some of the scales.

Using the NRLS as the initial solver, no difference was found when different subsequent orders of other solvers (NR, Broyden, BFGS, and Krylov-Newton) were investigated. It may be concluded that as long as a suitable initial solver is determined, the order of subsequent other solvers do not have significant impact on the convergence. It is beneficial to note that this finding may be specific to the investigated structure since this investigation is not repeated for other structures. However, it is still a useful conclusion because of two reasons. First, this finding sets the NLS to be a suitable initial solver as the first simulation trial of future nonlinear models. Second,

it shows to the analyst the importance of proper selection of the initial solver compared to trying a variety of solver combinations afterwards. The same observations were found for the two other Bridges B and C.

Table 8.2 The convergence failure time [sec] of simulations for different initial nonlinear solvers under GM31 for Bridge A with Type II abutment modeling.

Scale Factor	NR	Krylov-Newton	Broyden	NRLS	BFGS
1.0	Completed	21.820	Completed	Completed	Completed
1.1	35.645	21.820	35.660	Completed	35.820
1.2	35.650	21.820	Completed	Completed	41.010
1.3	35.655	6.115	35.655	Completed	Completed
1.4	Completed	6.115	35.260	Completed	27.985
1.5	Completed	6.115	77.505	Completed	Completed
1.6	Completed	6.115	Completed	Completed	42.600
1.7	Completed	6.115	Completed	Completed	36.155
1.8	35.710	6.115	Completed	Completed	37.270
1.9	Completed	6.115	35.265	Completed	35.915
2.0	35.730	6.115	52.540	Completed	24.675

8.3.2 Convergence Test Type

The following five convergence tests: Energy Increment, Norm Displacement Increment, Relative Norm Displacement Increment, Total Relative Displacement Increment, and Relative Energy Increment, are compared for the 4 ground motions (GM18, GM19, GM28 and GM31) with scale factors ranging from 1.0 to 2.0. The comparisons are based on counting the total number of iterations for each simulation, see Table 8.3 for Bridge A with Type II abutment modeling. It is observed that the Energy Increment test leads to significantly less number of iterations compared to the other test types. It is to be noted that very small response differences are obtained from the simulations with different convergence tests, as indicated by Max_{error} for the longitudinal direction displacements of one of the nodes of the abutment, i.e., node 100 (Figure 8.1) in Table 8.4. Here, Max_{error} is calculated for the simulations with different convergence tests considering the simulations with the Energy Increment test as the reference.

It is beneficial to note that the same tolerance value of 10^{-8} is used for all the convergence tests, which is the main factor that makes the Energy Increment test to have the least amount of iterations. Multiplication of the displacement increment with the unbalanced force, both less than 1.0, results in a norm value smaller than the other norms. However, aside from this explanation, observing that the simulations with the less stringent Energy Increment leads to practically the same results with significantly less number of iterations compared to the other tests, it is concluded that the Energy Increment test is the most suitable convergence test for the analyzed model. Similar to the investigation in previous sections, this finding may be specific to the investigated model. However, for similar reasons as those mentioned above, it is still a useful conclusion by providing an initial trial suggestion for other models and simulations.

Table 8.3 Total number of iterations for simulations with different convergence tests under GM31 for Bridge A with Type II abutment modeling.

Scale Factor	EnergyIncr	NormDisIncr	RelativeNorm DispIncr	RelativeTotal NormDisIncr	Relative EnergyIncr
1.0	31227	48225	55821	55817	40949
1.1	31510	48514	56481	56472	41726
1.2	31671	48983	56656	56664	42324
1.3	32021	49340	56734	56733	42505
1.4	31979	49567	57093	57075	42605
1.5	32272	49844	57187	57187	42715
1.6	32580	50035	57023	57023	42522
1.7	32573	50074	57015	57011	42162
1.8	33077	50683	57291	57219	42077
1.9	33397	51537	57381	57372	42439
2.0	33780	Failed	61986	57876	42664

Table 8.4 Max_{error} in long. deformation of node 100 for GM31 (different convergence tests) for Bridge A with Type II abutment modeling.

Scale Factor	NormDisIncr	RelativeNorm DispIncr	RelativeTotal NormDisIncr	Relative EnergyIncr
1.0	1.82×10^{-6}	1.82×10^{-6}	1.82×10^{-6}	1.82×10^{-6}
1.1	0.0	0.0	0.0	0.0
1.2	1.30×10^{-4}	0.0	0.0	0.0
1.3	7.67×10^{-6}	7.67×10^{-6}	7.67×10^{-6}	0.0
1.4	0.0	0.0	0.0	0.0
1.5	0.0	0.0	0.0	0.0
1.6	0.0	0.0	0.0	0.0
1.7	0.0	0.0	0.0	0.0
1.8	0.0	0.0	0.0	2.21×10^{-6}
1.9	0.0	0.0	0.0	0.0
2.0	Failed	1.91×10^{-4}	2.38×10^{-3}	2.70×10^{-6}

8.3.3 Convergence Tolerance

For Bridge B with Type II abutment modeling, the effect of different tolerances of 1.0, 0.1, 10^{-3} and 10^{-5} on the convergence and accuracy of the obtained results is investigated using the Energy Increment test. Analyses are conducted for all 40 GMs with 5 different tolerances, including the ones with 10^{-8}, with scaling factors presented in Figure 8.5, i.e., the maximum scaling factors without convergence issues. In order for the comparison, the longitudinal direction deformation of one of the nodes of the abutment, corresponding to node 100 (refer to Figure 8.1), and the longitudinal displacement of a column node, node12, are selected. Figure 8.6 presents the largest Max_{error} of 40 GMs of these selected two nodes for the simulations with 4 different tolerances. In the calculation of these error quantities, simulations with the tolerance of 10^{-8} are considered as the reference.

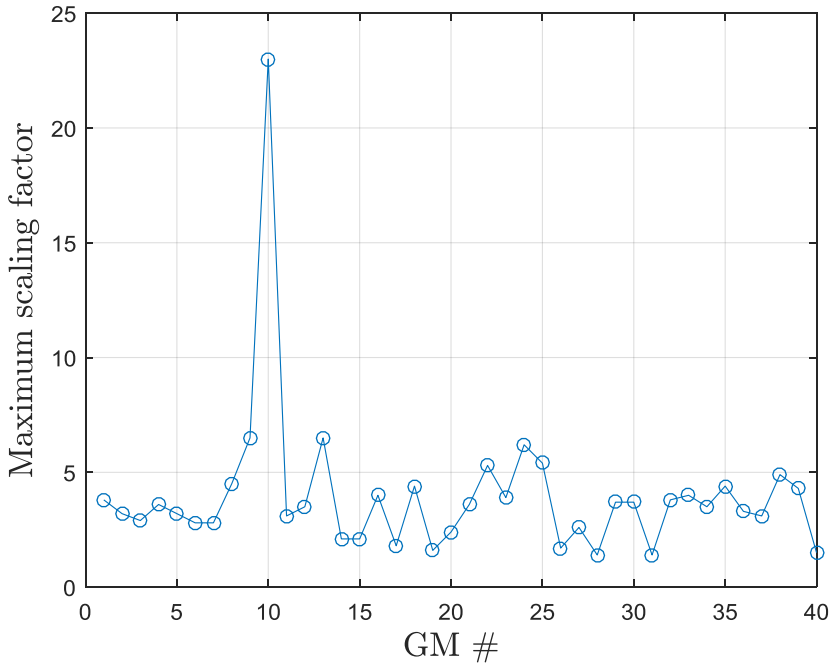

Figure 8.5 The maximum scaling factors for 40 GMs.

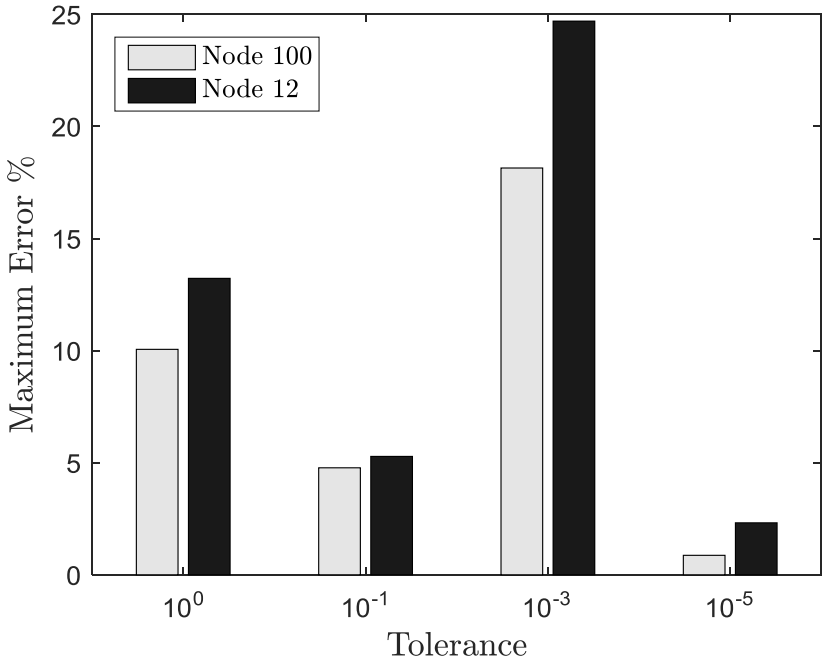

Figure 8.6 Max_{error} of each tolerance for node 100 and node 12 (longitudinal displacement).

Selected tolerances may have considerable effect on the nonlinear response. A large tolerance may result in a premature convergence and corresponding deviation from the true response. The small errors between the simulations with tolerances of 10^{-5} and 10^{-8} under the effect of the considered ground motions resulting in highly nonlinear response indicate that the increase of the tolerance can be used as a reasonable option to overcome convergence issues, while

preserving accuracy. It is to be noted that the above tolerance values are used for all the integration time steps of a particular simulation. Considering that a common application is the increase of the convergence tolerance only at the integration time steps with convergence problems, the errors in the obtained results in such cases of *selective adoption of tolerance values* will be even less than the errors plotted in Figure 8.6.

8.3.4 Integration Time Step

Use of a smaller integration time step during the simulation does not necessarily improve the convergence behavior as seen from Table 8.5, which compares the convergence condition for the simulations with different scales of GM31 using Newton-Raphson as the initial solver for Bridge A with Type II abutment modeling. Based on the simulations conducted with the seed Bridges A, B and C in this study, it is observed that reduction of the integration time step, only when needed, is useful to overcome the convergence problems. However, this requires attention to be paid to preventing the simulation from being completed before the duration of the external excitation, where the integration time step should be reset to its original value after completion of all of the reduced time steps that represent the original step size, e.g., using *automatic adaptive time increments* [DIANA 2005].

Table 8.5 The convergence failure time [sec] of simulations for different integration time steps under GM31 for Bridge A with abutment modeling.

Scale Factor	$\Delta t = 0.01$	$\Delta t = 0.005$	$\Delta t = 0.0025$	$\Delta t = 0.001$
1.0	Completed	Completed	Completed	Completed
1.1	35.6500	35.6450	35.6375	35.6360
1.2	35.6600	35.6500	35.6450	35.6430
1.3	35.6700	35.6550	35.6525	35.6510
1.4	Completed	Completed	Completed	Completed
1.5	Completed	Completed	Completed	Completed
1.6	Completed	Completed	Completed	Completed
1.7	Completed	Completed	Completed	Completed
1.8	35.7200	35.7100	35.7050	35.7040
1.9	Completed	Completed	41.7225	62.6450
2.0	35.7400	35.7300	36.3475	36.3460

8.3.5 Adaptive Switching of Integration Algorithms

As mentioned and demonstrated in the previous sections, the explicit OS integration algorithm is a suitable alternative of the IN to avoid the problems of convergence. However, there exist some conditions where this algorithm is not applicable. For example, aside from the chosen integration method, formulations of some of the elements and materials, such as the force-based beam-column elements or the Bouc-Wen material in OpenSees [McKenna et al. 2010], are iterative. Accordingly, the implicit algorithms may be the only option for NLTA of models containing such elements and materials if problems of convergence at the element and material levels cannot be eliminated while

using the explicit OS integrator. This does not, however, prevent taking advantage of the explicit algorithms in certain time steps where the implicit algorithm fails to converge. In OpenSees (2010), the adaptive switching of integration algorithms, i.e., from IN to OS, is triggered when IN fails to converge, say at time step $i+1$. Then, the simulation automatically returns to the previously converged time step, i.e. time step i, and is rerun from time step i to $i+1$ using the OS algorithm. Subsequently, the integration algorithm is switched back to IN. Therefore, IN is reused for the simulation starting from time step $i+1$ until another convergence difficulty is encountered. As demonstrated in the previous sections, the OS algorithm possesses similar stability and accuracy properties to those of the IN integration. Therefore, adaptive switching from IN to OS at problematic time steps, where convergence issues are bypassed, does not affect the stability and accuracy of simulations [Liang and Mosalam 2015, 2016a].

NTHA results in Table 8.6 are selected examples from simulations for the seismic response of bridges investigated in more detail in the next section. It is observed from Table 8.6 that the IN algorithm fails to converge at the indicated times in the 4th column, where the responses are at high levels of nonlinearity. It is noted that the ground motions in this table are identified by its sequence number in [NGA database 2011]. On the other hand, the simulations with the same ground motions are completed using adaptive switching between integration algorithms, i.e. from IN to OS, at the time steps when IN fails to converge. Therefore, the adaptive switching of algorithms is considered to be a viable and readily available option, e.g., in OpenSees (2010), to overcome the problems of convergence. Moreover, this statement is supported by the previously conducted theoretical investigation [Liang and Mosalam 2015, 2016a] and successful completion of the simulations discussed in the next chapter.

Table 8.6 The convergence failure time [sec] of simulations for different implicit integration methods.

NGA Sequence Number	Bridge	Scale factor	Implicit Newmark	Switching Integration algorithms	TRBDF2
182	A	2.80	6.160	Completed	Completed
1271	A	1.08	13.720	Completed	Completed
964	A	1.47	2.690	Completed	Completed
1263	B	3.00	17.420	Completed	Completed
1011	B	2.10	1.310	Completed	Completed
1541	C	1.00	31.120	Completed	Completed
755	C	1.70	0.495	Completed	Completed
1542	C	1.37	25.040	Completed	Completed

From Table 8.6, it is also observed that simulations that experienced problems of convergence are all completed with the use of TRBDF2. This superior convergence performance of TRBDF2 is attributed to the numerical damping introduced by the three point backward Euler scheme. It is noted that several simulations in Table 8.6 fails to converge at as early as 0.495 sec when IN is used. This early stage convergence issues can be attributed to several possible reasons, such as near fault ground motions that cause nonlinear responses very early or the abrupt stiffness change due to the opening and closing of the gap elements used in the modeling of abutments.

8.4 SEISMIC RESPONSE OF BRIDGES

The solutions for efficient NTHA in previous sections are applied to investigation of the seismic response of the three RC highway bridges A, B, and C. The nonlinear structural response of the bridge systems, similar to other complex structures, is intricate and it is often highly sensitive to the selection and modification of the input ground motions [Liang et al. 2014a, 2016a]. This section makes use of different ground motion selection and modification methods for the identification of predominantly first-mode *EDP*s under earthquake excitation. An important stage of PBEE [Günay and Mosalam 2013] is structural analysis, which may require an extensive number of NTHA. The results of computationally expensive NTHA can be predicted by computationally less demanding nonlinear static analysis procedures, such as pushover analysis, for structures with first-mode dominant response. In this regard, the identification of predominantly first-mode EDPs is beneficial for efficient, practical and routine application of PBEE.

This investigation requires a large number of NTHA that produce highly nonlinear response and may face problems of convergence. Therefore, the solutions for overcoming such problems discussed in the previous sections are used in the conducted NTHA simulations.

The maximum column drift ratio, column base shear, and deck total acceleration are selected as the investigated *EDP*s. With reference to Figure 8.1, these three *EDP*s correspond to the column drift ratio of Node 12, column base shear of Node 11, and deck total acceleration of Node 110 in Bridge B. Two groups of ground motions are selected from the NGA Database [2011] for the purpose of this investigation. The first group, expected to result primarily in the first-mode response, is selected using the conditional mean spectrum, namely the *CMS* method [Baker 2011]. The second group, which serves as the reference for comparison, is selected to match a chosen scenario response spectrum, the shape of which allows higher mode response. Therefore, the ground motions in the second group are considered as the ones with higher mode effects. Both groups of ground motions are selected using a method that seeks to match the mean and variance of the target spectrum [Jayaram et al. 2011].

For each bridge, three earthquake scenarios are considered, namely those with 2%, 10% and 50% probability of exceedance (POE) in 50 years. The attenuation model by Campbell and Bozorgnia (2008) is used to generate these three hazard levels. The *CMS* (Baker 2011), which is a response spectrum associated with a target value of the spectral acceleration S_a at a single period, is the target spectrum for the first group of ground motions. In this study, this single period is the fundamental one of the bridge. The second "reference" group is selected to match the spectrum predicted by the attenuation model of Campbell and Bozorgnia (2008).

Fig. 8.7a shows the response spectrum by the attenuation model from Campbell and Bozorgnia (2008) at hazard level of 10% POE in 50 years for Bridge B site, i.e., the target spectrum for the second "reference" group. Also shown in Fig. 8.7a is the *CMS* [Baker 2011] anchored at the Bridge B fundamental period of 1.1 sec, which is the target spectrum for the first group. As mentioned before, both groups of ground motions are selected using a method proposed by Jayaram et al. (2011) that seeks to match the mean and variance of the target spectrum (Fig. 8.7b). A detailed explanation of this method can be found in [Jayaram et al. 2011].

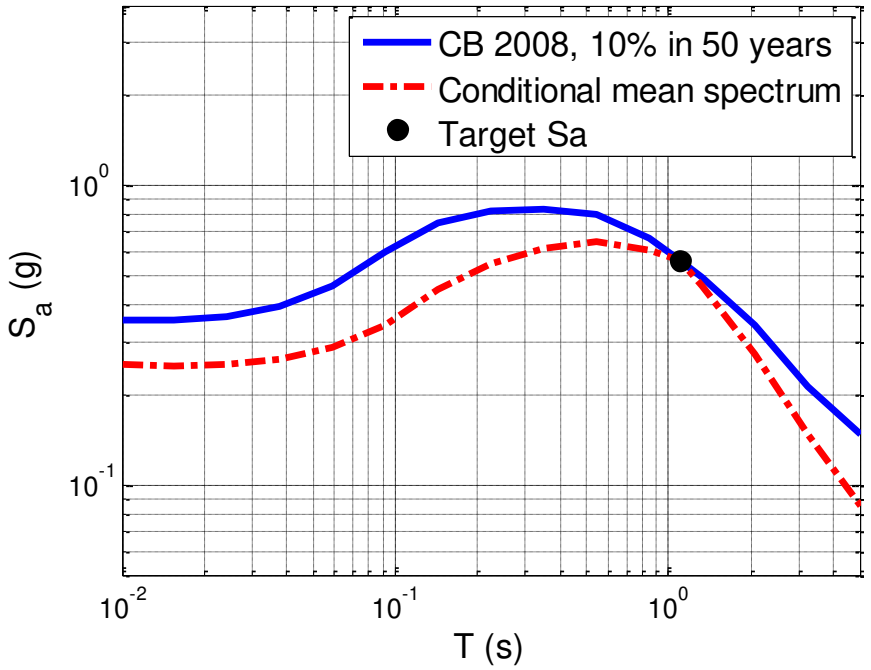

a) Median

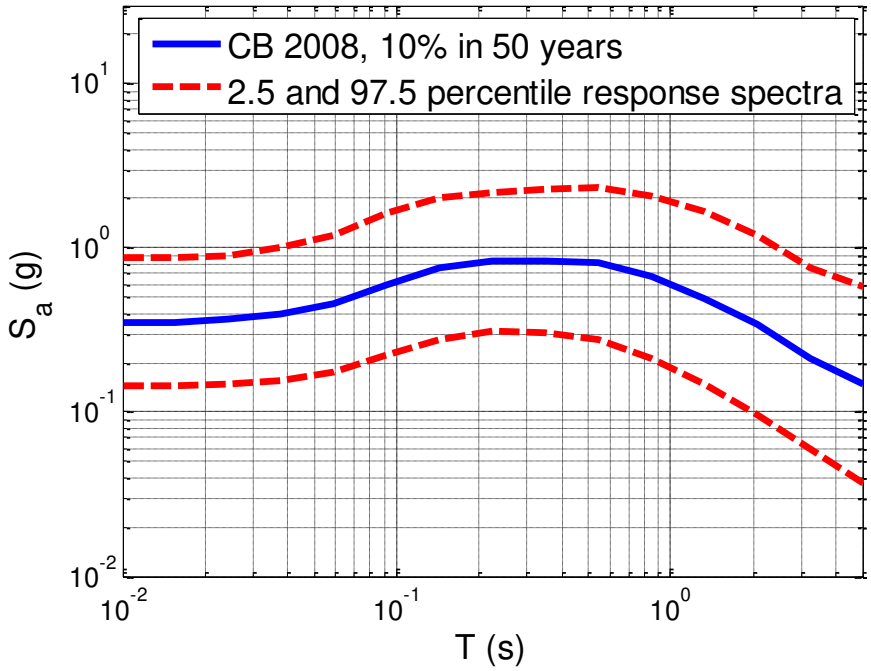

b) Median and variance

Figure 8.7 Campbell and Bozorgnia (CB) 2008 spectrum and *CMS* for 10% POE in 50 years for Bridge B site.

As discussed before, two approaches for abutment modeling, namely Type I and Type II (Figure 7.5), are considered. For each abutment modeling (2) of each scenario (3), 40 GM records are selected for each ground motion group (2). These GM records are documented in Appendix E. Therefore, 40×2×3×2×3=1440 NTHA simulations in total are conducted for the considered bridge systems (3). A large number of problems related to convergence, e.g., those indicated in Table 8.6, are encountered. Most of these problems are overcome by the proposed solutions, i.e., OS, TRBDF2, and approaches to improve convergence properties of IN presented in Section 8.3. The NTHA simulations that still fail to converge are primarily due to the large ground motions, e.g., several ones in the "reference" group at hazard level of 2% POE in 50 years, which lead to significantly large nonlinear responses in the range of collapse limit state and probably correspond to physical partial or complete bridge collapse.

Figures 8.8-8.10 present the ratios of the median *EDP*s obtained from the ground motions of the first group (*CMS*), i.e., first-mode dominant, to those obtained from the ground motions of the second "reference" group, i.e., higher mode response. Therefore, the smaller the ratio, the more the considered EDP is affected by the higher modes. It is observed that the ratio for the column base shear is close to 1.0 and almost invariant for both modeling cases and all three scenarios. On the other hand, the ratios for the column drift and deck acceleration are always less than 1.0 and generally reduce as the hazard level and the corresponding nonlinearity level increase. Accordingly, it is concluded that the higher mode effects are more pronounced on column displacements and deck accelerations than on column shear forces. Moreover, the effects of higher modes on the column drift and deck acceleration increase with increasing hazard level and nonlinearity. The column base shear is likely to be a first-mode dominant *EDP*, irrespective of the hazard level. Accordingly, an investigation that uses the base shear as the *EDP* of interest may make use of computationally less demanding single mode nonlinear static analyses in PBEE computations. On the contrary, NTHA must be used if the column drift and deck acceleration are the important *EDP*s.

The results in Figures 8.8-8.10 are in agreement with the statement that the higher modes affect the response of bridges to a greater extent than that of buildings in [Kappos et al. 2013]. To evaluate the accuracy of the two methods of ground motion selection, an estimate of the true response can be obtained using the concept of high-end prediction (HEP) [Haselton et al. 2009], which is discussed in the next chapter.

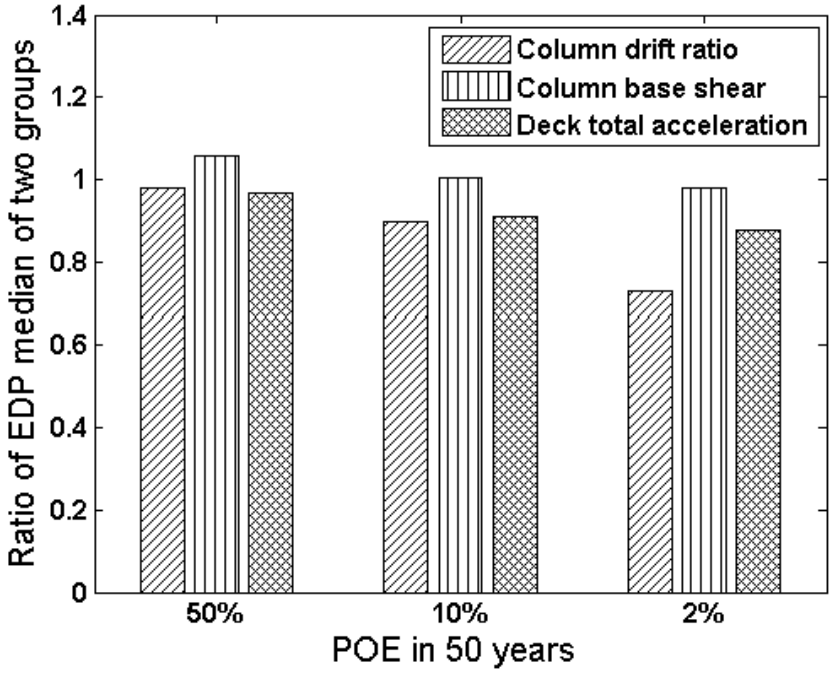

a) Type I abutment modeling

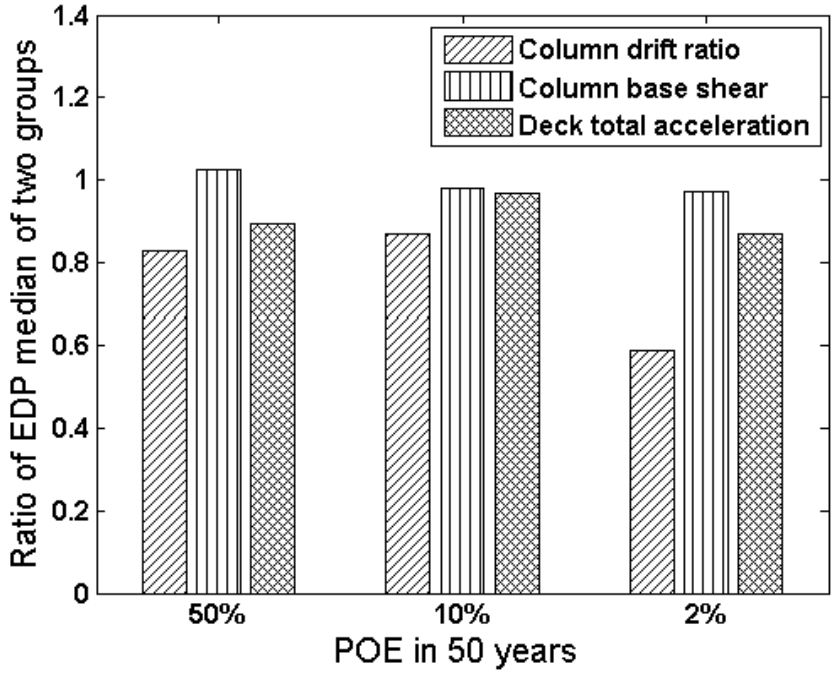

b) Type II abutment modeling

Figure 8.8 Ratios of median EDPs for the two abutment modeling cases of Bridge A.

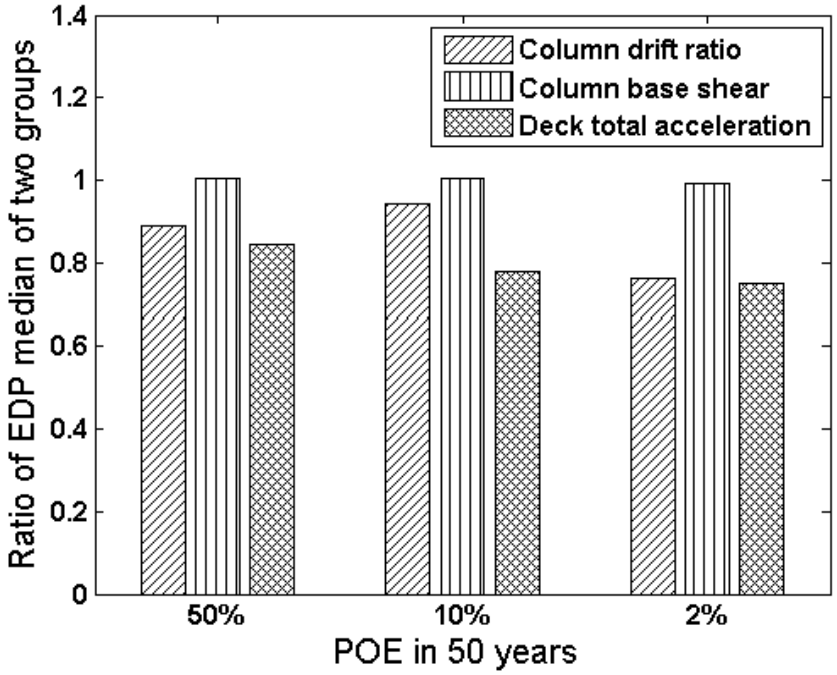

a) Type I abutment modeling

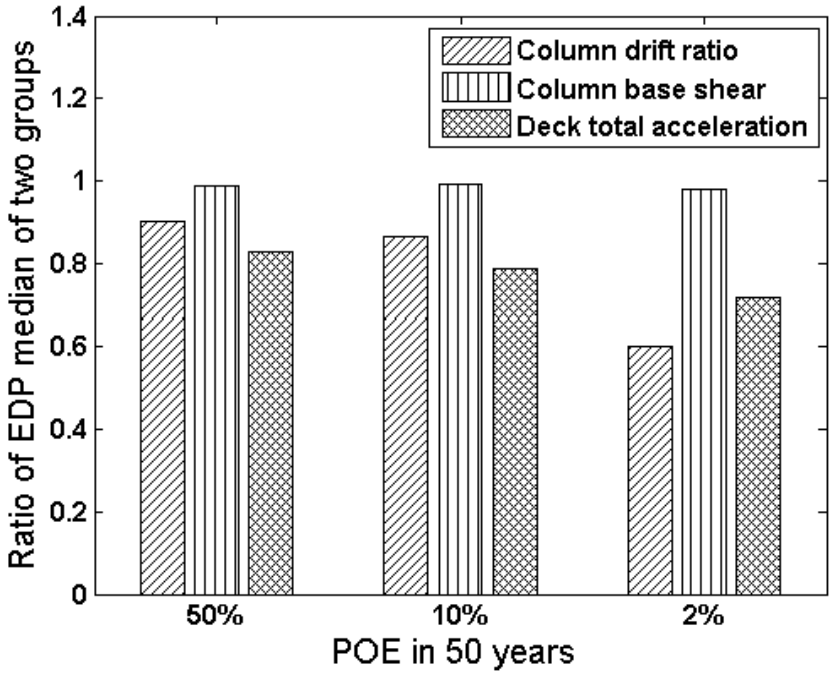

b) Type II abutment modeling

Figure 8.9 Ratios of median EDPs for the two abutment modeling cases of Bridge B.

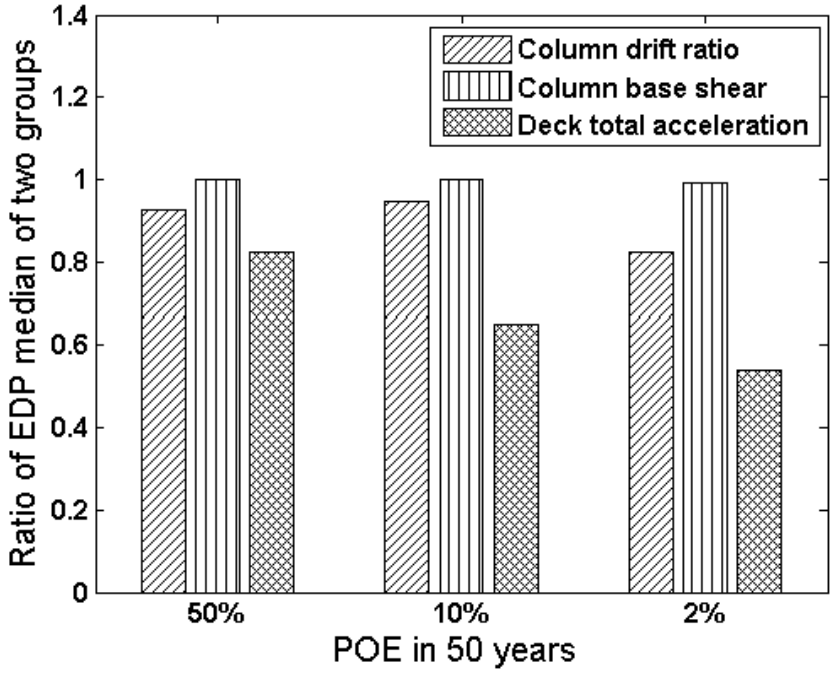

a) Type I abutment modeling

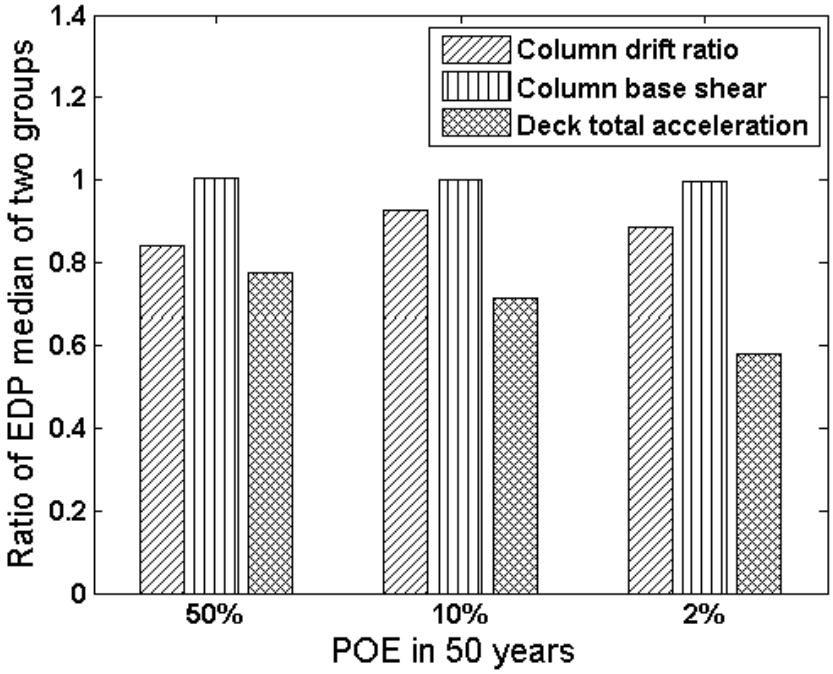

b) Type II abutment modeling

Figure 8.10 Ratios of median EDPs for the two abutment modeling cases of Bridge C.

9 Probabilistic Evaluation of Ground Motion Selection and Modification Procedures

9.1 INTRODUCTION

The objective of this chapter is to evaluate several popular GMSM procedures in predicting the *PDSD* of RC highway bridges with nonlinear response due to large earthquakes [Liang and Mosalam 2016e, 2017]. In engineering practice, the seismic design on the basis of a prescribed earthquake scenario is a common approach. Therefore, all conducted analyses in this chapter are based on a selected large earthquake scenario. In the context of a given large earthquake scenario, this study takes advantage of the framework proposed in Chapter 6 to develop the reference benchmark *PDSD* for the investigated bridge structures considering different intercept angles of the input GMs. The intercept angle is defined herein as the angle between the Fault-Normal direction (i.e., strike-normal GM component) and the longitudinal direction of the bridge structure [Kaviani et al. 2014] as shown in Figure 9.1. The accuracy and reliability of all *PDSD* estimates from the investigated GMSM procedures are then evaluated against this reference benchmark *PDSD*. Such evaluations are conducted on several selected *EDP*s for the three selected RC highway bridges described in Chapter 7.

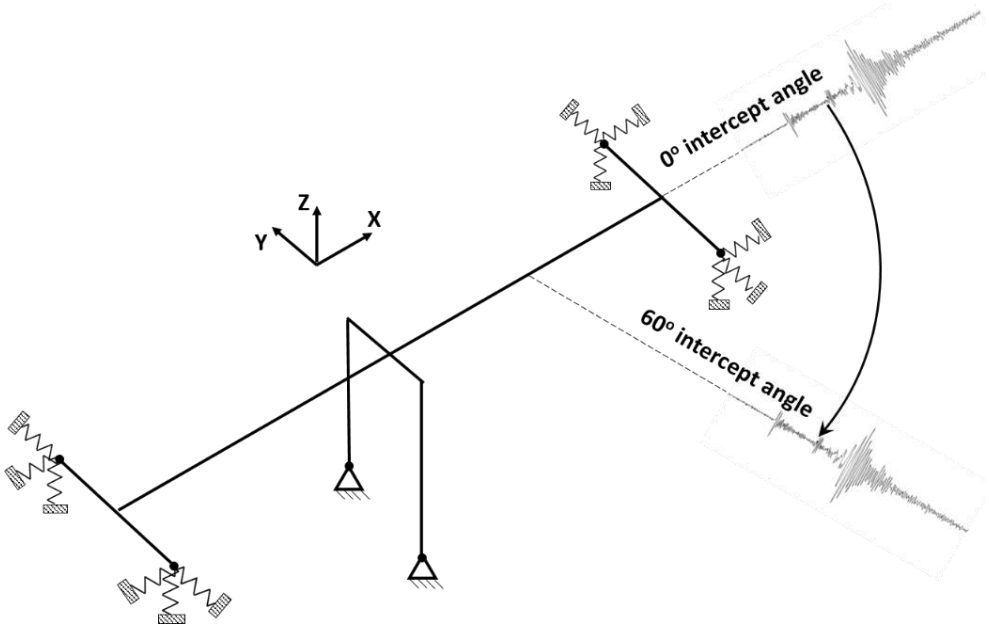

Figure 9.1 GM intercept angle scheme for the strike-normal component.

9.2 EARTHQUAKE SCENARIO

The evaluation of the *PDSD* estimates from the investigated GMSM procedures against the reference benchmark *PDSD* in this study is based on a selected large earthquake scenario defined as follows:

> ***M7 Scenario****: A magnitude* (*M*) 7.0 *earthquake event occurring on a strike-slip fault, at a site that is at a distance ® 10 km from the fault rupture on a soil with* V_{s30} (*shear wave velocity for the top 30 m of the soil profile*) *based on the bridge soil profile from* [Omrani et al. 2015]. *The target spectrum for this scenario is selected as the one with* 1.5 *standard deviation above* (i.e., $+1.5\varepsilon$) *the median spectrum using the attenuation model in* [Campbell and Bozorgnia 2008].

This scenario is selected to be consistent with a typical level of far-field GM used for the evaluation of a Caltrans bridge [Caltrans SDC 2013]. Figure 9.2 shows the median and $+1.5\varepsilon$ spectra in terms of spectral acceleration, S_a, associated with this scenario from the selected attenuation model [Campbell and Bozorgnia 2008]. Also shown in Figure 9.2 is the conditional mean spectrum (*CMS*) [Baker 2011] anchored at the fundamental period of Bridge B, i.e., $T = 1.1\text{sec}$.

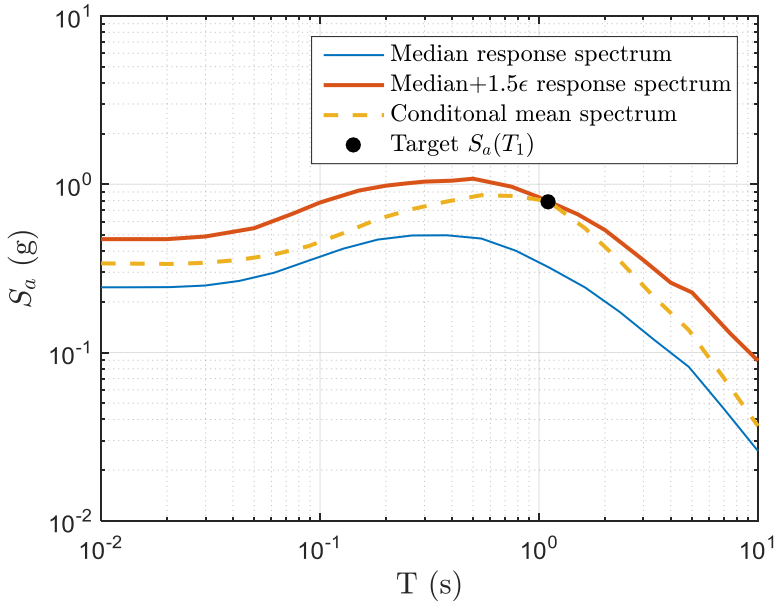

Figure 9.2 Response spectra for the selected earthquake scenario of Bridge B site.

9.3 BENCHMARK PROBABILITY DISTRIBUTION OF SEISMIC DEMANDS

In this chapter, a reference benchmark *PDSD* is developed based on the framework proposed in Chapter 6. The following sub-sections present detailed procedures of developing the benchmark *PDSD* for the RC highway bridge systems.

9.3.1 Ground Motion Selection for the Benchmark PDSD

The reference benchmark *PDSD* is developed from a large amount of NTHA simulations. The GM records for these simulations are selected based on the following procedure:

1. Select bidirectional GM records from an expanded range of the given earthquake scenario. In this study, the selection criteria are as follows:

   c) $6.5 \le M \le 7.5$;

   d) $0.0\ km < R \le 20.0\ km$;

   e) $V_{s30} \ge 183\ m/s$;

   f) Lowest usable frequency = 0.25 Hz;

   g) Faulting: Not constrained.

   Thus, 99 pairs of bidirectional horizontal GM records are selected from the PEER Next Generation Attenuation (NGA) Project GM database [PEER 2011].

2. Scale the selected 99 pairs of GM records based on peak ground velocities (*PGV*s) of one standard deviation above ($+\varepsilon$) and one standard deviation below ($-\varepsilon$) the *PGV* of the target earthquake scenario, i.e.,

$$SF^{i}_{\max/\min} = \frac{PGV_{\text{Target}\pm\varepsilon}}{\sqrt{PGV^{i}_{1} \cdot PGV^{i}_{2}}} \tag{9.1}$$

   where $SF^{i}_{\max}$ and $SF^{i}_{\min}$ are the maximum and minimum scaling factors for the *i*-th GM pair of components defined by subscripts 1 and 2 and scaled by the same scaling factor. Two rules are applied simultaneously to exclude the GM pairs that are over modified or unrealistic:

   i. Exclude the GM pair of components whose maximum scaling factor is larger than 5 to avoid excessive modification;

   ii. Exclude the GM pair of components if any peak ground acceleration (*PGA*) of its components after scaling is larger than 1.6*g* to avoid unrealistic large *PGA*.

   60 pairs of bidirectional horizontal GMs (documented in Appendix F) are left after the application of these two rules.

3. Interpolate between $SF^{\max}_{i}$ and $SF^{\min}_{i}$ to obtain 10 scale factors in total for each GM pair yielding a total of 600 pairs of bidirectional horizontal GMs.

For evaluating the *PDSD* estimates from different GMSM procedures, four *EDP*s are selected, namely the peak abutment unseating displacement, the column drift ratio, the column base shear, and the column top curvature. Moreover, different intercept angles, varying from 0^{o} to 150^{o} with an increment of 30^{o}, are investigated. Therefore, considering the three selected RC highway bridges, two abutment analytical modeling types I and II, and the above-mentioned six intercept angles for all 600 scaled GMs, 600×3×2×6=21,600 NTHA simulations are performed in total for the determination of the reference benchmark *PDSD*.

9.3.2 Intensity Measures

Many research efforts were devoted to the intensity measures, e.g., Bradley 2013. Various studies have shown that *PGV* can be considered as a reasonable GM intensity measure that correlates well with the peak nonlinear oscillator response, e.g., Riddell 2007, Akkar and Özen 2005, Kurama and Farrow 2003, and Akkar and Küçükdoğan 2008. Küçükdoğan (2007) also demonstrated that *PGV* reveals a good correlation with the global nonlinear seismic demands. In this study, the natural logarithm of *PGV*s of two directions of GM records are selected as the intensity measures, i.e., $\mathbf{IM} = \left[\ln\left(PGV_1\right) \;\; \ln\left(PGV_2\right)\right]$, to account for the distinct behaviors in the longitudinal and transverse directions of the considered bridge structures. Therefore, $f_{\mathbf{IM}}(\boldsymbol{im})$ in Eq. (6.2) becomes the joint PDF of $\ln\left(PGV_1\right)$ and $\ln\left(PGV_2\right)$. In this study, on the basis of 600 pairs of PGV_1 and PGV_2 for each investigated RC highway bridge, Eq. (6.5) becomes

$$\begin{aligned}\hat{f}_{\mathbf{IM}}(\boldsymbol{im}) &= \hat{f}_{\ln(PGV_1),\ln(PGV_2)}\left[\ln\left(pgv_1\right),\ln\left(pgv_2\right)\right] \\ &= \frac{1}{600}\sum_{i=1}^{600}\frac{1}{h_1 h_2}K\left[\frac{\ln\left(pgv_1\right)-\ln\left(PGV_{i1}\right)}{h_1},\frac{\ln\left(pgv_2\right)-\ln\left(PGV_{i2}\right)}{h_2}\right]\end{aligned} \tag{9.2}$$

where h_1 and h_2 are the bandwidths for $\ln\left(PGV_1\right)$ and $\ln\left(PGV_2\right)$, respectively. In addition, the whitening transformation in Eq. (6.6) is applied to the 600 pairs of $\ln\left(PGV_1\right)$ and $\ln\left(PGV_2\right)$, i.e., 600×2 matrix $\ln\left(\mathbf{PGV}_0\right)$, as follows:

$$\begin{aligned}\ln\left(\mathbf{PGV}_{\mu}\right) &= \ln\left(\mathbf{PGV}_0\right)-\boldsymbol{\mu} \\ \ln\left(\mathbf{PGV}_{white}\right) &= \ln\left(\mathbf{PGV}_{\mu}\right)\boldsymbol{\Sigma}^{-1/2}\end{aligned} \tag{9.3}$$

where $\boldsymbol{\mu}$ is a 600×2 matrix with all entries of the first and second columns are equal to the means of $\ln\left(PGV_1\right)$ and $\ln\left(PGV_2\right)$, respectively, and $\boldsymbol{\Sigma}$ is the 2×2 covariance matrix of the two columns of $\ln\left(\mathbf{PGV}_{\mu}\right)$. After this whitening transformation, each column of $\ln\left(\mathbf{PGV}_{white}\right)$ has zero mean and identity covariance matrix. The kernel density estimator for K and a bandwidth selection method for h_1 and h_2 introduced in Chapter 6 [Botev et al. 2010)], are adopted to estimate the joint PDF $f_{\mathbf{IM}}(\boldsymbol{im})$. After such estimation, similar to Eq. (6.7), $\ln\left(\mathbf{PGV}_{white}\right)$ is transformed back to $\ln\left(\mathbf{PGV}_0\right)$, i.e.,

$$\ln\left(\mathbf{PGV}\right) = \ln\left(\mathbf{PGV}_{white}\right)\boldsymbol{\Sigma}^{1/2}+\boldsymbol{\mu} \tag{9.4}$$

The procedures of density estimation discussed above are applied to the investigated three RC highway bridges. As an example, the joint PDF for Bridge B is illustrated in Figure 9.3. It is noted that the results of this process depend on the selected 600 pairs of GM records, which are based on the selected earthquake scenario and V_{s30} of the bridge site [Omrani et al. 2015]. Therefore, the 600 GM records are different for the three considered bridges as their sites have different V_{s30}.

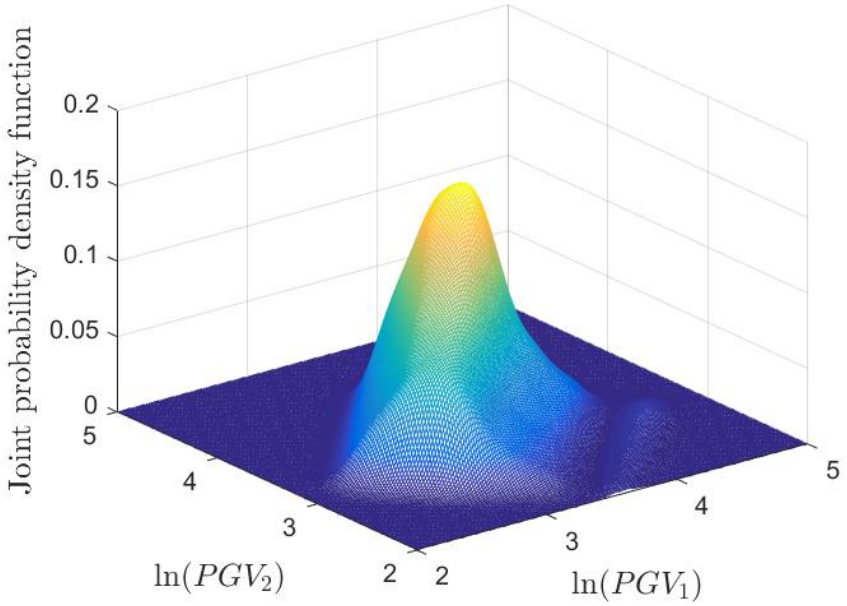

Figure 9.3 Joint PDF of $\ln(PGV_1)$ and $\ln(PGV_2)$ of Bridge B by kernel density estimation.

9.3.3 Collapse Consideration

In this study, two failure criteria are defined: (1) deck unseating and (2) column excessive rotation; whichever takes place first will imply the occurrence of collapse. Deck unseating is assumed to occur when the relative displacement between the bridge deck and the abutment is larger than the length of the abutment seat, which is taken as 33.85 inches (Table 6.1). The limit state corresponding to column excessive rotation is defined as exceeding certain threshold value of the column drift ratio, $\overline{DR}$. Hutchinson et al. (2004) demonstrated that, on the basis of the mean trend from their experimental data, if the maximum drift ratios are less than about 8%, the residual drift ratios are generally less than 1%, which is the allowable residual drift ratio suggested in [MacRae and Kawashima 1997]. The maximum drift ratios of about 6% were recommended in [Hutchinson et al. 2004] if a higher degree of confidence is required. In this study, $\overline{DR}$ is assumed to have a gamma distribution (Figure 9.4) with mean and mode equal to 8% and 6%, respectively.

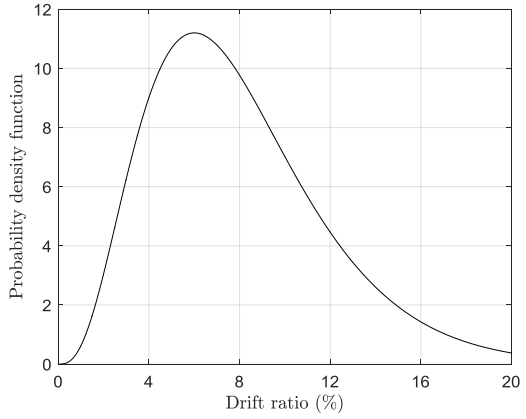

Figure 9.4 Assumed gamma distribution of $\overline{DR}$.

From the prescribed collapse criteria above, Eq. (6.10) is further manipulated as follows:

$$G(edp\,|\,\boldsymbol{im}) = \int_{\overline{dr}} \{\Pr(\mathrm{C}\,|\,\boldsymbol{im}) + G(edp\,|\,\boldsymbol{im},\mathrm{NC}) \times [1 - \Pr(\mathrm{C}\,|\,\boldsymbol{im})]\} f_{\overline{DR}}(\overline{dr})\, d\,\overline{dr} \tag{9.5}$$

where $f_{\overline{DR}}(\overline{dr})$ is the PDF of the $\overline{DR}$ defined in Figure 9.4. Based on Eq. (6.11), the fragility surface or conditional probability of collapse, i.e., $\Pr(\mathrm{C}\,|\,\boldsymbol{im})$, is estimated using multivariate binary logistic regression [Wasserman 2010] as follows

$$\hat{\Pr}(\mathrm{C}\,|\,\boldsymbol{im}) = \frac{\exp[\hat{\alpha}_0 + \hat{\alpha}_1 \ln(pgv_1) + \hat{\alpha}_2 \ln(pgv_2)]}{1 + \exp[\hat{\alpha}_0 + \hat{\alpha}_1 \ln(pgv_1) + \hat{\alpha}_2 \ln(pgv_2)]} \tag{9.6}$$

where the coefficients $\hat{\alpha}_0$, $\hat{\alpha}_1$ and $\hat{\alpha}_2$ are obtained by the reweighted least squares algorithm [Wasserman 2010]. For illustration, Figure 9.5 presents $\hat{\Pr}(\mathrm{C}\,|\,\boldsymbol{im})$ for Bridge B with Type I abutment model when $\overline{DR}$ equals 8%, i.e., the mean of the gamma distribution in Figure 9.4.

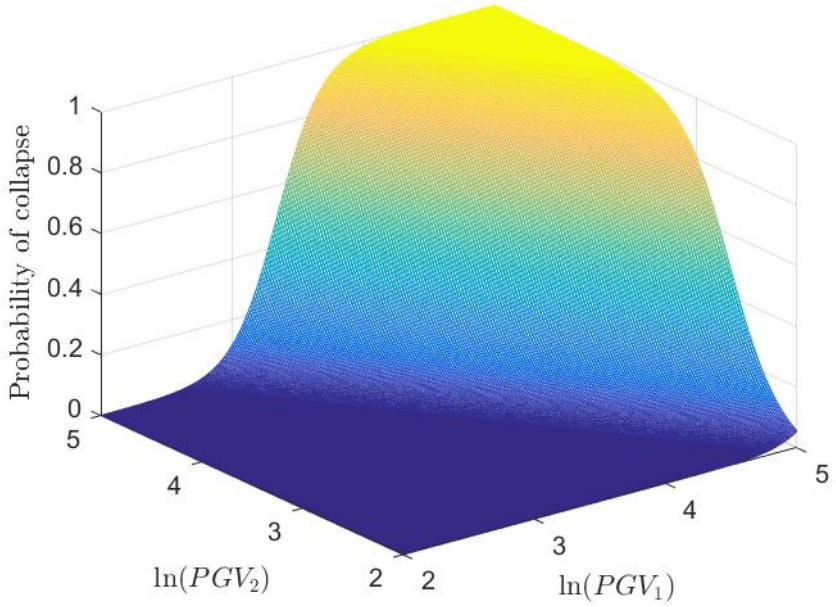

Figure 9.5 The fragility surface for Bridge B (Type I abutment model) with $\overline{DR} = 8\%$.

9.3.4 Non-collapse Structural Responses

Based on Eq. (6.12), for a given pair of $\ln(pgv_1)$ and $\ln(pgv_2)$ under non-collapse scenario, the mean value of $\ln(EDP)$ is as follows:

$$\hat{\mu}_{\ln(edp)|\boldsymbol{im}} = \hat{\beta}_0 + \hat{\beta}_1 \ln(pgv_1) + \hat{\beta}_2 \ln(pgv_2) \tag{9.7}$$

where coefficients $\hat{\beta}_0$, $\hat{\beta}_1$ and $\hat{\beta}_2$ are determined from the least square estimate [Wasserman 2010). An unbiased estimate of the variance of the distribution, i.e., Eqs. (6.13) and (6.14) become

$$\hat{\sigma}^2_{\ln(edp)|\boldsymbol{im}} = \left[1/(N-3)\right]\sum_{i=1}^{N}\hat{\varepsilon}_i^2 \tag{9.8}$$

$$\hat{\varepsilon}_i = \hat{\beta}_0 + \hat{\beta}_1 \ln\left(PGV_1^i\right) + \hat{\beta}_2 \ln\left(PGV_2^i\right) - \ln\left(EDP_i\right) \tag{9.9}$$

where PGV_1^i , PGV_2^i and EDP_i are the i-th sampling point of PGV_1 , PGV_2 and EDP, respectively. N is the total number of sampling points that produce NC. The probability that the EDP exceeds the demand level of edp given $\boldsymbol{im}$ and for the NC scenario can now be calculated using the normal CCDF in Eq. (6.15). Figure 9.6 illustrates the linear regression surface of the column drift for Bridge B with Type I abutment model when $\overline{DR}$ equals 8%.

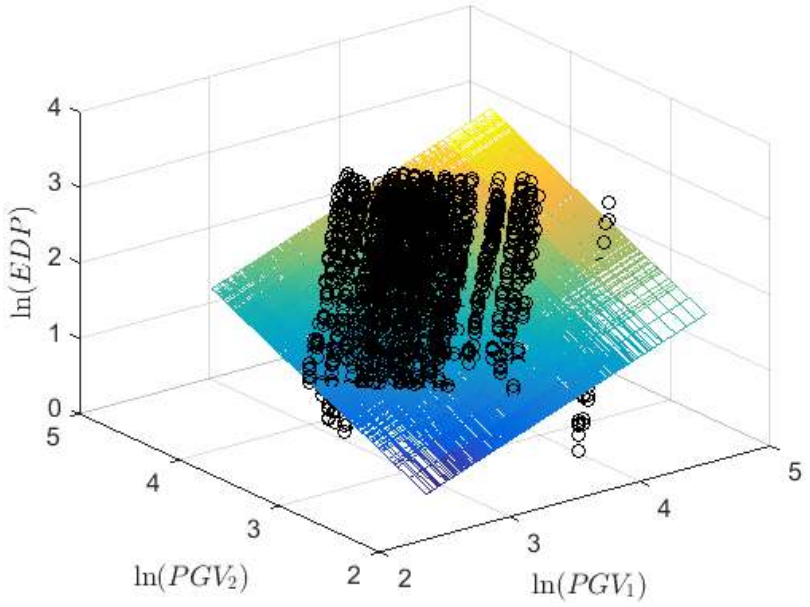

Figure 9.6 Linear regression surface of column drift for Bridge B (Type I abutment model) with $\overline{DR} = 8\%$.

9.3.5 Integration of Intensity Measures and Structural Responses

Combination of the intensity measures from the kernel density estimator and the structural responses, including C and NC cases, i.e., substituting Eq. (9.5) and the required estimates of its different terms, as discussed above, into Eq. (6.2), leads to the followingL

$$\hat{G}(edp) = \int_{\boldsymbol{im}}\int_{\overline{dr}} \left\{\hat{\Pr}(\mathrm{C}\,|\,\boldsymbol{im}) + \hat{G}(edp\,|\,\boldsymbol{im},\mathrm{NC})\times\left[1-\hat{\Pr}(\mathrm{C}\,|\,\boldsymbol{im})\right]\right\}\hat{f}_{\overline{DR}}\left(\overline{dr}\right)\hat{f}_{\mathbf{IM}}(\boldsymbol{im})\,d\,\overline{dr}\,d\boldsymbol{im} \tag{9.10}$$

In general, it is impossible to determine the exact solution of the integrations in Eq. (9.10). Instead, in practice, $\hat{G}(edp)$ in Eq. (9.10) is computed from the following discretized form:

$$\hat{G}(edp) \cong \sum_k\sum_j\sum_i \left\{\hat{\Pr}\left(\mathrm{C}_i\,|\,\boldsymbol{im}_{jk}\right) + \hat{G}\left(edp\,|\,\boldsymbol{im}_{jk},\mathrm{NC}_i\right)\times\left[1-\hat{\Pr}\left(\mathrm{C}_i\,|\,\boldsymbol{im}_{jk}\right)\right]\right\}\hat{\Pr}\left(\overline{dr}_i\right)\hat{\Pr}\left(\boldsymbol{im}_{jk}\right) \tag{9.11}$$

where $\hat{\Pr}(\mathrm{C}_i \mid \boldsymbol{im}_{jk})$ and $\hat{G}(edp \mid \boldsymbol{im}_{jk}, \mathrm{NC}_i)$ are respectively the estimated probabilities of collapse and exceedance in the context of NC, when $dr = \overline{dr}_i$, conditioning on $\mathbf{IM} = \boldsymbol{im}_{jk}$, i.e., $\ln(PGV_1) = \ln(pgv_1^j)$ and $\ln(PGV_2) = \ln(pgv_2^k)$. $\hat{\Pr}(\overline{dr}_i)$ and $\hat{\Pr}(\boldsymbol{im}_{jk})$ are estimated from:

$$\hat{\Pr}(\overline{dr}_i) = \hat{f}_{\overline{DR}}(\overline{dr}_i) \Big/ \sum_{j=1}^{N_{dr}} \hat{f}_{\overline{DR}}(\overline{dr}_i) \tag{9.12a}$$

$$\hat{\Pr}(\boldsymbol{im}_{jk}) = \hat{f}_{\mathbf{IM}}(\boldsymbol{im}_{jk}) \Big/ \sum_{p=1}^{N_{im1}} \sum_{q=1}^{N_{im2}} \hat{f}_{\mathbf{IM}}(\boldsymbol{im}_{pq}) \tag{9.12b}$$

where N_{dr}, N_{im1} and N_{im2} are the numbers of points considered for $\overline{DR}$, $\ln(PGV_1)$ and $\ln(PGV_2)$, respectively. Thus, as expected, $\sum_{i=1}^{N_{dr}} \hat{\Pr}(\overline{dr}_i) = 1$ and $\sum_{j=1}^{N_{im1}} \sum_{k=1}^{N_{im2}} \hat{\Pr}(\boldsymbol{im}_{jk}) = 1$. In this study, $N_{dr} = 100$ and $N_{im1} = N_{im2} = 64$. Comparing Eq. (9.11) with Eq. (9.10), the integrals, the PDF and the joint PDF are replaced with the summations, the probability mass function (PMF) and the joint PMF, respectively. In Eq. (9.11), the symbol "$\cong$" signifies the approximation due to the discretization of the continuous integral of the seismic hazard and structural demand.

9.3.6 Effects of Intercept Angles on PDSD Estimates

The reference benchmark *PDSD* is developed on the basis of the implicit assumption that the earthquake is likely to occur at the previously mentioned six different intercept angles with equal probability. In this section, *PDSD* estimates from each intercept angle are compared against the benchmark to investigate the effects of intercept angles. Figures 9.7-9.9 present such comparisons for several *EDP*s of samples of the studied three bridges where the percentage error is defined as follows:

$$error_i = \frac{PDSD^{\,i} - PDSD_{Ref}^{i}}{PDSD_{Ref}^{i}} \times 100 \tag{9.13}$$

where $PDSD_{Ref}^{i}$ and $PDSD^{\,i}$ are the *i*-th *EDP* point from the benchmark *PDSD* and the *PDSD* estimate from each of the six intercept angles, respectively. Therefore, the positive or negative $error_i$ signifies the overestimation or underestimation of the *i*-th *EDP* point, respectively.

Figures 9.10-9.12 present the maximum errors, defined as $\max_i |error_i|$, of different intercept angles for all four investigated *EDP*s of the three bridges with both Types I and II abutment modeling. It can be observed that the maximum errors are generally below 10%, with few exceptions, but clearly not negligible. As shown in Figures 9.7b and 9.10b, the maximum error can be as large as about 20%. Therefore, the intercept angle causes certain differences in estimating the *PDSD*. This is expected as bridge structures clearly possess different geometric properties in the longitudinal and transverse directions. It is to be noted that the results presented in Figures 9.10-9.12 are based on NTHA simulations of 600 GM records for each intercept angle. Larger differences are expected if the number of GM records for NTHA simulations is much less than

600 as will be shown in a latter section in which only 40 GM records are selected from each investigated GMSM procedure.

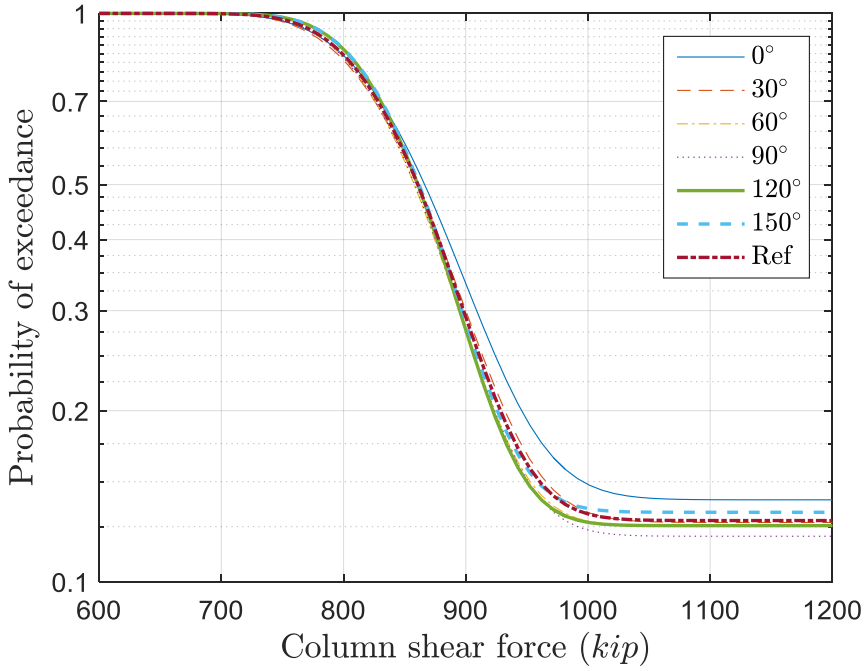

a) *PDSD* comparison

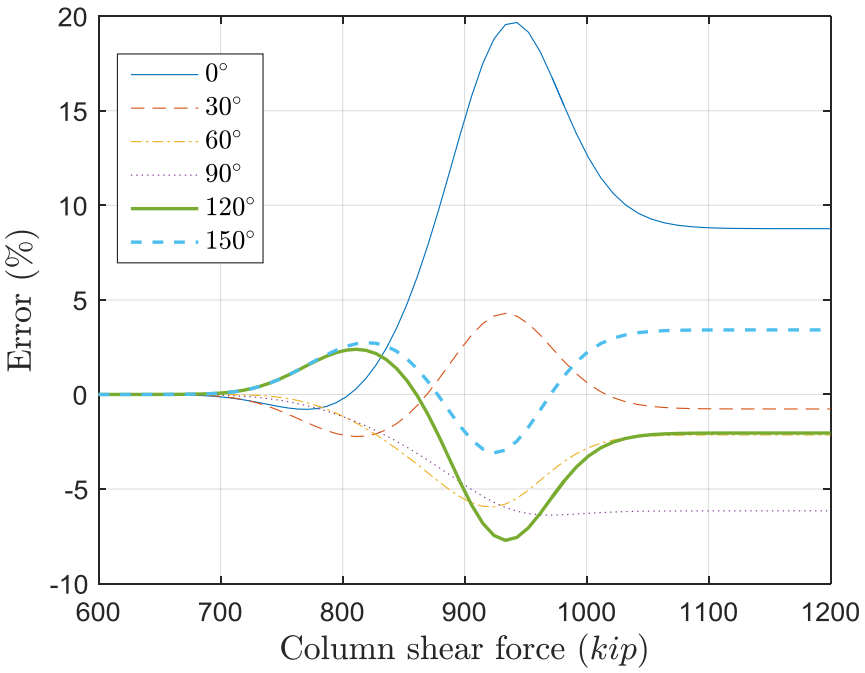

b) Error comparison

Figure 9.7 *PDSD* and error for column shear force of Bridge A with Type II abutment model.

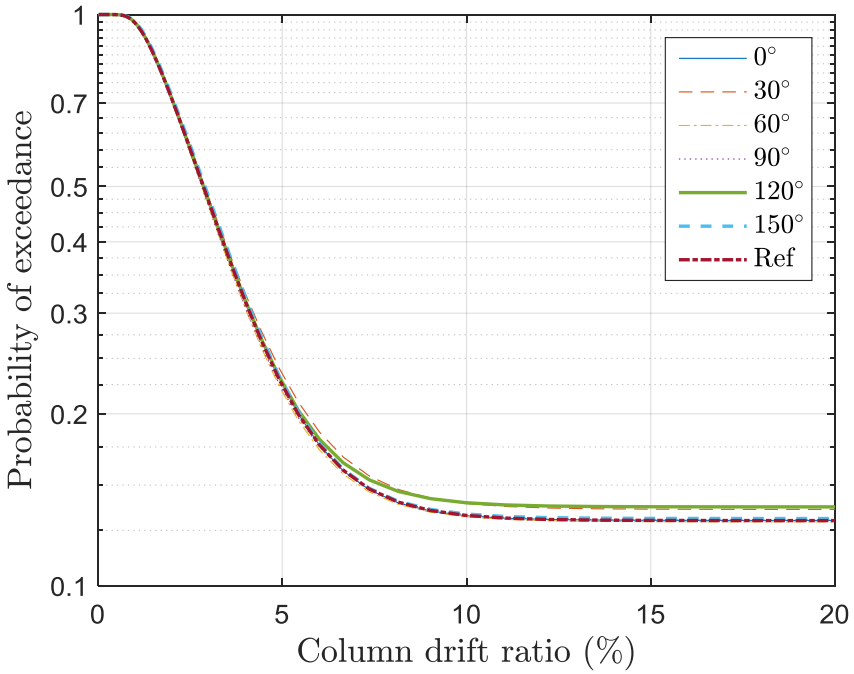

a) *PDSD* comparison

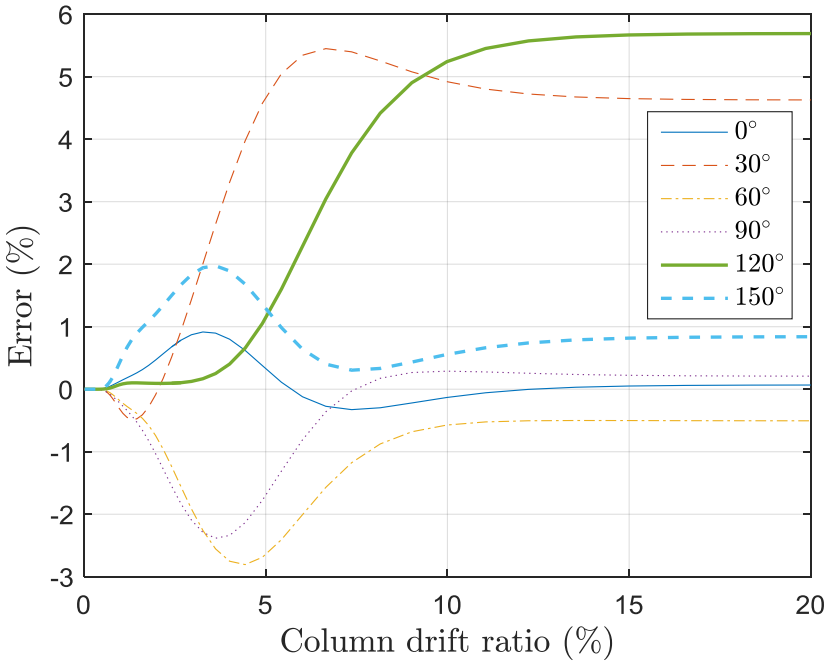

b) Error comparison

Figure 9.8 *PDSD* and error for column drift ratio of Bridge B with Type I abutment model.

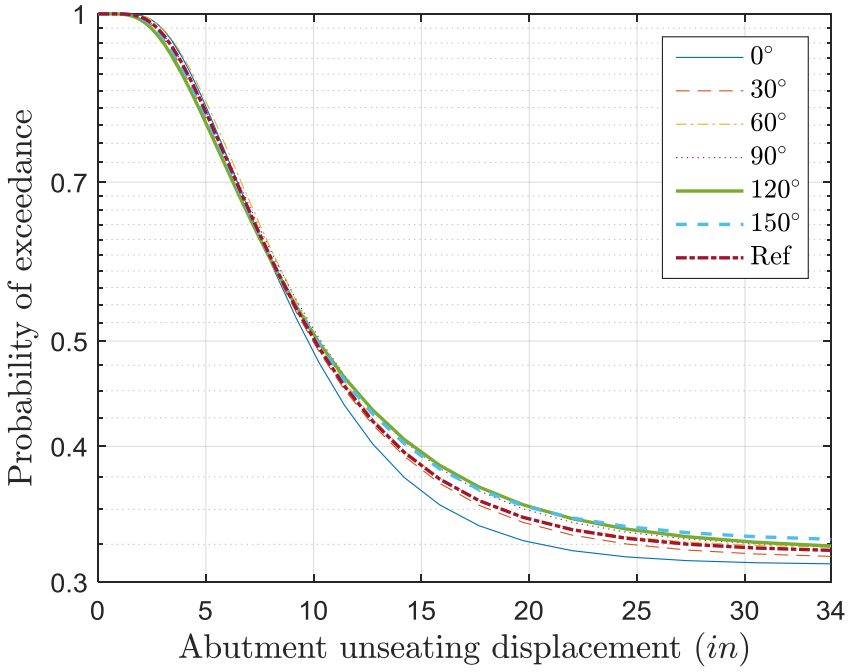

a) *PDSD* comparison

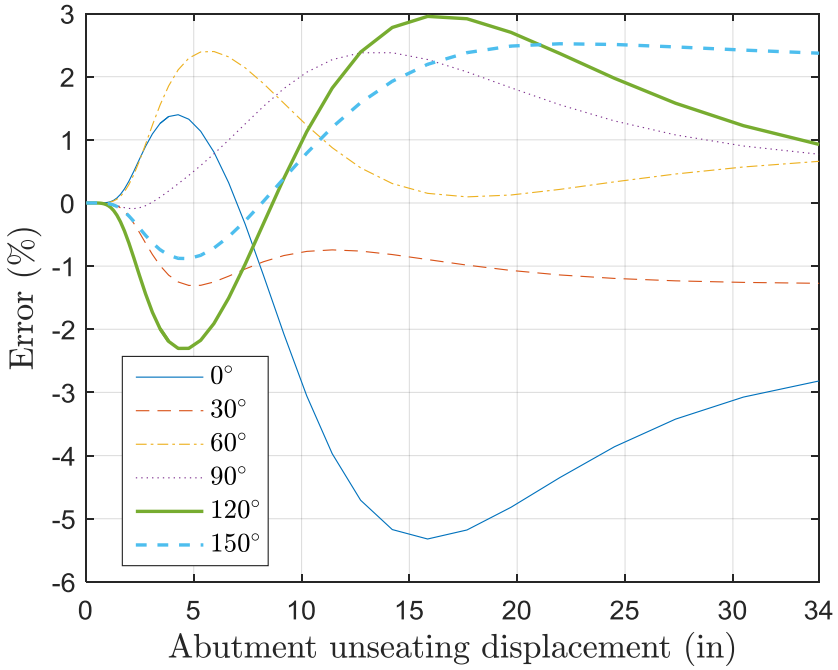

b) Error comparison

Figure 9.9 *PDSD* and error for abutment unseating displacement of Bridge C with Type I abutment model.

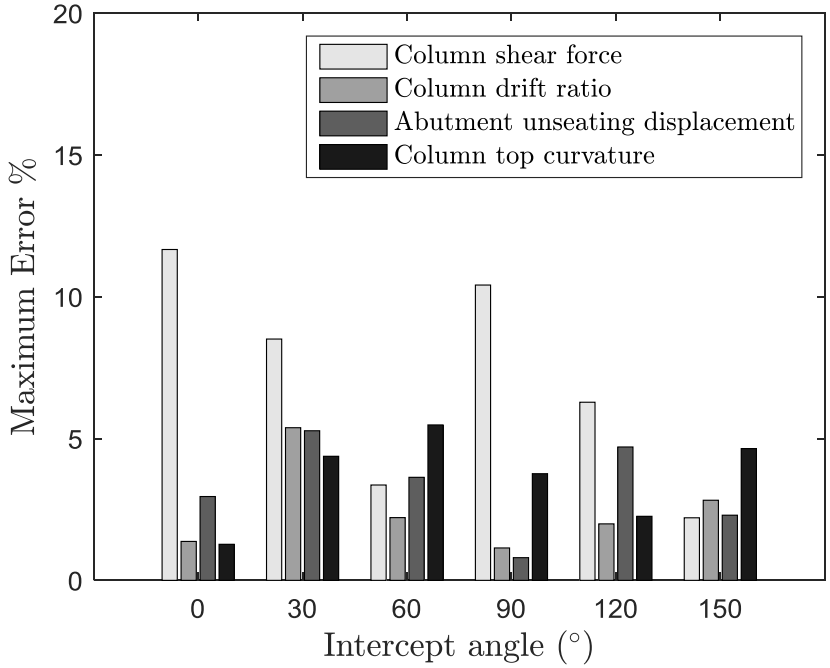

a) Type I abutment modeling

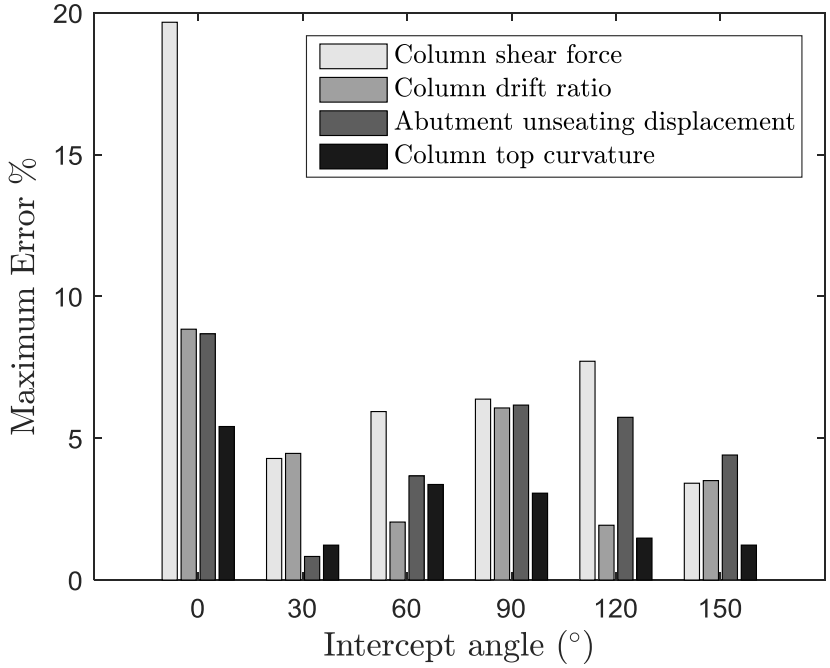

b) Type II abutment modeling

Figure 9.10 Maximum errors of different intercept angles for Bridge A.

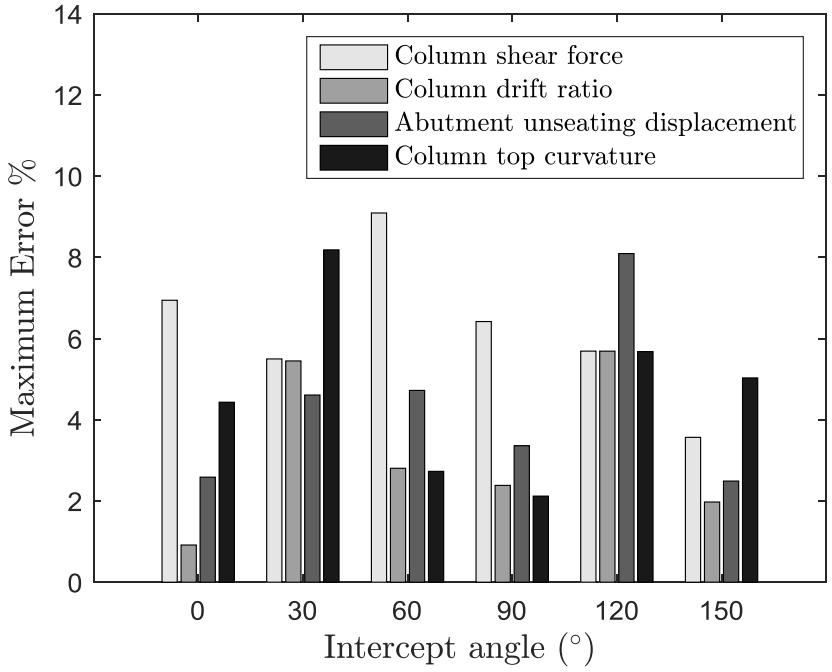

a) Type I abutment modeling

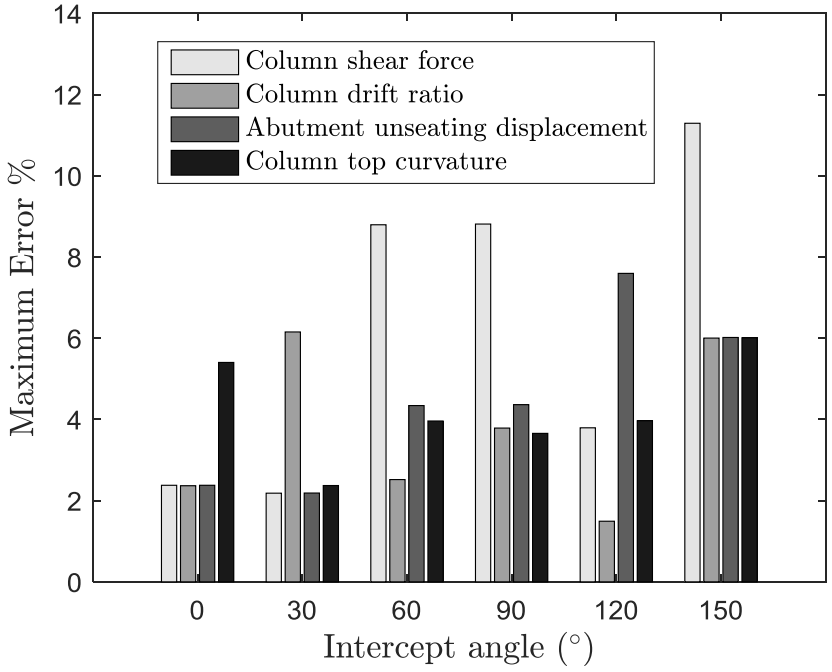

b) Type II abutment modeling

Figure 9.11 Maximum errors of different intercept angles for Bridge B.

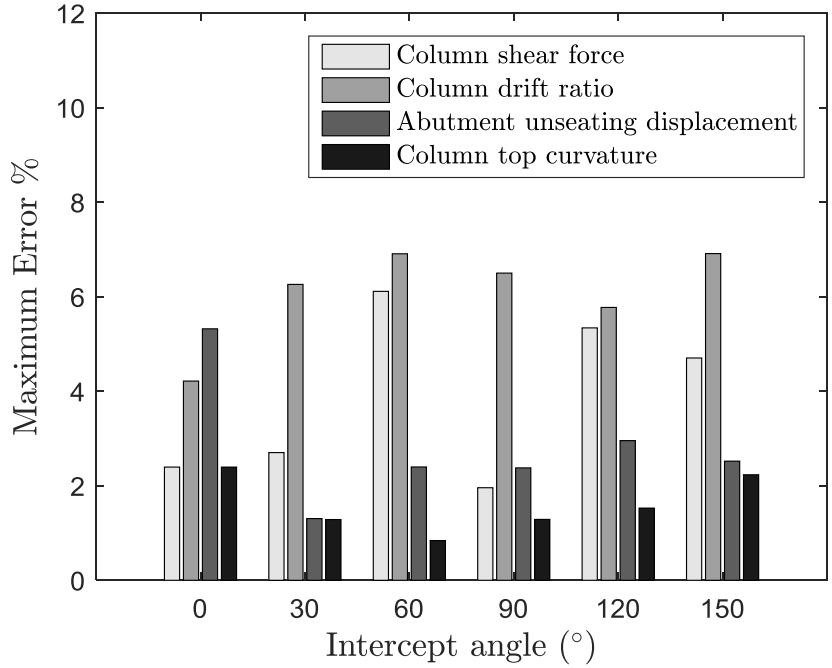

a) Type I abutment modeling

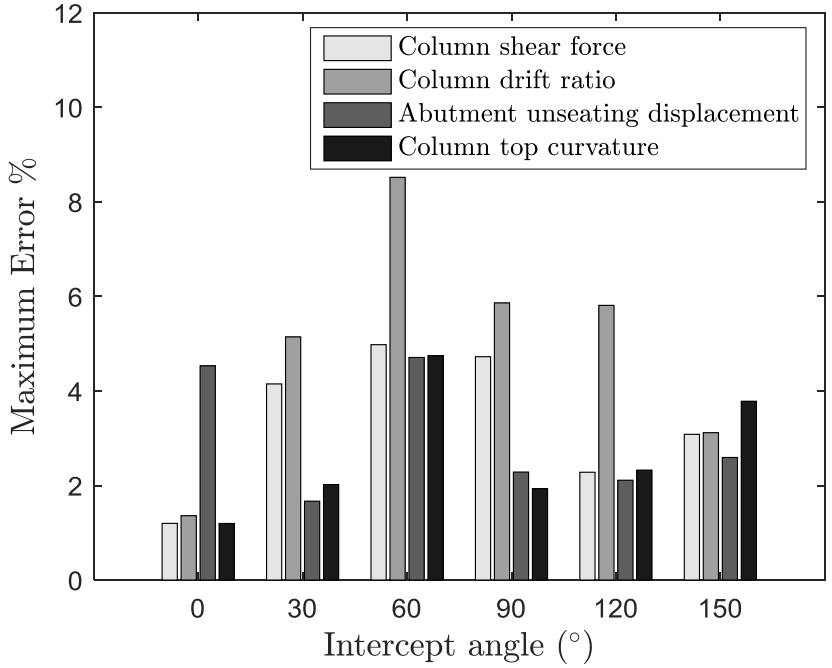

b) Type II abutment modeling

Figure 9.12 Maximum errors of different intercept angles for Bridge C.

9.4 GMSM PROCEDURES

Three GMSM procedures from the two categories previously mentioned in Chapter 6 are investigated in this study. The first is an amplitude scaling procedure using the conventional first

mode spectral acceleration, i.e., $S_a(T_1)$, selection and scaling method. The other two, namely the conditional mean spectrum (*CMS*) and the unconditional selection (*US*) methods, are spectrum shape matching procedures. The following sub-sections describe these three methods and their selection procedures, as considered in this study, in detail.

9.4.1 $S_a(T_1)$ Selection and Scaling Method

This method selects GM records from earthquakes with magnitude *M* and type of faulting *F*, recorded at sites with distance *R* and soil classification *S* as close as possible to those of the earthquake scenario of interest. After applying the selection criteria, the GMs are selected randomly from the candidate set of motions if the number of eligible ground motions is larger than the target number; otherwise, the selection criteria would need to be relaxed.

Once the GMs are selected, each of them is scaled in amplitude such that its $S_a(T_1)$ is equal to the target $S_a(T_1)$ of the earthquake scenario. This procedure to select and scale GMs does not take into account the shape or the variability of the target response spectrum, as it considers only the target $S_a(T_1)$. The selection procedure of $S_a(T_1)$ scaling method is summarized below:

1. Select the GM based on an *M*-*R*-*S*-*F* (magnitude, source-to-site distance, site classification and type of faulting) bin that is consistent with the given earthquake scenario. The criteria utilized in this GMSM procedure are:
   i. $6.6 \le M \le 7.4$;
   ii. $5.0\ km < R \le 15.0\ km$;
   iii. $V_{s30} \ge 183\ m/s$;
   iv. Lowest usable frequency = 0.25 Hz;
   v. Faulting: Not constrained.
2. Scale each component of record to the target GM level based on their geometric mean as given by Eq. (9.14). The target $S_a(T_1)$ is the median $+ 1.5\varepsilon$ predicted by the attenuation model from [Campbell and Bozorgnia 2008] for the given *M*, *R*, *S* and *F* scenario.

$$SF_i = \frac{S_a(T_1)_{\text{Target}}}{\sqrt{[S_a(T_1)]_1^i \cdot [S_a(T_1)]_2^i}} \tag{9.14}$$

   where SF_i is the scaling factor of the *i*-th GM pair of components with subscripts 1 and 2 and having the same scaling factor.
3. Select desired number of records from the bin. In this study, 40 records are selected, which are determined by the following two algorithms:
   i. Based on the equation for the proportion of pulse-like records [Hayden et al. 2012],

$$\text{Proportion of pulse motions} = \frac{\exp\left(0.891 - 0.188R + 1.230\varepsilon\right)}{1 + \exp\left(0.891 - 0.188R + 1.230\varepsilon\right)} \tag{9.15}$$

substitution of R = 10 km and $\varepsilon = 1.5$ in Eq. (9.15) results in the value of proportion = 0.7. Thus, 28 of the 40 motions should be pulse-type. Select 28 records from the pulse-type bin and 12 records from the no pulse-type bin with smallest scaling factors from step 2. This procedure is denoted as $S_a(T_1)_p$ method in this dissertation.

ii. Another algorithm is to select 40 records solely based on the scaling factors. Thus, 40 records with smallest scaling factors are selected from the bin with both pulse-type and no pulse-type GMs. This procedure is called $S_a(T_1)$ method in this dissertation.

9.4.2 Conditional Mean Spectrum (*CMS*) Method

This method selects GMs such that their response spectra match the mean and variance of the *CMS* in the period range of interest. The method consists of two stages: (1) Determination of the *CMS* and (2) application of the GM selection algorithm for matching a target response spectrum mean and variance proposed by [Jayaram et al. 2011]. The *CMS* is a response spectrum associated with a target S_a value at a single period, i.e., $S_a(T_1)$ in this study. According to [Baker 2011], the steps for computing this response spectrum are:

1. Determine the target S_a at a given period of interest T_1, $S_a(T_1)$, for the associated M, R and ε. Similar to the previous GMSM method, the target $S_a(T_1)$ is computed as the median $+1.5\varepsilon$ predicted by the attenuation model from (Campbell and Bozorgnia 2008). The M, R and ε are those of the previously defined target GM scenario, i.e., M = 7.0, R = 10 *km* and $\varepsilon = 1.5$. Given an arbitrary period, T, ε is defined as the number of standard deviations by which the natural logarithm of $S_a(T)$, i.e., $\ln(S_a(T))$, differs from the predicted mean of $\ln(S_a(T))$ for a given M and R. ε is defined as follows:

$$\varepsilon(T) = \left[\ln(S_a(T)) - \mu_{\ln(S_a)}(M,R,T)\right] / \sigma_{\ln(S_a)}(M,R,T) \tag{9.16}$$

where $\mu_{\ln(S_a)}(M,R,T)$ and $\sigma_{\ln(S_a)}(M,R,T)$ are the predicted mean and standard deviation of $\ln\left(S_a(T)\right)$, respectively, computed from (Campbell and Bozorgnia 2008). From Eq. (9.16), the target $\ln\left(S_a(T_1)\right)$ can be expressed as follows:

$$\ln(S_a(T_1)) = \varepsilon(T_1)\sigma_{\ln(S_a)}(M,R,T_1) + \mu_{\ln(S_a)}(M,R,T_1) \tag{9.17}$$

2. Compute the mean and standard deviation of the response spectrum at other periods, given M and R. They are the quantities in Step 1, i.e., $\mu_{\ln(S_a)}(M,R,T)$ and $\sigma_{\ln(S_a)}(M,R,T)$, respectively. In this step, these values are computed at periods included in the range of interest. Existing GM models, such as the attenuation model from [Campbell and Bozorgnia 2008] used in this study, can be used to compute these terms.

3. Compute ε at other periods, given $\varepsilon(T_1)$. This step consists of computing conditional mean ε-values, $\mu_{\varepsilon(T_i)|\varepsilon(T_1)}$, for the other periods T_i, which can be calculated as the product of $\varepsilon(T_1)$ and the correlation coefficient between the ε-values at the two periods $\rho(T_i,T_1)$, i.e.,

$$\mu_{\varepsilon(T_i)|\varepsilon(T_1)} = \rho(T_i,T_1)\varepsilon(T_1) \tag{9.17}$$

According to [Baker 2011], the following simple predictive equation, valid for periods between 0.05 and 5.0 sec. can be used to obtain $\rho(T_i,T_1)$:

$$\rho(T_{\min},T_{\max}) = 1-\cos\left[\frac{\pi}{2}-\left(0.359+0.163I_{(T_{\min}<0.189)}\ln\left(\frac{T_{\min}}{0.189}\right)\right)\ln\left(\frac{T_{\max}}{T_{\min}}\right)\right] \tag{9.18}$$

where $I_{(T_{\min}<0.189)}$ is an indicator function that equals 1.0 if $T_{\min}<0.189$ sec and 0.0 otherwise, and $T_{\min}$ and $T_{\max}$ are respectively smaller and larger periods of interest.

4. Compute *CMS*. At each period of interest, T_i, the corresponding spectral accelerations that define the *CMS* can be computed by substituting Eq. (9.17) in place of $\varepsilon(T_1)$ in Eq. (9.16) after replacing T_1 with T_i of both sides, i.e.,

$$\mu_{\ln(S_a(T_i))|\ln(S_a(T_1))} = \mu_{\ln(S_a)}(M,R,T_i) + \rho(T_i,T_1)\varepsilon(T_1)\sigma_{\ln(S_a)}(M,R,T_i) \tag{9.19}$$

where $\mu_{\ln(S_a)}(M,R,T_i)$ and $\sigma_{\ln(S_a)}(M,R,T_i)$ are derived from [Campbell and Bozorgnia 2008], $\rho(T_i,T_1)$ is computed from Eq. (27), and values of *M*, *R* and $\varepsilon(T_1)$ are those indicated in Step 1.

As mentioned earlier, once the *CMS* associated with a period of interest is determined, the GM selection algorithm proposed by Jayaram et al. (2011) is used to select and modify sets of records that match the target *CMS* and its variance. With a target distribution, Monte Carlo simulation is used to probabilistically generate multiple realizations of response spectra, and then GM records whose response spectra individually match the simulated response spectra are selected. Furthermore, a greedy optimization is applied to improve the match between the target and the sample means and variances. This is performed by replacing one previously selected GM record at a time with a record from the database that generates the best improvement in the match. A detailed explanation of this method can be found in [Jayaram et al. 2011]. Similar to the $S_a(T_1)$ scaling method, 40 records are considered herein.

9.4.3 Unconditional Selection (*US*) Method

This method uses exactly the same algorithm for matching both the mean and variance of the target spectrum mentioned in the previous section. However, instead of the *CMS* used in the *CMS* method, the median $+1.5\varepsilon$ spectrum associated with the selected earthquake scenario defined with the attenuation model by [Campbell and Bozorgnia 2008] is used as the target spectrum. Similar to the first two methods, 40 GM records are selected herein. All the GMs selected from these investigated GMSM procedures for the three selected bridges are documented in Appendix F.

9.5 EVALUATION OF THE GMSM PROCEDURES

For each bridge with each abutment modeling, 40 GM records are selected for each investigated GMSM procedure, including two versions of $S_a(T_1)$ scaling and selection method, i.e. a total of four GMSM procedures. Similar to the development of the reference benchmark *PDSD*, these GMs are applied to each bridge with six different intercept angles. Thus, besides the 21,600 NTHA simulations for the development of the benchmark *PDSD*, 40×4×3×2×6=5,760 more NTHA analyses are performed for all the four GMSM procedures.

The *PDSD* estimates by the 40 GM records from each GMSM investigated procedures are compared against the benchmark *PDSD* to evaluate their accuracy and reliability. Based on Eq. (6.19), $\Pr(\mathrm{C})$ in Eq. (6.18) is the probability of collapse estimated as:

$$\hat{\Pr}(\mathrm{C}) = \frac{\#\text{ of records causing collapse}}{40} \tag{9.20}$$

The probability of exceedance for the NC cases, i.e., $G(edp \mid \mathrm{NC})$ in Eq. (6.18), can be estimated by Eq. (6.20). Recall the previously discussed collapse criterion, along with the estimates in Eqs. (6.20) and (9.20), the *PDSD* estimate, i.e., $\hat{G}(edp)$, is obtained as follows:

$$\hat{G}(edp) = \int_{\overline{dr}} \left\{ \hat{\Pr}(\mathrm{C}) + \hat{G}(edp \mid \mathrm{NC}) \times \left[1 - \hat{\Pr}(\mathrm{C}) \right] \right\} \hat{f}_{\overline{DR}}(\overline{dr}) d\overline{dr} \tag{9.21}$$

Following similar procedure from Eqs. (9.10) and (9.11), $\hat{G}(edp)$ in Eq. (9.21) is computed from the following discretized form:

$$\hat{G}(edp) \cong \sum_i \{ \hat{\Pr}(\mathrm{C}_i) + \hat{G}(edp \mid \mathrm{NC}_i) \times [1 - \hat{\Pr}(\mathrm{C}_i)] \} \hat{\Pr}(\overline{dr}_i) \tag{9.22}$$

where $\hat{\Pr}(\mathrm{C}_i)$ and $\hat{G}(edp \mid \mathrm{NC}_i)$ are respectively the estimated probabilities of collapse and exceedance in the NC cases when $dr = \overline{dr}_i$, and $\hat{\Pr}(\overline{dr}_i)$ is estimated by Eq. (9.12a). Figures 9.13-9.44 present the comparison of the *PDSD* estimates from the four investigated GMSM procedures and the benchmark *PDSD*. Such comparisons are given for all four selected *EDP*s of the six different intercept angles on Bridges A and B with both Types I and II abutment modeling. Figures 9.45-9.48 show the *PDSD* estimates of the peak column drift ratio from the four GMSM procedures on Bridge C with Types I and II abutment modeling. As mentioned previously, comparing to the difference of the *PDSD* estimated by the 600 GMs, larger differences, e.g., from Figures 9.21-9.28, are observed in the *PDSD* estimates from the different intercept angles.

It is observed from Figures 9.13-9.20 that the *PDSD* estimates from the $S_a(T_1)$ and $S_a(T_1)_p$ procedures generally underestimate the seismic demands from the benchmark *PDSD* for Bridge A with both abutment modeling. However, the $S_a(T_1)_p$ method gives reasonably accurate *PDSD* estimates of the three global *EDP*s, i.e., peak column shear force (Figure 9.17a), drift ratio (9.18a), and abutment unseating displacement (9.19a), for Bridge A with Type I abutment modeling. In general, e.g., from the comparison of Figures 9.29-9.32 and 9.33-9.36, the *PDSD* estimates from

the $S_a(T_1)_p$ procedure are larger and more accurate than the ones estimated from the $S_a(T_1)$ procedure. Such observations are attributed to the fact that more pulse motions that result in large responses are selected in the $S_a(T_1)_p$ procedure. From Figures 9.21-9.24 and 9.37-9.40, the *PDSD* estimates from the *CMS* method almost always underestimate the seismic demands of all four *EDP*s, especially on the large values of *EDP*s (the tail of the *PDSD* curve), for Bridges A and B with both abutment modeling. In contrast, as shown in Figures 9.25-9.28 and 9.41-9.44, the *PDSD* estimates by the *US* method are almost always on the conservative side with approximately 10-20% overestimation of the probability of exceedance over the benchmark *PDSD*. For bridge C, all four GMSM procedures overestimates the seismic demands of all four investigated *EDP*s (only the peak column drift ratio is shown in Figures 9.45-9.48 for brevity) for both Type I (Figures 9.45 and 9.46) and Type II (Figures 9.47 and 9.48) abutment modeling. It is observed from Figures 9.13-9.48 that the *PDSD* estimates by the first mode GMSM procedures, i.e., *CMS*, $S_a(T_1)$ and $S_a(T_1)_p$ methods, generally underestimate the benchmark *PDSD* for Bridges A and B, and overestimate the benchmark *PDSD* for bridges C. Also, the overestimations of *PDSD* by *US* method for bridges A, B and C are about 10%, 20% and 25%, respectively. Among these three investigated RC highway bridges, it can be concluded that the effects of higher modes are most pronounced on Bridge A, a bridge with two spans supported on a single-column bent, and are the least on Bridge C, a bridge with three spans and two three-column bents.

Based on the simulation results, the estimates by the *US* procedure are almost always on the conservative side and are usually the most conservative of all GMSM procedures for all three bridges. The $S_a(T_1)$ and $S_a(T_1)_p$ procedures show some superiority over the *CMS* method (e.g., in predicting the *PDSD* for bridges A and B); while they sometimes underestimate the responses, e.g., in bridge A. As discussed previously, RC highway bridges play a crucial role in transportation and thus require short downtime after severe earthquakes from an emergency response and, more generally, community resiliency points of view. Therefore, among these four investigated GMSM procedures, it is suggested to use the *US* method for the selection and modification of GMs.

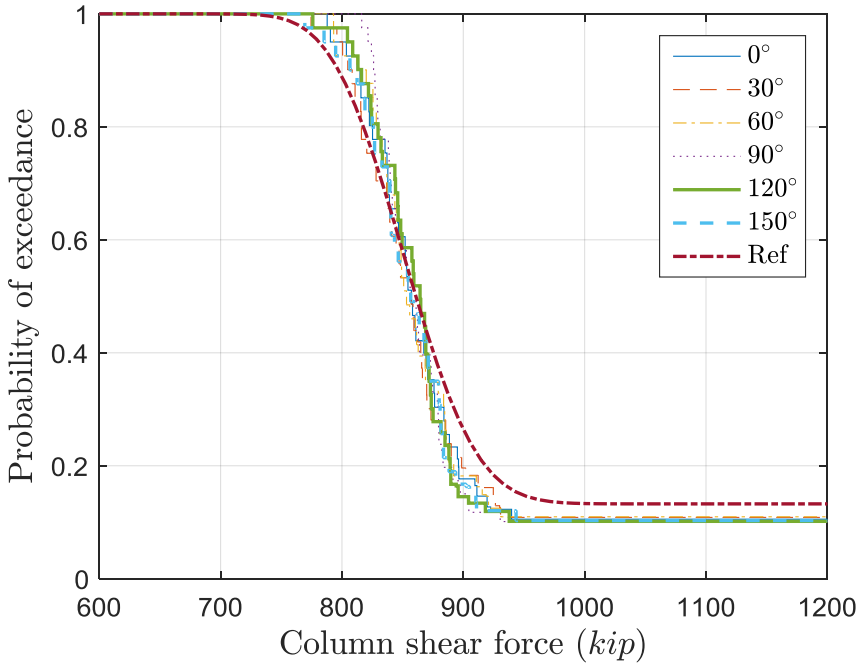

a) Type I abutment modeling

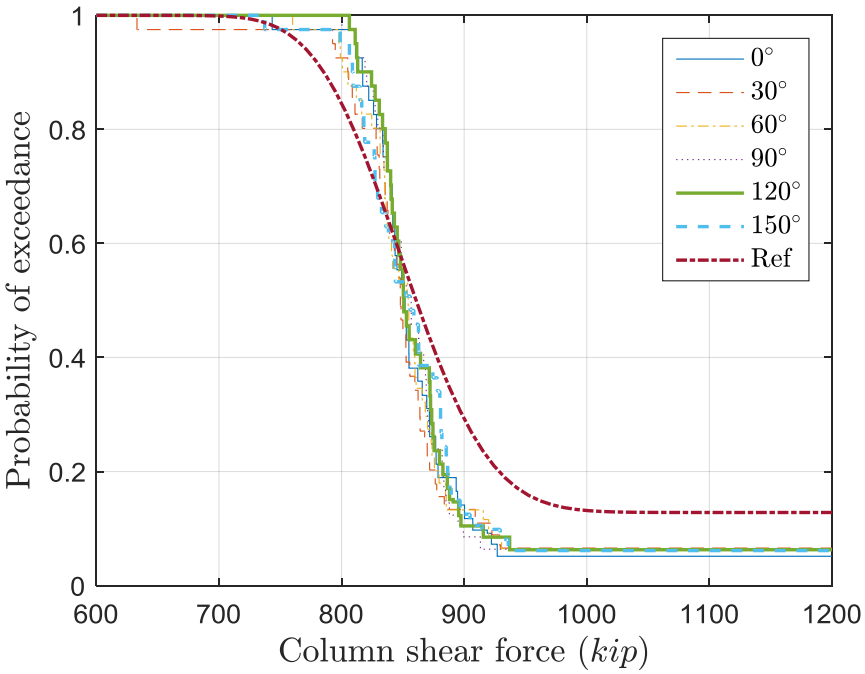

b) Type II abutment modeling

Figure 9.13 *PDSD* estimates of column shear force of different intercept angles from $S_a(T_1)$ procedure for Bridge A.

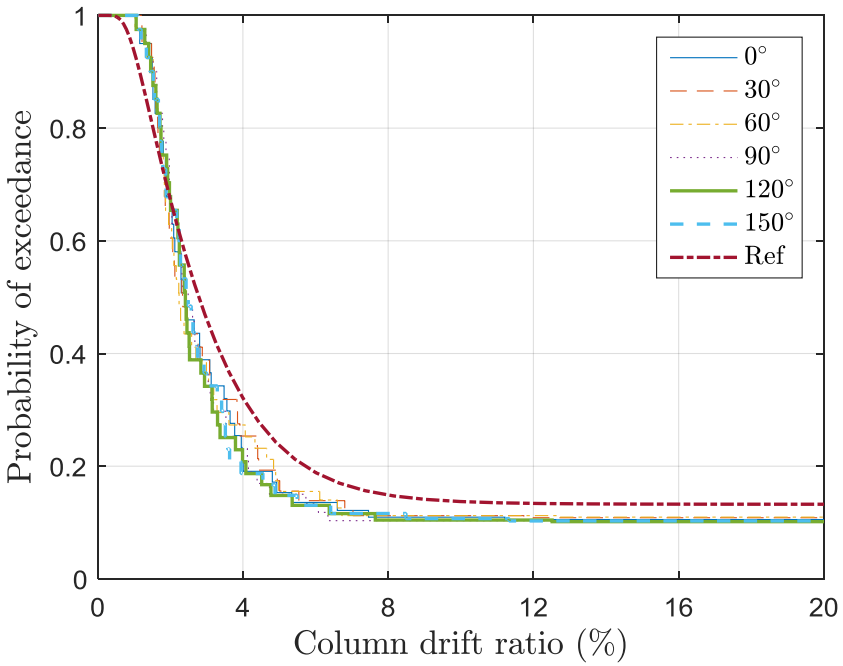

a) Type I abutment modeling

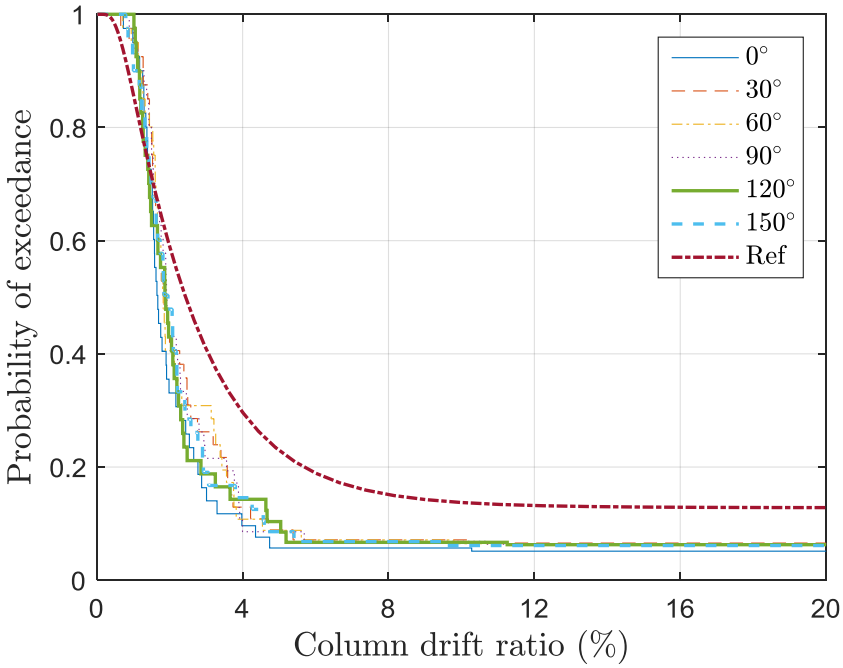

b) Type II abutment modeling

Figure 9.14 *PDSD* estimates of column drift ratio of different intercept angles from $S_a(T_1)$ procedure for Bridge A.

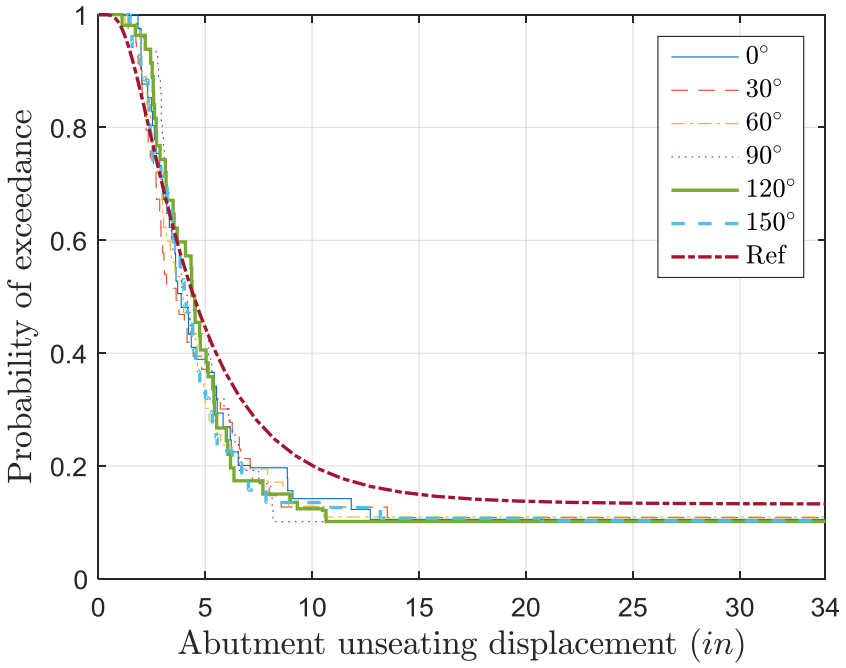

a) Type I abutment modeling

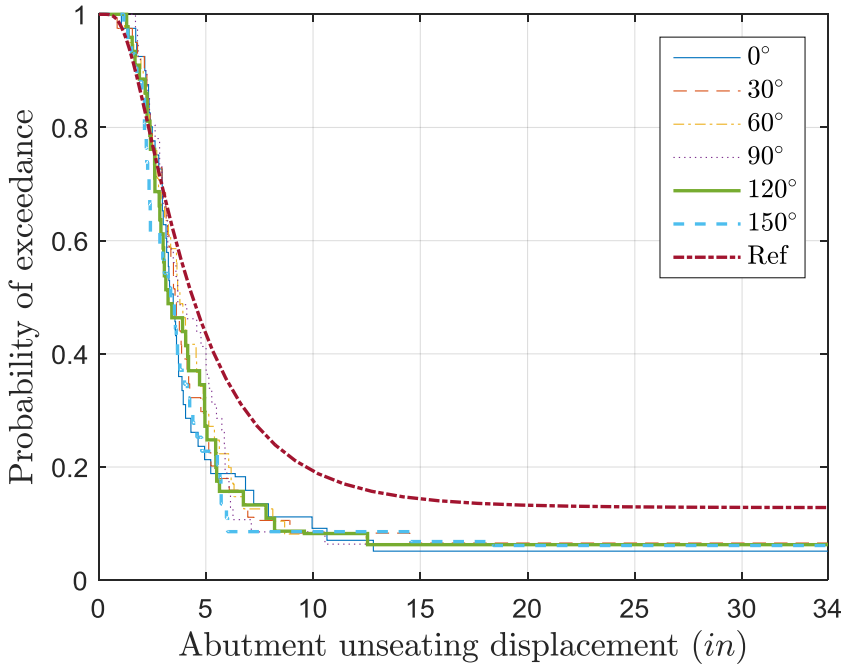

b) Type II abutment modeling

Figure 9.15 *PDSD* estimates of abutment unseating displacement of different intercept angles from $S_a(T_1)$ procedure of for Bridge A.

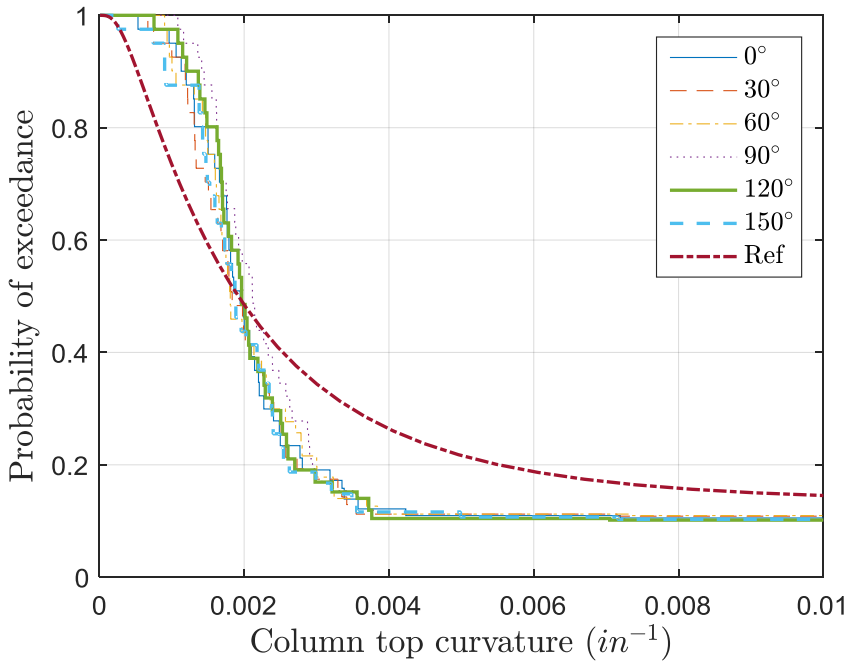

a) Type I abutment modeling

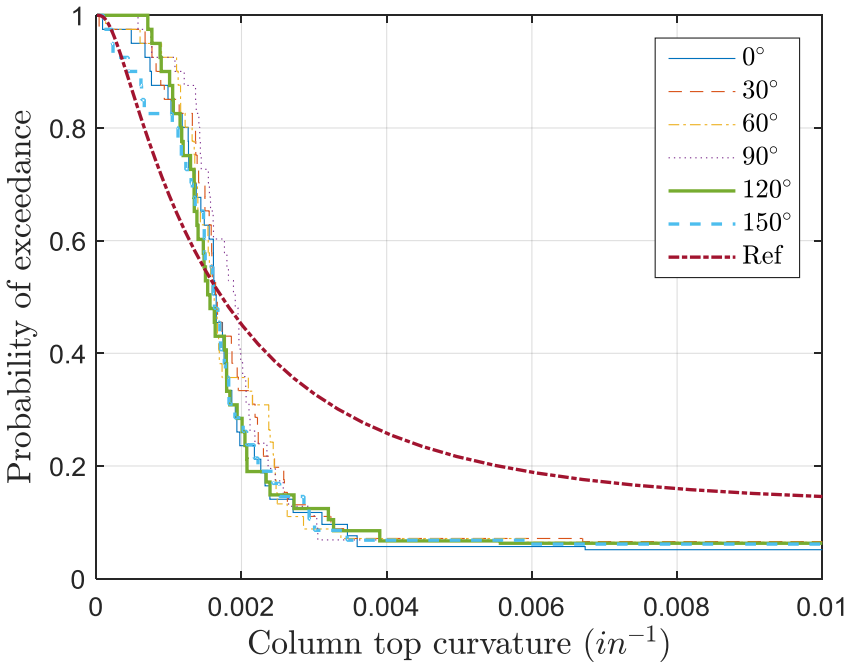

b) Type II abutment modeling

Figure 9.16 *PDSD* estimates of column top curvature of different intercept angles from $S_a(T_1)$ procedure for Bridge A.

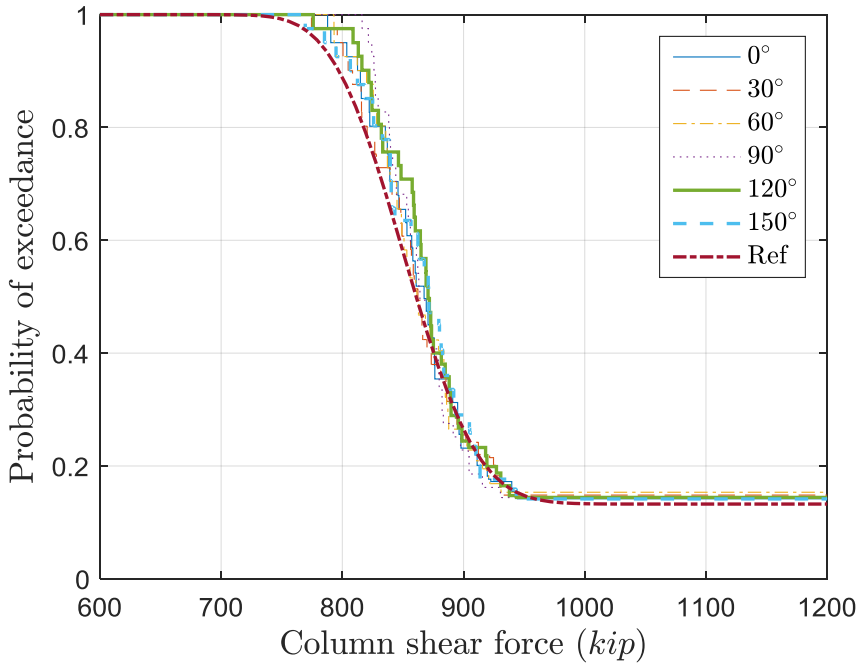

a) Type I abutment modeling

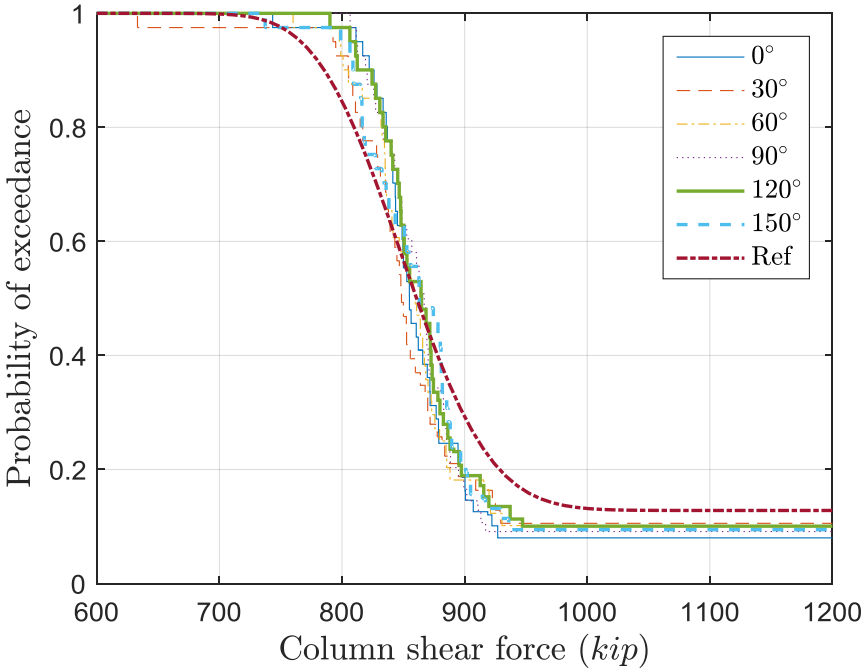

b) Type II abutment modeling

Figure 9.17 *PDSD* estimates of column shear force of different intercept angles from $S_a(T_1)_p$ procedure for Bridge A.

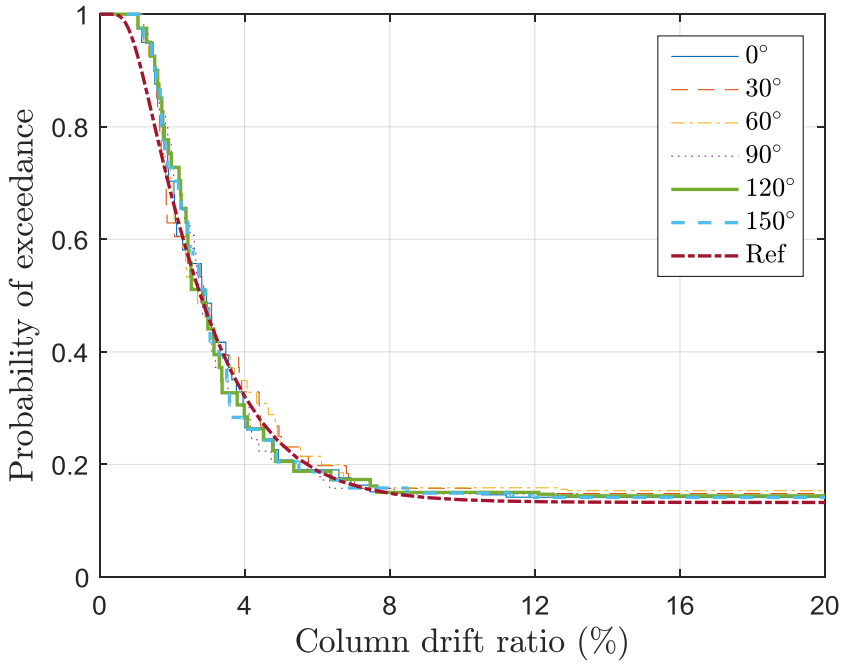

a) Type I abutment modeling

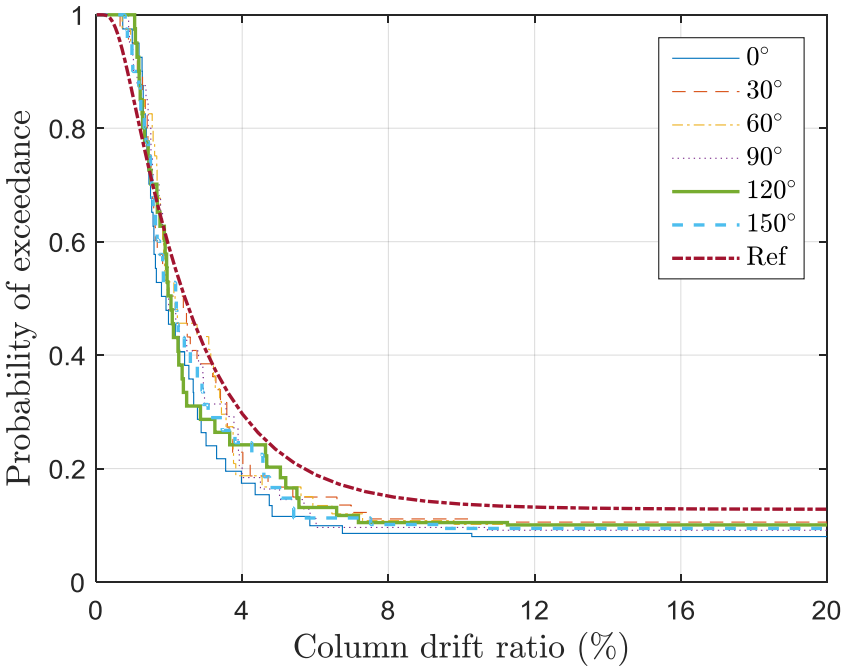

b) Type II abutment modeling

Figure 9.18 *PDSD* estimates of column drift ratio of different intercept angles from $S_a(T_1)_p$ procedure for Bridge A.

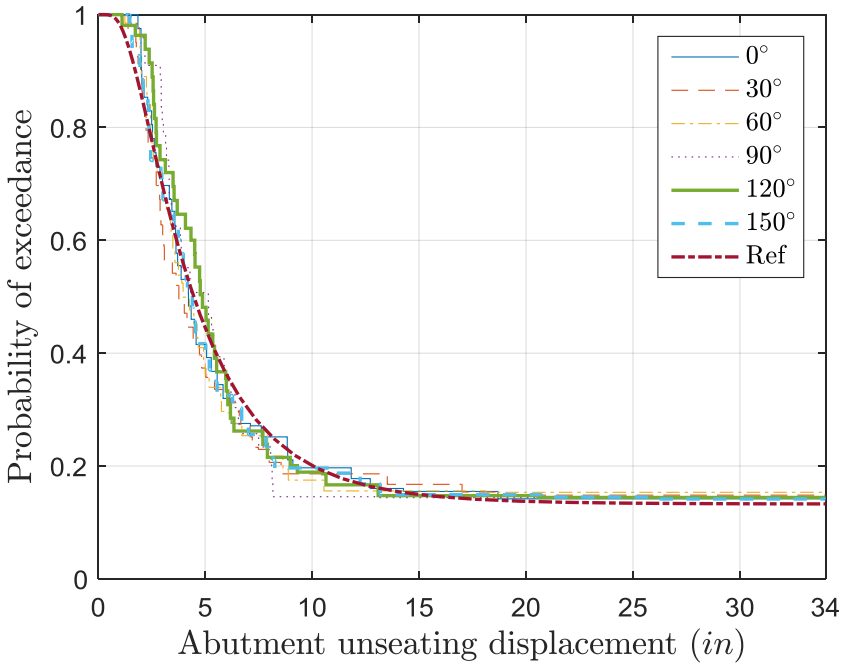

a) Type I abutment modeling

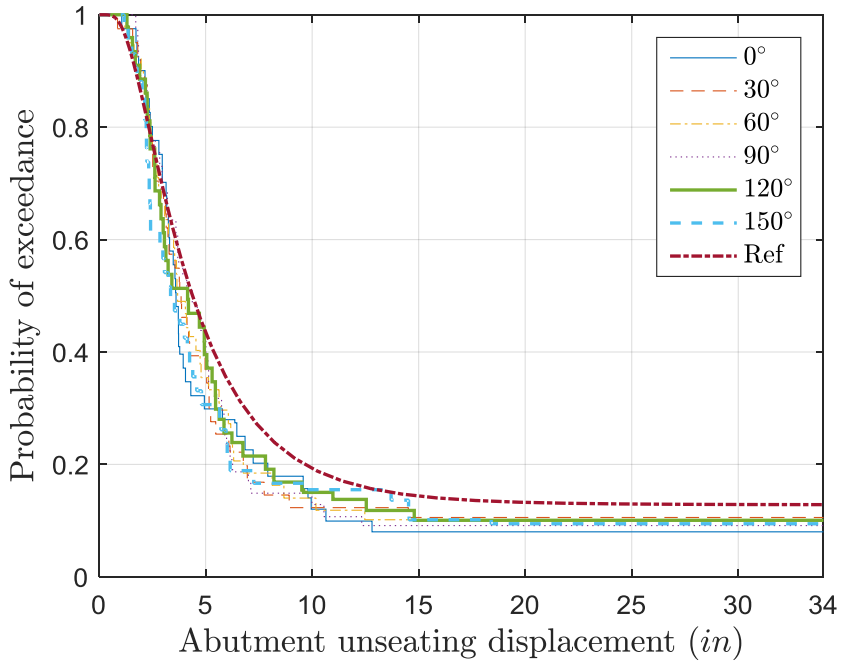

b) Type II abutment modeling

Figure 9.19 *PDSD* estimates of abutment unseating displacement of different intercept angles from $S_a(T_1)_p$ procedure for Bridge A.

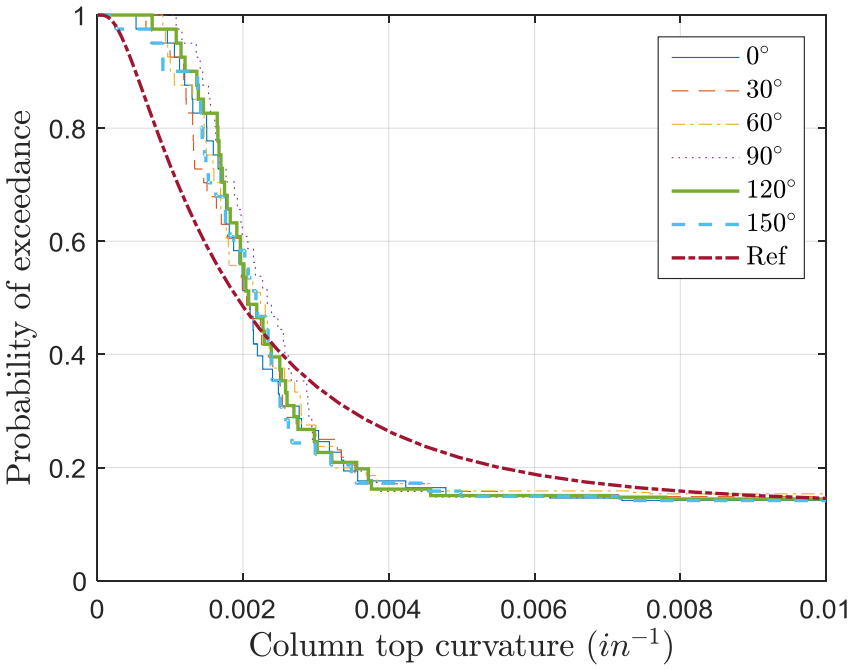

a) Type I abutment modeling

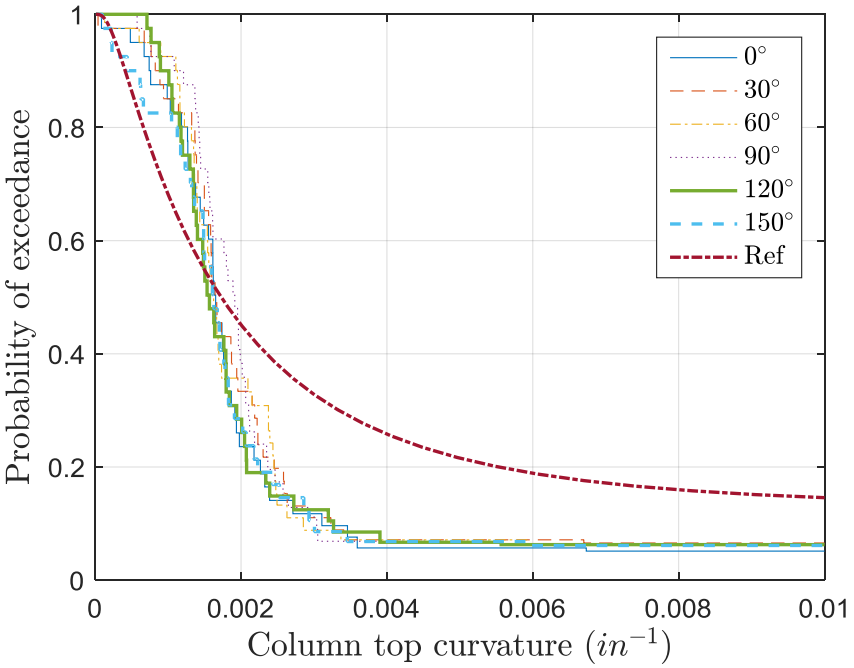

b) Type II abutment modeling

Figure 9.20 *PDSD* estimates of column top curvature of different intercept angles from $S_a(T_1)_p$ procedure for Bridge A.

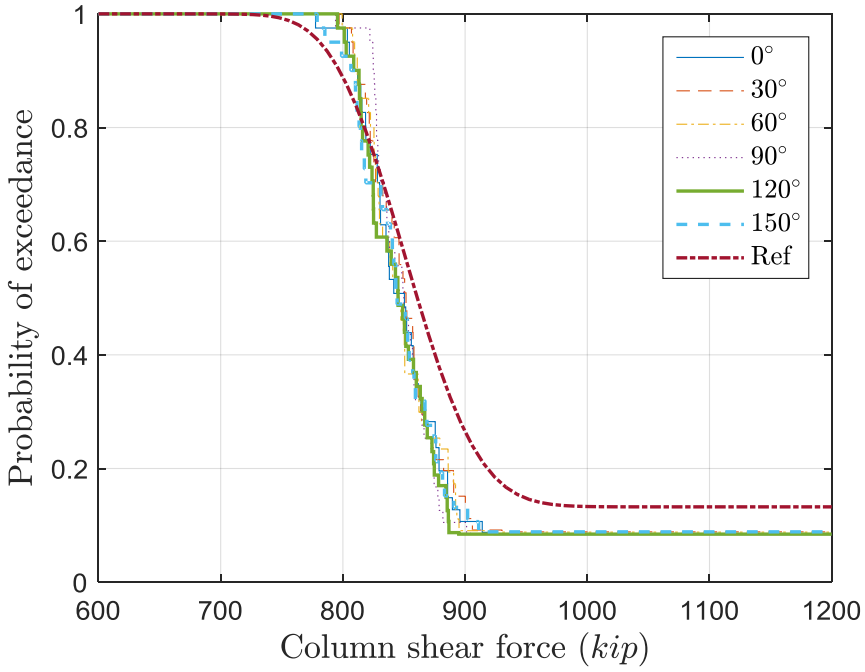

a) Type I abutment modeling

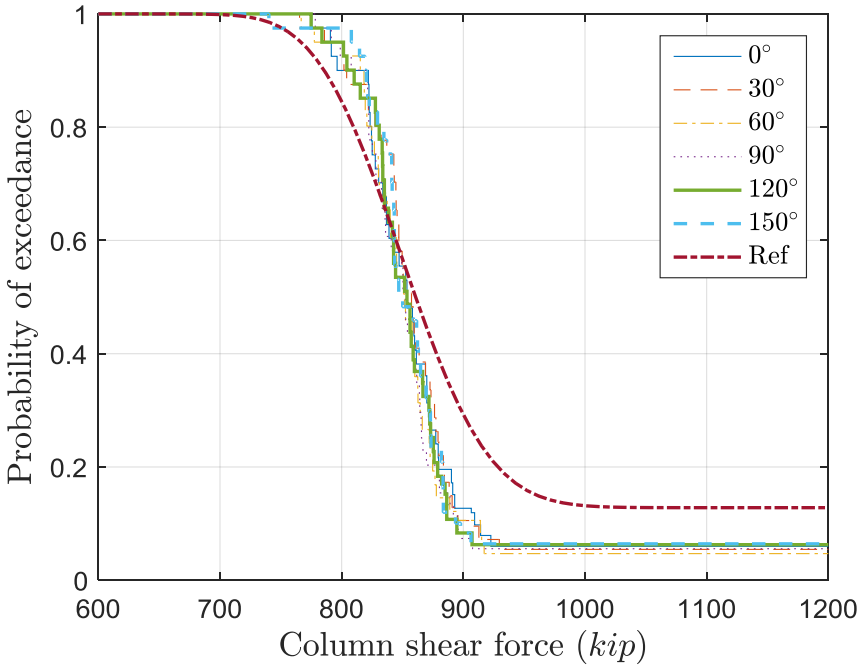

b) Type II abutment modeling

Figure 9.21 *PDSD* estimates of column shear force of different intercept angles from *CMS* procedure for Bridge A.

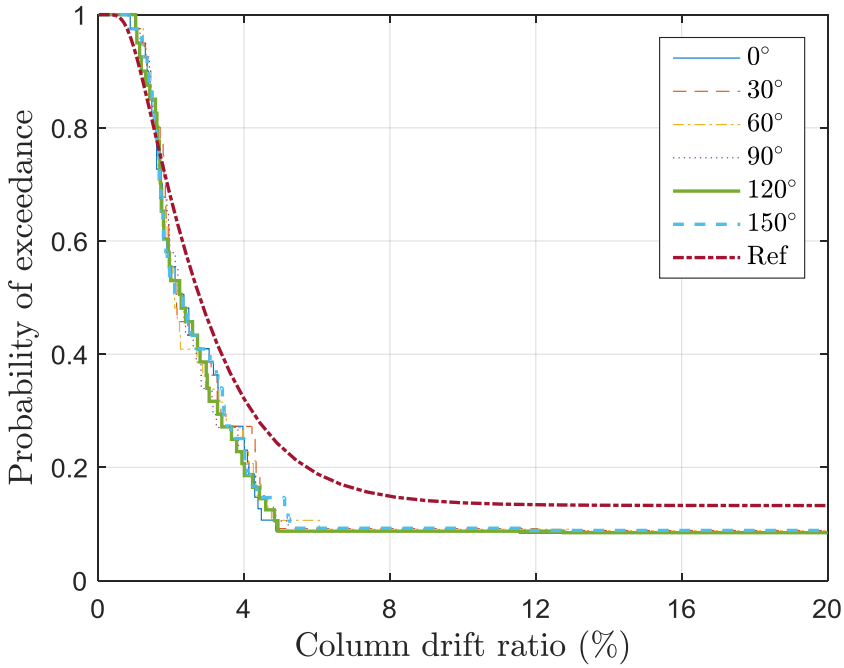

a) Type I abutment modeling

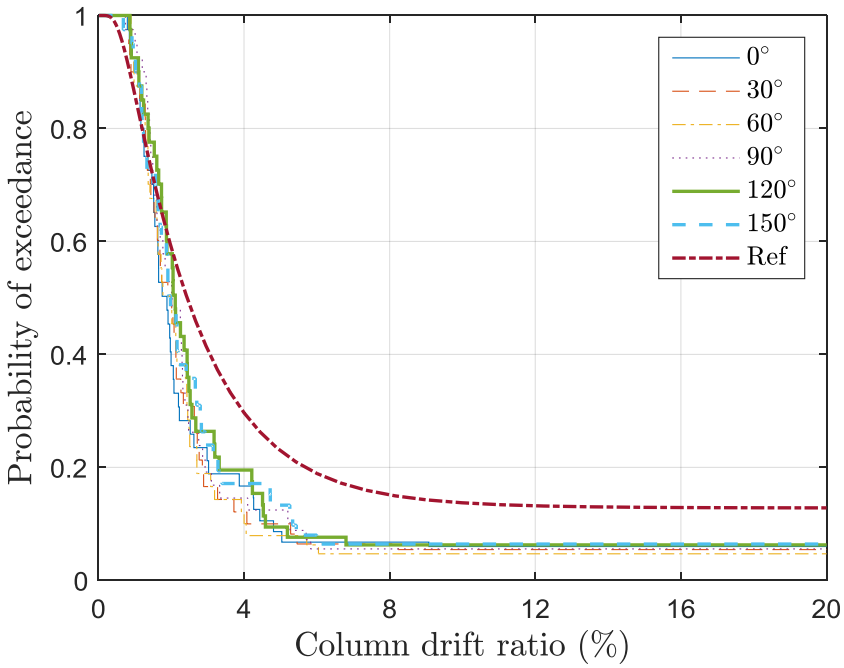

b) Type II abutment modeling

Figure 9.22 *PDSD* estimates of column drift ratio of different intercept angles from *CMS* procedure for Bridge A.

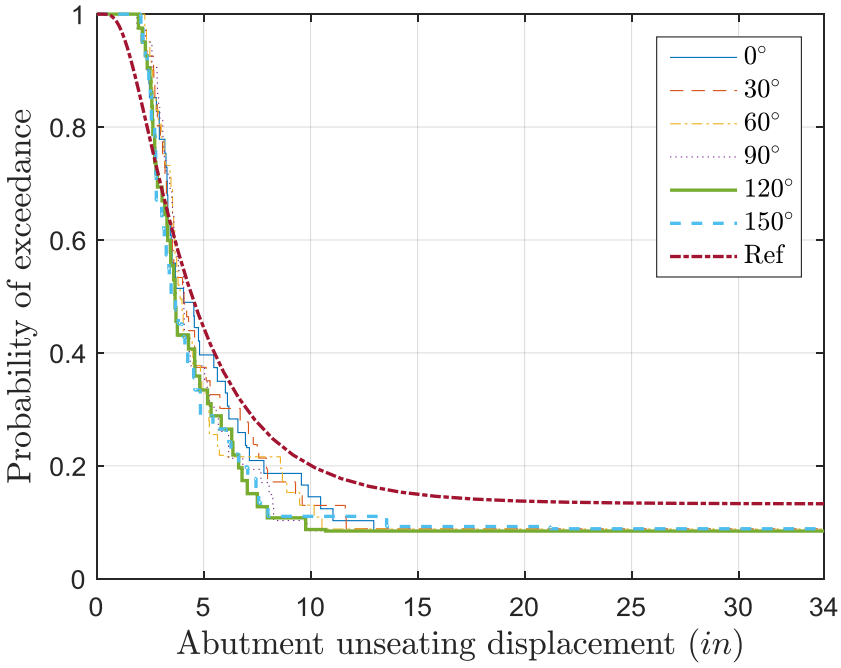

a) Type I abutment modeling

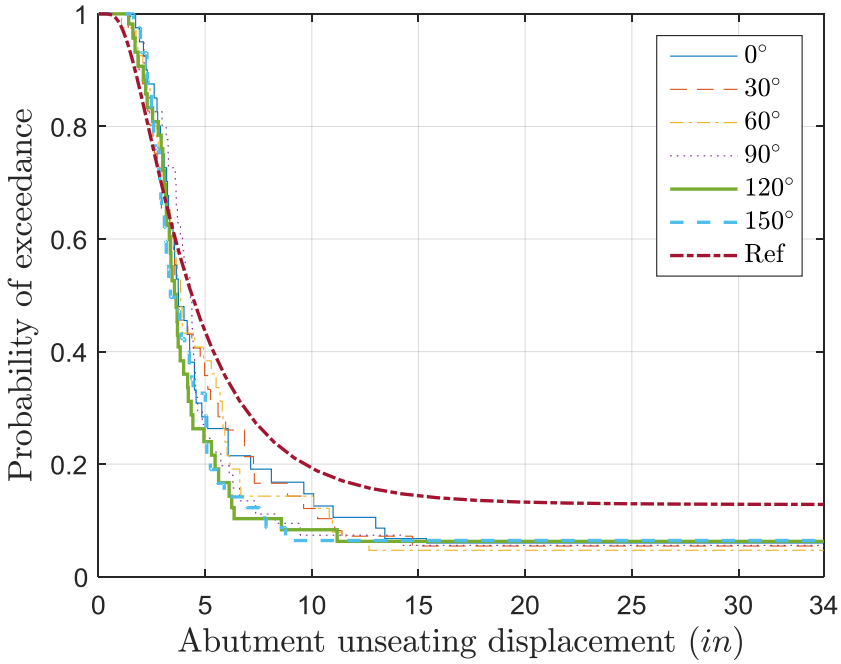

b) Type II abutment modeling

Figure 9.23 *PDSD* estimates of abutment unseating displacement of different intercept angles from *CMS* procedure for Bridge A.

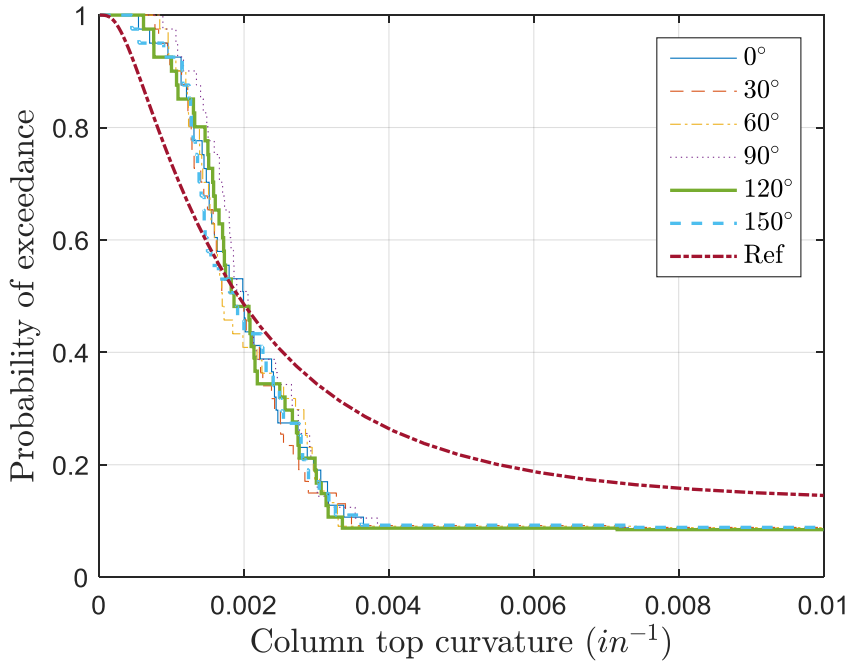

a) Type I abutment modeling

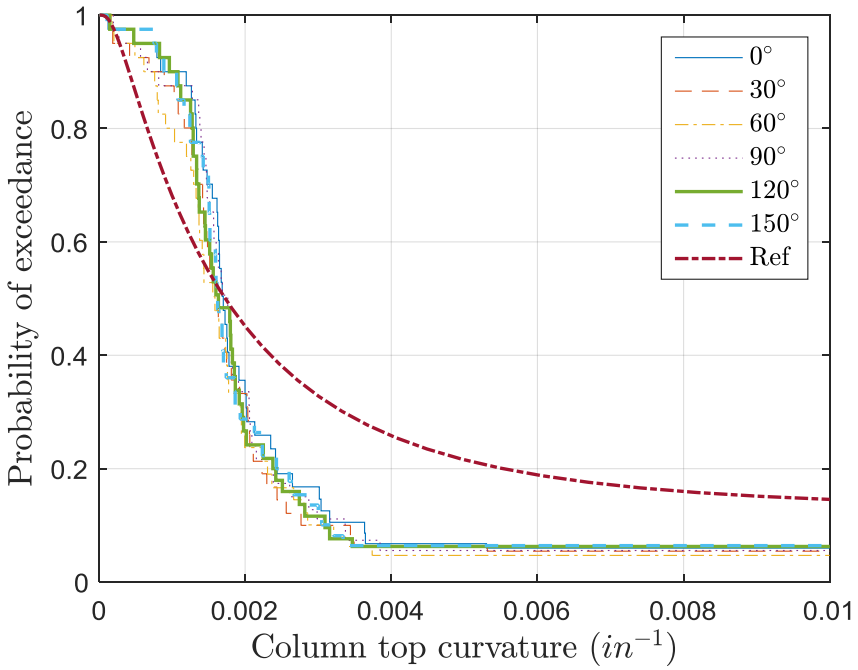

b) Type II abutment modeling

Figure 9.24 *PDSD* estimates of column top curvature of different intercept angles from *CMS* procedure for Bridge A.

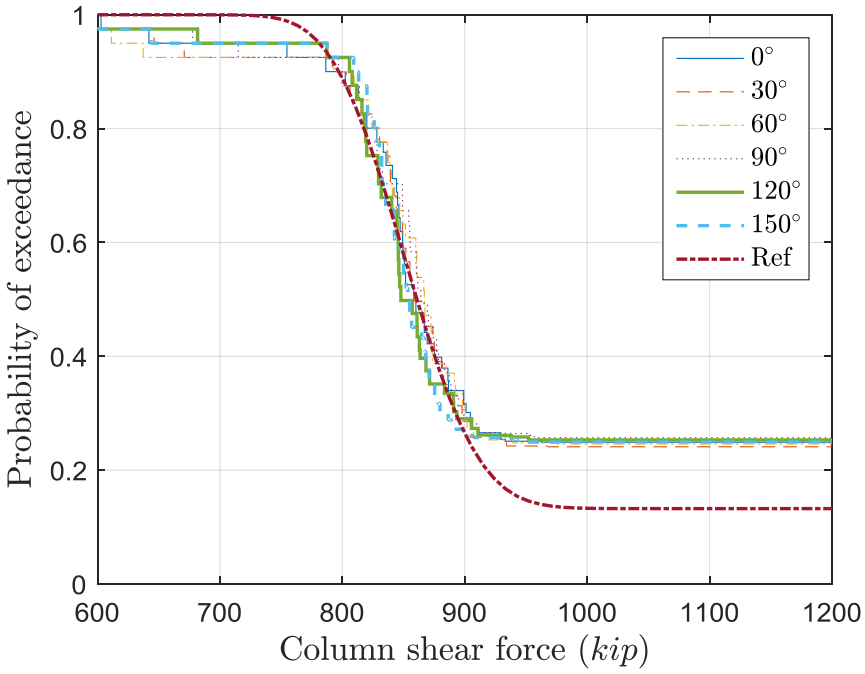

a) Type I abutment modeling

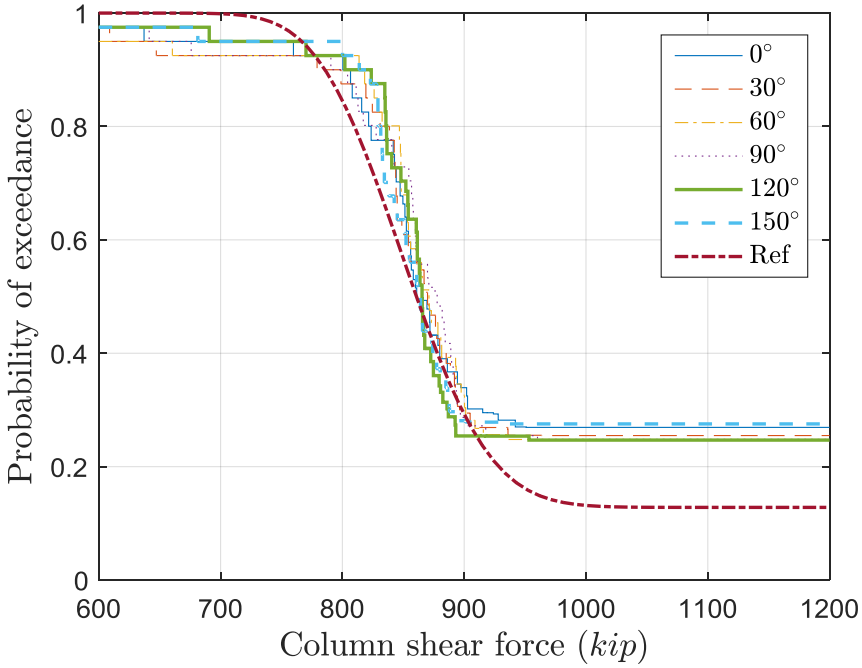

b) Type II abutment modeling

Figure 9.25 *PDSD* estimates of column shear force of different intercept angles from *US* procedure for Bridge A.

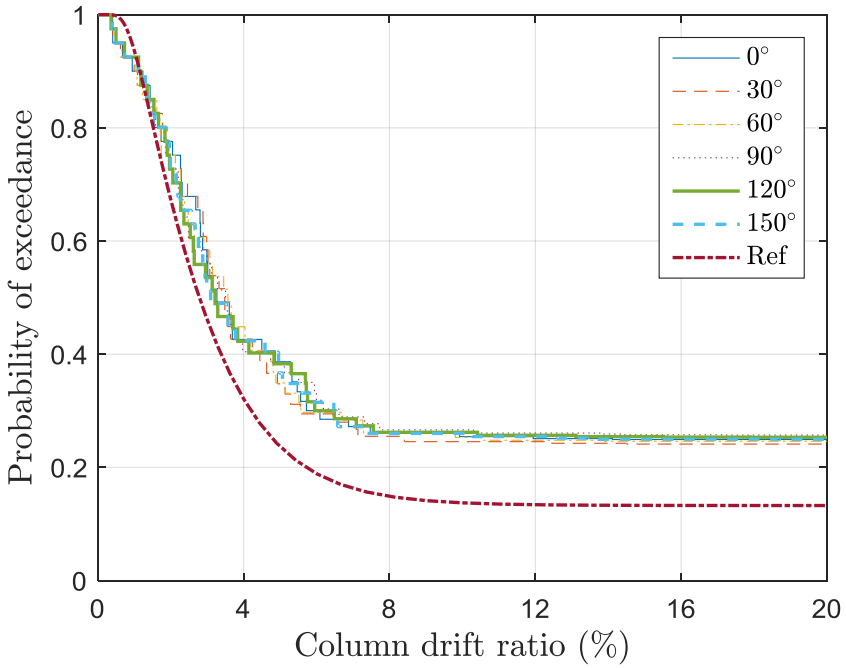

a) Type I abutment modeling

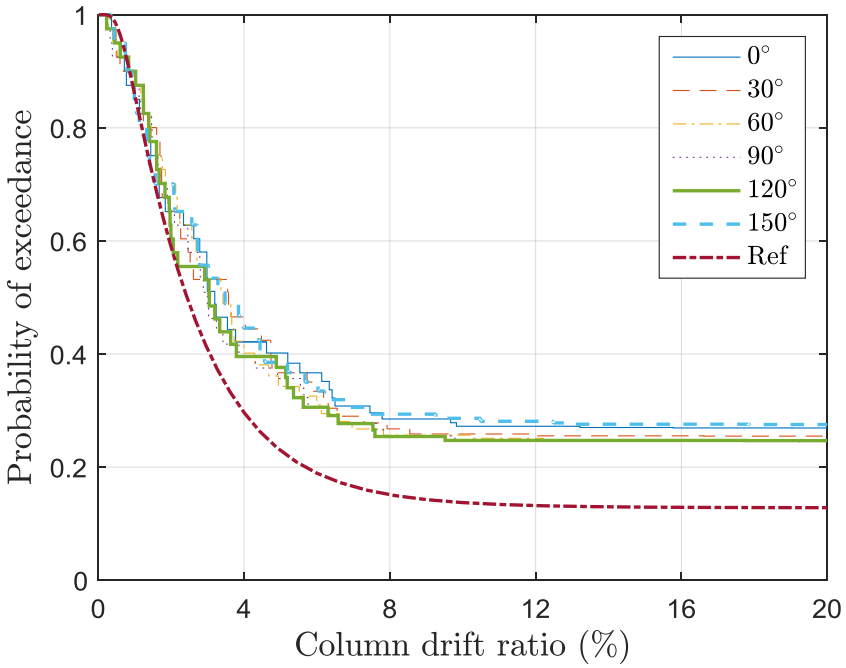

b) Type II abutment modeling

Figure 9.26 *PDSD* estimates of column drift ratio of different intercept angles from *US* procedure for Bridge A.

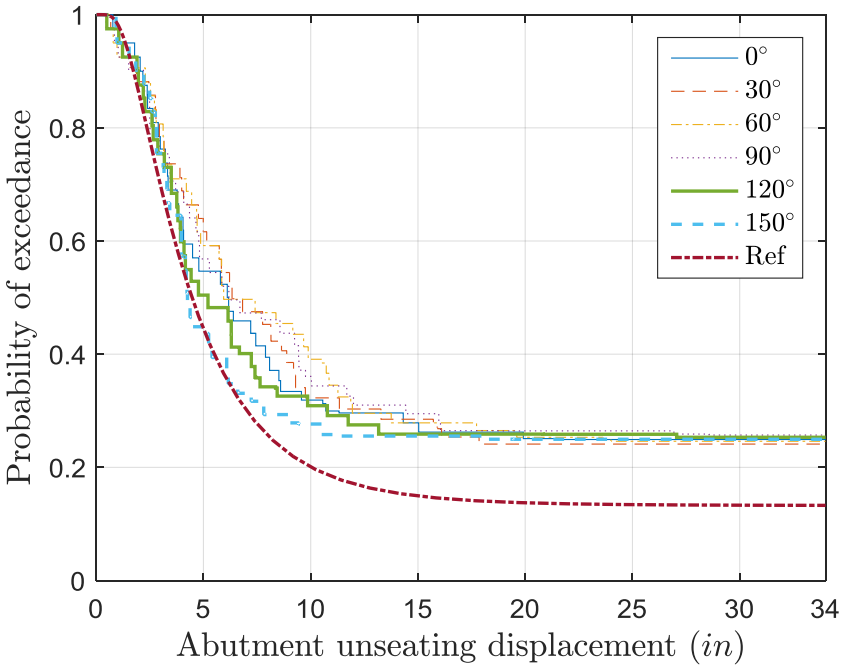

a) Type I abutment modeling

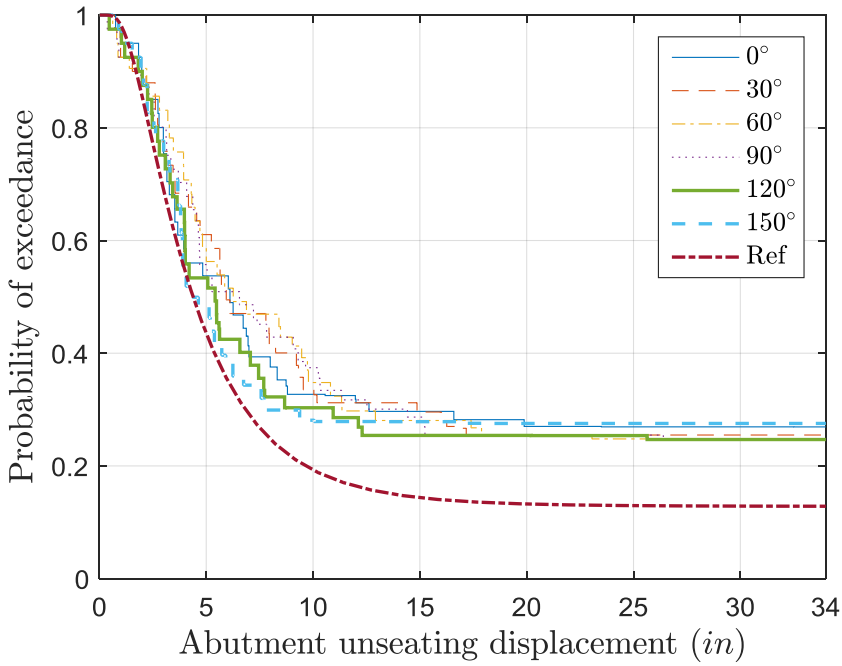

b) Type II abutment modeling

Figure 9.27 *PDSD* estimates of abutment unseating displacement of different intercept angles from *US* procedure for Bridge A.

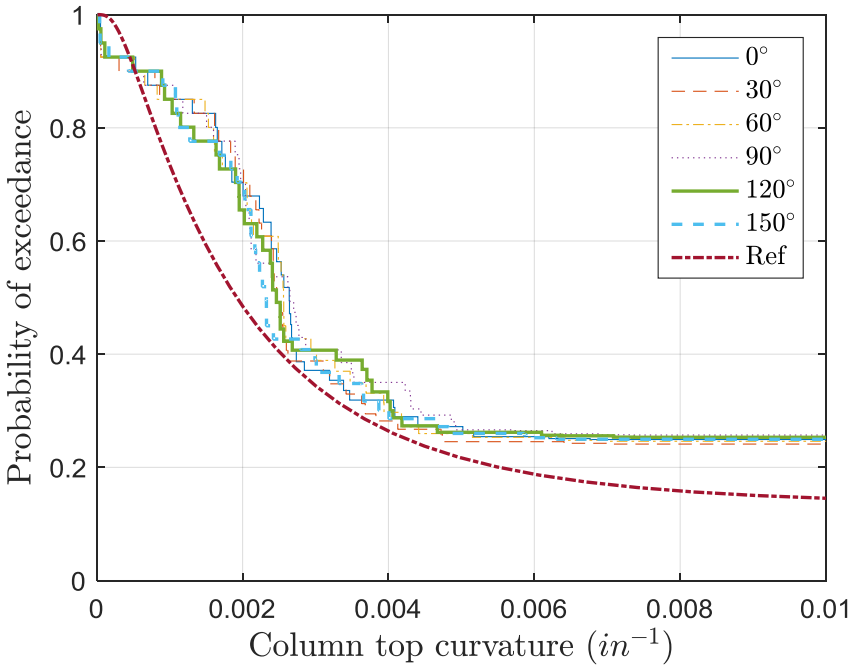

a) Type I abutment modeling

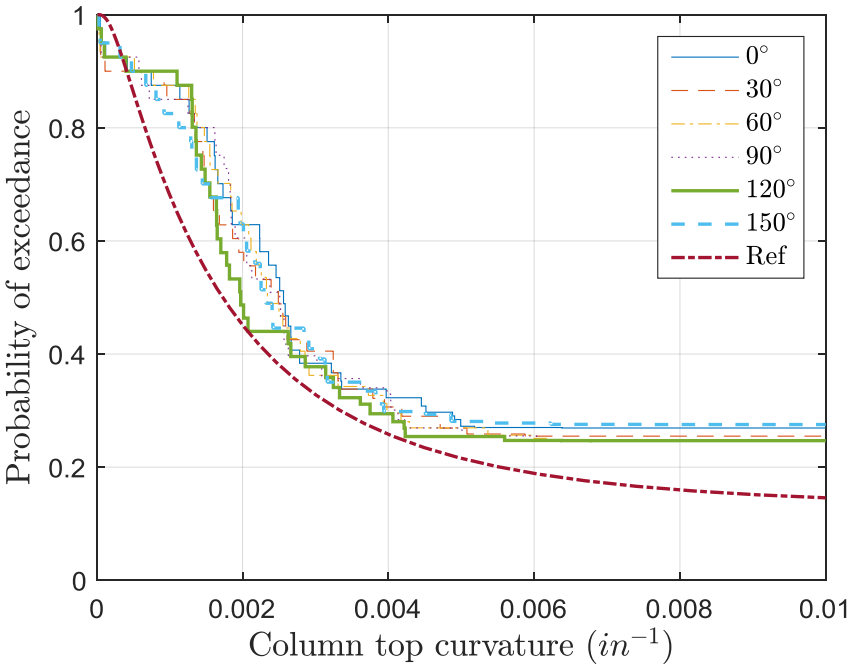

b) Type II abutment modeling

Figure 9.28 *PDSD* estimates of column top curvature of different intercept angles from *US* procedure for Bridge A.

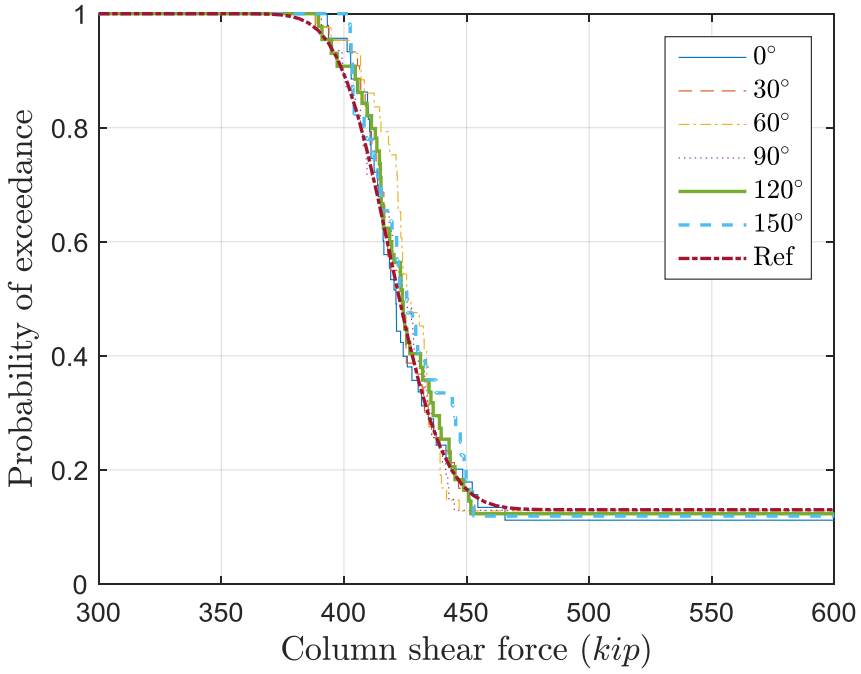

a) Type I abutment modeling

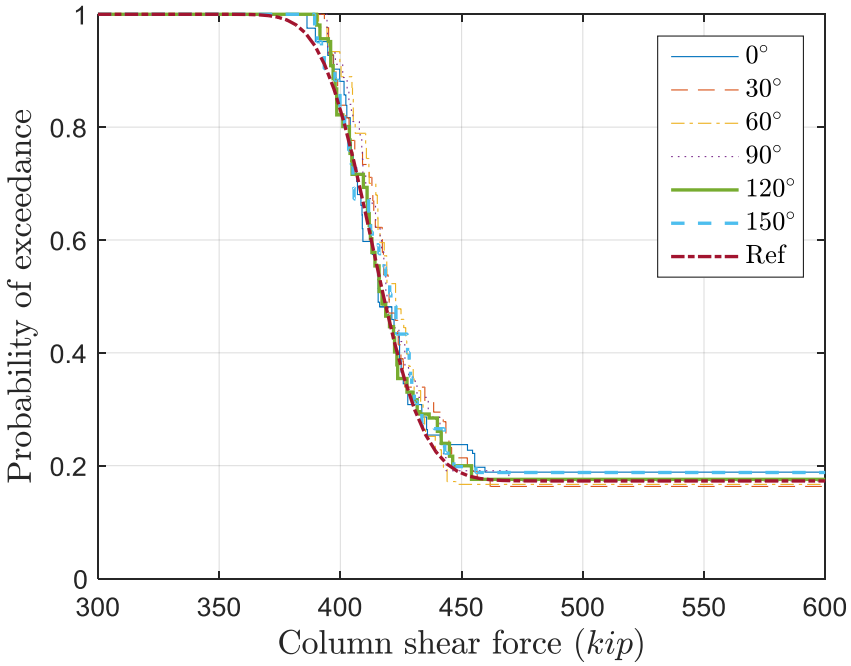

b) Type II abutment modeling

Figure 9.29 *PDSD* estimates of column shear force of different intercept angles from $S_a(T_1)$ procedure for Bridge B.

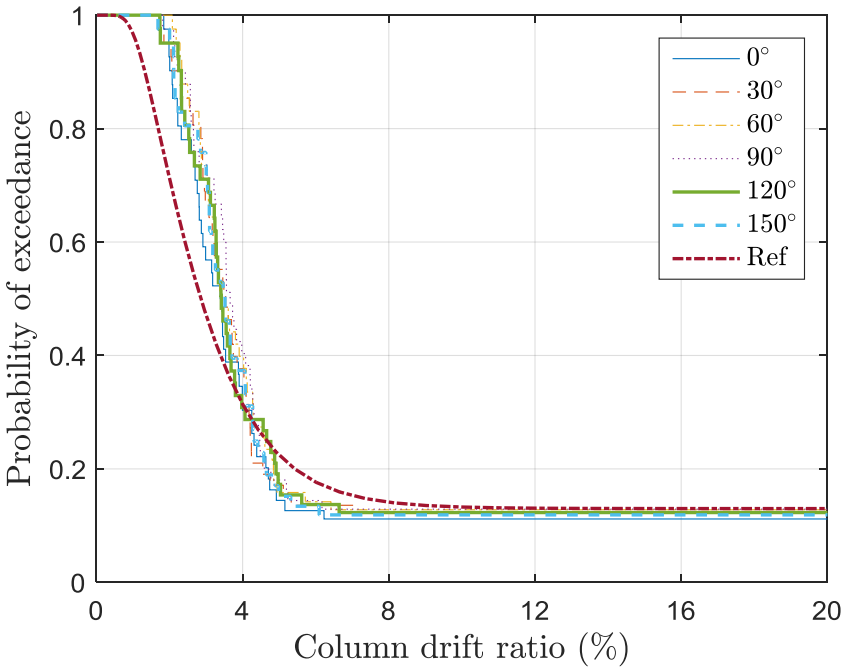

a) Type I abutment modeling

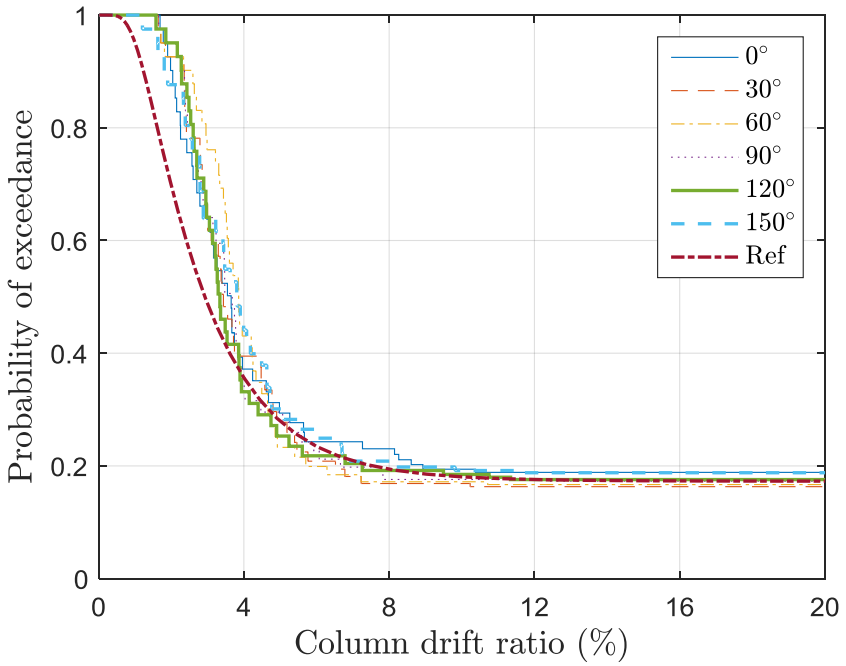

b) Type II abutment modeling

Figure 9.30 *PDSD* estimates of column drift ratio of different intercept angles from $S_a(T_1)$ procedure for Bridge B.

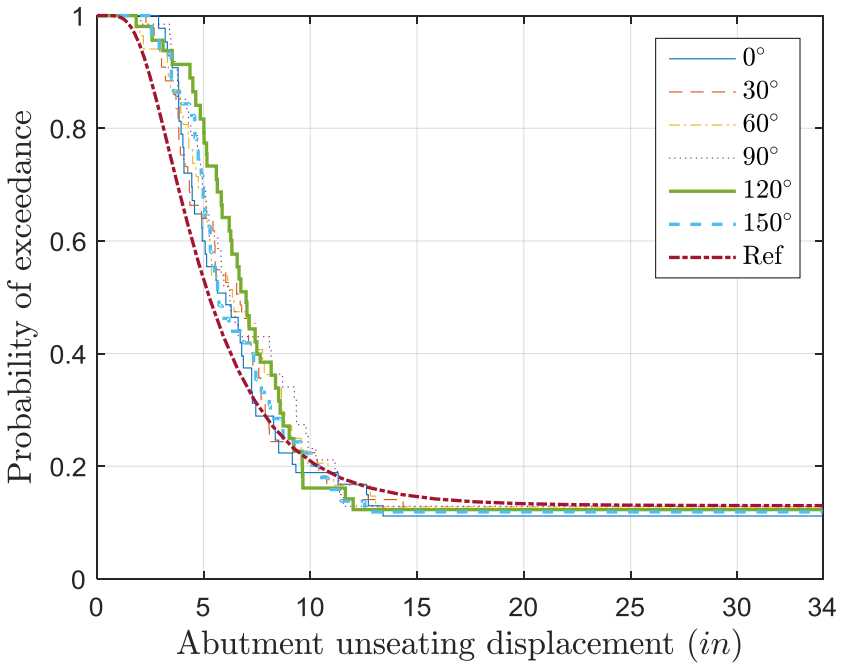

a) Type I abutment modeling

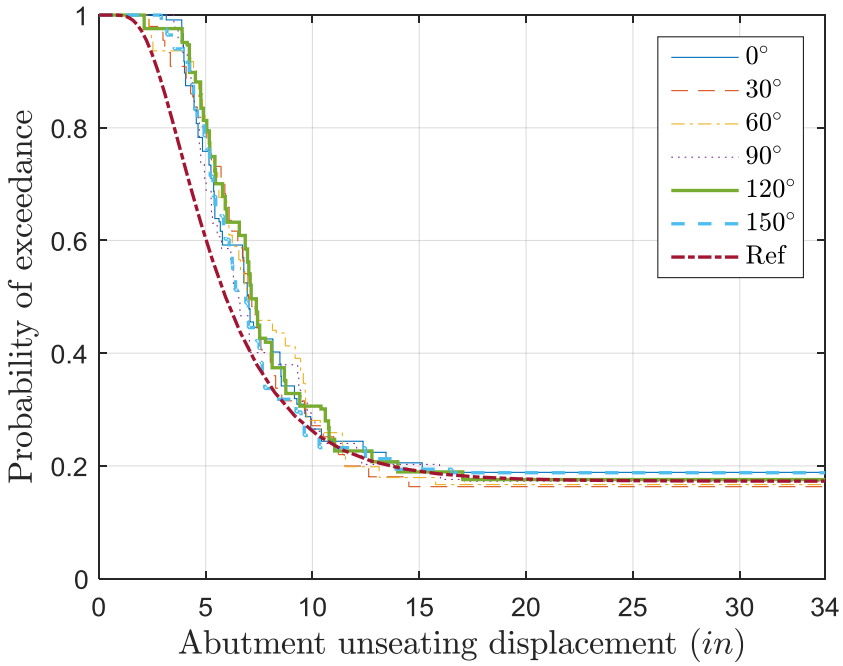

b) Type II abutment modeling

Figure 9.31 *PDSD* estimates of abutment unseating displacement of different intercept angles from $S_a(T_1)$ procedure for Bridge B.

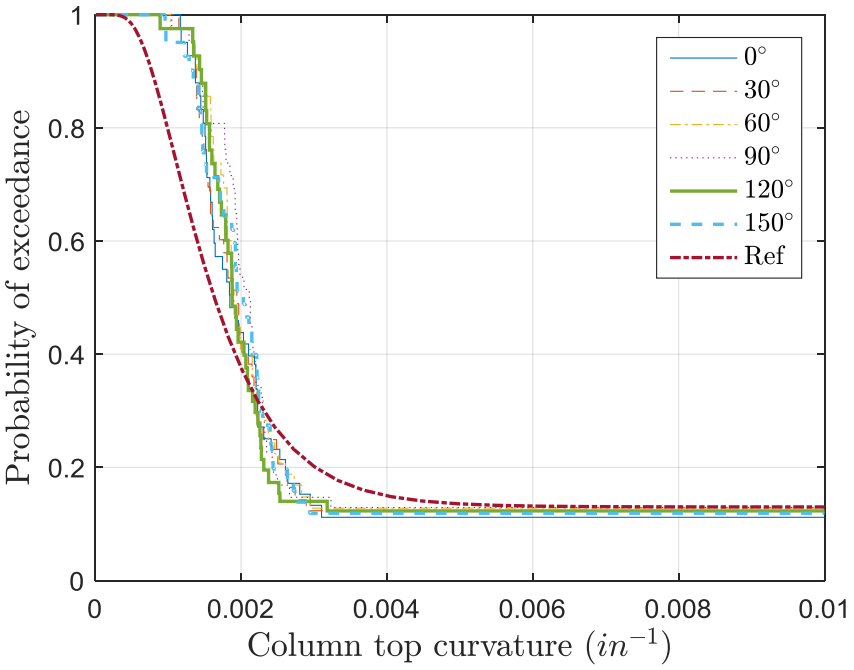

a) Type I abutment modeling

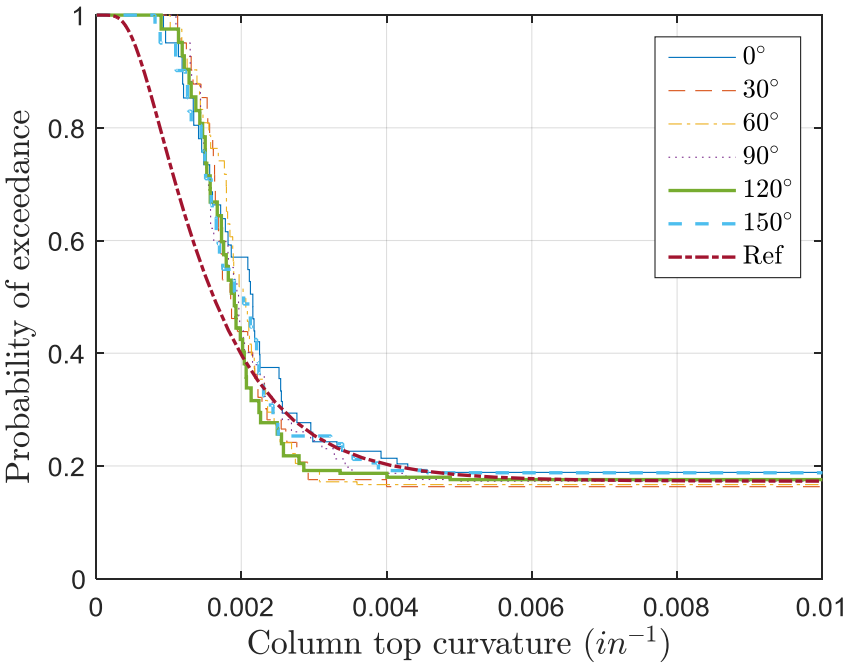

b) Type II abutment modeling

Figure 9.32 *PDSD* estimates of column top curvature of different intercept angles from $S_a(T_1)$ procedure for Bridge B.

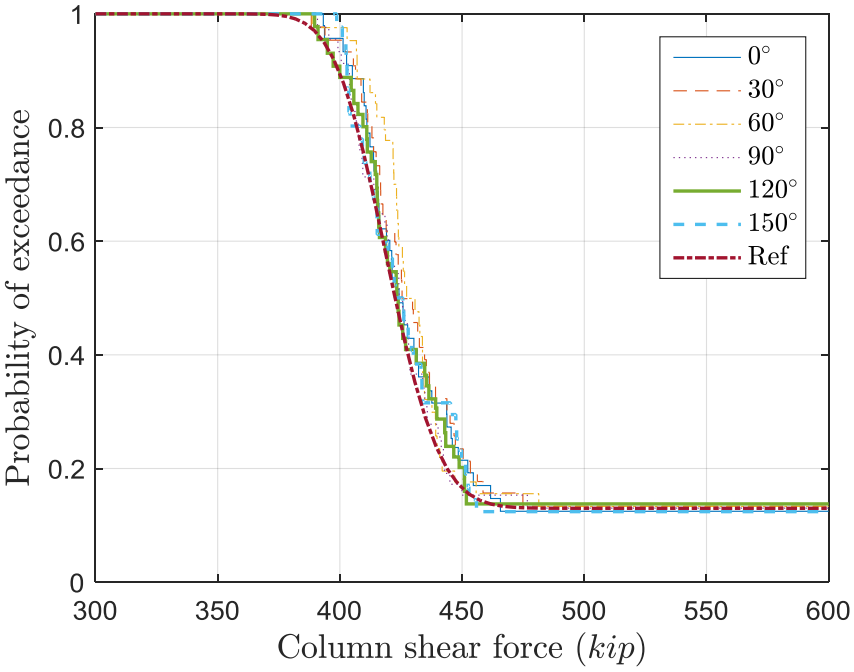

a) Type I abutment modeling

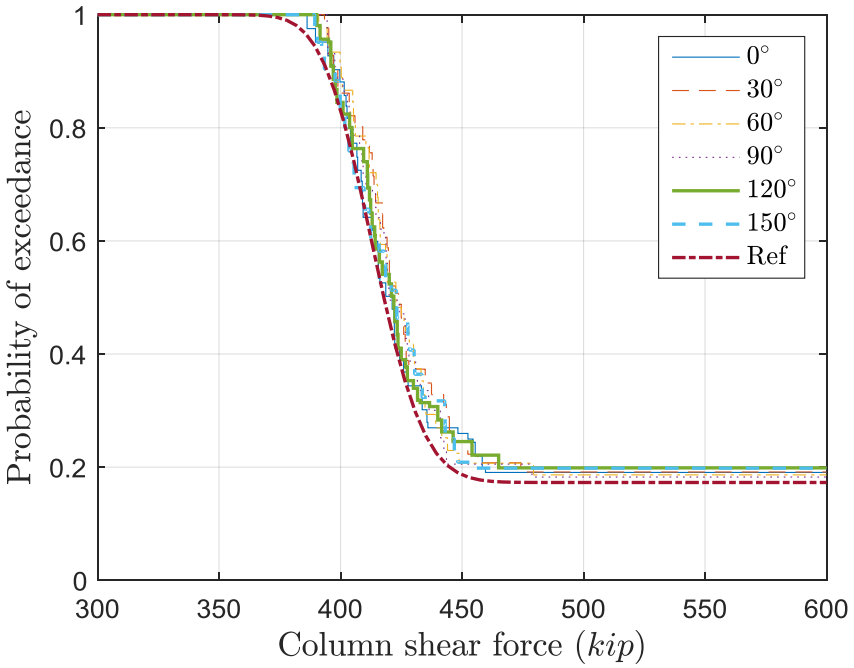

b) Type II abutment modeling

Figure 9.33 *PDSD* estimates of column shear force of different intercept angles from $S_a(T_1)_P$ procedure for Bridge B.

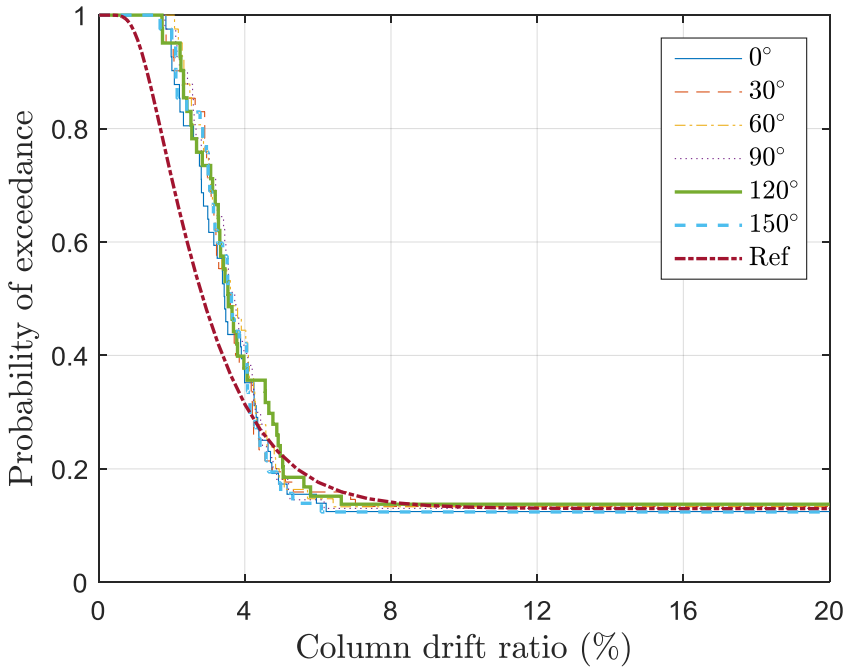

a) Type I abutment modeling

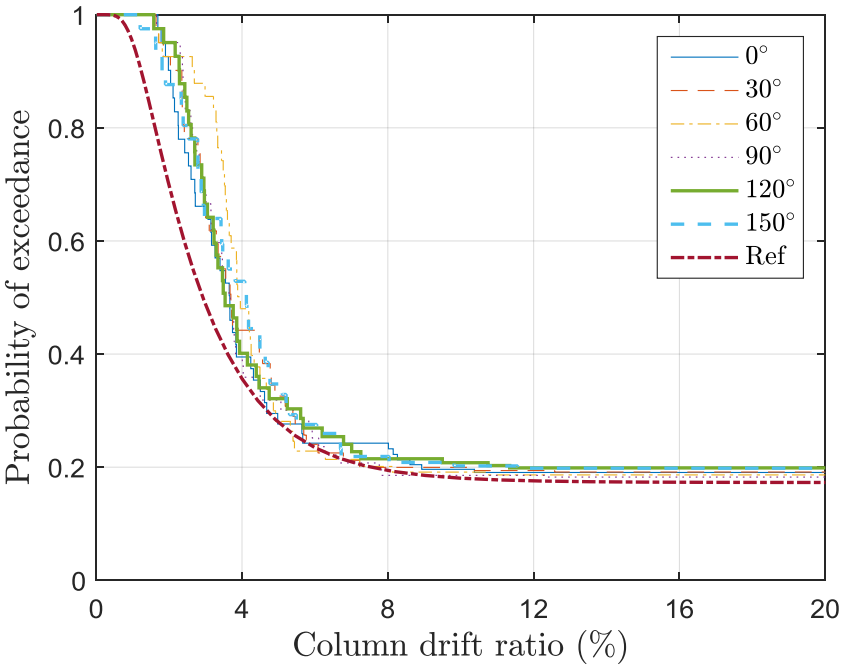

b) Type II abutment modeling

Figure 9.34 *PDSD* estimates of column drift ratio of different intercept angles from $S_a(T_1)_P$ procedure for Bridge B.

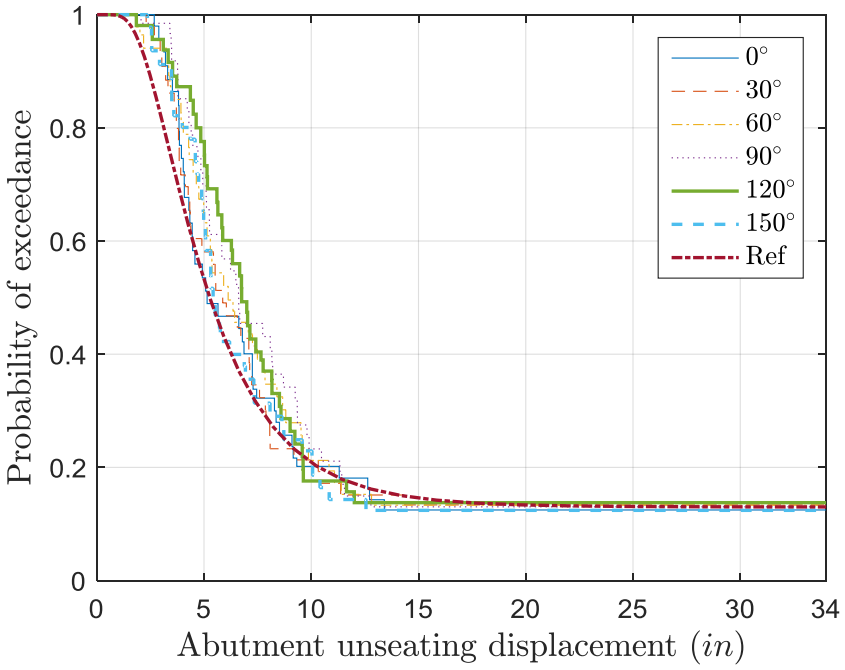

a) Type I abutment modeling

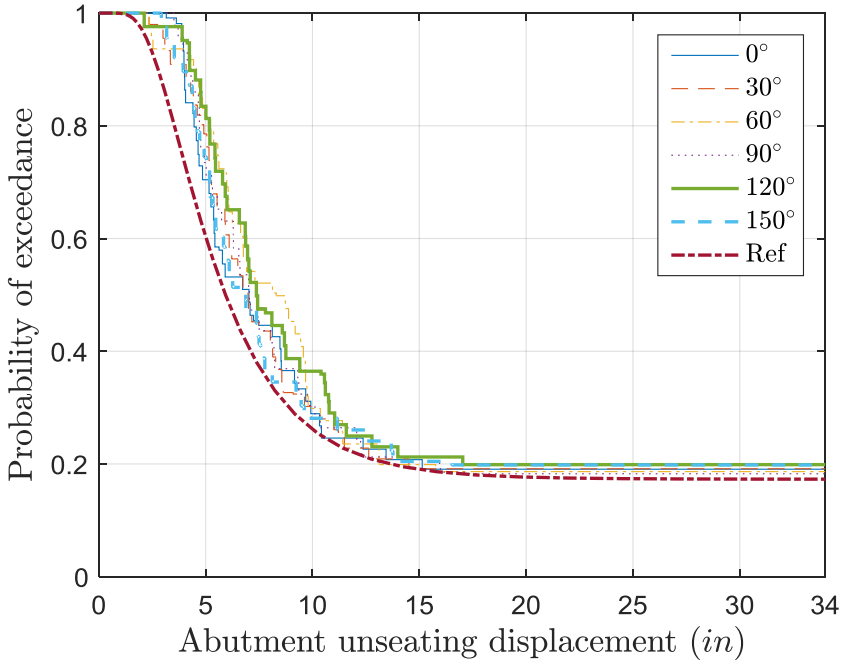

b) Type II abutment modeling

Figure 9.35 *PDSD* estimates of abutment unseating displacement of different intercept angles from $S_a(T_1)_P$ procedure for Bridge B.

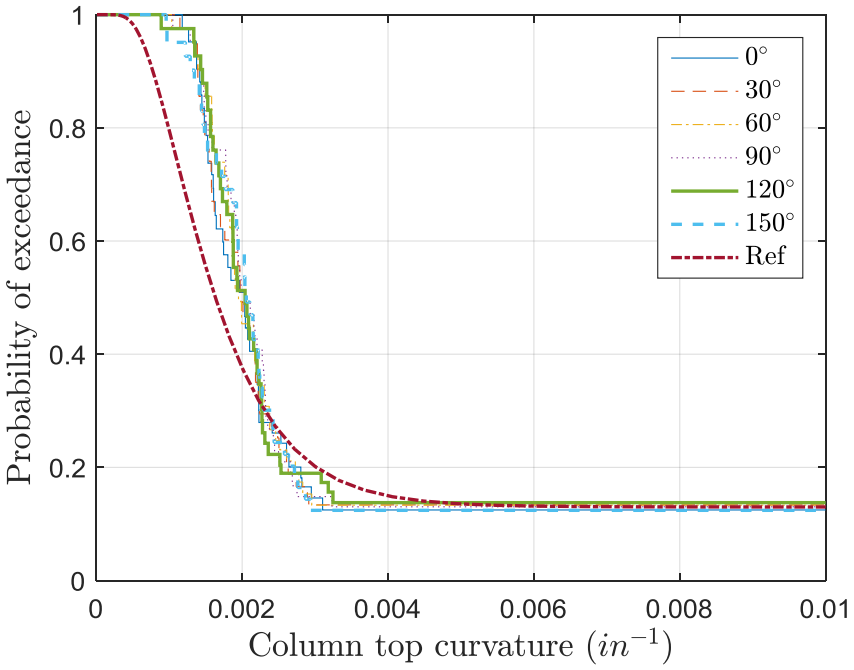

a) Type I abutment modeling

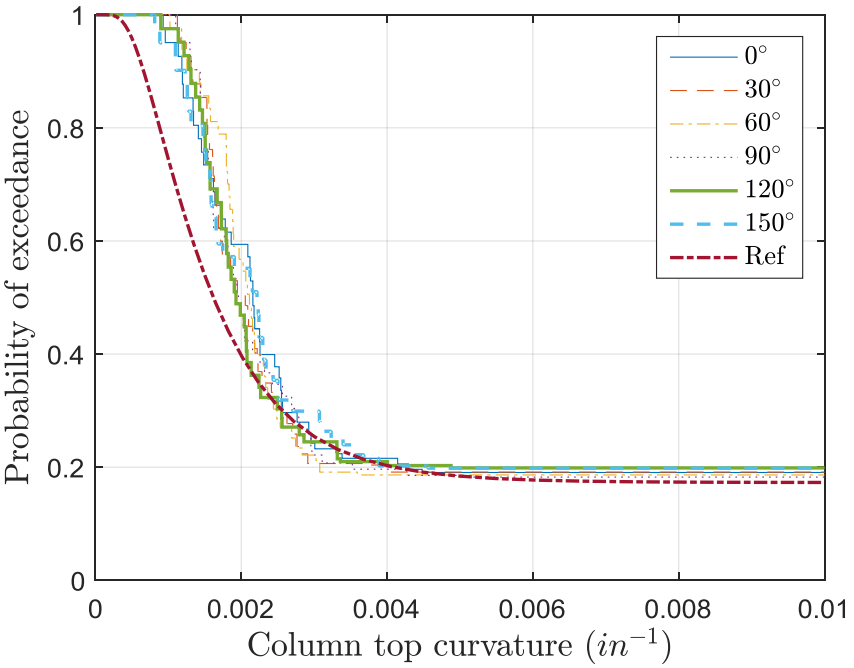

b) Type II abutment modeling

Figure 9.36 *PDSD* estimates of column top curvature of different intercept angles from $S_a(T_1)_P$ procedure for Bridge B.

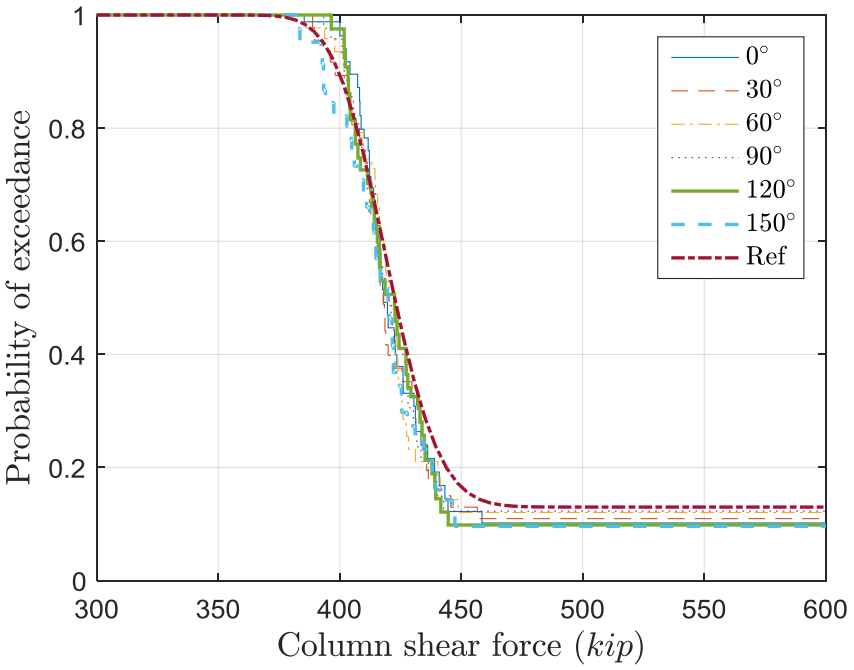

a) Type I abutment modeling

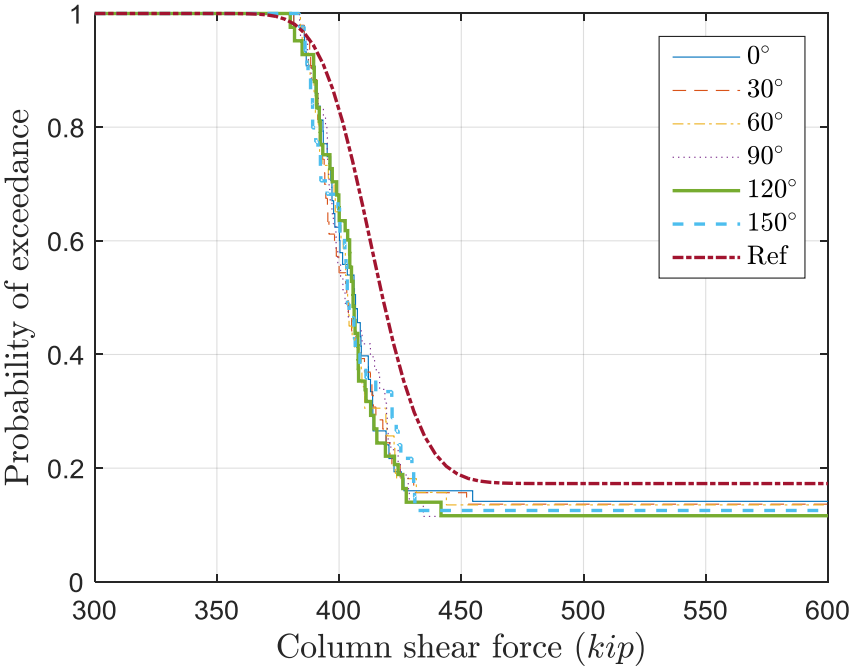

b) Type II abutment modeling

Figure 9.37 *PDSD* estimates of column shear force of different intercept angles from *CMS* procedure for Bridge B.

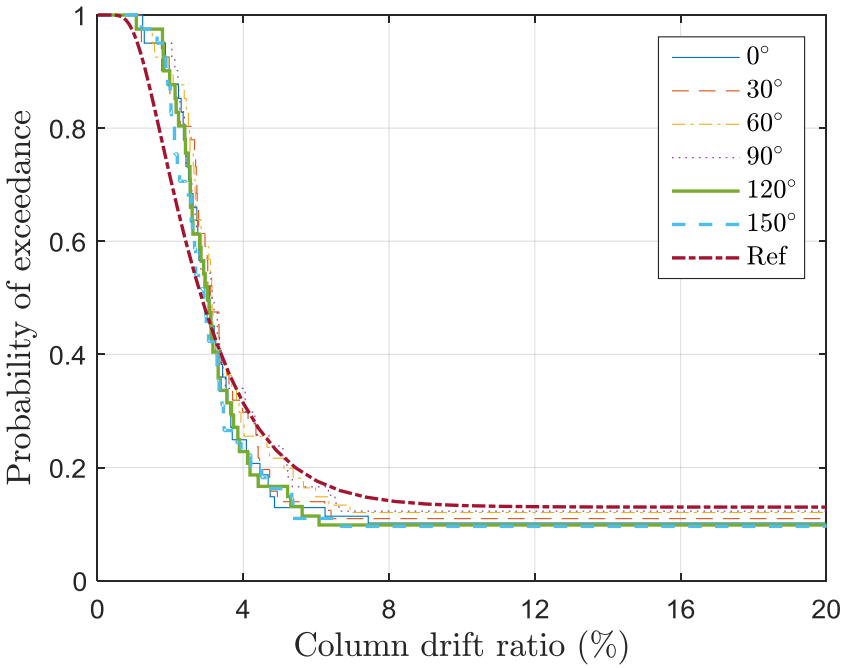

a) Type I abutment modeling

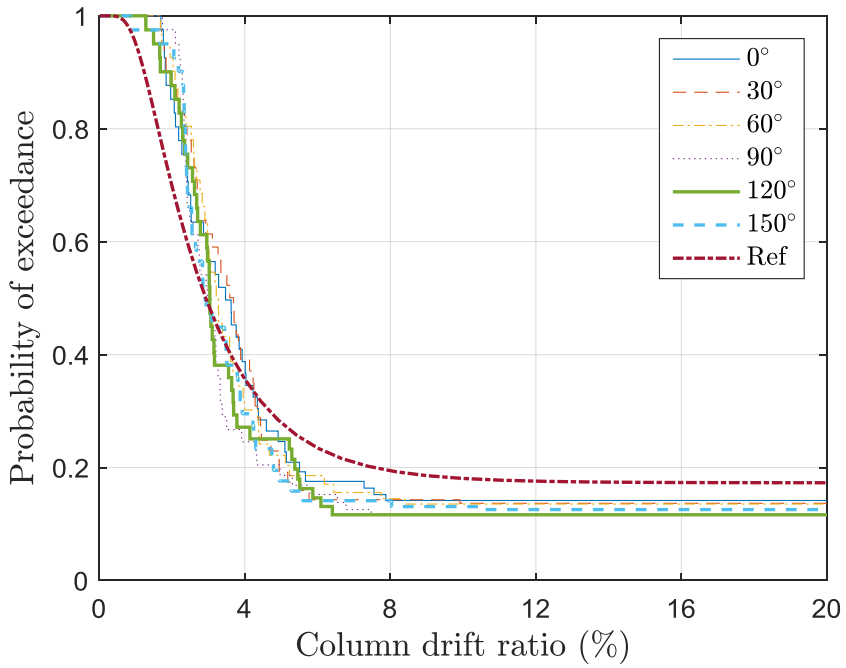

b) Type II abutment modeling

Figure 9.38 *PDSD* estimates of column drift ratio of different intercept angles from *CMS* procedure for Bridge B.

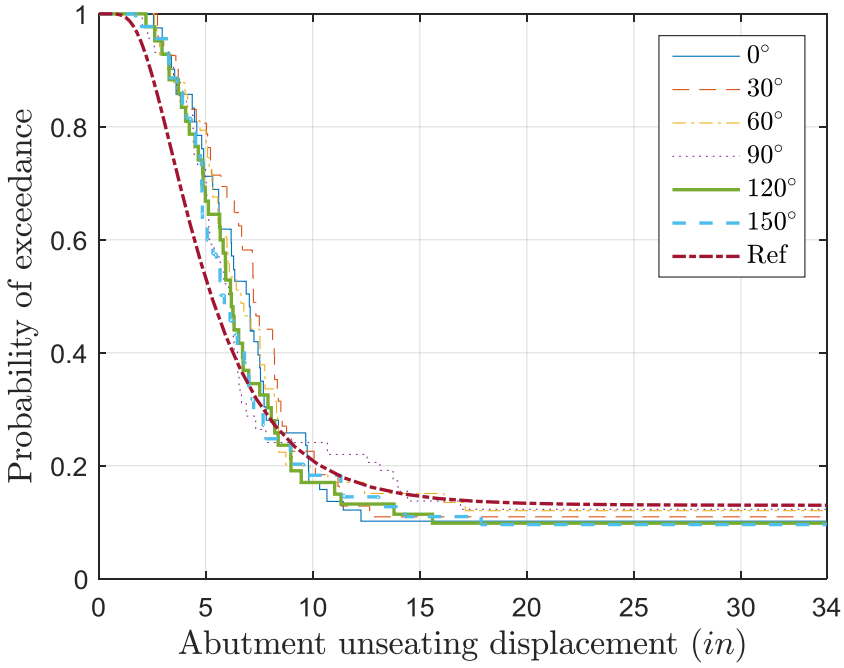

a) Type I abutment modeling

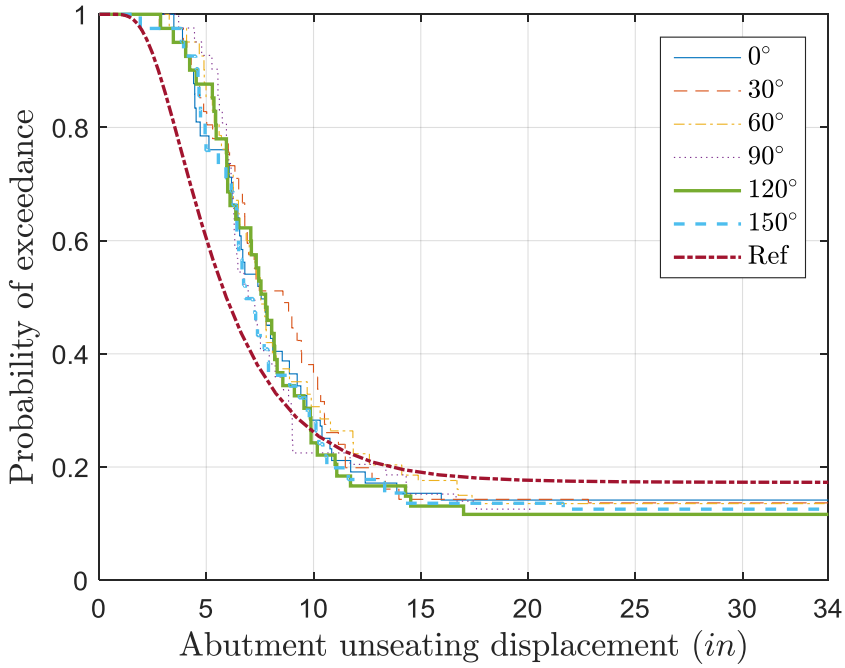

b) Type II abutment modeling

Figure 9.39 *PDSD* estimates of abutment unseating displacement of different intercept angles from *CMS* procedure for Bridge B.

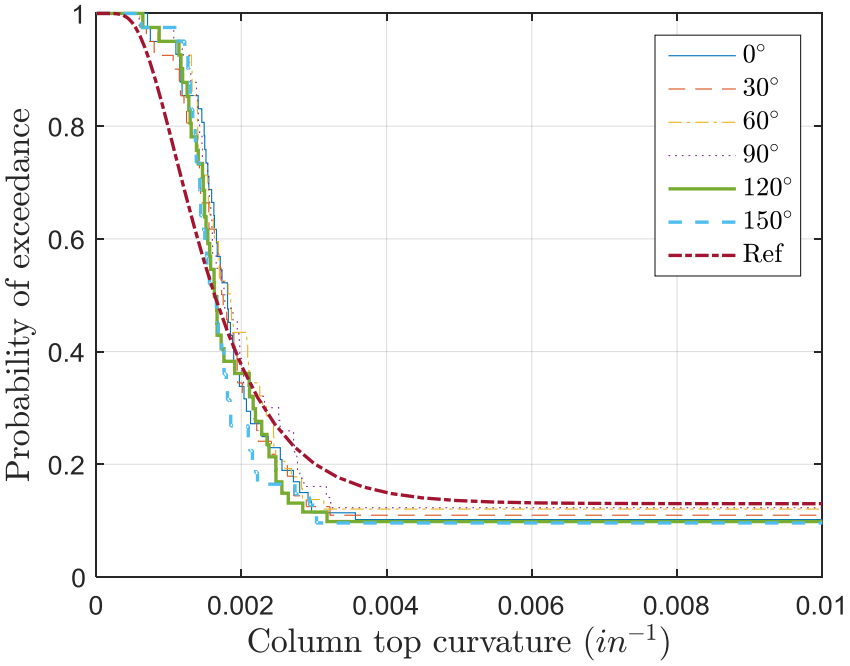

a) Type I abutment modeling

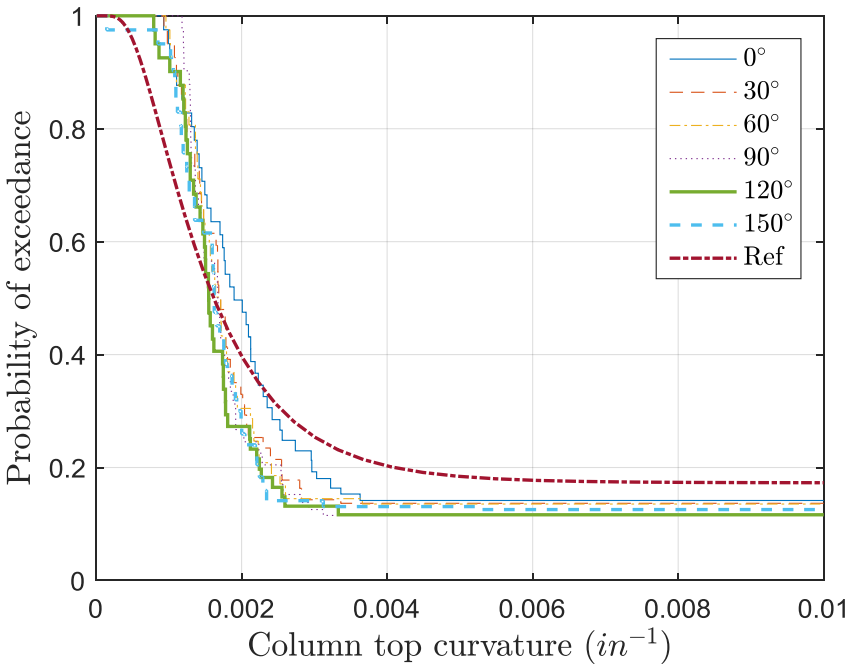

b) Type II abutment modeling

Figure 9.40 *PDSD* estimates of column top curvature of different intercept angles from *CMS* procedure for Bridge B.

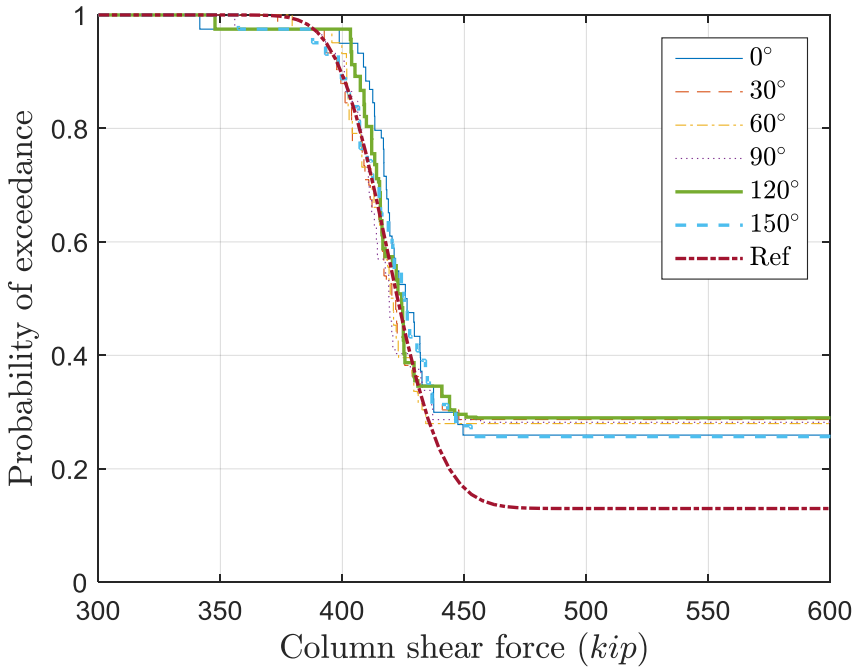

a) Type I abutment modeling

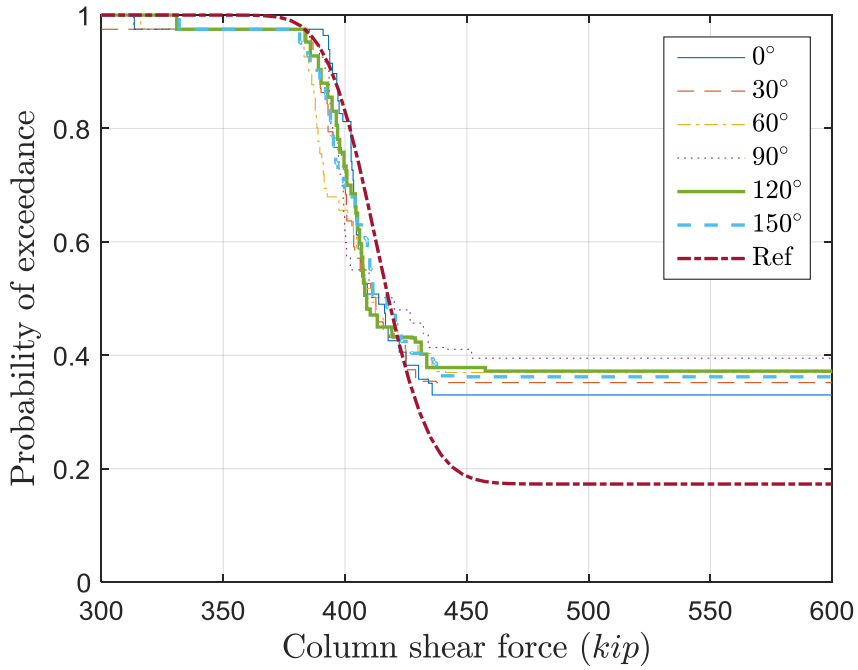

b) Type II abutment modeling

Figure 9.41 *PDSD* estimates of column shear force of different intercept angles from *US* procedure for Bridge B.

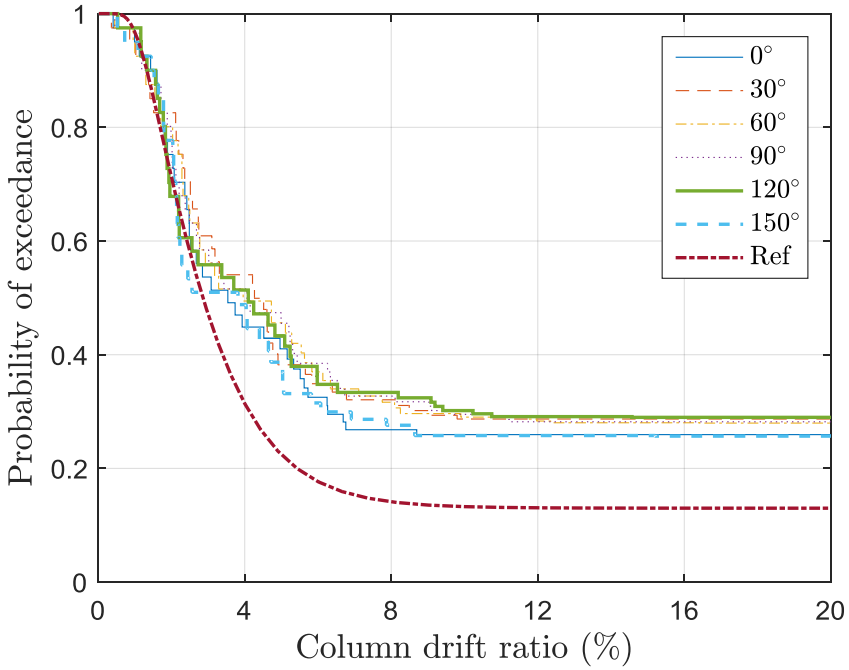

a) Type I abutment modeling

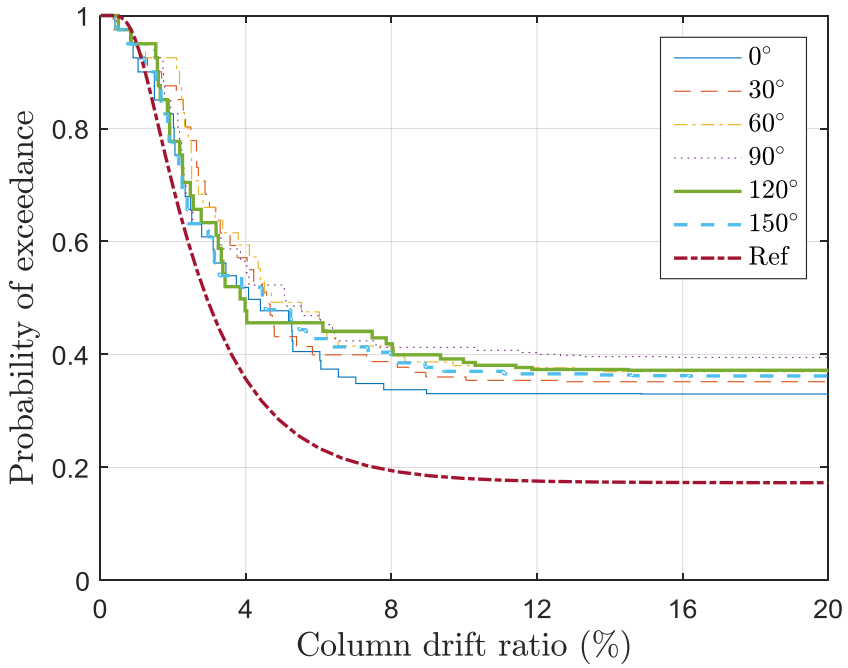

b) Type II abutment modeling

Figure 9.42 *PDSD* estimates of column drift ratio of different intercept angles from *US* procedure for Bridge B.

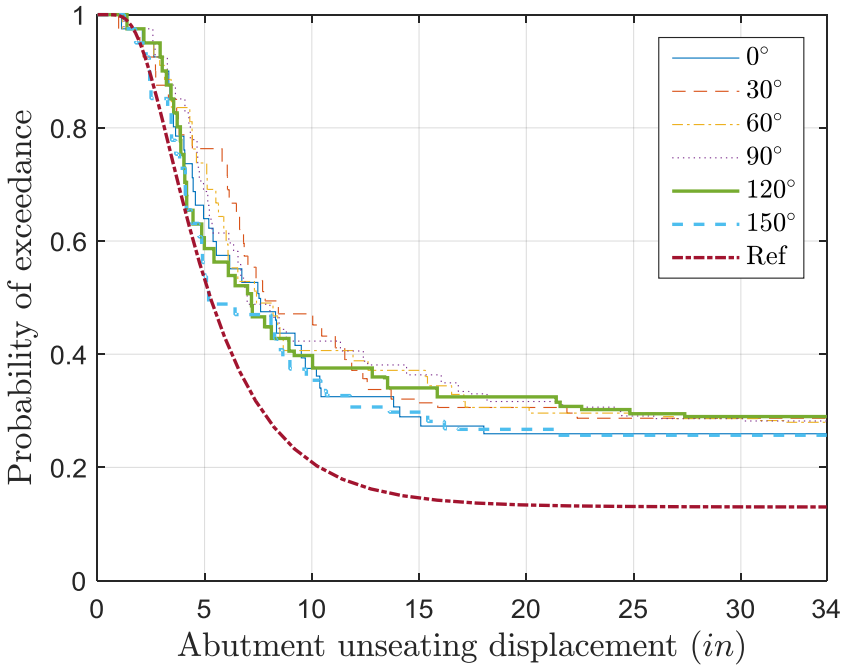

a) Type I abutment modeling

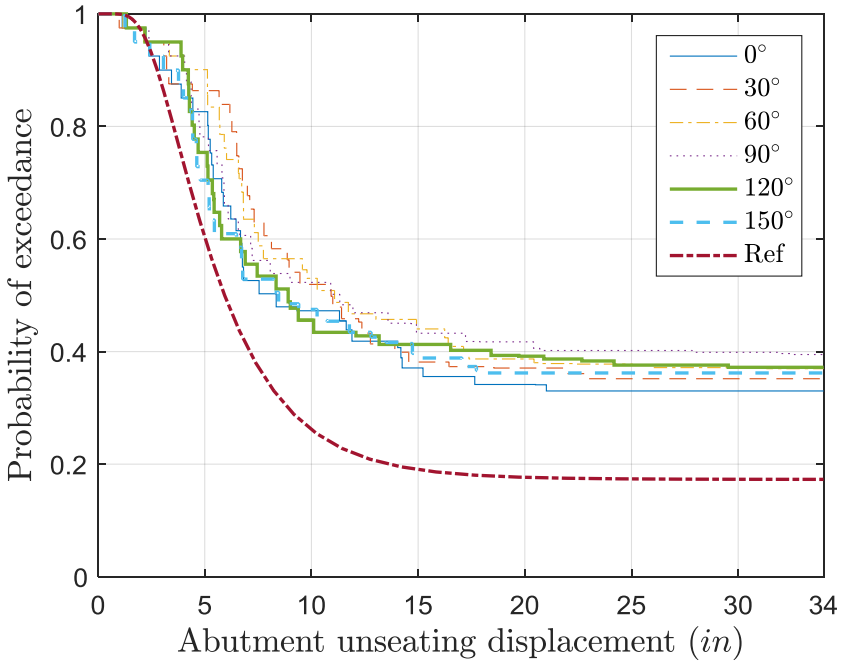

b) Type II abutment modeling

Figure 9.43 *PDSD* estimates of abutment unseating displacement of different intercept angles from *US* procedure for Bridge B.

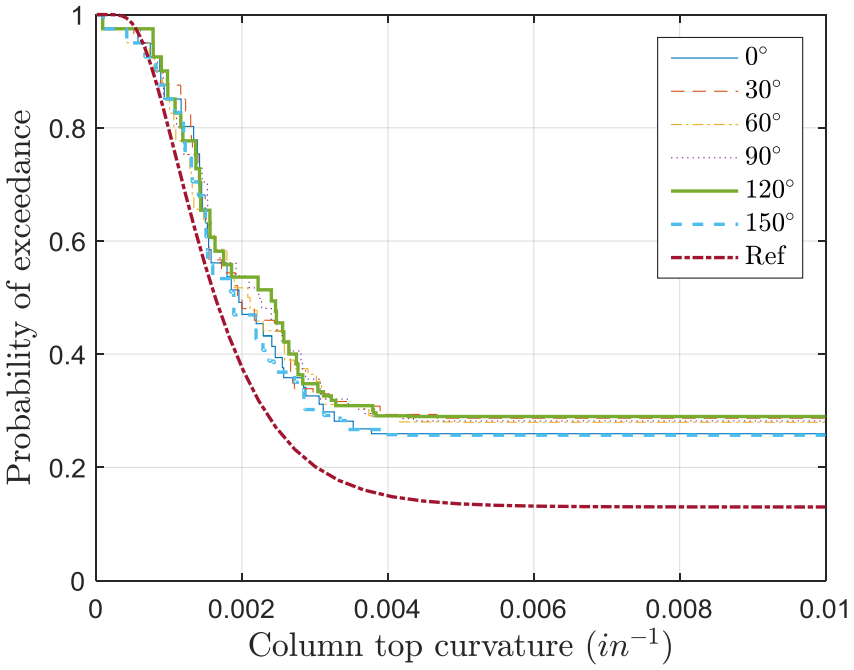

a) Type I abutment modeling

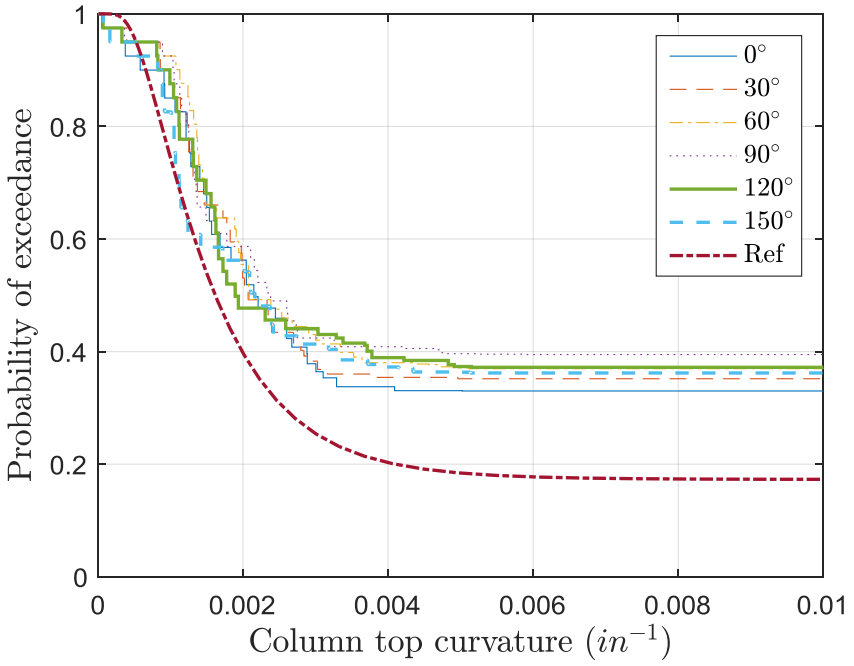

b) Type II abutment modeling

Figure 9.44 *PDSD* estimates of column top curvature of different intercept angles from *US* procedure for Bridge B.

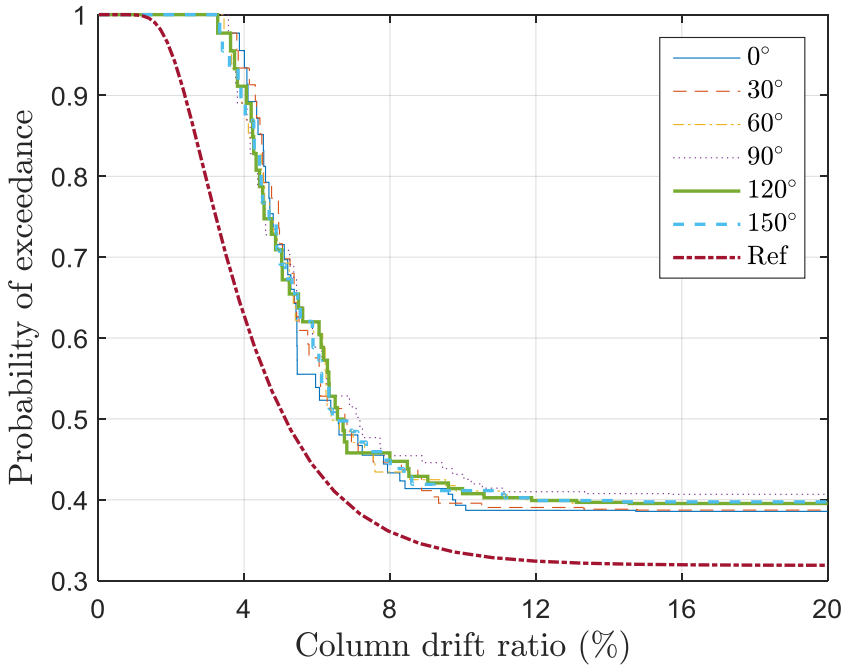

a) $S_a(T_1)$

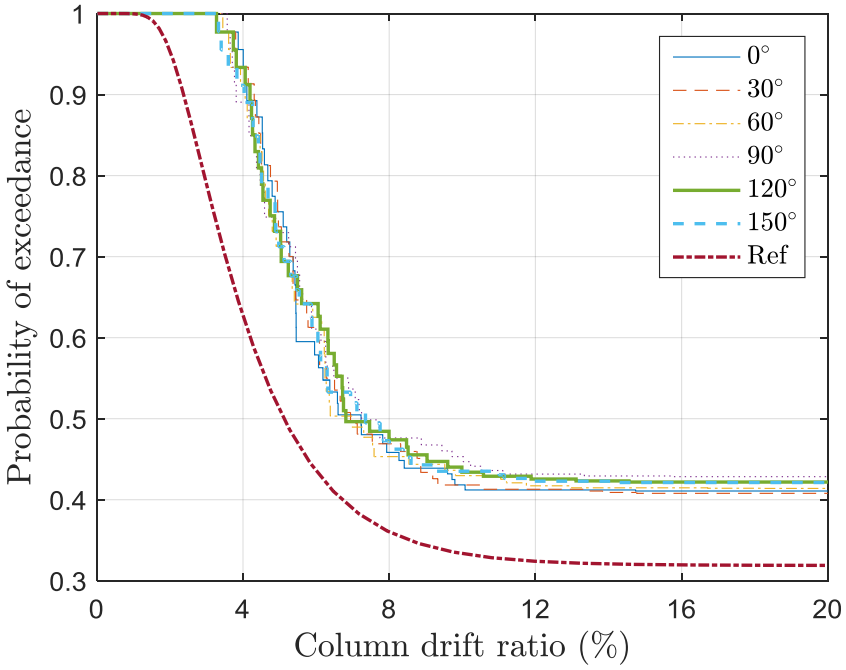

b) $S_a(T_1)_P$

Figure 9.45 *PDSD* estimates of column drift ratio of different intercept angles from $S_a(T_1)$ and $S_a(T_1)_P$ procedures for Bridge C with Type I abutment modeling.

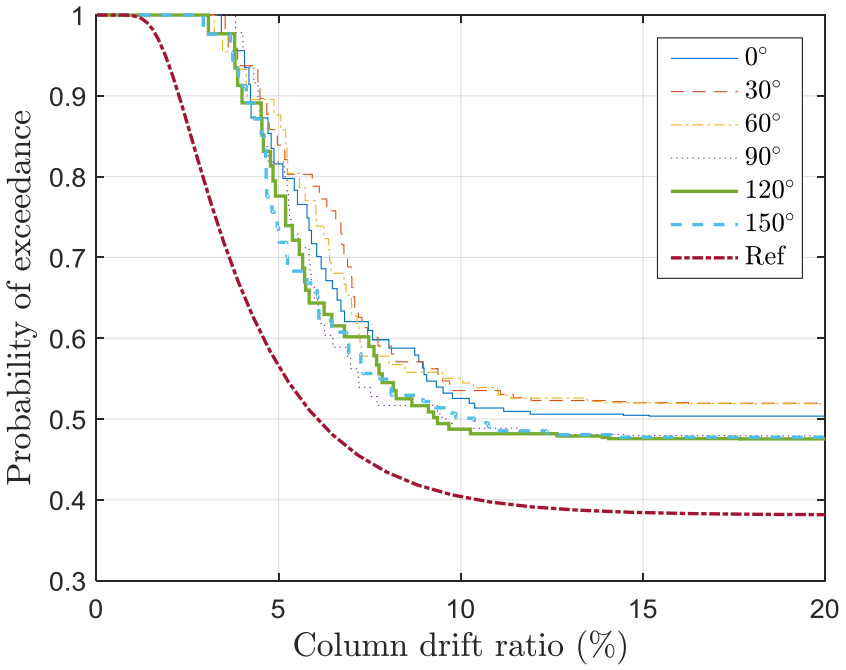

a) $S_a(T_1)$

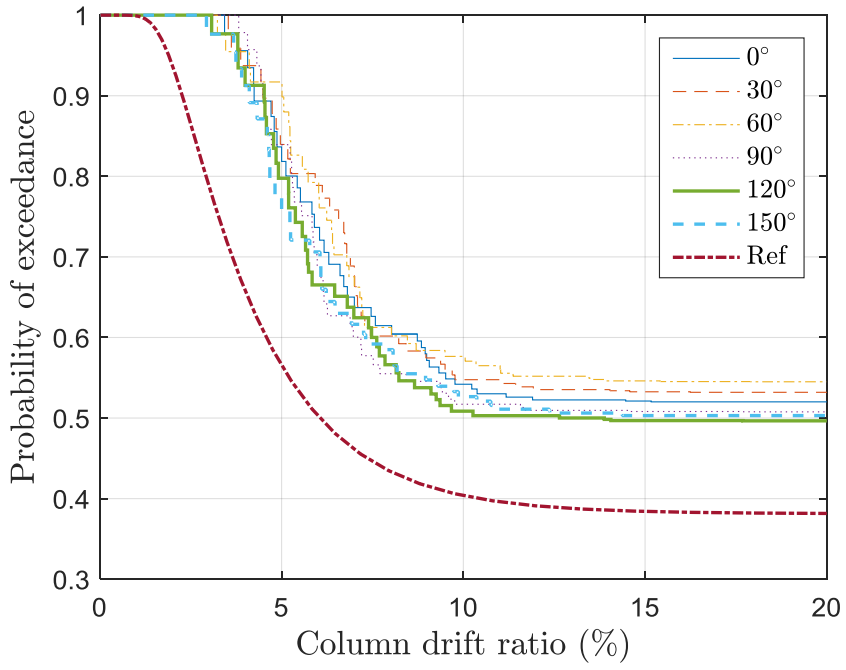

b) $S_a(T_1)_P$

Figure 9.46 *PDSD* estimates of column drift ratio of different intercept angles from $S_a(T_1)$ and $S_a(T_1)_P$ procedures for Bridge C with Type II abutment modeling.

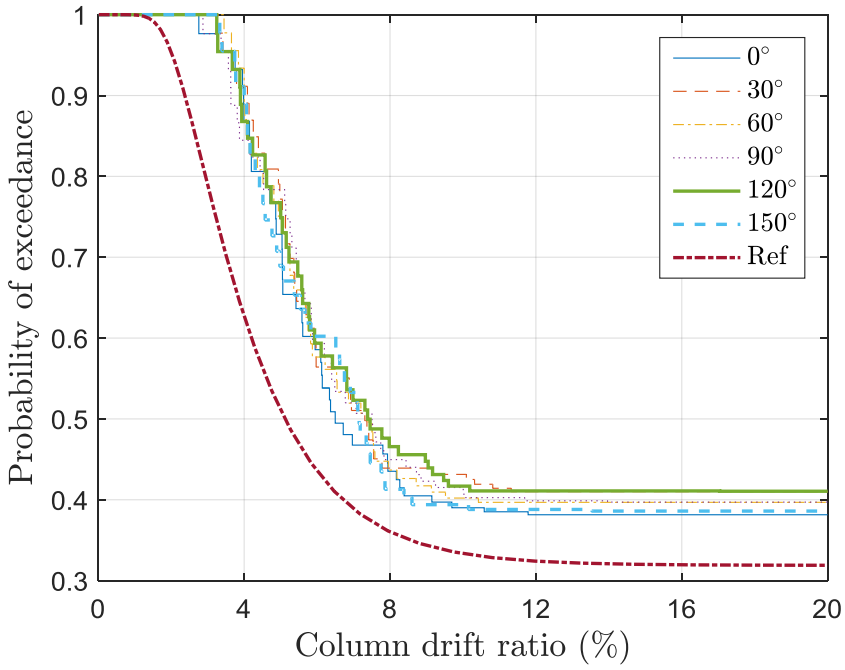

a) *CMS*

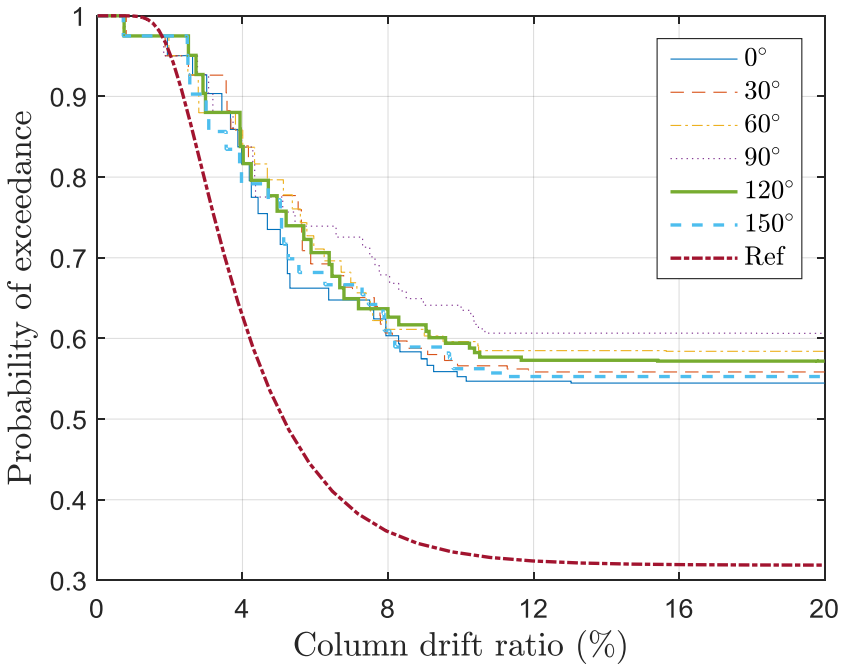

b) *US*

Figure 9.47 *PDSD* estimates of column drift ratio of different intercept angles from *CMS* and *US* procedures for Bridge C with Type I abutment modeling.

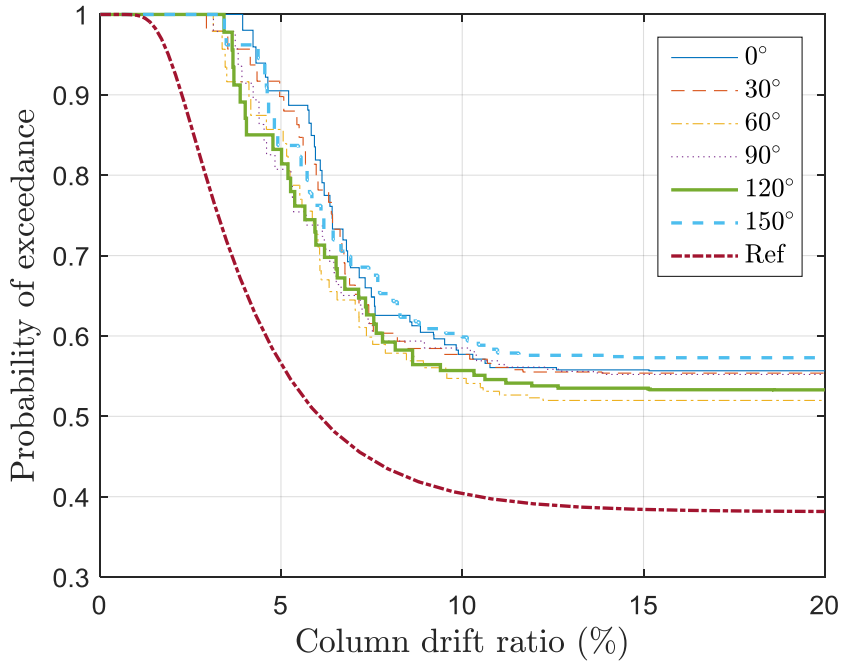

a) *CMS*

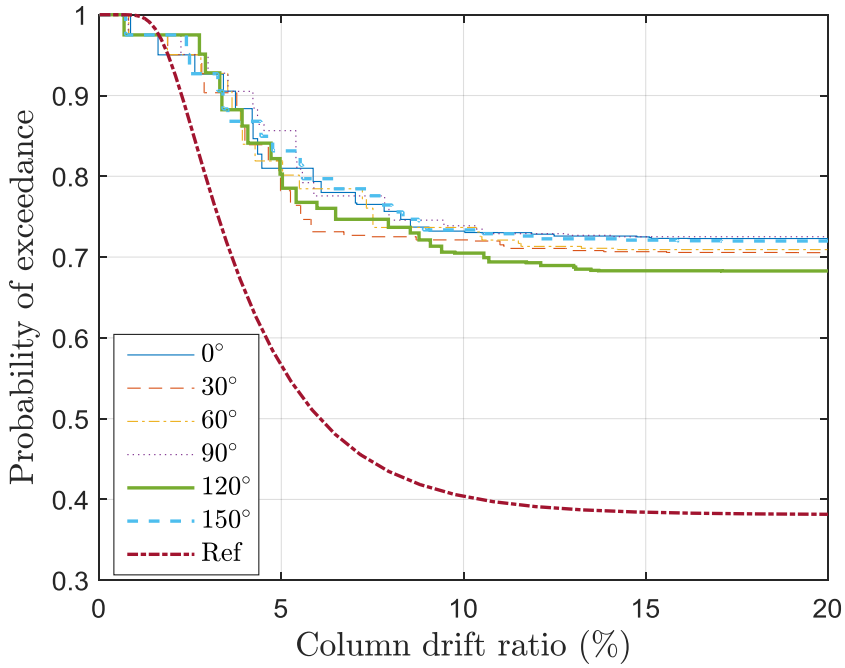

b) *US*

Figure 9.48 *PDSD* estimates of column drift ratio of different intercept angles from *CMS* and *US* procedures for Bridge C with Type II abutment modeling.

10 Summary, Conclusions and Future Extensions

10.1 SUMMARY

The study completed in this dissertation investigated two key challenges related to the application of the performance-based earthquake engineering (PBEE) approach such as the methodology developed with the Pacific Earthquake Engineering Research (PEER) Center. Accurate and robust nonlinear time history analysis (NTHA) that is fundamental to estimate the seismic demands of structures is the first challenge investigated in this study. It involved the use of different types of direct integration algorithms and nonlinear equation solvers where their stability performance and convergence behavior are of great significance to ensure accurate and robust NTHA simulations, especially for nonlinear multi-degree of freedom (MDOF) structural systems. Lyapunov stability theory, the most complete framework for stability analysis of dynamical systems, was introduced in this study. Based on this theory, a new nonlinear equation solver was developed and its convergence performance was theoretically formulated and verified by several examples. In addition, two Lyapunov-based approaches were proposed to perform stability analysis of nonlinear structural systems. The first approach transformed the stability analysis to a problem of existence that can be solved via convex optimization, over the discretized domain of interest of the restoring force. The second approach was specifically applicable to explicit algorithms for nonlinear single-degree of freedom (SDOF) and MDOF systems considering strictly positive real lemma. In this approach, a generic explicit algorithm was formulated for a system governed by a nonlinear function of the basic force without adopting any approximations. Starting from this formulation and based on the Lyapunov stability theory, the stability analysis of the formulated nonlinear system was transformed to investigating the strictly positive realness of its corresponding transfer function matrix. The two Lyapunov-based approaches of stability analysis were demonstrated by several SDOF and MDOF numerical examples.

The second challenge experienced in the PBEE approach is the selection of the ground motion selection and modification (GMSM) procedure that determine the input GM records for the NTHA simulations. Therefore, proper selection of GMSM approach is vital and represents an important prerequisite for the accurate and robust NTHA simulation and thus for the entire PBEE approach. In this dissertation, a framework for probabilistic evaluation of GMSM procedures was developed in the context of a selected large earthquake scenario with bidirectional GM excitations.

As an important application, the aforementioned theoretical developments were investigated for reinforced concrete (RC) highway bridge systems, which are key components of the infrastructure in urban cities. Solutions for overcoming the problems of convergence

encountered in NTHA of RC highway bridges were presented and recommendations were given. In addition, this dissertation evaluated several GMSM procedures in predicting the probability distribution of the seismic demands (*PDSD*) of RC highway bridges subjected to large earthquakes that result in highly nonlinear responses. The accuracy and reliability of all the *PDSD* estimates from the investigated GMSM procedures were evaluated against the reference benchmark *PDSD* developed by the PEER PBEE framework. Such evaluations were conducted considering four selected engineering demand parameters (*EDP*s) of three representative RC highway bridges in California accounting for two types of abutment modeling. In total, 27,360 NTHA simulations, where 21,600 ones for the development of the benchmark *PDSD* and 5,760 ones for the *PDSD* estimates by the GMSM procedures, were performed for this evaluation.

10.2 CONCLUSIONS

The major developments and findings of this study are summarized as follows:

- A new nonlinear equation solver is developed on the basis of reformulation of the equations of motion into a hypothetical dynamical system characterized by a set of ordinary differential equations. The equilibrium points of this hypothetical system are the solutions of the nonlinear structural problems. Starting from the Lyapunov stability theory, it is demonstrated that this hypothetical dynamical system is characterized by a globally asymptotic stability, i.e., convergence, to equilibrium points for structural dynamics. This feature overcomes the inherent limitations of the traditional iterative minimization algorithms and has no restriction on the selection of the initial guess for various structural nonlinear behaviors.

- Another important feature of the proposed Lyapunov-based nonlinear equation solver, as shown in the several numerical examples, is its ability to solve the equilibrium equations for models where a numerically consistent tangent may be difficult to determine.

- An integration algorithm is stable if its Lyapunov artificial energy function is bounded. The general condition that the boundedness of $\prod_{j=i}^{1} \mathbf{A}_j = \mathbf{A}_i \mathbf{A}_{i-1} \cdots \mathbf{A}_2 \mathbf{A}_1$ for $i \to \infty$ is derived from the boundedness of the Lyapunov function. For linear structures, the stability criterion is that the spectral radius of the approximation operator is less than or equal to 1.0, which is applied to nonlinear structures by some researchers. It should be emphasized that the stability limit for linear structures, however, does not automatically hold for nonlinear structures. Therefore, basic methodologies used in some well-known stability limits of direct integration algorithms, e.g., the Operator-Splitting (OS) algorithm with initial stiffness ($OS_{initial}$), are not applicable to nonlinear problems.

- The study also investigates the OS algorithm that uses tangent stiffness in the formulation (OS_{tagent}), which has not been previously studied. It is shown that this explicit algorithm possesses similar stability properties to those of the implicit Newmark (IN) integration.

- An approach is proposed to perform the stability analysis numerically. This approach transforms the stability analysis to the solution of a convex optimization problem over the discretized domain of interest of the restoring force. The proposed approach is shown to be generally applicable to direct integration algorithms for nonlinear problems and can potentially be extended to MDOF systems

- A geometrically nonlinear pendulum problem with a closed-form exact solution is used to investigate the accuracy of the investigated integration algorithms. The period is shortened by explicit Newmark and elongated by the other algorithms. The $OS_{tangent}$ and IN algorithms present similar period elongations. The more computationally expensive TRBDF2 has the smallest period change. All algorithms present no amplitude decay except the TRBDF2 method undergoes some amplitude decay due to the introduced numerical damping. Observed period elongation (< ±3%) and amplitude decay (< 1%) values are practically acceptable. Moreover, the incorrectness of the stability criterion of the $OS_{initial}$ algorithm from past studies and the suitability of the proposed numerical stability analysis approach herein have been demonstrated by the same nonlinear pendulum example.

- The systematic approach to investigate the Lyapunov stability of explicit direct integration algorithms for MDOF systems considering strictly positive real lemma is presented. The stability analysis of two types of MDOF nonlinear systems (stiffening and softening) has been presented using the proposed approach. The explicit algorithm is formulated for a generic nonlinear MDOF system represented by a general nonlinear restoring force vector. In this study, the *l*–th basic resisting force of the system is a nonlinear function bounded in the sector between $\bar{k}^l_{Min}\bar{u}^l$ and $\bar{k}^l_{Max}\bar{u}^l$, where $\bar{k}^l_{Min}$ and $\bar{k}^l_{Max}$ are lower and upper bounds for the *l*–th basic resisting force of the system and $\bar{u}^l$ is a linear combination of the DOFs. Based on this formulation, the approach transforms the stability analysis to investigating the strictly positive realness of the transfer function matrix for the formulated system. Furthermore, this is equivalent to a problem of convex optimization that can be solved numerically. *A sufficient condition*, in terms of the difference between the upper and lower bounds of each basic resisting force of the system, where the explicit algorithm is stable in the sense of Lyapunov can be obtained numerically. Moreover, the explicit algorithm is *asymptotically stable* if the basic resisting force vector is strictly within a specific range defined in Eq. (5.49).

- The proposed approach to investigate the Lyapunov stability of the explicit Newmark and the generalized-α predictor-corrector explicit algorithms is demonstrated by several numerical examples of nonlinear SDOF and MDOF systems with stiffening or softening structural behavior. The structural systems investigated in these numerical examples include a bridge system and multi-story (number of stories ranging from 1 to 25) shear building systems. Detailed results from these examples have been presented. Moreover, detailed Lyapunov stability analysis has been demonstrated by an example of a nonlinear 2-story shear building. For the multi-story shear building, the difference between the upper and lower bounds of the stiffness of the first story (δ^1), where high levels of nonlinearity may occur, is observed to increase with the increase of the damping values. It was also observed that δ^1 increases with the increase of the number of stories for the stiffening system or softening system with low damping. On the other hand, δ^1 decreases with the increase of the number of stories for the softening system with high damping. It is noted that the matrix $\bar{\mathbf{k}}$, representing the difference between the upper and lower bounds of the basic resisting force of the system, depends on the selection of the coefficient matrix and the cost function. In conclusion, the proposed approach is shown to be applicable for investigating the Lyapunov stability of explicit direct integration algorithms used to determine the dynamic response of nonlinear MDOF structural systems.

- Solutions for overcoming the problems of convergence associated with the NTHA of RC highway bridges is presented in terms of efficient direct integration algorithms. For this

purpose, the applicability of the explicit OS and implicit TRBDF2 has been investigated for three RC highway bridges in California. The simulations of the investigated three bridges show that the OS and TRBDF2 algorithms provide very close results to those of the IN algorithm. Moreover, the TRBDF2 algorithm shows improved convergence performance as compared to the IN algorithm. Accordingly, the OS and TRBDF2 are suitable alternatives to the IN for NTHA of RC highway bridges.

- For the implicit integration methods, Newton-Raphson with Line Search is observed to be the most suitable initial nonlinear solver in terms of convergence. Accordingly, an analyst can start with this method as the initial solver in the first simulation trial of an analytical model.

- The sequence of the nonlinear solvers after a proper selection of the initial solver is observed to be insignificant. Accordingly, an analyst should pay more attention to the determination of the initial solver than the determination of the sequence of the subsequent solvers in the NTHA.

- Simulations with the convergence test based on the Energy Increment lead to the same solution with significantly less number of iterations compared to other convergence tests. Accordingly, an analyst can consider the Energy Increment test in the first simulation trial of an analytical model subjected to NTHA.

- Simulations conducted with tolerances of 10^{-5} and 10^{-8} selected for the Energy Increment test for all the integration time steps (of the simulation) are observed to result in very similar response calculations. Accordingly, the increase of the convergence tolerance for the integration time steps with convergence problems is a valid option to achieve convergence improvement.

- Use of a smaller integration time step during the simulation does not necessarily improve the convergence behavior. However, selective reduction of the integration time step, i.e., only when needed, is useful to overcome the convergence problems, as long as the integration time step is reset to its original value after completion of the reduced time steps representing the original size of a time step. This resetting process is essential to prevent the simulation from being completed before the duration of the ground motion input.

- Adaptive switching of integration algorithms shows improved convergence performance as compared to the use of IN algorithm only. Therefore, use of explicit integrators, e.g., OS algorithm, only at the numerically problematic steps is a viable and effective option to overcome the problems of convergence.

- The efficacy of the proposed solutions is presented for a challenging subject in the context of PBEE that requires a large number of NTHA. This subject is the identification of predominantly first-mode *EDP*s under earthquake excitation by making use of different GMSM methods. In that regard, 1,440 NTHA were conducted where a significant number of problems related to convergence were encountered and overcome using the proposed solutions. The results obtained from these NTHA indicate that the higher mode effects are more pronounced on column displacements and deck accelerations than on column shear forces. Therefore, the column base shear is likely to be a first-mode dominant *EDP*, irrespective of the hazard level. Moreover, the effect of higher modes is observed to increase with increasing the hazard level and the nonlinearity.

- Taking advantage of the PBEE approach, a framework for probabilistic evaluation of the GMSM procedures is developed in the context of a selected large earthquake scenario with bidirectional GM excitations.
- Two intensity measures are selected to account for the distinct behaviors in the longitudinal and the transverse directions of the bridge structures. A non-parametric inference, multivariate kernel density estimation, is utilized to estimate the joint probability density function (PDF) of the two intensity measures.
- The structural collapse scenario, including the uncertainty of the collapse criteria, is considered and incorporated into the *PDSD* estimate. The conditional probability of collapse and that of *EDP*s are respectively estimated by multivariate binary logistic and linear regressions.
- The reference benchmark *PDSD* is developed on the basis of equally treating the probability of earthquake occurrence at six different intercept angles between the direction of the earthquake and that of the longitudinal axis of the bridge. The difference of the *PDSD* estimate from each intercept angle and the benchmark is generally below 10% but can be up to 20% in few cases. Thus, the effect of the intercept angle on *PDSD* estimates is considerable.
- The procedures of the benchmark *PDSD* development in the context of a given large earthquake scenario can be readily extended to the case of multiple earthquake scenarios. Future investigation will focus on simulations considering such multiple scenarios.
- In general, the *PDSD* estimates from the amplitude scaling procedure using the spectral acceleration at the fundamental period (T_1) with special attention to the pulse-like GMs, $S_a(T_1)_p$, are larger and more accurate than the ones estimated from the $S_a(T_1)$ procedure without special consideration of the pulse-like GMs. The $S_a(T_1)$ and $S_a(T_1)_p$ procedures present certain superiority over the spectrum shape matching procedure using the conditional mean spectrum (*CMS*) while all three procedures underestimate the seismic demands for some bridges.
- The *PDSD* estimates by the spectrum shape matching procedure using the unconditional selection (*US*) are almost always on the conservative side and accordingly the most conservative of all investigated GMSM procedures. The RC highway bridges are essential lifelines of the transportation infrastructure and thus their possible long downtime after severe earthquakes is not affordable for both the emergency response and community resiliency. Thus, among all four investigated GMSM procedures, it is recommended to use the *US* for selection and modification of GMs.

10.3 FUTURE EXTENSIONS

Several research topics that are appropriate for future investigations can be extended from this study. A list of such topics is given below:

1. Implement the proposed Lyapunov-based nonlinear equation solver in some software framework, e.g., OpenSees, and apply it to more complex structural systems, e.g., RC highway bridge systems utilized in this dissertation.
2. Develop a new parameterized direct integration algorithm on the basis of Lyapunov stability theory and considering its applicability for nonlinear problems to investigate the stability performance.
3. In this study, the distributions of the intercept angle for input GMs, the threshold drift ratio for failure criterion, and the *EDP*s conditioning on the intensity measures are respectively assumed to be of uniform, gamma, and lognormal distributions. These three assumptions can be revisited considering, e.g., the Kernel Density Maximum Entropy Method (KDMEM), refer to [Alibrandi and Mosalam, 2016], which is a method that determines the least biased distribution of a random variable from a sample data, which is very useful for good approximations of the tails (corresponding to low probability as in collapse) of the distribution.
4. Stochastic GM simulated procedure can be included in the evaluation process.
5. The GMSM selection and evaluation can be extended to the case of multiple earthquake scenarios.

Bibliography

Abramowitz, M. and Stegun, I. A. (1972). *Handbook of Mathematical Functions with Formulas, Graphs, and Mathematical Tables*, Dover Publications, New York.

Alibrandi U. and Mosalam K. M. (2016). "Kernel Density Maximum Entropy with Generalized Moments for the Evaluation of Probability Distributions and Applications to Seismic Fragility Functions," *under preparation*.

Aviram, A., Mackie, K. R. and Stojadinović, B. (2008). *Guidelines for Nonlinear Analysis of Bridge Structures in California*, Pacific Earthquake Engineering Research Center, 2008/03, University of California, Berkeley, CA.

Akkar, S. and Küçükdoğan, B. (2008). "Direct use of PGV for estimating peak nonlinear oscillator displacements," *Earthquake Engineering and Structural Dynamics*, 37(12), 1411–1433.

Akkar, S. and Özen, Ö. (2005). "Effect of peak ground velocity on deformation demands for SDOF systems," *Earthquake Engineering and Structural Dynamics*, 34(13), 1551–1571.

Baker, J. W. (2007). "Probabilistic structural response assessment using vector-valued intensity measures," *Earthquake Engineering and Structural Dynamics*, 36(13), 1861–1883.

Baker, J. W. (2011). "Conditional mean spectrum: Tool for ground-motion selection," *ASCE Journal of Structural Engineering*, 137(3), 322–331.

Baker, J. W. and Cornell, C. A. (2005). "A vector-valued ground motion intensity measure consisting of spectral acceleration and epsilon," *Earthquake Engineering and Structural Dynamics*, 34(10), 1193–1217.

Baker J. W., Lin T. and Shahi S. K. (2011). *New Ground Motion Selection Procedures and Selected Motions for the PEER Transportation Research Program*, Pacific Earthquake Engineering Research Center, 2011/03, University of California, Berkeley, CA.

Bank, R. E., Coughran, W. M., Fichter, W., Grosse, E.H., Rose, D.J. and Smith, R.K. (1985). "Transient simulations of silicon devices and circuits," *IEEE Transactions on Computer-Aided Design*, 4, 436–451.

Bathe, K. J. (2006). *Finite Element Procedures*, Prentice Hall, Englewood Cliffs, N.J.

Bathe, K. J. (2007). "Conserving Energy and Momentum in Nonlinear Dynamics: A Simple Implicit Time Integration Scheme," *Computers and Structures*, 83(31–32), 437–445.

Bathe, K. J. and Baig, M. M. I. (2005). "On a composite implicit time integration procedure for nonlinear dynamics," *Comput. Struct.*, 83, 2513–2524.

Bathe, K. J. and Cimento, A. P. (1980). "Some Practical Procedures for the Solution of Nonlinear Finite Element Equations," *Computer Methods in Applied Mechanics and Engineering*, 22, 59-85.

Bathe, K. J. and Wilson, E. L. (1972). "Stability and accuracy analysis of direct integration methods," *Earthquake Engineering and Structural Dynamics*, 1(3), 283–291.

Beléndez, A., Pascual, C., Méndez, D. I., Beléndez, T. and Neipp, C. (2007). "Exact solution for the nonlinear pendulum," *Revista Brasileira de Ensino de Física*, 29(4), 645–648.

Benzoti, G., Ohtaki, T., Pristley, M. J. N., Seible, F. (1996). *Seismic performance of circular reinforced concrete columns under varying axial load*, Division of Structural Engineering, 96/04, University of California, San Diego, CA.

Boyd, S., El Ghaoui L., Feron E. and Balakrishnan V. (1994). *Linear Matrix Inequalities in System and Control Theory*, SIAM, Philadelphia, PA.

Boyd, S. and Vandenberghe, L. (2004). *Convex Optimization*, Cambridge University Press, Cambridge, UK.

Bradley, B. A. (2010). "A generalized conditional intensity measure approach and holistic ground-motion selection," *Earthquake Engineering and Structural Dynamics*, 39(12), 1321–1342.

Bradley, B. A. (2012). "The seismic demand hazard and importance of the conditioning intensity measure," *Earthquake Engineering and Structural Dynamics*, 41(11), 1417–1437.

Bradley, B. A. (2013). "A comparison of intensity-based demand distributions and the seismic demand hazard for seismic performance assessment," *Earthquake Engineering and Structural Dynamics*, 42(15), 2235–2253.

Broyden, C. G. (1965). "A Class of Methods for Solving Nonlinear Simultaneous Equations," *Mathematics of Computation*, 19(92), 577–593.

Broyden, C. G. (1970). "The convergence of a double-rank minimisation. 2: The new algorithm," *IMA Journal of Applied Mathematics*, 6(3), 222–231.

Botev, Z. I., Grotowaski, J. F. and Kroese, D. P. (2010). "Kernel density estimation via diffusion," *The Annals of Statistics*, 38(5), 2916–2957.

Cains, P. E. *Linear Stochastic Systems*, New York, Wiley, 1989.

Caltrans SDC 1.6 (2010), *Caltrans Seismic Design Criteria*, Version 1.7, California Department of Transportation, Sacramento, CA.

Caltrans SDC 1.7 (2013), *Caltrans Seismic Design Criteria*, Version 1.7, California Department of Transportation, Sacramento, CA.

Campbell, K. W. and Bozorgnia, Y. (2008). "NGA Ground Motion Model for the Geometric Mean Horizontal Component of PGA, PGV, PGD and 5% Damped Linear Elastic Response Spectra for Periods Ranging from 0.01 to 10s," *Earthquake Spectra*, 24(1), 139–171.

Chen, C. and Ricles, J. M. (2008). "Stability analysis of direct integration algorithms applied to nonlinear structural dynamics," *ASCE Journal of Engineering Mechanics*, 134(9), 703–711.

Chopra, A. K. (2006). *Dynamics of Structures: Theory and Applications to Earthquake Engineering*, Pearson Prentice Hall, 3rd Edition, Upper Saddle River, N.J.

Chung, J., and Hulbert G. M. (1993). "A Time Integration Algorithm for Structural Dynamics with Improved Numerical Dissipation: The Generalized-α Method," *ASME Journal of Applied Mechanics*, 60(2), 371–375.

Combescure, D. and Pegon, P. (1997). "α-Operator splitting time integration technique for pseudodynamic testing error propagation analysis," *Soil Dynamics and Earthquake Engineering*, 16, 427–443.

Cornell, C. A. and Krawinkler, H. (2000). Progress and challenges in seismic performance assessment, *PEER Center News*, 3(2), 1–3.

Crisfield, M. A. (1991). *Non-linear finite element analysis of solids and structures*, Vol. 1, Wiley, New York.

CVX Research, Inc. (2011). *CVX: Matlab software for disciplined convex programming*, version 2.0. http://cvxr.com/cvx

Dormand, J. R. and Prince, P. J. (1980). "A family of embedded Runge-Kutta formulae," *Journal of Computational and Applied Mathematics*, 6(1), 19–26.

Franklin, G. F., Powell J. D. and Emami-Naeini A. (2015). *Feedback Control of Dynamic Systems*, 7th Edition, Pearson Higher Education Inc., Upper Saddle River, N.J.

Fletcher, R. (1970). "A new approach to variable metric algorithms," *Computer Journal*, 13, 317–322.

Goldfarb, D. (1970). "A family of variable-metric methods derived by variational means," *Mathematics of Computation*, 24(109), 23–26.

Günay, S. and Mosalam, K.M. (2013). "PEER performance-based earthquake engineering methodology, revisited," *Journal of Earthquake Engineering*, 17(6), 829–858.

Haddad, W. M. and Chellaboina V. (2008). *Nonlinear Dynamical Systems and Control: A Lyapunov-Based Approach*, Princeton Universtiy Press, Princeton, N.J.

Hancock, J., Bommer, J. J. and Stafford, P. J. (2008). "Numbers of scaled and matched accelerograms required for inelastic dynamic analyses," *Earthquake Engineering and Structural Dynamics*, 37(14), 1585–1607.

Härdle, W., Muller, M., Sperlich, S. and Werwatz, A. (2004) *Nonparametric and Semiparametric Models: An Introduction*, Springer New York.

Haselton, C. B., Baker, J. W., Bozorgnia, Y., Goulet, C. A., Kalkan, E., Luco, N., Shantz, T. J., Shome, N., Stewart, J. P., Tothong, P., Watson-Lamprey, J. A. and Zareian, F. (2009). *Evaluation of Ground Motion Selection and Modification Methods: Predicting Median Interstory Drift Response of Buildings*, Pacific Earthquake Engineering Research Center, 2009/01, University of California, Berkeley, CA.

Hayden, C., Bray, J., Abrahamson, N. and Acevedo-Cabrera, A. L. (2012). "Selection of Near-Fault Pulse Motions for Use in Design," *15th International World Conference on Earthquake Engineering (15WCEE)*, Lisbon, Portugal.

Heo, Y., Kunnath, S. K. and Abrahamson, N. (2010). "Amplitude-scaled versus spectrum-matched ground motions for seismic performance assessment," *ASCE Journal of Structural Engineering*, 137(3), 278–288.

Hilber, H. M., Hughes, T. J. R., and Taylor, R. L. (1977). "Improved numerical dissipation for time integration algorithms in structural mechanics," *Earthquake Engineering and Structural Dynamics*, 5(3), 283–292

Hughes, T. J. R. (1976). "Stability, convergence and growth and decay of energy of the average acceleration method in nonlinear structural dynamics," *Computers and Structures*, 6(4–5), 313–324.

Hughes, T. J. R. (1987). The finite-element method Linear static and dynamic finite-element analysis, Prentice-Hall, Englewood Cliffs, N.J.

Hughes, T. J. R., Pister, K. S. and Taylor, R. L. (1979). "Implicit-Explicit Finite Elements in Nonlinear Transient Analysis," *Computational Methods in Applied Mechanics and Engineering*, 17(18), 159–182.

Hulbert G. M., and Chung J. (1996). "Explicit Time Integration Algorithms for Structural Dynamics with Optimal Numerical Dissipation," *Computational Methods in Applied Mechanics and Engineering*, 137(2), 175–188.

Hutchinson, T. C., Chai, Y. H. and Boulanger, R. W. (2004). "Inelastic seismic response of extended pile-shaft-supported bridge structures," *Earthquake Spectra*, 20(4), 1057–1080.

Jayaram, N., Lin, T., Baker, J. W. (2011). "A Computationally Efficient Ground-Motion Selection Algorithm for Matching a Target Response Spectrum Mean and Variance," *Earthquake Spectra*, 27(3), 797–815.

Kalkan, E., Chopra, A. K. (2011). "Modal-pushover-based ground-motion scaling procedure," *ASCE Journal of Structural Engineering*, 137, 298–310.

Kapila, V., and Haddad, W. M. (1996). "A Multivariable Extension of the Tsypkin Criterion Using a Lyapunov-Function Approach," *IEEE Transactions on Automatic Control*, 41(1), 149–152.

Katsanos, E. I., Sextos, A. G. and Manolis, G. D. (2010). "Selection of earthquake ground motion records: A state-of-the-art review from a structural engineering perspective," *Soil Dynamics and Earthquake Engineering*, 30(4), 157–169.

Kappos A. J., Gkatzogias K. I., Gidaris I. G. (2013). "Extension of Direct Displacement-Based Design Methodology for Bridges to Account for Higher Mode Effects," *Earthquake Engineering and Structural Dynamics*, 42, 581–602.

Kaviani, P., Zareian, F. and Taciroglu, E. (2012). "Seismic Behavior of Reinforced Concrete Bridges with Skew-Angled Seat-Type Abutments," *Engineering Structure*, 45, 137–150.

Kaviani, P., Zareian, F. and Taciroglu, E. (2014). *Performance-Based Seismic Assessment of Skewed Bridges*, Pacific Earthquake Engineering Research Center, 2014/01, University of California, Berkeley, CA.

Khalil, H. K. (2002). *Nonlinear Systems*, Pearson Prentice Hall, 3rd Edition, Upper Saddle River, N.J.

Kottenstette, N. and Antsaklis P. J. (2010). "Relationship Between Positive Real, Passive Dissipative, & Positive Systems," *Proceeding of American Control Conference*, Baltimore, MD, USA.

Kottke, A, and Rathje, E. M. (2008). "A semi-automated procedure for selecting and scaling

recorded earthquake motions for dynamic analysis," *Earthquake Spectra*, 24(4), 911–932.

Krizhevsky, A. and Hinton, G. (2009). *Learning multiple layers of features from tiny images*, Technical report, 2009/4/8, University of Toronto.

Küçükdoğan, B. (2007). Investigation of the effect of ground-motion intensity measures on seismic demand parameters using probabilistic methods. *M.Sc. Thesis*, Department of Civil Engineering, Middle East Technical University, Ankara, Turkey.

Kuhl D. and Crisfield M. A. (1999) "Energy Conserving and Decaying Algorithms in Non-Linear Structural Dynamics," *International Journal for Numerical Methods in Engineering*, 45, 569–599.

Kunimatsu, S., Sang-Hoon K., Fujii T., and Ishitobi M. (2008). "On Positive Real Lemma for Non-minimal Realization Systems," *Proceeding of the 17th World Congress, the International Federation of Automatic Control* (*IFAC*), Seoul, Korea.

Kunnath, S. K. (2006). *Application of the PEER PBEE Methodology to the I-880 Viaduct*, Pacific Earthquake Engineering Research Center, 2006/10, University of California, Berkeley, CA.

Kunnath, S. K., Larson, L., and Miranda, E. (2006). "Modeling considerations in probabilistic performance-based seismic evaluation: case study of the I-880 viaduct," *Earthquake Engineering and Structural Dynamic*, 35(1), 57–75.

Kurama, Y. C. and Farrow, K. T. (2003). "Ground motion scaling methods for different site conditions and structure characteristics," *Earthquake Engineering and Structural Dynamics*, 32(15), 2425–2450.

Kwong, N. S. and Chopra, A. K. (2016). "Evaluation of the exact conditional spectrum and generalized conditional intensity measure methods for ground motion selection," *Earthquake Engineering and Structural Dynamics*, 45(5), 757–777.

Kwong, N. S., Chopra, A. K., and McGuire, R. K. (2015). "A framework for the evaluation of ground motion selection and modification procedures," *Earthquake Engineering and Structural Dynamics*, 44(5), 795–815.

Lee L. and Chen J. (2003). "Strictly Positive Real Lemma and Absolutely Stability for Discrete-Time Descriptor Systems," *IEEE Transactions on Circuits System I: Fundamental Theory and Applications*, 50(6), 788–794.

Liang, X. and Mosalam, K. M. (2015). *Lyapunov Stability and Accuracy of Direct Integration Algorithms in Nonlinear Dynamic Problems and Considering the Strictly Positive Real Lemma*, SEMM Technical Report UCB/SEMM-2015/01, April.

Liang, X. and Mosalam, K. M. (2016a). "Lyapunov Stability and Accuracy of Direct Integration Algorithms Applied to Nonlinear Dynamic Problems," *ASCE Journal of Engineering Mechanics*, 142(5), 04016022.

Liang, X. and Mosalam, K. M. (2016b). "Lyapunov Stability Analysis of Explicit Direct Integration Algorithms Considering Strictly Positive Real Lemma," *ASCE Journal of Engineering Mechanics*, 10.1061/(ASCE)EM.1943-7889.0001143, 04016079.

Liang, X. and Mosalam, K. M. (2016c). "Lyapunov Stability Analysis of Explicit Direct Integration Algorithms Applied to Multi-Degree of Freedom Nonlinear Dynamic Problems,"

ASCE Journal of Engineering Mechanics, 10.1061/(ASCE)EM.1943-7889.0001162, in press and available online.

Liang, X. and Mosalam, K. M. (2016d). "Stability Investigation of Direct Integration Algorithms Using Lyapunov-Based Approaches," *7th International Conference on Computational Methods* (*ICCM 2016*), Berkeley, CA, August 1-4.

Liang, X. and Mosalam, K. M. (2016e). "Probabilistic Evaluation of Ground Motion Selection and Modification Procedures for Reinforced Concrete Highway Bridges," *submitted to Earthquake Engineering and Structural Dynamics*.

Liang, X. and Mosalam, K. M. (2017). "Probabilistic Evaluation of Ground Motion Selection and Modification Procedures for Reinforced Concrete Highway Bridges," *submitted to the 16th World Conference on Earthquake Engineering* (*16WCEE*), Santiago, Chile, January 9-13.

Liang, X., Günay, S. and Mosalam, K. M. (2014a). "Seismic Response of Bridges Considering Different Ground Motion Selection Methods," *Istanbul Bridge Conference*, Istanbul, Turkey, August 11-13.

Liang, X., Günay, S. and Mosalam, K. M. (2014b). "Integrators for Nonlinear Response History Analysis: Revisited," *Istanbul Bridge Conference*, Istanbul, Turkey, August 11-13.

Liang, X., Günay, S. and Mosalam, K. M. (2016a). *Chapter 12: Seismic Response of Bridges Considering Different Ground Motion Selection Methods*, in *Developments in International Bridge Engineering*, Springer Tracts on Transportation and Traffic 9, Springer Int. Publishing, Switzerland.

Liang, X., Mosalam, K. M. and Günay, S. (2016b), "Direct Integration Algorithms for Efficient Nonlinear Seismic Response of Reinforced Concrete Highway Bridges," *ASCE Journal of Bridge Engineering*, 21(7), 04016041.

Lin, T., Haselton, C. B. and Baker, J. W. (2013). "Conditional spectrum-based ground motion selection. Part I: Hazard consistency for risk-based assessments," *Earthquake Engineering and Structural Dynamics*, 42(12), 1847–1865.

Lin, T., Harmsen, S. C., Baker, J. W. and Luco, N. (2013). "Conditional spectrum computation incorporating multiple causal earthquakes and ground-motion prediction models," *Bulletin of the Seismological Society of America*, 103(2A), 1103–1116.

Luco, N., Cornell, C. A. (2007). "Structure-specific scalar intensity measures for near-source and ordinary earthquake ground motions," *Earthquake Spectra*, 23(2), 357–392.

Lyapunov, A. M. (1892). The General Problem of the Stability of Motion (In Russian), *Doctoral dissertation*, Kharkov National University, Ukraine.

MacRae, G.A., and Kawashima, K. (1997). "Post-earthquake Residual Displacements of Bilinear Oscillators," *Earthquake Engineering and Structural Dynamics*, 26(7), 701–716.

Mander, J. B., Priestley, M. J. N., Park, R. (1988). "Theoretical stress-strain model for confined concrete," *ASCE Journal of Engineering*, 114(8), 1804–1825.

Mathworks, Inc. (2015). *MATLAB*, Version 7.0, Natick, Mass.

McKenna, F., Fenves, G. L. and Filippou, F. C. (2010). *The Open System for Earthquake Engineering Simulation*, University of California, Berkeley, CA.

Milando, F. (2009). "Continuous Newton's Method for Power Flow Analysis," *IEEE Transactions on Power Systems*, 24(1), 50–57.

Moehle, J. P. and Deierlein G. G. (2004). "A Framework Methodology for Performance-based Earthquake Engineering," *13th International World Conference on Earthquake Engineering (13WCEE)*, Vancouver, Canada.

Mosalam, K. M., Liang, X., Günay, S. and Schellenberg, A. (2013). "Alternative Integrators and Parallel Computing for Efficient Nonlinear Response History Analyses," *4th International Conference on Computational Methods in Structural Dynamics and Earthquake Engineering* (*COMPDYN*), Kos Island, Greece.

Naeim, F., Alimoradi, A. and Pezeshk, S. (2004). "Selection and Scaling of Ground Motion Time Histories for Structural Design Using Genetic Algorithms," *Earthquake Spectra*, 20(2), 413-426.

Nakashima, M., Kaminosono, T., Ishida, M., Ando, K. (1990). "Integration technique for substructure pseudodynamic test," *Proceedings of the 4th U.S. National Conference on Earthquake Engineering*, Palm Springs, CA, 12, 515–524.

Newmark, N. M. (1959). "A method of computation for structural dynamics," *ASCE Journal of Engineering Mechanics Division*, 85(3), 67–94.

Omrani R., Mobasher B., Liang, X., Günay, S., Mosalam, K. M., Zareian, F. and Taciroglu, E. (2015). *Guidelines for Nonlinear Seismic Analysis of Ordinary Bridges: Version 2.0*, CA 15-2266, California Department of Transportation, Sacramento, CA.

OpenSees Wiki: <http://opensees.berkeley.edu/wiki/index.php/Command_Manual> (Last Access: July, 2016).

PEER (Pacific Earthquake Engineering Research Center) (2011). *PEER NGA Ground Motion Database*, http://peer.berkeley.edu/nga.

Rezaeian, S. and Der Kiureghian, A. (2011). "Simulation of Orthogonal Horizontal Ground Motion Components for Specified Earthquake and Site Characteristics," *Earthquake Engineering and Structural Dynamics*, 41(2), 335-353.

Riddell, R. (2007). "On ground motion intensity indices," *Earthquake Spectra*, 23(1), 147–173.

Scott, M.H. and Fenves, G.L. (2010). "Krylov Subspace Accelerated Newton Algorithm: Application to Dynamic Progressive Collapse Simulation of Frames," *ASCE Journal of Structural Engineering*, 136, 473-480.

Shanno, D. F. (1970). "Conditioning of quasi-Newton methods for function minimization," *Mathematics of Computation*, 24, 322–334.

Shome, N. (1999). Probabilistic seismic demand analysis of nonlinear structures, *Ph.D. Thesis*, Stanford University, CA.

Shome, N., Cornell, C. A., Bazzurro, P. and Carballo, J. E. (1998). "Earthquakes, records, and nonlinear response," *Earthquake Spectra*, 14(3), 469–500.

Spacone, E., Filippou, F. C. and Taucer, F. F. (1996). "Fibre beam-column model for non-linear analysis of R/C frames: Part I. Formulation," *Earthquake Engineering and Structural Dynamics*, 25(7), 711–726.

Tamma K. K., Zhou X., and Sha D. (2000). "The Time Dimension: A Theory Towards the Evolution, Classification, Characterization and Design of Computational Algorithms for Transient/Dynamic Applications," *Archives of Computational Methods in Engineering*, 7(2), 67–290.

Tothong, P., Luco, N. (2007). "Probabilistic seismic demand analysis using advanced ground motion intensity measures," *Earthquake Engineering and Structural Dynamics*, 36(13), 1837–1860.

Vamvatsikos, D. and Cornell, C. A. (2004). "Applied incremental dynamic analysis," *Earthquake Spectra*, 20(2), 523–553.

Wasserman, L. (2010). *All of statistics: a concise course in statistical inference*, Springer, New York.

Watson-Lamprey, J. A., Abrahamson, N. (2006). "Selection of ground motion time series and limits on scaling," *Soil Dynamics and Earthquake Engineering*, 26(5), 477–482.

Xiao, C., and Hill, D. J. (1999). "Generalizations and New Proof of the Discrete-Time Positive Real Lemma and Bounded Real Lemma," *IEEE Transactions on Circuits System I: Fundamental Theory and Applications*, 46(6), 740–743.

Xie, N., Torelli, F., Bompard, E. and Vaccaro, A. (2013). "Dynamic computing paradigm for comprehensive power flow analysis," *IET Generation, Transmission and Distribution*, 7(8), 832–842.

Zhong H. G., and Crisfield M. A. (1998). "An energy conserving co-rotational procedure for the dynamics of shell structures," *Engineering Computations*, 15(5): 552–576.

Appendix A: Base Functions Used for Numerical Stability Analysis

This Appendix gives an example set of base functions used for numerical stability analysis presented in Chapter 4. This example set includes constant ($\mathbf{\Phi}_1$ to $\mathbf{\Phi}_6$), linear ($\mathbf{\Phi}_7$ to $\mathbf{\Phi}_{12}$) and nonlinear ($\mathbf{\Phi}_{13}$ to $\mathbf{\Phi}_{18}$) base functions.

$$\mathbf{\Phi}_1 = \begin{bmatrix} 1 & 0 & 0 \\ 0 & 0 & 0 \\ 0 & 0 & 0 \end{bmatrix}, \quad \mathbf{\Phi}_2 = \begin{bmatrix} 0 & 0 & 0 \\ 0 & 1 & 0 \\ 0 & 0 & 0 \end{bmatrix}, \quad \mathbf{\Phi}_3 = \begin{bmatrix} 0 & 0 & 0 \\ 0 & 0 & 0 \\ 0 & 0 & 1 \end{bmatrix}, \quad \mathbf{\Phi}_4 = \begin{bmatrix} 0 & 1 & 0 \\ 1 & 0 & 0 \\ 0 & 0 & 0 \end{bmatrix},$$

$$\mathbf{\Phi}_5 = \begin{bmatrix} 0 & 0 & 1 \\ 0 & 0 & 0 \\ 1 & 0 & 0 \end{bmatrix}, \quad \mathbf{\Phi}_6 = \begin{bmatrix} 0 & 0 & 0 \\ 0 & 0 & 1 \\ 0 & 1 & 0 \end{bmatrix}, \quad \mathbf{\Phi}_7 = \begin{bmatrix} \delta_{i+1} & 0 & 0 \\ 0 & 0 & 0 \\ 0 & 0 & 0 \end{bmatrix}, \quad \mathbf{\Phi}_8 = \begin{bmatrix} 0 & 0 & 0 \\ 0 & \delta_{i+1} & 0 \\ 0 & 0 & 0 \end{bmatrix},$$

$$\mathbf{\Phi}_9 = \begin{bmatrix} 0 & 0 & 0 \\ 0 & 0 & 0 \\ 0 & 0 & \delta_{i+1} \end{bmatrix}, \quad \mathbf{\Phi}_{10} = \begin{bmatrix} 0 & \delta_{i+1} & 0 \\ \delta_{i+1} & 0 & 0 \\ 0 & 0 & 0 \end{bmatrix}, \quad \mathbf{\Phi}_{11} = \begin{bmatrix} 0 & 0 & \delta_{i+1} \\ 0 & 0 & 0 \\ \delta_{i+1} & 0 & 0 \end{bmatrix}, \quad \mathbf{\Phi}_{12} = \begin{bmatrix} 0 & 0 & 0 \\ 0 & 0 & \delta_{i+1} \\ 0 & \delta_{i+1} & 0 \end{bmatrix},$$

$$\mathbf{\Phi}_{13} = \begin{bmatrix} \delta_{i+1}^2 & 0 & 0 \\ 0 & 0 & 0 \\ 0 & 0 & 0 \end{bmatrix}, \quad \mathbf{\Phi}_{14} = \begin{bmatrix} 0 & 0 & 0 \\ 0 & \delta_{i+1}^2 & 0 \\ 0 & 0 & 0 \end{bmatrix}, \quad \mathbf{\Phi}_{15} = \begin{bmatrix} 0 & 0 & 0 \\ 0 & 0 & 0 \\ 0 & 0 & \delta_{i+1}^2 \end{bmatrix}, \quad \mathbf{\Phi}_{16} = \begin{bmatrix} 0 & \delta_{i+1}^2 & 0 \\ \delta_{i+1}^2 & 0 & 0 \\ 0 & 0 & 0 \end{bmatrix},$$

$$\mathbf{\Phi}_{17} = \begin{bmatrix} 0 & 0 & \delta_{i+1}^2 \\ 0 & 0 & 0 \\ \delta_{i+1}^2 & 0 & 0 \end{bmatrix}, \quad \mathbf{\Phi}_{18} = \begin{bmatrix} 0 & 0 & 0 \\ 0 & 0 & \delta_{i+1}^2 \\ 0 & \delta_{i+1}^2 & 0 \end{bmatrix}$$

Appendix B: Derivation of α and β for the Bridge Structure

This appendix presents the derivation of **α** and **β** for the MDOF bridge structure depicted in Figure 5.4 to illustrate the Lyapunov-based approach of stability analysis proposed in Chapter 5. In the linear range of the investigated bridge structure, shown in Figure B.1 with identified DOFs and circled element numbers, the restoring forces are as follows:

$$f^1 = \frac{12E_cI_c}{L_1^3}u^1 + \frac{6E_cI_c}{L_1^2}u^2 = \frac{6E_cI_c}{L_1^2}\left(\frac{2}{L_1}u^1 + u^2\right)$$

$$\begin{aligned} f^2 &= \frac{6E_cI_c}{L_1^2}u^1 + \frac{4E_cI_c}{L_1}u^2 + \frac{4E_bI_b}{L_3}u^2 + \frac{4E_bI_b}{L_4}u^2 + \frac{6E_bI_b}{L_3^2}u^3 + \frac{2E_bI_b}{L_3}u^4 - \frac{6E_bI_b}{L_4^2}u^5 + \frac{2E_bI_b}{L_4}u^6 \\ &= \frac{2E_cI_c}{L_1}\left(\frac{3}{L_1}u^1 + 2u^2\right) + \frac{2E_bI_b}{L_3}\left(2u^2 + \frac{3}{L_3}u^3 + u^4\right) + \frac{2E_bI_b}{L_4}\left(2u^2 - \frac{3}{L_4}u^5 + u^6\right) \end{aligned}$$

$$\begin{aligned} f^3 &= \frac{6E_bI_b}{L_3^2}u^2 + \frac{12E_bI_b}{L_3^3}u^3 + \frac{3E_bI_b}{L_2^3}u^3 + \frac{6E_bI_b}{L_3^2}u^4 - \frac{3E_bI_b}{L_2^2}u^4 \\ &= \frac{3E_bI_b}{L_2^2}\left(\frac{1}{L_2}u^3 - u^4\right) + \frac{6E_bI_b}{L_3^2}\left(u^2 + \frac{2}{L_3}u^3 + u^4\right) \end{aligned}$$

$$\begin{aligned} f^4 &= \frac{2E_bI_b}{L_3}u^2 + \frac{6E_bI_b}{L_3^2}u^3 - \frac{3E_bI_b}{L_2^2}u^3 + \frac{4E_bI_b}{L_3}u^4 + \frac{3E_bI_b}{L_2}u^4 \\ &= \frac{3E_bI_b}{L_2}\left(-\frac{1}{L_2}u^3 + u^4\right) + \frac{2E_bI_b}{L_3}\left(u^2 + \frac{3}{L_3}u^3 + 2u^4\right) \end{aligned}$$

$$\begin{aligned} f^5 &= -\frac{6E_bI_b}{L_4^2}u^2 + \frac{12E_bI_b}{L_4^3}u^5 + \frac{3E_bI_b}{L_5^3}u^5 - \frac{6E_bI_b}{L_4^2}u^6 + \frac{3E_bI_b}{L_5^2}u^6 \\ &= \frac{6E_bI_b}{L_4^2}\left(-u^2 + \frac{2}{L_4}u^5 - u^6\right) + \frac{3E_bI_b}{L_5^2}\left(\frac{1}{L_5}u^5 + u^6\right) \end{aligned}$$

$$f^6 = \frac{2E_bI_b}{L_4}u^2 - \frac{6E_bI_b}{L_4^2}u^5 + \frac{3E_bI_b}{L_5^2}u^5 + \frac{4E_bI_b}{L_4}u^6 + \frac{3E_bI_b}{L_5}u^6$$
$$= \frac{2E_bI_b}{L_4}\left(u^2 - \frac{3}{L_4}u^5 + 2u^6\right) + \frac{3E_bI_b}{L_5}\left(\frac{1}{L_5}u^5 + u^6\right)$$

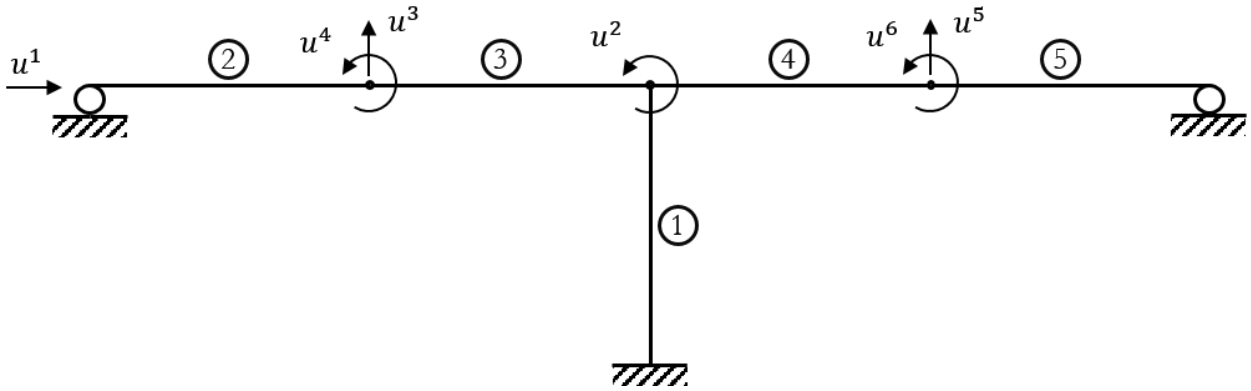

Figure B.1 A MDOF bridge with identified DOFs and element numbers.

Table B.1 List of elements contributing to the restoring force associated with each DOF.

DOF Number	Number of Elements	Associated Elements
1	1	1
2	3	1, 3, 4
3	2	2, 3
4	2	2, 3
5	2	4, 5
6	2	4, 5

Table B.1 shows the list of basic resisting forces that contribute to the restoring force associated with each DOF. For example, only one basic resisting force, which is from the column element (element 1), contributes to the restoring force associated with u^1. Therefore, the total number of the basic resisting forces is $N = 1+3+2+2+2+2 = 12$. Based on the restoring forces in the linear range, redefine the DOFs $\mathbf{u}^T = [u^1, u^2, \ldots, u^6]$ using linear transformation to $\bar{\mathbf{u}}^T = [\bar{u}^1, \bar{u}^2, \ldots, \bar{u}^{12}]$, i.e. $\bar{\mathbf{u}} = \boldsymbol{\beta}\mathbf{u}$, as follows:

$$\bar{u}^1 = \frac{2}{L_1}u^1 + u^2, \quad \bar{u}^2 = \frac{3}{L_1}u^1 + 2u^2, \quad \bar{u}^3 = 2u^2 + \frac{3}{L_3}u^3 + u^4, \quad \bar{u}^4 = 2u^2 - \frac{3}{L_4}u^5 + u^6$$

$$\bar{u}^5 = \frac{1}{L_2}u^3 - u^4, \quad \bar{u}^6 = u^2 + \frac{2}{L_3}u^3 + u^4, \quad \bar{u}^7 = -\frac{1}{L_2}u^3 + u^4, \quad \bar{u}^8 = u^2 + \frac{3}{L_3}u^3 + 2u^4$$

$$\bar{u}^9 = -u^2 + \frac{2}{L_4}u^5 - u^6, \quad \bar{u}^{10} = \frac{1}{L_5}u^5 + u^6, \quad \bar{u}^{11} = u^2 - \frac{3}{L_4}u^5 + 2u^6, \quad \bar{u}^{12} = \frac{1}{L_5}u^5 + u^6$$

Accordingly, the 12×6 matrix $\boldsymbol{\beta}$ can be written as follows:

$$\boldsymbol{\beta}^T = \begin{bmatrix} 2/L_1 & 3/L_1 & 0 & 0 & 0 & 0 & 0 & 0 & 0 & 0 & 0 & 0 \\ 1 & 2 & 2 & 2 & 0 & 1 & 0 & 1 & -1 & 0 & 1 & 0 \\ 0 & 0 & 3/L_3 & 0 & 1/L_2 & 2/L_3 & -1/L_2 & 3/L_3 & 0 & 0 & 0 & 0 \\ 0 & 0 & 1 & 0 & -1 & 1 & 1 & 2 & 0 & 0 & 0 & 0 \\ 0 & 0 & 0 & -3/L_4 & 0 & 0 & 0 & 0 & 2/L_4 & 1/L_5 & -3/L_4 & 1/L_5 \\ 0 & 0 & 0 & 1 & 0 & 0 & 0 & 0 & -1 & 1 & 2 & 1 \end{bmatrix}$$

Defining the *l*–th basic resisting force q^l as a function of $\bar{u}^l, l \in [1, N]$, the restoring forces in the nonlinear range, i.e. $\mathbf{f} = \boldsymbol{\alpha}\mathbf{q}$, can be written as follows:

$$f^1 = q^1, \quad f^2 = q^2 + q^3 + q^4, \quad f^3 = q^5 + q^6, \quad f^4 = q^7 + q^8, \quad f^5 = q^9 + q^{10}, \quad f^6 = q^{11} + q^{12}$$

Accordingly, the 6×12 matrix $\boldsymbol{\alpha}$ can be written as follows:

$$\boldsymbol{\alpha} = \begin{bmatrix} 1 & 0 & 0 & 0 & 0 & 0 & 0 & 0 & 0 & 0 & 0 & 0 \\ 0 & 1 & 1 & 1 & 0 & 0 & 0 & 0 & 0 & 0 & 0 & 0 \\ 0 & 0 & 0 & 0 & 1 & 1 & 0 & 0 & 0 & 0 & 0 & 0 \\ 0 & 0 & 0 & 0 & 0 & 0 & 1 & 1 & 0 & 0 & 0 & 0 \\ 0 & 0 & 0 & 0 & 0 & 0 & 0 & 0 & 1 & 1 & 0 & 0 \\ 0 & 0 & 0 & 0 & 0 & 0 & 0 & 0 & 0 & 0 & 1 & 1 \end{bmatrix}$$

The initial bounds, i.e. lower and upper bounds for stiffening and softening systems, respectively, for the basic resisting forces based on the numerical values in Eqs. (42), are as follows:

$$\bar{k}_I^1 = \frac{6E_cI_c}{L_1^2} = 6\times10^4, \quad \bar{k}_I^2 = \frac{2E_cI_c}{L_1} = 2\times10^6, \quad \bar{k}_I^3 = \frac{2E_bI_b}{L_3} = 2\times10^6, \quad \bar{k}_I^4 = \frac{2E_bI_b}{L_4} = 2\times10^6$$

$$\bar{k}_I^5 = \frac{3E_bI_b}{L_2^2} = 3\times10^4, \quad \bar{k}_I^6 = \frac{6E_bI_b}{L_3^2} = 6\times10^4, \quad \bar{k}_I^7 = \frac{3E_bI_b}{L_2} = 3\times10^6, \quad \bar{k}_I^8 = \frac{2E_bI_b}{L_3} = 2\times10^6$$

$$\bar{k}_I^9 = \frac{6E_bI_b}{L_4^2} = 6\times10^4, \quad \bar{k}_I^{10} = \frac{3E_bI_b}{L_5^2} = 3\times10^4, \quad \bar{k}_I^{11} = \frac{2E_bI_b}{L_4} = 2\times10^6, \quad \bar{k}_I^{12} = \frac{3E_bI_b}{L_5} = 3\times10^6.$$

Therefore, the initial bound matrix $\bar{\mathbf{k}}_I$ is defined as $\bar{\mathbf{k}}_I = \text{diag}[\bar{k}_I^1, \bar{k}_I^2, \ldots, \bar{k}_I^{12}]$.

Appendix C: Derivation of α and β for the Multi-Story Shear Building

This appendix presents the derivation of $\boldsymbol{\alpha}$ and $\boldsymbol{\beta}$ for the MDOF shear building depicted in Figure 5.5. Due to its assumed shear mode behavior, the number of the basic resisting forces, N, is equal to the number of DOFs, n. In the linear range of this shear building, the *j*–th restoring force is as follows:

$$f^j = -\bar{k}_I^j u^{j-1} + \left(\bar{k}_I^j + \bar{k}_I^{j+1}\right)u^j - \bar{k}_I^{j+1}u^{j=1} = \bar{k}_I^j\left(u^j - u^{j-1}\right) - \bar{k}_I^{j+1}\left(u^{j+1} - u^j\right)$$

where $j = l:1 \to n$ with $\bar{k}_I^{n+1} = 0$, $u^0 = 0$ and $\bar{k}_I^j$ is the initial stiffness of the *j*–th story. For such a building, the elements of the $n \times n$ ($N = n$) matrices $\boldsymbol{\alpha}$ and $\boldsymbol{\beta}$ are as follows:

$$\alpha_{jl} = \begin{cases} 1 & j = l,\ j:1 \to n \\ -1 & j = l-1,\ j:1 \to n-1 \\ 0 & otherwise \end{cases} \qquad \beta_{lj} = \begin{cases} 1 & l = j,\ l:1 \to n \\ -1 & l = j+1,\ j:1 \to n-1 \\ 0 & otherwise \end{cases}$$

Thus, the elements of the row vectors $\boldsymbol{\alpha}^j$ and $\boldsymbol{\beta}^l$, based on Eqs. (10) and (12), are as follows:

$$\alpha_l^j = \begin{cases} 1 & l = j,\ j:1 \to n \\ -1 & l = j+1,\ j:1 \to n-1 \\ 0 & otherwise \end{cases} \qquad \beta_j^l = \begin{cases} 1 & j = l,\ l:1 \to n \\ -1 & j = l-1,\ l:1 \to n \\ 0 & otherwise \end{cases}$$

Based on Eqs. (9) and (11), we have

$$f^j = \boldsymbol{\alpha}^j \mathbf{q} = q^l - q^{l+1}$$

$$\bar{\mathrm{u}}^l = \boldsymbol{\beta}^l \mathbf{u} = u^j - u^{j-1} = \Delta u^j$$

where $j = l:1 \to n$ with $q^{n+1} = 0$, $u^0 = 0$ and q^j is the resisting force of the *j*–th story. Therefore, the resisting force of the *j*–th story, q^j, is a function of the relative displacement of the *j*–th story, Δu^j.

Appendix D: Numerical Results for the 2-Story Shear Building

This appendix documents all the numerical results for the 2-story shear building (Figure 5.5 with $n = 2$) with stiffening and softening systems using the Lyapunov-based approach of stability analysis proposed in Chapter 5.

$$\mathbf{A}_e = \begin{bmatrix} -0.0041 & 0.0016 & -0.0082 & 0.0032 & -0.0030 & 0.0015 \\ 0.0016 & -0.0025 & 0.0032 & -0.0050 & 0.0015 & -0.0015 \\ 0.4979 & 0.0008 & 0.9959 & 0.0016 & -0.0015 & 0.0008 \\ 0.0008 & 0.4988 & 0.0016 & 0.9975 & 0.0008 & -0.0008 \\ 0.5000 & 0.0000 & 1.0000 & 0.0000 & 1.0000 & 0.0000 \\ 0.0000 & 0.5000 & 0.0000 & 1.0000 & 0.0000 & 1.0000 \end{bmatrix}$$

$$\mathbf{C} = \begin{bmatrix} 0.5000 & 0.0000 & 1.0000 & 0.0000 & 1.0000 & 0.0000 \\ -0.5000 & 0.5000 & -1.0000 & 1.0000 & -1.0000 & 1.0000 \end{bmatrix}$$

Stiffening Systems

$$\mathbf{P} = \mathbf{P}^T = 10^9 \times \begin{bmatrix} 0.6215 & 0.0978 & 0.5915 & 0.1951 & 0.0029 & -0.0009 \\ & 0.7211 & 0.1954 & 0.7910 & -0.0016 & 0.0027 \\ & & 1.1845 & 0.3906 & 0.0036 & -0.0008 \\ & & & 1.5814 & -0.0022 & 0.0043 \\ & (sym) & & & 0.0033 & -0.0013 \\ & & & & & 0.0020 \end{bmatrix}$$

$$\mathbf{B}_e = \mathbf{B}_1 \boldsymbol{\alpha} = 10^{-5} \times \begin{bmatrix} 0.1504 & 0.0001 & 0.0752 & 0.0001 & 0.0000 & 0.0000 \\ -0.1503 & 0.1504 & -0.0751 & 0.0752 & 0.0000 & 0.0000 \end{bmatrix}^T$$

Softening Systems

$$\mathbf{P} = \mathbf{P}^T = 10^9 \times \begin{bmatrix} 0.6154 & 0.0890 & 0.5773 & 0.1776 & 0.0026 & -0.0008 \\ & 0.7033 & 0.1779 & 0.7357 & -0.0014 & 0.0025 \\ & & 1.1561 & 0.3556 & 0.0034 & -0.0008 \\ & & & 1.5068 & -0.0019 & 0.0040 \\ & (sym) & & & 0.0027 & -0.0011 \\ & & & & & 0.0016 \end{bmatrix}$$

$$\mathbf{B}_e = \mathbf{B}_2\boldsymbol{\alpha} = -\mathbf{B}_1\boldsymbol{\alpha}$$

Appendix E: Documentation of the Utilized Ground Motions in Chapter 8

This appendix documents all the 40 pulse-like GMs utilized to demonstrate the applicability of investigated integration algorithms and nonlinear solvers. Moreover, the GMs utilized for the identification of predominantly first-mode *EDP*s under earthquake excitation are documented in this appendix.

Table E.1 Documentation of 40 pulse-like GMs.

Record Number	NGA Record Sequence Number	Earthquake Name	Station	Magnitude
1	170	Imperial Valley-06	EC County Center FF	6.53
2	171	Imperial Valley-06	EC Meloland Overpass FF	6.53
3	179	Imperial Valley-06	El Centro Array #4	6.53
4	180	Imperial Valley-06	El Centro Array #5	6.53
5	181	Imperial Valley-06	El Centro Array #6	6.53
6	182	Imperial Valley-06	El Centro Array #7	6.53
7	183	Imperial Valley-06	El Centro Array #8	6.53
8	184	Imperial Valley-06	El Centro Differential Array	6.53
9	451	Morgan Hill	Coyote Lake Dam (SW Abut)	6.19
10	763	Loma Prieta	Gilroy-Gavilan Coll.	6.93
11	779	Loma Prieta	LGPC	6.93
12	879	Landers	Lucerne	7.28
13	900	Landers	Yermo Fire Station	7.28
14	982	Northridge-01	Jensen Filter Plant	6.69
15	983	Northridge-01	Jensen Filter Plant Generator	6.69
16	1044	Northridge-01	Newhall-Fire Sta	6.69
17	1045	Northridge-01	Newhall - W Pico Canyon Rd.	6.69
18	1063	Northridge-01	Rinaldi Receiving Sta	6.69
19	1084	Northridge-01	Sylmar-Converter Sta	6.69
20	1085	Northridge-01	Sylmar-Converter Sta East	6.69
21	1086	Northridge-01	Sylmar-Olive View Med FF	6.69
22	1106	Kobe, Japan	KJMA	6.90
23	1119	Kobe, Japan	Takarazuka	6.90
24	1161	Kocaeli, Turkey	Gebze	7.51
25	1197	Chi-Chi, Taiwan	CHY028	7.62
26	1244	Chi-Chi, Taiwan	CHY101	7.62
27	1489	Chi-Chi, Taiwan	TCU049	7.62
28	1492	Chi-Chi, Taiwan	TCU052	7.62
29	1493	Chi-Chi, Taiwan	TCU053	7.62
30	1494	Chi-Chi, Taiwan	TCU054	7.62

Table E.1 (Cont.) Documentation of 40 pulse-like GMs.

Record Number	NGA Record Sequence Number	Earthquake Name	Station	Magnitude
31	1505	Chi-Chi, Taiwan	TCU068	7.62
32	1510	Chi-Chi, Taiwan	TCU075	7.62
33	1511	Chi-Chi, Taiwan	TCU076	7.62
34	1515	Chi-Chi, Taiwan	TCU082	7.62
35	1519	Chi-Chi, Taiwan	TCU087	7.62
36	1528	Chi-Chi, Taiwan	TCU101	7.62
37	1529	Chi-Chi, Taiwan	TCU102	7.62
38	1530	Chi-Chi, Taiwan	TCU103	7.62
39	1546	Chi-Chi, Taiwan	TCU122	7.62
40	1595	Chi-Chi, Taiwan	WGK	7.62

Table E.2 Documentation of 40 GMs of *CMS* group of Bridge A with Type I abutment modeling for 50% POE in 50 years.

Record Number	NGA Record Sequence Number	Earthquake Name	Station	Magnitude	Scaling Factor
1	974	Northridge-01	Glendale-Las Palmas	6.69	1.65
2	1454	Chi-Chi, Taiwan	TAP090	7.62	0.73
3	2116	Denali, Alaska	TAPS Pump Station #12	7.90	2.03
4	1427	Chi-Chi, Taiwan	TAP035	7.62	1.20
5	323	Coalinga-01	Parkfield-Cholame 12W	6.36	2.27
6	1211	Chi-Chi, Taiwan	CHY052	7.62	1.23
7	756	Loma Prieta	Dublin-Fire Station	6.93	1.48
8	464	Morgan Hill	Hollister Diff Array #3	6.19	1.67
9	1293	Chi-Chi, Taiwan	HWA046	7.62	1.68
10	1275	Chi-Chi, Taiwan	HWA026	7.62	1.60
11	1797	Hector Mine	LA-City Terrace	7.13	2.67
12	1206	Chi-Chi, Taiwan	CHY042	7.62	1.36
13	2472	Chi-Chi, Taiwan-03	CHY046	6.20	2.30
14	184	Imperial Valley-06	El Centro Differential Array	6.53	0.37
15	1256	Chi-Chi, Taiwan	HWA002	7.62	2.29
16	993	Northridge-01	LA-Fletcher Dr	6.69	0.71
17	1574	Chi-Chi, Taiwan	TTN022	7.62	1.46
18	1277	Chi-Chi, Taiwan	HWA028	7.62	0.92
19	881	Landers	Morongo Valley	7.28	0.56
20	1094	Northridge-01	West Covina-S Orange Ave	7.62	2.23
21	1541	Chi-Chi, Taiwan	TCU116	7.62	0.68
22	1349	Chi-Chi, Taiwan	ILA066	7.62	1.19
23	1318	Chi-Chi, Taiwan	ILA014	7.62	1.47
24	779	Loma Prieta	LGPC	6.93	0.17
25	1068	Northridge-01	San Bernardino-Co Service	6.69	2.94
26	1247	Chi-Chi, Taiwan	HWA025	7.62	1.18
27	1795	Hector Mine	Joshua Tree N.M.-Keys View	7.62	2.53
28	760	Loma Prieta	Foster City-Menhaden Court	6.93	0.71
29	2743	Chi-Chi, Taiwan-04	CHY087	6.20	2.24
30	1433	Chi-Chi, Taiwan	TAP047	7.62	2.03
31	3342	Chi-Chi, Taiwan-06	HWA029	6.30	2.27
32	1547	Chi-Chi, Taiwan	TCU123	7.62	0.75
33	1452	Chi-Chi, Taiwan	TAP086	7.62	2.55
34	1295	Chi-Chi, Taiwan	HWA049	7.62	1.25
35	126	Gazli, USSR	Karakyr	6.80	0.30
36	266	Victoria, Mexico	Chihuahua	6.33	0.98
37	549	Chalfant Valley-02	Bishop-LADWP South St	6.19	0.92
38	749	Loma Prieta	Berkeley-Strawberry Canyon	6.93	2.58
39	1019	Northridge-01	Lake Hughes #1	6.69	1.11
40	1789	Hector Mine	Hesperia-4th & Palm	7.13	2.09

Table E.3 Documentation of 40 GMs of *CMS* group of Bridge A with Type II abutment modeling for 50% POE in 50 years.

Record Number	NGA Record Sequence Number	Earthquake Name	Station	Magnitude	Scaling Factor
1	974	Northridge-01	Glendale-Las Palmas	6.69	1.24
2	1221	Chi-Chi, Taiwan	CHY052	7.62	0.63
3	860	Landers	Hemet Fire Station	7.28	2.68
4	2490	Chi-Chi, Taiwan-03	CHY074	6.20	1.40
5	1242	Chi-Chi, Taiwan	CHY099	7.62	1.64
6	1427	Chi-Chi, Taiwan	TAP035	7.62	1.43
7	1587	Chi-Chi, Taiwan	TTN042	7.62	2.10
8	1271	Chi-Chi, Taiwan	HWA022	7.62	1.08
9	1256	Chi-Chi, Taiwan	HWA002	7.62	1.89
10	1155	Kocaeli, Turkey	Bursa Tofas	7.51	0.91
11	2699	Chi-Chi, Taiwan-04	CHY024	6.20	2.06
12	2694	Chi-Chi, Taiwan-04	CHY015	6.20	1.16
13	1291	Chi-Chi, Taiwan	HWA044	7.62	1.69
14	851	Landers	Downey-Co Maint Bldg	7.28	2.81
15	1177	Kocaeli, Turkey	Zeytinburnu	7.51	0.98
16	753	Loma Prieta	Corralitos	6.93	0.23
17	3313	Chi-Chi, Taiwan-06	CHY094	6.30	1.90
18	1452	Chi-Chi, Taiwan	TAP086	7.62	2.41
19	1791	Hector Mine	Indio-Coachella Canal	7.13	1.29
20	1120	Kobe, Japan	Takatori	6.90	0.21
21	1211	Chi-Chi, Taiwan	CHY052	7.62	0.96
22	734	Loma Prieta	APEEL 3E Hayward CSUH	6.93	2.07
23	990	Northridge-01	LA-City Terrace	6.69	0.96
24	1318	Chi-Chi, Taiwan	ILA014	7.62	1.41
25	1019	Northridge-01	Lake Hughes #1	6.69	1.24
26	1541	Chi-Chi, Taiwan	TCU116	7.62	0.69
27	1775	Hector Mine	Castaic-Old Ridge Route	7.13	2.57
28	3503	Chi-Chi, Taiwan-06	TCU122	6.30	1.42
29	1426	Chi-Chi, Taiwan	TAP034	7.62	2.13
30	1279	Chi-Chi, Taiwan	HWA030	7.62	1.61
31	796	Loma Prieta	SF-Presidio	6.93	0.96
32	964	Northridge-01	Compton-Castlegate St	6.69	1.47
33	1198	Chi-Chi, Taiwan	CHY029	7.62	0.36
34	850	Landers	Desert Hot Springs	7.28	1.02
35	1445	Chi-Chi, Taiwan	TAP075	7.62	1.72
36	993	Northridge-01	LA-Fletcher Dr	6.69	0.56
37	1210	Chi-Chi, Taiwan	CHY050	7.62	1.91
38	2465	Chi-Chi, Taiwan-03	CHY034	6.20	1.56
39	1345	Chi-Chi, Taiwan	ILA061	7.62	2.22
40	1528	Chi-Chi, Taiwan	TCU101	7.62	0.53

Table E.4 Documentation of 40 GMs of *CMS* group of Bridge A with Type I abutment modeling for 10% POE in 50 years.

Record Number	NGA Record Sequence Number	Earthquake Name	Station	Magnitude	Scaling Factor
1	1238	Chi-Chi, Taiwan	CHY092	7.62	2.43
2	1350	Chi-Chi, Taiwan	ILA067	7.62	1.48
3	547	Chalfant Valley-01	Zack Brothers Ranch	5.77	1.81
4	1176	Kocaeli, Turkey	Yarimca	7.51	0.80
5	838	Landers	Barstow	7.28	1.97
6	900	Landers	Yermo Fire Station	7.28	1.29
7	778	Loma Prieta	Hollister Diff. Array	6.93	0.68
8	1243	Chi-Chi, Taiwan	CHY100	7.62	2.61
9	773	Loma Prieta	Hayward-BART Sta	6.93	2.74
10	1317	Chi-Chi, Taiwan	ILA013	7.62	1.03
11	1329	Chi-Chi, Taiwan	ILA037	7.62	2.45
12	1605	Duzce, Turkey	Duzce	7.14	0.45
13	162	Imperial Valley-06	Calexico Fire Station	6.53	1.70
14	1268	Chi-Chi, Taiwan	HWA017	7.62	2.48
15	756	Loma Prieta	Dublin-Fire Station	6.93	2.90
16	762	Loma Prieta	Fremont-Mission San Jose	6.93	2.34
17	779	Loma Prieta	LGPC	6.93	0.33
18	1206	Chi-Chi, Taiwan	CHY042	7.62	2.66
19	139	Tabas, Iran	Dayhook	7.35	1.40
20	3271	Chi-Chi, Taiwan-06	CHY032	6.30	2.46
21	1303	Chi-Chi, Taiwan	HWA058	7.62	2.18
22	1234	Chi-Chi, Taiwan	CHY086	7.62	1.25
23	1349	Chi-Chi, Taiwan	ILA066	7.62	2.34
24	170	Imperial Valley-06	EC County Center FF	6.53	0.98
25	467	Morgan Hill	Hollister Diff. Array	6.19	2.51
26	1784	Hector Mine	Frink	7.13	2.77
27	1490	Chi-Chi, Taiwan	TCU050	7.62	1.37
28	1263	Chi-Chi, Taiwan	HWA012	7.62	2.53
29	761	Loma Prieta	Fremont-Emerson Court	6.93	1.80
30	772	Loma Prieta	Halls Valley	6.93	1.63
31	1149	Kocaeli, Turkey	Atakoy	7.51	2.84
32	1810	Hector Mine	Mecca-CVWD Yard	7.13	1.98
33	2715	Chi-Chi, Taiwan-04	CHY047	6.20	2.67
34	3276	Chi-Chi, Taiwan-06	CHY037	6.30	1.79
35	1187	Chi-Chi, Taiwan	CHY015	7.62	1.36
36	2714	Chi-Chi, Taiwan-04	CHY046	6.20	2.64
37	1489	Chi-Chi, Taiwan	TCU049	7.62	1.08
38	1048	Northridge-01	Northridge-17645 Saticoy St	6.69	0.73
39	850	Landers	Desert Hot Springs	7.28	1.71
40	1536	Chi-Chi, Taiwan	TCU110	7.62	1.00

Table E.5 Documentation of 40 GMs of *CMS* group of Bridge A with Type II abutment modeling for 10% POE in 50 years.

Record Number	NGA Record Sequence Number	Earthquake Name	Station	Magnitude	Scaling Factor
1	1336	Chi-Chi, Taiwan	ILA048	7.62	1.90
2	3312	Chi-Chi, Taiwan-06	CHY093	6.30	2.92
3	2110	Chi-Chi, Taiwan-02	CHY111	5.90	2.52
4	1332	Chi-Chi, Taiwan	ILA042	7.62	2.03
5	1481	Chi-Chi, Taiwan	TCU038	7.62	1.38
6	1350	Chi-Chi, Taiwan	ILA067	7.62	1.36
7	183	Imperial Valley-06	El Centro Array #8	6.53	0.73
8	1528	Chi-Chi, Taiwan	TCU101	7.62	1.03
9	1810	Hector Mine	Mecca-CVWD Yard	7.13	1.79
10	126	Gazli, USSR	Karakyr	6.80	0.52
11	1211	Chi-Chi, Taiwan	CHY052	7.62	1.88
12	1074	Northridge-01	Sandberg - Bald Mtn	6.69	2.71
13	1508	Chi-Chi, Taiwan	TCU072	7.62	0.51
14	1293	Chi-Chi, Taiwan	HWA046	7.62	2.60
15	1187	Chi-Chi, Taiwan	CHY015	7.62	1.42
16	3503	Chi-Chi, Taiwan-06	TCU122	6.30	2.78
17	1478	Chi-Chi, Taiwan	TCU033	7.62	1.69
18	1206	Chi-Chi, Taiwan	CHY042	7.62	2.89
19	3473	Chi-Chi, Taiwan-06	TCU078	6.30	1.05
20	801	Loma Prieta	San Jose-Santa Teresa Hills	6.93	1.08
21	3271	Chi-Chi, Taiwan-06	CHY032	6.30	2.08
22	1555	Chi-Chi, Taiwan	TCU147	7.62	2.13
23	465	Morgan Hill	Hollister Diff Array #4	6.19	2.96
24	2461	Chi-Chi, Taiwan-03	CHY028	6.20	1.68
25	2458	Chi-Chi, Taiwan-03	CHY025	6.20	2.43
26	3510	Chi-Chi, Taiwan-06	TCU139	6.30	2.14
27	983	Northridge-01	Jensen Filter Plant Generator	6.69	0.58
28	1295	Chi-Chi, Taiwan	HWA049	7.62	2.54
29	1509	Chi-Chi, Taiwan	TCU074	7.62	0.46
30	754	Loma Prieta	Coyote Lake Dam (Downst)	6.93	1.83
31	1049	Northridge-01	Pacific Palisades-Sunset	6.69	1.41
32	300	Irpinia, Italy-02	Calitri	6.20	1.34
33	1177	Kocaeli, Turkey	Zeytinburnu	7.51	1.92
34	2715	Chi-Chi, Taiwan-04	CHY047	6.20	2.50
35	1791	Hector Mine	Indio-Coachella Canal	7.13	2.53
36	1263	Chi-Chi, Taiwan	HWA012	7.62	2.70
37	1427	Chi-Chi, Taiwan	TAP035	7.62	2.80
38	832	Landers	Amboy	7.28	2.36
39	1087	Northridge-01	Tarzana-Cedar Hill A	6.69	0.22
40	1546	Chi-Chi, Taiwan	TCU122	7.62	1.13

Table E.6 Documentation of 40 GMs of *CMS* group of Bridge A with Type I abutment modeling for 2% POE in 50 years.

Record Number	NGA Record Sequence Number	Earthquake Name	Station	Magnitude	Scaling Factor
1	1520	Chi-Chi, Taiwan	TCU088	7.62	2.39
2	1186	Chi-Chi, Taiwan	CHY014	7.62	1.03
3	182	Imperial Valley-06	El Centro Array #7	6.53	0.81
4	1045	Northridge-01	Newhall-W Pico Canyon Rd.	6.69	1.36
5	1155	Kocaeli, Turkey	Bursa Tofas	7.51	2.43
6	1234	Chi-Chi, Taiwan	CHY086	7.62	2.08
7	1794	Hector Mine	Joshua Tree	7.13	2.87
8	1282	Chi-Chi, Taiwan	HWA033	7.62	2.41
9	2632	Chi-Chi, Taiwan-03	TCU084	6.20	2.59
10	776	Loma Prieta	Hollister-South & Pine	6.93	1.32
11	779	Loma Prieta	LGPC	6.93	0.54
12	821	Erzican, Turkey	Erzincan	6.69	0.95
13	900	Landers	Yermo Fire Station	7.28	2.15
14	1489	Chi-Chi, Taiwan	TCU049	7.62	1.79
15	1454	Chi-Chi, Taiwan	TAP090	7.62	2.38
16	1297	Chi-Chi, Taiwan	HWA051	7.62	2.87
17	1204	Chi-Chi, Taiwan	CHY039	7.62	2.81
18	1120	Kobe, Japan	Takatori	6.90	0.66
19	1509	Chi-Chi, Taiwan	TCU074	7.62	0.52
20	1493	Chi-Chi, Taiwan	TCU053	7.62	1.94
21	1495	Chi-Chi, Taiwan	TCU055	7.62	1.82
22	761	Loma Prieta	Fremont-Emerson Court	6.93	2.98
23	1158	Kocaeli, Turkey	Duzce	7.51	1.38
24	723	Superstition Hills-02	Parachute Test Site	6.54	1.06
25	803	Loma Prieta	Saratoga-W Valley Coll.	6.93	1.47
26	1198	Chi-Chi, Taiwan	CHY029	7.62	1.16
27	1201	Chi-Chi, Taiwan	CHY034	7.62	1.09
28	316	Westmorland	Parachute Test Site	5.90	1.99
29	1521	Chi-Chi, Taiwan	TCU089	7.62	1.92
30	1044	Northridge-01	Newhall-Fire Sta	6.69	0.62
31	772	Loma Prieta	Halls Valley	6.93	2.71
32	1187	Chi-Chi, Taiwan	CHY015	7.62	2.26
33	881	Landers	Morongo Valley	7.28	1.84
34	796	Loma Prieta	SF-Presidio	6.93	2.26
35	558	Chalfant Valley-02	Zack Brothers Ranch	6.19	0.84
36	1300	Chi-Chi, Taiwan	HWA055	7.62	2.84
37	1529	Chi-Chi, Taiwan	TCU102	7.62	1.26
38	1481	Chi-Chi, Taiwan	TCU038	7.62	2.43
39	1490	Chi-Chi, Taiwan	TCU050	7.62	2.28
40	755	Loma Prieta	Coyote Lake Dam (SW Abut)	6.93	1.67

Table E.7 Documentation of 40 GMs of *CMS* group of Bridge A with Type II abutment modeling for 2% POE in 50 years.

Record Number	NGA Record Sequence Number	Earthquake Name	Station	Magnitude	Scaling Factor
1	1205	Chi-Chi, Taiwan	CHY041	7.62	0.79
2	1088	Northridge-01	Terminal Island-S Seaside	6.69	2.57
3	412	Coalinga-05	Pleasant Valley P.P.-yard	5.77	1.91
4	1350	Chi-Chi, Taiwan	ILA067	7.62	2.22
5	1201	Chi-Chi, Taiwan	CHY034	7.62	0.92
6	1116	Kobe, Japan	Shin-Osaka	6.90	1.36
7	1481	Chi-Chi, Taiwan	TCU038	7.62	2.25
8	184	Imperial Valley-06	El Centro Differential Array	6.53	1.26
9	755	Loma Prieta	Coyote Lake Dam (SW Abut)	6.93	1.48
10	1509	Chi-Chi, Taiwan	TCU074	7.62	0.76
11	801	Loma Prieta	San Jose-Santa Teresa Hills	6.93	1.77
12	779	Loma Prieta	LGPC	6.93	0.61
13	1456	Chi-Chi, Taiwan	TAP095	7.62	2.08
14	900	Landers	Yermo Fire Station	7.28	2.67
15	1434	Chi-Chi, Taiwan	TAP049	7.62	2.92
16	1810	Hector Mine	Mecca-CVWD Yard	7.13	2.93
17	730	Spitak, Armenia	Gukasian	6.77	2.99
18	1155	Kocaeli, Turkey	Bursa Tofas	7.51	2.93
19	1317	Chi-Chi, Taiwan	ILA013	7.62	1.48
20	1234	Chi-Chi, Taiwan	CHY086	7.62	2.10
21	1165	Kocaeli, Turkey	Izmit	7.51	1.96
22	986	Northridge-01	LA-Brentwood VA Hospital	6.69	2.00
23	1519	Chi-Chi, Taiwan	TCU087	7.62	2.42
24	1292	Chi-Chi, Taiwan	HWA045	7.62	2.79
25	1508	Chi-Chi, Taiwan	TCU072	7.62	0.83
26	1009	Northridge-01	LA-Wadsworth VA Hospital	6.69	2.2
27	1529	Chi-Chi, Taiwan	TCU102	7.62	1.52
28	1187	Chi-Chi, Taiwan	CHY015	7.62	2.33
29	1493	Chi-Chi, Taiwan	TCU053	7.62	2.10
30	2461	Chi-Chi, Taiwan-03	CHY028	6.20	2.75
31	1282	Chi-Chi, Taiwan	HWA033	7.62	2.55
32	1495	Chi-Chi, Taiwan	TCU055	7.62	1.76
33	731	Loma Prieta	APEEL 10-Skyline	6.93	2.85
34	776	Loma Prieta	Hollister-South & Pine	6.93	1.38
35	778	Loma Prieta	Hollister Diff. Array	6.93	1.27
36	1158	Kocaeli, Turkey	Duzce	7.51	1.27
37	1515	Chi-Chi, Taiwan	TCU082	7.62	1.70
38	1048	Northridge-01	Northridge-17645 Saticoy St	6.69	1.08
39	1227	Chi-Chi, Taiwan	CHY074	7.62	1.86
40	2467	Chi-Chi, Taiwan-03	CHY036	6.20	2.94

Table E.8 Documentation of 40 GMs of reference group of Bridge A for 50% POE in 50 years.

Record Number	NGA Record Sequence Number	Earthquake Name	Station	Magnitude	Scaling Factor
1	2650	Chi-Chi, Taiwan-03	TCU116	6.20	3.00
2	2899	Chi-Chi, Taiwan-04	TCU141	6.20	1.60
3	1177	Kocaeli, Turkey	Zeytinburnu	7.51	2.70
4	900	Landers	Yermo Fire Station	7.28	0.80
5	1164	Kocaeli, Turkey	Istanbul	7.51	2.90
6	1315	Chi-Chi, Taiwan	ILA010	7.62	3.00
7	1799	Hector Mine	LA-Obregon Park	7.13	2.80
8	1531	Chi-Chi, Taiwan	TCU104	7.62	0.50
9	1148	Kocaeli, Turkey	Arcelik	7.51	1.20
10	2756	Chi-Chi, Taiwan-04	CHY114	6.20	2.80
11	2695	Chi-Chi, Taiwan-04	CHY016	6.20	2.60
12	1350	Chi-Chi, Taiwan	ILA067	7.62	1.10
13	761	Loma Prieta	Fremont-Emerson Court	6.93	2.20
14	439	Borah Peak, ID-01	TAN-719	6.88	2.80
15	803	Loma Prieta	Saratoga-W Valley Coll.	6.93	0.60
16	2655	Chi-Chi, Taiwan-03	TCU122	6.20	1.50
17	1577	Chi-Chi, Taiwan	TTN025	7.62	2.70
18	833	Landers	Anaheim-W Ball Rd	7.28	2.30
19	776	Loma Prieta	Hollister-South & Pine	6.93	0.70
20	946	Northridge-01	Antelope Buttes	6.69	2.00
21	1049	Northridge-01	Pacific Palisades-Sunset	6.69	1.20
22	1783	Hector Mine	Fort Irwin	7.13	1.10
23	2706	Chi-Chi, Taiwan-04	CHY032	6.20	2.60
24	1762	Hector Mine	Amboy	7.13	1.00
25	780	Loma Prieta	Larkspur Ferry Terminal (FF)	6.93	2.30
26	1358	Chi-Chi, Taiwan	KAU012	7.62	1.90
27	751	Loma Prieta	Calaveras Reservoir	6.93	1.30
28	1206	Chi-Chi, Taiwan	CHY042	7.62	1.90
29	1400	Chi-Chi, Taiwan	NCU	7.62	1.70
30	28	Parkfield	Cholame-Shandon Array #12	6.19	1.40
31	333	Coalinga-01	Parkfield-Cholame 8W	6.36	2.90
32	2994	Chi-Chi, Taiwan-05	CHY116	6.20	2.80
33	1503	Chi-Chi, Taiwan	TCU065	7.62	0.70
34	2646	Chi-Chi, Taiwan-03	TCU109	6.20	2.10
35	792	Loma Prieta	SF-1295 Shafter	6.93	1.20
36	247	Mammoth Lakes-06	Bishop-Paradise Lodge	5.94	2.10
37	2639	Chi-Chi, Taiwan-03	TCU100	6.20	2.40
38	855	Landers	Fort Irwin	7.28	1.50
39	1551	Chi-Chi, Taiwan	TCU138	7.62	0.60
40	1434	Chi-Chi, Taiwan	TAP049	7.62	1.40

Table E.9 Documentation of 40 GMs of reference group of Bridge A for 10% POE in 50 years.

Record Number	NGA Record Sequence Number	Earthquake Name	Station	Magnitude	Scaling Factor
1	1310	Chi-Chi, Taiwan	ILA004	7.62	2.60
2	1201	Chi-Chi, Taiwan	CHY034	7.62	3.00
3	1472	Chi-Chi, Taiwan	TCU017	7.62	2.30
4	1488	Chi-Chi, Taiwan	TCU048	7.62	1.10
5	1147	Kocaeli, Turkey	Ambarli	7.51	1.50
6	1244	Chi-Chi, Taiwan	CHY101	7.62	0.60
7	1476	Chi-Chi, Taiwan	TCU029	7.62	1.10
8	1794	Hector Mine	Joshua Tree	7.13	3.00
9	171	Imperial Valley-06	EC Meloland Overpass FF	6.53	1.70
10	1234	Chi-Chi, Taiwan	CHY086	7.62	2.20
11	143	Tabas, Iran	Tabas	7.35	0.30
12	1350	Chi-Chi, Taiwan	ILA067	7.62	0.80
13	888	Landers	San Bernardino-E Hospitality	7.28	2.30
14	1614	Duzce, Turkey	Lamont 1061	7.14	2.90
15	126	Gazli, USSR	Karakyr	6.80	0.50
16	880	Landers	Mission Creek Fault	7.28	2.70
17	285	Irpinia, Italy-01	Bagnoli Irpinio	6.90	1.60
18	3509	Chi-Chi, Taiwan-06	TCU138	6.30	2.40
19	1193	Chi-Chi, Taiwan	CHY024	7.62	1.20
20	825	Cape Mendocino	Cape Mendocino	7.01	0.60
21	767	Loma Prieta	Gilroy Array #3	6.93	0.60
22	1493	Chi-Chi, Taiwan	TCU053	7.62	2.30
23	3266	Chi-Chi, Taiwan-06	CHY026	6.30	1.90
24	2458	Chi-Chi, Taiwan-03	CHY025	6.20	1.10
25	184	Imperial Valley-06	El Centro Differential Array	6.53	0.80
26	1148	Kocaeli, Turkey	Arcelik	7.51	1.70
27	1116	Kobe, Japan	Shin-Osaka	6.90	1.90
28	1507	Chi-Chi, Taiwan	TCU071	7.62	1.10
29	730	Spitak, Armenia	Gukasian	6.77	1.60
30	900	Landers	Yermo Fire Station	7.28	2.00
31	2655	Chi-Chi, Taiwan-03	TCU122	6.20	0.70
32	755	Loma Prieta	Coyote Lake Dam (SW Abut)	6.93	2.60
33	1547	Chi-Chi, Taiwan	TCU123	7.62	2.60
34	185	Imperial Valley-06	Holtville Post Office	6.53	1.40
35	879	Landers	Lucerne	7.28	1.20
36	1503	Chi-Chi, Taiwan	TCU065	7.62	0.50
37	1521	Chi-Chi, Taiwan	TCU089	7.62	0.70
38	2473	Chi-Chi, Taiwan-03	CHY047	6.20	2.70
39	1495	Chi-Chi, Taiwan	TCU055	7.62	2.00
40	1491	Chi-Chi, Taiwan	TCU051	7.62	1.40

Table E.10 Documentation of 40 GMs of reference group of Bridge A for 2% POE in 50 years.

Record Number	NGA Record Sequence Number	Earthquake Name	Station	Magnitude	Scaling Factor
1	190	Imperial Valley-06	Superstition Mtn Camera	6.53	1.90
2	1476	Chi-Chi, Taiwan	TCU029	7.62	1.90
3	1486	Chi-Chi, Taiwan	TCU046	7.62	2.00
4	900	Landers	Yermo Fire Station	7.28	2.00
5	1505	Chi-Chi, Taiwan	TCU068	7.62	0.80
6	1147	Kocaeli, Turkey	Ambarli	7.51	3.00
7	1521	Chi-Chi, Taiwan	TCU089	7.62	2.40
8	1503	Chi-Chi, Taiwan	TCU065	7.62	0.50
9	1478	Chi-Chi, Taiwan	TCU033	7.62	2.70
10	1176	Kocaeli, Turkey	Yarimca	7.51	2.40
11	170	Imperial Valley-06	EC County Center FF	6.53	2.30
12	1511	Chi-Chi, Taiwan	TCU076	7.62	2.30
13	285	Irpinia, Italy-01	Bagnoli Irpinio	6.90	2.80
14	1541	Chi-Chi, Taiwan	TCU116	7.62	2.60
15	1488	Chi-Chi, Taiwan	TCU048	7.62	1.70
16	1244	Chi-Chi, Taiwan	CHY101	7.62	0.90
17	723	Superstition Hills-02	Parachute Test Site	6.54	2.30
18	879	Landers	Lucerne	7.28	1.60
19	728	Superstition Hills-02	Westmorland Fire Sta	6.54	2.50
20	182	Imperial Valley-06	El Centro Array #7	6.53	2.80
21	779	Loma Prieta	LGPC	6.93	1.00
22	1149	Kocaeli, Turkey	Atakoy	7.51	2.80
23	1048	Northridge-01	Northridge-17645 Saticoy St	6.69	1.20
24	1529	Chi-Chi, Taiwan	TCU102	7.62	1.90
25	1525	Chi-Chi, Taiwan	TCU096	7.62	3.00
26	126	Gazli, USSR	Karakyr	6.80	0.70
27	803	Loma Prieta	Saratoga-W Valley Coll.	6.93	1.80
28	184	Imperial Valley-06	El Centro Differential Array	6.53	3.00
29	721	Superstition Hills-02	El Centro Imp. Co. Cent	6.54	2.30
30	1534	Chi-Chi, Taiwan	TCU107	7.62	2.60
31	1762	Hector Mine	Amboy	7.13	2.80
32	1297	Chi-Chi, Taiwan	HWA051	7.62	2.40
33	175	Imperial Valley-06	El Centro Array #12	6.53	2.30
34	1158	Kocaeli, Turkey	Duzce	7.51	2.70
35	1198	Chi-Chi, Taiwan	CHY029	7.62	2.20
36	1546	Chi-Chi, Taiwan	TCU122	7.62	2.40
37	1111	Kobe, Japan	Nishi-Akashi	6.90	1.90
38	3472	Chi-Chi, Taiwan-06	TCU076	6.30	2.40
39	1527	Chi-Chi, Taiwan	TCU100	7.62	2.10
40	776	Loma Prieta	Hollister-South & Pine	6.93	1.60

Table E.11 Documentation of 40 GMs of *CMS* group of Bridge B for 50% POE in 50 years.

Record Number	NGA Record Sequence Number	Earthquake Name	Station	Magnitude	Scaling Factor
1	2709	Chi-Chi, Taiwan-04	CHY035	6.20	1.05
2	354	Coalinga-01	Parkfield-Gold Hill 5W	6.36	2.13
3	900	Landers	Yermo Fire Station	7.28	0.73
4	12	Kern County	LA-Hollywood Stor FF	7.36	2.95
5	1551	Chi-Chi, Taiwan	TCU138	7.62	0.77
6	1267	Chi-Chi, Taiwan	HWA016	7.62	2.12
7	838	Landers	Barstow	7.28	1.52
8	126	Gazli, USSR	Karakyr	6.80	0.46
9	1297	Chi-Chi, Taiwan	HWA051	7.62	1.22
10	993	Northridge-01	LA-Fletcher Dr	6.69	1.68
11	1092	Northridge-01	Ventura-Harbor & California	6.69	1.77
12	2490	Chi-Chi, Taiwan-03	CHY074	6.20	2.98
13	762	Loma Prieta	Fremont-Mission San Jose	6.93	2.52
14	1262	Chi-Chi, Taiwan	HWA011	7.62	1.15
15	885	Landers	Pomona-4th & Locust FF	7.28	2.29
16	1791	Hector Mine	Indio-Coachella Canal	7.13	1.36
17	1177	Kocaeli, Turkey	Zeytinburnu	7.51	2.05
18	892	Landers	Sun Valley-Roscoe Blvd	7.28	2.95
19	1206	Chi-Chi, Taiwan	CHY042	7.62	1.62
20	721	Superstition Hills-02	El Centro Imp. Co. Cent	6.54	0.78
21	1817	Hector Mine	North Shore - Durmid	7.13	2.39
22	266	Superstition Hills-02	El Centro Imp. Co. Cent	6.54	1.56
23	882	Landers	North Palm Springs	7.28	1.65
24	803	Loma Prieta	Saratoga-W Valley Coll.	6.93	0.41
25	1349	Chi-Chi, Taiwan	ILA066	7.62	2.35
26	1155	Kocaeli, Turkey	Bursa Tofas	7.51	1.17
27	1511	Chi-Chi, Taiwan	TCU076	7.62	0.58
28	1459	Chi-Chi, Taiwan	TAP100	7.62	1.36
29	2459	Chi-Chi, Taiwan-03	CHY026	6.20	2.79
30	1275	Chi-Chi, Taiwan	HWA026	7.62	2.33
31	759	Loma Prieta	Foster City-APEEL 1	6.93	0.49
32	1243	Chi-Chi, Taiwan	CHY100	7.62	2.14
33	1337	Chi-Chi, Taiwan	ILA049	7.62	1.22
34	1454	Chi-Chi, Taiwan	TAP090	7.62	0.94
35	1489	Chi-Chi, Taiwan	TCU049	7.62	0.75
36	730	Spitak, Armenia	Gukasian	6.77	1.21
37	2467	Chi-Chi, Taiwan-03	CHY036	6.20	2.00
38	1334	Chi-Chi, Taiwan	ILA044	7.62	0.95
39	1476	Chi-Chi, Taiwan	TCU029	7.62	1.34
40	2461	Chi-Chi, Taiwan-03	CHY028	6.20	0.91

Table E.12 Documentation of 40 GMs of *CMS* group of Bridge B for 10% POE in 50 years.

Record Number	NGA Record Sequence Number	Earthquake Name	Station	Magnitude	Scaling Factor
1	1080	Northridge-01	Simi Valley-Katherine Rd	6.69	1.04
2	1297	Chi-Chi, Taiwan	HWA051	7.62	2.64
3	1113	Kobe, Japan	OSAJ	6.90	2.55
4	900	Landers	Yermo Fire Station	7.28	1.58
5	827	Cape Mendocino	Fortuna-Fortuna Blvd	7.01	2.95
6	1550	Chi-Chi, Taiwan	TCU136	7.62	1.38
7	1155	Kocaeli, Turkey	Bursa Tofas	7.51	2.52
8	1317	Chi-Chi, Taiwan	ILA013	7.62	2.14
9	1492	Chi-Chi, Taiwan	TCU052	7.62	0.53
10	1530	Chi-Chi, Taiwan	TCU103	7.62	2.08
11	1529	Chi-Chi, Taiwan	TCU102	7.62	0.91
12	1534	Chi-Chi, Taiwan	TCU107	7.62	1.73
13	1472	Chi-Chi, Taiwan	TCU017	7.62	2.37
14	182	Imperial Valley-06	El Centro Array #7	6.53	0.93
15	1414	Chi-Chi, Taiwan	TAP008	7.62	2.62
16	1204	Chi-Chi, Taiwan	CHY039	7.62	2.96
17	856	Landers	Fountain Valley-Euclid	7.28	2.97
18	776	Loma Prieta	Hollister-South & Pine	6.93	0.91
19	1295	Chi-Chi, Taiwan	HWA049	7.62	2.58
20	1149	Kocaeli, Turkey	Atakoy	7.51	2.42
21	1264	Chi-Chi, Taiwan	HWA013	7.62	1.78
22	1787	Hector Mine	Hector	7.13	1.23
23	803	Loma Prieta	Saratoga-W Valley Coll.	6.93	0.89
24	1459	Chi-Chi, Taiwan	TAP100	7.62	2.93
25	126	Gazli, USSR	Karakyr	6.80	1.00
26	1044	Northridge-01	Newhall-Fire Sta	6.69	0.63
27	1489	Chi-Chi, Taiwan	TCU049	7.62	1.63
28	170	Imperial Valley-06	EC County Center FF	6.53	1.59
29	1329	Chi-Chi, Taiwan	ILA037	7.62	2.96
30	3265	Chi-Chi, Taiwan-06	CHY025	6.30	2.59
31	864	Landers	Joshua Tree	7.28	1.04
32	1262	Chi-Chi, Taiwan	HWA011	7.62	2.49
33	1234	Chi-Chi, Taiwan	CHY086	7.62	2.32
34	1536	Chi-Chi, Taiwan	TCU110	7.62	1.34
35	1147	Kocaeli, Turkey	Ambarli	7.51	1.29
36	1509	Chi-Chi, Taiwan	TCU074	7.62	0.61
37	1039	Northridge-01	Moorpark-Fire Sta	6.69	2.31
38	285	Irpinia, Italy-01	Bagnoli Irpinio	6.90	2.06
39	1541	Chi-Chi, Taiwan	TCU116	7.62	1.49
40	1334	Chi-Chi, Taiwan	ILA044	7.62	2.06

Table E.13 Documentation of 40 GMs of *CMS* group of Bridge B for 2% POE in 50 years.

Record Number	NGA Record Sequence Number	Earthquake Name	Station	Magnitude	Scaling Factor
1	1419	Chi-Chi, Taiwan	TAP017	7.62	2.35
2	732	Loma Prieta	APEEL 2-Redwood City	6.93	1.07
3	1264	Chi-Chi, Taiwan	HWA013	7.62	2.79
4	1410	Chi-Chi, Taiwan	TAP003	7.62	2.48
5	1492	Chi-Chi, Taiwan	TCU052	7.62	0.83
6	776	Loma Prieta	Hollister-South & Pine	6.93	1.43
7	1044	Northridge-01	Newhall-Fire Sta	6.69	0.99
8	1201	Chi-Chi, Taiwan	CHY034	7.62	1.78
9	341	Coalinga-01	Parkfield-Fault Zone 2	6.36	2.85
10	1084	Northridge-01	Sylmar - Converter Sta	6.69	0.58
11	759	Loma Prieta	Foster City-APEEL 1	6.93	1.66
12	1045	Northridge-01	Newhall-W Pico Canyon Rd.	6.69	1.34
13	300	Irpinia, Italy-02	Calitri	6.20	2.17
14	1411	Chi-Chi, Taiwan	TAP005	7.62	2.23
15	1504	Chi-Chi, Taiwan	TCU067	7.62	1.22
16	780	Loma Prieta	Larkspur Ferry Terminal (FF)	6.93	2.42
17	1547	Chi-Chi, Taiwan	TCU123	7.62	2.19
18	744	Loma Prieta	Bear Valley #12	6.93	1.81
19	1517	Chi-Chi, Taiwan	TCU084	7.62	0.69
20	1529	Chi-Chi, Taiwan	TCU102	7.62	1.43
21	1147	Kocaeli, Turkey	Ambarli	7.51	2.02
22	1182	Chi-Chi, Taiwan	CHY006	7.62	1.53
23	1509	Chi-Chi, Taiwan	TCU074	7.62	0.96
24	1116	Kobe, Japan	Shin-Osaka	6.90	2.75
25	900	Landers	Yermo Fire Station	7.28	2.48
26	1498	Chi-Chi, Taiwan	TCU059	7.62	1.88
27	182	Imperial Valley-06	El Centro Array #7	6.53	1.46
28	771	Loma Prieta	Golden Gate Bridge	6.93	2.68
29	803	Loma Prieta	Saratoga-W Valley Coll.	6.93	1.40
30	126	Gazli, USSR	Karakyr	6.80	1.57
31	1536	Chi-Chi, Taiwan	TCU110	7.62	2.11
32	864	Landers	Joshua Tree	7.28	1.63
33	1292	Chi-Chi, Taiwan	HWA045	7.62	2.35
34	527	N. Palm Springs	Morongo Valley	6.06	2.32
35	1550	Chi-Chi, Taiwan	TCU136	7.62	2.16
36	1457	Chi-Chi, Taiwan	TAP097	7.62	2.85
37	1120	Kobe, Japan	Takatori	6.90	0.51
38	1503	Chi-Chi, Taiwan	TCU065	7.62	0.78
39	723	Superstition Hills-02	Parachute Test Site	6.54	1.24
40	1541	Chi-Chi, Taiwan	TCU116	7.62	2.34

Table E.14 Documentation of 40 GMs of reference group of Bridge B for 50% POE in 50 years

Record Number	NGA Record Sequence Number	Earthquake Name	Station	Magnitude	Scaling Factor
1	2497	Chi-Chi, Taiwan-03	CHY082	6.20	1.40
2	1536	Chi-Chi, Taiwan	TCU110	7.62	1.60
3	900	Landers	Yermo Fire Station	7.28	1.20
4	1397	Chi-Chi, Taiwan	KAU086	7.28	3.00
5	186	Imperial Valley-06	Niland Fire Station	6.53	2.00
6	2700	Chi-Chi, Taiwan-04	CHY025	6.20	2.10
7	879	Landers	Lucerne	7.28	0.40
8	880	Landers	Mission Creek Fault	7.28	0.60
9	1011	Northridge-01	LA-Wonderland Ave	6.69	2.10
10	1147	Kocaeli, Turkey	Ambarli	7.51	1.00
11	1553	Chi-Chi, Taiwan	TCU141	7.28	1.10
12	1505	Chi-Chi, Taiwan	TCU068	7.28	0.40
13	126	Gazli, USSR	Karakyr	6.80	0.50
14	728	Superstition Hills-02	Westmorland Fire Sta	6.54	1.30
15	1791	Hector Mine	Indio-Coachella Canal	7.13	2.30
16	762	Loma Prieta	Fremont-Mission San Jose	6.93	0.80
17	1148	Kocaeli, Turkey	Arcelik	7.51	1.50
18	1267	Chi-Chi, Taiwan	HWA016	7.28	1.90
19	2893	Chi-Chi, Taiwan-04	TCU122	6.20	2.00
20	549	Chalfant Valley-02	Bishop-LADWP South St	6.19	1.40
21	862	Landers	Indio-Coachella Canal	7.28	2.60
22	2115	Denali, Alaska	TAPS Pump Station #11	7.90	2.40
23	1057	Northridge-01	Playa Del Rey-Saran	6.69	1.50
24	739	Loma Prieta	Anderson Dam (Downstream)	6.93	1.40
25	293	Irpinia, Italy-01	Torre Del Greco	6.90	3.00
26	767	Loma Prieta	Gilroy Array #3	6.93	0.60
27	1193	Chi-Chi, Taiwan	CHY024	7.28	1.00
28	1297	Chi-Chi, Taiwan	HWA051	7.28	1.80
29	171	Imperial Valley-06	EC Meloland Overpass FF	6.53	1.10
30	1074	Northridge-01	Sandberg - Bald Mtn	6.69	2.50
31	778	Loma Prieta	Hollister Diff. Array	6.93	2.00
32	2715	Chi-Chi, Taiwan-04	CHY047	6.20	2.30
33	1762	Hector Mine	Amboy	7.13	1.70
34	1113	Kobe, Japan	OSAJ	6.90	3.00
35	1324	Chi-Chi, Taiwan	ILA030	7.28	1.90
36	1158	Kocaeli, Turkey	Duzce	7.51	0.60
37	1552	Chi-Chi, Taiwan	TCU140	7.28	2.90
38	1287	Chi-Chi, Taiwan	HWA038	7.28	2.50
39	1776	Hector Mine	Desert Hot Springs	7.13	2.20
40	761	Loma Prieta	Fremont-Emerson Court	6.93	2.60

Table E.15 Documentation of 40 GMs of reference group of Bridge B for 10% POE in 50 years.

Record Number	NGA Record Sequence Number	Earthquake Name	Station	Magnitude	Scaling Factor
1	587	New Zealand-02	Matahina Dam	5.99	3.00
2	755	Loma Prieta	Coyote Lake Dam (SW Abut)	6.93	3.00
3	1528	Chi-Chi, Taiwan	TCU101	7.62	2.50
4	1762	Hector Mine	Amboy	7.13	2.50
5	161	Imperial Valley-06	Brawley Airport	6.53	2.10
6	1488	Chi-Chi, Taiwan	TCU048	7.62	1.40
7	183	Imperial Valley-06	El Centro Array #8	6.53	1.20
8	2115	Denali, Alaska	TAPS Pump Station #11	7.90	3.00
9	1481	Chi-Chi, Taiwan	TCU038	7.62	1.70
10	1147	Kocaeli, Turkey	Ambarli	7.51	1.70
11	143	Tabas, Iran	Tabas	7.35	0.60
12	1492	Chi-Chi, Taiwan	TCU052	7.62	2.40
13	1509	Chi-Chi, Taiwan	TCU074	7.62	1.30
14	2752	Chi-Chi, Taiwan-04	CHY101	6.20	3.00
15	900	Landers	Yermo Fire Station	7.28	2.40
16	1531	Chi-Chi, Taiwan	TCU104	7.62	2.70
17	985	Northridge-01	LA-Baldwin Hills	6.69	2.20
18	1505	Chi-Chi, Taiwan	TCU068	7.62	0.70
19	1483	Chi-Chi, Taiwan	TCU040	7.62	3.00
20	1547	Chi-Chi, Taiwan	TCU123	7.62	3.00
21	827	Cape Mendocino	Fortuna-Fortuna Blvd	7.01	2.30
22	855	Landers	Fort Irwin	7.28	2.30
23	1501	Chi-Chi, Taiwan	TCU063	7.62	2.30
24	1201	Chi-Chi, Taiwan	CHY034	7.62	1.30
25	1198	Chi-Chi, Taiwan	CHY029	7.62	3.00
26	1503	Chi-Chi, Taiwan	TCU065	7.62	1.00
27	1263	Chi-Chi, Taiwan	HWA012	7.62	3.00
28	723	Superstition Hills-02	Parachute Test Site	6.54	2.40
29	1471	Chi-Chi, Taiwan	TCU015	7.62	1.00
30	803	Loma Prieta	Saratoga-W Valley Coll.	6.93	1.60
31	179	Imperial Valley-06	El Centro Array #4	6.53	2.10
32	1553	Chi-Chi, Taiwan	TCU141	7.62	2.20
33	266	Victoria, Mexico	Chihuahua	6.33	2.10
34	730	Spitak, Armenia	Gukasian	6.77	2.60
35	719	Superstition Hills-02	Brawley Airport	6.54	1.70
36	1545	Chi-Chi, Taiwan	TCU120	7.62	1.30
37	171	Imperial Valley-06	EC Meloland Overpass FF	6.53	1.50
38	1476	Chi-Chi, Taiwan	TCU029	7.62	2.80
39	2710	Chi-Chi, Taiwan-04	CHY036	6.20	3.00
40	1045	Northridge-01	Newhall-W Pico Canyon Rd.	6.69	2.20

Table E.16 Documentation of 40 GMs of reference group of Bridge B for 2% POE in 50 years.

Record Number	NGA Record Sequence Number	Earthquake Name	Station	Magnitude	Scaling Factor
1	1468	Chi-Chi, Taiwan	TCU010	7.62	2.90
2	1477	Chi-Chi, Taiwan	TCU031	7.62	3.00
3	900	Landers	Yermo Fire Station	7.28	3.00
4	1550	Chi-Chi, Taiwan	TCU136	7.62	3.00
5	728	Superstition Hills-02	Westmorland Fire Sta	6.54	2.50
6	1488	Chi-Chi, Taiwan	TCU048	7.62	2.70
7	776	Loma Prieta	Hollister-South & Pine	6.93	3.00
8	1503	Chi-Chi, Taiwan	TCU065	7.62	2.70
9	1148	Kocaeli, Turkey	Arcelik	7.51	3.00
10	1491	Chi-Chi, Taiwan	TCU051	7.62	3.00
11	1198	Chi-Chi, Taiwan	CHY029	7.62	3.00
12	1476	Chi-Chi, Taiwan	TCU029	7.62	2.00
13	1149	Kocaeli, Turkey	Atakoy	7.51	2.10
14	1528	Chi-Chi, Taiwan	TCU101	7.62	2.40
15	1492	Chi-Chi, Taiwan	TCU052	7.62	2.40
16	143	Tabas, Iran	Tabas	7.35	1.00
17	1084	Northridge-01	Sylmar-Converter Sta	6.69	3.00
18	1505	Chi-Chi, Taiwan	TCU068	7.62	1.60
19	1509	Chi-Chi, Taiwan	TCU074	7.62	2.00
20	1078	Northridge-01	Santa Susana Ground	6.69	2.90
21	719	Superstition Hills-02	Brawley Airport	6.54	2.00
22	1787	Hector Mine	Hector	7.13	2.50
23	1548	Chi-Chi, Taiwan	TCU128	7.62	2.80
24	1478	Chi-Chi, Taiwan	TCU033	7.62	2.90
25	1106	Kobe, Japan	KJMA	6.90	2.50
26	803	Loma Prieta	Saratoga-W Valley Coll.	6.93	2.90
27	1486	Chi-Chi, Taiwan	TCU046	7.62	2.70
28	1529	Chi-Chi, Taiwan	TCU102	7.62	2.80
29	1176	Kocaeli, Turkey	Yarimca	7.51	3.00
30	184	Imperial Valley-06	El Centro Differential Array	6.53	2.20
31	723	Superstition Hills-02	Parachute Test Site	6.54	2.20
32	802	Loma Prieta	Saratoga-Aloha Ave	6.93	1.80
33	1498	Chi-Chi, Taiwan	TCU059	7.62	3.00
34	1244	Chi-Chi, Taiwan	CHY101	7.62	1.60
35	1510	Chi-Chi, Taiwan	TCU075	7.62	2.80
36	1542	Chi-Chi, Taiwan	TCU117	7.62	3.00
37	721	Superstition Hills-02	El Centro Imp. Co. Cent	6.54	2.20
38	170	Imperial Valley-06	EC County Center FF	6.53	2.10
39	779	Loma Prieta	LGPC	6.93	1.70
40	1501	Chi-Chi, Taiwan	TCU063	7.62	2.80

Table E.17 Documentation of 40 GMs of *CMS* group of Bridge C for 50% POE in 50 years.

Record Number	NGA Record Sequence Number	Earthquake Name	Station	Magnitude	Scaling Factor
1	2463	Chi-Chi, Taiwan-03	CHY032	6.20	1.67
2	1538	Chi-Chi, Taiwan	TCU112	7.62	0.69
3	1234	Chi-Chi, Taiwan	CHY086	7.62	1.18
4	1817	Hector Mine	North Shore-Durmid	7.13	1.76
5	1304	Chi-Chi, Taiwan	HWA059	7.62	1.59
6	3297	Chi-Chi, Taiwan-06	CHY069	6.30	1.95
7	900	Landers	Yermo Fire Station	7.28	0.46
8	784	Loma Prieta	Oakland-Title & Trust	6.93	0.59
9	983	Northridge-01	Jensen Filter Plant Generator	6.69	0.25
10	1154	Kocaeli, Turkey	Bursa Sivil	7.51	1.34
11	1783	Hector Mine	Fort Irwin	7.13	2.36
12	2598	Chi-Chi, Taiwan-03	TCU039	6.20	2.74
13	1359	Chi-Chi, Taiwan	KAU015	7.62	1.81
14	1491	Chi-Chi, Taiwan	TCU051	7.62	0.54
15	464	Morgan Hill	Hollister Diff Array #3	6.19	1.81
16	1383	Chi-Chi, Taiwan	KAU062	7.62	2.41
17	1791	Hector Mine	Indio-Coachella Canal	7.13	1.30
18	1259	Chi-Chi, Taiwan	HWA006	7.62	2.57
19	803	Loma Prieta	Saratoga-W Valley Coll.	6.93	0.34
20	1426	Chi-Chi, Taiwan	TAP034	7.62	2.54
21	1587	Chi-Chi, Taiwan	TTN042	7.62	2.34
22	1834	Hector Mine	Sylmar-County Hospital	7.13	2.92
23	1185	Chi-Chi, Taiwan	CHY012	7.62	1.51
24	1232	Chi-Chi, Taiwan	CHY081	7.62	1.32
25	1504	Chi-Chi, Taiwan	TCU067	7.62	0.22
26	981	Northridge-01	Inglewood-Union Oil	6.69	1.73
27	1574	Chi-Chi, Taiwan	TTN022	7.62	1.31
28	1314	Chi-Chi, Taiwan	ILA008	7.62	0.83
29	176	Imperial Valley-06	El Centro Array #13	6.53	1.32
30	1495	Chi-Chi, Taiwan	TCU055	7.62	0.49
31	800	Loma Prieta	Salinas-John & Work	6.93	1.64
32	1794	Hector Mine	Joshua Tree	7.13	0.99
33	1611	Duzce, Turkey	Lamont 1058	7.14	1.22
34	1503	Chi-Chi, Taiwan	TCU065	7.62	0.17
35	1521	Chi-Chi, Taiwan	TCU089	7.62	0.59
36	1287	Chi-Chi, Taiwan	HWA038	7.62	2.16
37	785	Loma Prieta	Olema-Point Reyes Station	6.93	1.01
38	1317	Chi-Chi, Taiwan	ILA013	7.62	0.59
39	2654	Chi-Chi, Taiwan-03	TCU120	6.20	1.05
40	2711	Chi-Chi, Taiwan-04	CHY039	6.20	1.83

Table E.18 Documentation of 40 GMs of *CMS* group of Bridge C for 10% POE in 50 years.

Record Number	NGA Record Sequence Number	Earthquake Name	Station	Magnitude	Scaling Factor
1	2459	Chi-Chi, Taiwan-03	CHY026	6.20	2.37
2	1361	Chi-Chi, Taiwan	KAU020	7.62	1.63
3	1542	Chi-Chi, Taiwan	TCU117	7.62	0.84
4	2649	Chi-Chi, Taiwan-03	TCU115	6.20	2.84
5	2718	Chi-Chi, Taiwan-04	CHY054	6.20	2.74
6	883	Landers	Northridge-17645 Saticoy St	7.28	2.93
7	1295	Chi-Chi, Taiwan	HWA049	7.62	1.41
8	740	Loma Prieta	Anderson Dam (L Abut)	6.93	2.00
9	1418	Chi-Chi, Taiwan	TAP014	7.62	1.53
10	1457	Chi-Chi, Taiwan	TAP097	7.62	2.45
11	1232	Chi-Chi, Taiwan	CHY081	7.62	2.80
12	1574	Chi-Chi, Taiwan	TTN022	7.62	2.79
13	1509	Chi-Chi, Taiwan	TCU074	7.62	0.41
14	2650	Chi-Chi, Taiwan-03	TCU116	6.20	1.23
15	1412	Chi-Chi, Taiwan	TAP006	7.62	2.69
16	1494	Chi-Chi, Taiwan	TCU054	7.62	0.97
17	1541	Chi-Chi, Taiwan	TCU116	7.62	1.00
18	1787	Hector Mine	Hector	7.13	0.99
19	1297	Chi-Chi, Taiwan	HWA051	7.62	2.26
20	1791	Hector Mine	Indio-Coachella Canal	7.13	2.78
21	2744	Chi-Chi, Taiwan-04	CHY088	6.20	2.64
22	1263	Chi-Chi, Taiwan	HWA012	7.62	1.81
23	1147	Kocaeli, Turkey	Ambarli	7.51	1.17
24	169	Imperial Valley-06	Delta	6.53	0.79
25	1536	Chi-Chi, Taiwan	TCU110	7.62	0.54
26	900	Landers	Yermo Fire Station	7.28	0.97
27	1165	Kocaeli, Turkey	Izmit	7.51	1.19
28	1508	Chi-Chi, Taiwan	TCU072	7.62	0.69
29	1193	Chi-Chi, Taiwan	CHY024	7.62	0.91
30	2458	Chi-Chi, Taiwan-03	CHY025	6.20	1.48
31	1317	Chi-Chi, Taiwan	ILA013	7.62	1.26
32	755	Loma Prieta	Coyote Lake Dam (SW Abut)	6.93	1.70
33	2710	Chi-Chi, Taiwan-04	CHY036	6.20	2.72
34	326	Coalinga-01	Parkfield-Cholame 2WA	6.36	2.66
35	1158	Kocaeli, Turkey	Duzce	7.51	0.80
36	3265	Chi-Chi, Taiwan-06	CHY025	6.30	1.70
37	2708	Chi-Chi, Taiwan-04	CHY034	6.20	2.68
38	319	Westmorland	Westmorland Fire Sta	5.90	0.99
39	756	Loma Prieta	Dublin-Fire Station	6.93	2.59
40	836	Landers	Baker Fire Station	7.28	2.47

Table E.19 Documentation of 40 GMs of *CMS* group of Bridge C for 2% POE in 50 years.

Record Number	NGA Record Sequence Number	Earthquake Name	Station	Magnitude	Scaling Factor
1	341	Coalinga-01	Parkfield-Fault Zone 2	6.36	1.66
2	1575	Chi-Chi, Taiwan	TTN023	7.62	2.42
3	732	Loma Prieta	APEEL 2-Redwood City	6.93	1.73
4	1316	Chi-Chi, Taiwan	ILA012	7.62	2.20
5	2509	Chi-Chi, Taiwan-03	CHY104	6.20	1.83
6	1295	Chi-Chi, Taiwan	HWA049	7.62	2.28
7	1418	Chi-Chi, Taiwan	TAP014	7.62	2.48
8	1509	Chi-Chi, Taiwan	TCU074	7.62	0.67
9	1527	Chi-Chi, Taiwan	TCU100	7.62	1.98
10	885	Landers	Fort Irwin	7.28	2.91
11	1328	Chi-Chi, Taiwan	ILA036	7.62	2.83
12	2650	Chi-Chi, Taiwan-03	TCU116	6.20	1.99
13	1492	Chi-Chi, Taiwan	TCU052	7.62	0.48
14	1320	Chi-Chi, Taiwan	ILA016	7.62	2.83
15	1263	Chi-Chi, Taiwan	HWA012	7.62	2.93
16	1494	Chi-Chi, Taiwan	TCU054	7.62	1.58
17	1044	Northridge-01	Newhall-Fire Sta	6.69	0.83
18	1455	Chi-Chi, Taiwan	TAP094	7.62	2.61
19	1311	Chi-Chi, Taiwan	ILA005	7.62	2.87
20	1292	Chi-Chi, Taiwan	HWA045	7.62	2.64
21	1204	Chi-Chi, Taiwan	CHY039	7.62	2.35
22	2507	Chi-Chi, Taiwan-03	CHY101	6.20	1.98
23	1194	Chi-Chi, Taiwan	CHY025	7.62	1.45
24	2458	Chi-Chi, Taiwan-03	CHY025	6.20	2.40
25	2752	Chi-Chi, Taiwan-04	CHY101	6.20	2.43
26	1534	Chi-Chi, Taiwan	TCU107	7.62	1.59
27	776	Loma Prieta	Hollister-South & Pine	6.93	1.47
28	2663	Chi-Chi, Taiwan-03	TCU141	6.20	2.80
29	77	San Fernando	Pacoima Dam (upper left abut)	6.61	0.84
30	1187	Chi-Chi, Taiwan	CHY015	7.62	2.02
31	864	Landers	Joshua Tree	7.28	1.63
32	1536	Chi-Chi, Taiwan	TCU110	7.62	0.87
33	1116	Kobe, Japan	Shin-Osaka	6.90	2.26
34	1262	Chi-Chi, Taiwan	HWA011	7.62	2.22
35	900	Landers	Yermo Fire Station	7.28	1.58
36	803	Loma Prieta	Saratoga-W Valley Coll.	6.93	1.18
37	1542	Chi-Chi, Taiwan	TCU117	7.62	1.37
38	1317	Chi-Chi, Taiwan	ILA013	7.62	2.04
39	1361	Chi-Chi, Taiwan	KAU020	7.62	2.65
40	170	Imperial Valley-06	EC County Center FF	6.53	1.41

Table E.20 Documentation of 40 GMs of reference group of Bridge C for 50% POE in 50 years.

Record Number	NGA Record Sequence Number	Earthquake Name	Station	Magnitude	Scaling Factor
1	1498	Chi-Chi, Taiwan	TCU059	7.62	1.90
2	1424	Chi-Chi, Taiwan	TAP028	7.62	2.20
3	1117	Kobe, Japan	TOT	6.90	1.20
4	1476	Chi-Chi, Taiwan	TCU029	7.62	1.00
5	2893	Chi-Chi, Taiwan-04	TCU122	6.20	2.40
6	1377	Chi-Chi, Taiwan	KAU050	7.62	1.30
7	2714	Chi-Chi, Taiwan-04	CHY046	6.20	0.90
8	2756	Chi-Chi, Taiwan-04	CHY114	6.20	3.00
9	1618	Duzce, Turkey	Lamont 531	7.14	1.20
10	1817	Hector Mine	North Shore-Durmid	7.13	2.90
11	1223	Chi-Chi, Taiwan	CHY067	7.62	0.90
12	265	Victoria, Mexico	Cerro Prieto	6.33	1.30
13	1301	Chi-Chi, Taiwan	HWA056	7.62	1.60
14	2115	Denali, Alaska	TAPS Pump Station #11	7.90	1.20
15	1214	Chi-Chi, Taiwan	CHY057	7.62	2.10
16	1308	Chi-Chi, Taiwan	ILA002	7.62	3.00
17	1190	Chi-Chi, Taiwan	CHY019	7.62	2.20
18	1450	Chi-Chi, Taiwan	TAP083	7.62	1.90
19	1148	Kocaeli, Turkey	Arcelik	7.51	0.90
20	1182	Chi-Chi, Taiwan	CHY006	7.62	1.00
21	891	Landers	Silent Valley-Poppet Flat	7.28	2.70
22	1489	Chi-Chi, Taiwan	TCU049	7.62	1.00
23	266	Victoria, Mexico	Chihuahua	6.33	1.30
24	1261	Chi-Chi, Taiwan	HWA009	7.62	0.70
25	1465	Chi-Chi, Taiwan	TCU007	7.62	1.70
26	1512	Chi-Chi, Taiwan	TCU078	7.62	0.60
27	326	Coalinga-01	Parkfield-Cholame 2WA	6.36	2.10
28	1149	Kocaeli, Turkey	Atakoy	7.51	2.10
29	1164	Kocaeli, Turkey	Istanbul	7.51	1.80
30	2948	Chi-Chi, Taiwan-05	CHY032	6.20	2.20
31	1475	Chi-Chi, Taiwan	TCU026	7.62	1.80
32	178	Imperial Valley-06	El Centro Array #3	6.53	0.50
33	3267	Chi-Chi, Taiwan-06	CHY027	6.30	2.90
34	68	San Fernando	LA-Hollywood Stor FF	6.61	1.00
35	862	Landers	Indio-Coachella Canal	7.28	2.00
36	180	Imperial Valley-06	El Centro Array #5	6.53	0.20
37	2951	Chi-Chi, Taiwan-05	CHY039	6.20	1.70
38	808	Loma Prieta	Treasure Island	6.93	1.20
39	838	Landers	Barstow	7.28	1.20
40	2711	Chi-Chi, Taiwan-04	CHY039	6.20	2.70

Table E.21 Documentation of 40 GMs of reference group of Bridge C for 10% POE in 50 years.

Record Number	NGA Record Sequence Number	Earthquake Name	Station	Magnitude	Scaling Factor
1	2492	Chi-Chi, Taiwan-03	CHY076	6.20	1.50
2	1410	Chi-Chi, Taiwan	TAP003	7.62	3.00
3	1147	Kocaeli, Turkey	Ambarli	7.51	1.70
4	1611	Duzce, Turkey	Lamont 1058	7.14	2.50
5	900	Landers	Yermo Fire Station	7.28	1.40
6	2115	Denali, Alaska	TAPS Pump Station #11	7.90	2.90
7	744	Loma Prieta	Bear Valley #12	6.93	2.70
8	1184	Chi-Chi, Taiwan	CHY010	7.62	2.80
9	762	Loma Prieta	Fremont-Mission San Jose	6.93	3.00
10	1489	Chi-Chi, Taiwan	TCU049	7.62	1.20
11	1762	Hector Mine	Amboy	7.13	1.40
12	1541	Chi-Chi, Taiwan	TCU116	7.62	1.60
13	1615	Duzce, Turkey	Lamont 1062	7.14	2.40
14	801	Loma Prieta	San Jose-Santa Teresa Hills	6.93	1.90
15	1223	Chi-Chi, Taiwan	CHY067	7.62	3.00
16	730	Spitak, Armenia	Gukasian	6.77	1.20
17	1476	Chi-Chi, Taiwan	TCU029	7.62	1.20
18	1553	Chi-Chi, Taiwan	TCU141	7.62	3.00
19	1013	Northridge-01	LA Dam	6.69	1.50
20	1149	Kocaeli, Turkey	Atakoy	7.51	2.90
21	1498	Chi-Chi, Taiwan	TCU059	7.62	3.00
22	1554	Chi-Chi, Taiwan	TCU145	7.62	2.10
23	1198	Chi-Chi, Taiwan	CHY029	7.62	2.20
24	2700	Chi-Chi, Taiwan-04	CHY025	6.20	2.00
25	779	Loma Prieta	LGPC	6.93	0.70
26	1350	Chi-Chi, Taiwan	ILA067	7.62	0.80
27	2457	Chi-Chi, Taiwan-03	CHY024	6.20	2.70
28	1492	Chi-Chi, Taiwan	TCU052	7.62	0.70
29	880	Landers	Mission Creek Fault	7.28	1.50
30	1318	Chi-Chi, Taiwan	ILA014	7.62	3.00
31	879	Landers	Lucerne	7.28	0.70
32	2893	Chi-Chi, Taiwan-04	TCU122	6.20	2.50
33	169	Imperial Valley-06	Delta	6.53	0.90
34	1513	Chi-Chi, Taiwan	TCU079	7.62	0.70
35	796	Loma Prieta	SF-Presidio	6.93	3.00
36	184	Imperial Valley-06	El Centro Differential Array	6.53	1.50
37	143	Tabas, Iran	Tabas	7.35	0.50
38	838	Landers	Barstow	7.28	2.40
39	549	Chalfant Valley-02	Bishop-LADWP South St	6.19	1.70
40	767	Loma Prieta	Gilroy Array #3	6.93	1.30

Table E.22 Documentation of 40 GMs of reference group of Bridge C for 2% POE in 50 years.

Record Number	NGA Record Sequence Number	Earthquake Name	Station	Magnitude	Scaling Factor
1	1605	Duzce, Turkey	Duzce	7.14	2.60
2	1176	Kocaeli, Turkey	Yarimca	7.51	2.90
3	1492	Chi-Chi, Taiwan	TCU052	7.62	2.40
4	1509	Chi-Chi, Taiwan	TCU074	7.62	1.40
5	825	Cape Mendocino	Cape Mendocino	7.01	0.30
6	1147	Kocaeli, Turkey	Ambarli	7.51	2.40
7	1149	Kocaeli, Turkey	Atakoy	7.51	3.00
8	2115	Denali, Alaska	TAPS Pump Station #11	7.90	3.00
9	1234	Chi-Chi, Taiwan	CHY086	7.62	3.00
10	169	Imperial Valley-06	Delta	6.53	1.10
11	900	Landers	Yermo Fire Station	7.28	1.50
12	1528	Chi-Chi, Taiwan	TCU101	7.62	1.50
13	803	Loma Prieta	Saratoga-W Valley Coll.	6.93	1.20
14	779	Loma Prieta	LGPC	6.93	0.70
15	744	Loma Prieta	Bear Valley #12	6.93	3.00
16	1201	Chi-Chi, Taiwan	CHY034	7.62	1.80
17	1505	Chi-Chi, Taiwan	TCU068	7.62	1.40
18	721	Superstition Hills-02	El Centro Imp. Co. Cent	6.54	1.70
19	143	Tabas, Iran	Tabas	7.35	0.30
20	1148	Kocaeli, Turkey	Arcelik	7.51	3.00
21	1472	Chi-Chi, Taiwan	TCU017	7.62	2.90
22	1158	Kocaeli, Turkey	Duzce	7.51	1.20
23	175	Imperial Valley-06	El Centro Array #12	6.53	2.30
24	776	Loma Prieta	Hollister-South & Pine	6.93	1.80
25	1792	Hector Mine	Indio-Riverside Co Fair Grnds	7.13	2.30
26	1042	Northridge-01	N Hollywood-Coldwater Can	6.69	2.40
27	549	Chalfant Valley-02	Bishop-LADWP South St	6.19	2.30
28	767	Loma Prieta	Gilroy Array #3	6.93	2.80
29	183	Imperial Valley-06	El Centro Array #8	6.53	1.30
30	879	Landers	Lucerne	7.28	1.20
31	186	Imperial Valley-06	Niland Fire Station	6.53	2.80
32	1491	Chi-Chi, Taiwan	TCU051	7.62	2.70
33	1510	Chi-Chi, Taiwan	TCU075	7.62	1.90
34	1497	Chi-Chi, Taiwan	TCU057	7.62	2.40
35	729	Superstition Hills-02	Wildlife Liquef. Array	6.54	3.00
36	184	Imperial Valley-06	El Centro Differential Array	6.53	2.60
37	1488	Chi-Chi, Taiwan	TCU048	7.62	1.90
38	1504	Chi-Chi, Taiwan	TCU067	7.62	2.10
39	1533	Chi-Chi, Taiwan	TCU106	7.62	2.00
40	1476	Chi-Chi, Taiwan	TCU029	7.62	3.00

Appendix F: Documentation of the Utilized Ground Motions in Chapter 9

This appendix documents all the GMs utilized to develop reference benchmark *PDSD* for the investigated RC highway bridge systems. The GMs selected by the investigated four GMSM procedures are also documented in this appendix.

Table F.1 Documentation of 60 GMs used for the development of benchmark *PDSD*.

Record Number	NGA Record Sequence Number	Earthquake Name	Station	Magnitude
1	125	Friuli, Italy-01	Tolmezzo	6.50
2	126	Gazli, USSR	Karakyr	6.80
3	143	Tabas, Iran	Tabas	7.35
4	158	Imperial Valley-06	Aeropuerto Mexicali	6.53
5	159	Imperial Valley-06	Agrarias	6.53
6	161	Imperial Valley-06	Brawley Airport	6.53
7	165	Imperial Valley-06	Chihuahua	6.53
8	170	Imperial Valley-06	EC County Center FF	6.53
9	171	Imperial Valley-06	EC Meloland Overpass FF	6.53
10	173	Imperial Valley-06	El Centro Array #10	6.53
11	174	Imperial Valley-06	El Centro Array #11	6.53
12	179	Imperial Valley-06	El Centro Array #4	6.53
13	180	Imperial Valley-06	El Centro Array #5	6.53
14	181	Imperial Valley-06	El Centro Array #6	6.53
15	182	Imperial Valley-06	El Centro Array #7	6.53
16	183	Imperial Valley-06	El Centro Array #8	6.53
17	184	Imperial Valley-06	El Centro Differential Array	6.53
18	185	Imperial Valley-06	Holtville Post Office	6.53
19	285	Irpinia, Italy-01	Bagnoli Irpinio	6.90
20	292	Irpinia, Italy-01	Sturno	6.90
21	721	Superstition Hills-02	El Centro Imp. Co. Cent	6.54
22	722	Superstition Hills-02	Kornbloom Road (temp)	6.54
23	723	Superstition Hills-02	Parachute Test Site	6.54
24	725	Superstition Hills-02	Poe Road (temp)	6.54
25	728	Superstition Hills-02	Westmorland Fire Sta	6.54
26	741	Loma Prieta	BRAN	6.93
27	753	Loma Prieta	Corralitos	6.93
28	764	Loma Prieta	Gilroy-Historic Bldg.	6.93
29	766	Loma Prieta	Gilroy Array #2	6.93
30	768	Loma Prieta	Gilroy Array #4	6.93

Table F.1 (Cont.) Documentation of 60 GMs used for the development of benchmark *PDSD*.

Record Number	NGA Record Sequence Number	Earthquake Name	Station	Magnitude
31	779	Loma Prieta	LGPC	6.93
32	801	Loma Prieta	San Jose-Santa Teresa Hills	6.93
33	802	Loma Prieta	Saratoga-Aloha Ave	6.93
34	803	Loma Prieta	Saratoga-W Valley Coll.	6.93
35	821	Erzican, Turkey	Erzincan	6.69
36	827	Cape Mendocino	Fortuna-Fortuna Blvd	7.01
37	828	Cape Mendocino	Petrolia	7.01
38	829	Cape Mendocino	Rio Dell Overpass-FF	7.01
39	864	Landers	Joshua Tree	7.28
40	879	Landers	Lucerne	7.28
41	949	Northridge-01	Arleta-Nordhoff Fire Sta	6.69
42	953	Northridge-01	Beverly Hills-14145 Mulhol	6.69
43	959	Northridge-01	Canoga Park-Topanga Can	6.69
44	960	Northridge-01	Canyon Country-W Lost Cany	6.69
45	1004	Northridge-01	LA-Sepulveda VA Hospital	6.69
46	1013	Northridge-01	LA Dam	6.69
47	1042	Northridge-01	N Hollywood-Coldwater Can	6.69
48	1044	Northridge-01	Newhall-Fire Sta	6.69
49	1045	Northridge-01	Newhall-W Pico Canyon Rd.	6.69
50	1048	Northridge-01	Northridge-17645 Saticoy St	6.69
51	1050	Northridge-01	Pacoima Dam (downstr)	6.69
52	1052	Northridge-01	Pacoima Kagel Canyon	6.69
53	1063	Northridge-01	Rinaldi Receiving Sta	6.69
54	1086	Northridge-01	Sylmar-Olive View Med FF	6.69
55	1106	Kobe, Japan	KJMA	6.90
56	1111	Kobe, Japan	Nishi-Akashi	6.90
57	1116	Kobe, Japan	Shin-Osaka	6.90
58	1602	Duzce, Turkey	Bolu	7.14
59	1605	Duzce, Turkey	Duzce	7.14
60	1787	Hector Mine	Hector	7.13

Table F.2 Documentation of 40 GMs of $S_a(T_1)$ procedure for Bridge A with Type I abutment modeling.

Record Number	NGA Record Sequence Number	Earthquake Name	Station	Magnitude	Scaling Factor
1	179	Imperial Valley-06	El Centro Array #4	6.53	1.94
2	292	Irpinia, Italy-01	Sturno	6.90	2.41
3	829	Cape Mendocino	Rio Dell Overpass-FF	7.01	1.52
4	189	Imperial Valley-06	SAHOP Casa Flores	6.53	2.12
5	495	Nahanni, Canada	Site 1	6.76	1.65
6	725	Superstition Hills-02	Poe Road (temp)	6.54	2.34
7	949	Northridge-01	Arleta-Nordhoff Fire Sta	6.69	1.54
8	1082	Northridge-01	Sun Valley-Roscoe Blvd	6.69	1.45
9	170	Imperial Valley-06	EC County Center FF	6.53	1.94
10	184	Imperial Valley-06	El Centro Differential Array	6.53	1.43
11	766	Loma Prieta	Gilroy Array #2	6.93	1.64
12	767	Loma Prieta	Gilroy Array #3	6.93	2.13
13	802	Loma Prieta	Saratoga-Aloha Ave	6.93	2.28
14	803	Loma Prieta	Saratoga-W Valley Coll.	6.93	1.75
15	825	Cape Mendocino	Cape Mendocino	7.01	1.75
16	828	Cape Mendocino	Petrolia	7.01	0.61
17	983	Northridge-01	Jensen Filter Plant Generator	6.69	0.89
18	1013	Northridge-01	LA Dam	6.69	1.42
19	1044	Northridge-01	Newhall-Fire Sta	6.69	0.74
20	1045	Northridge-01	Newhall-W Pico Canyon Rd.	6.69	1.62
21	1050	Northridge-01	Pacoima Dam (downstr)	6.69	1.99
22	1051	Northridge-01	Pacoima Dam (upper left)	6.69	0.67
23	1063	Northridge-01	Rinaldi Receiving Sta	6.69	0.71
24	1084	Northridge-01	Sylmar-Converter Sta	6.69	0.78
25	1085	Northridge-01	Sylmar-Converter Sta East	6.69	1.00
26	1086	Northridge-01	Sylmar-Olive View Med FF	6.69	0.96
27	1602	Duzce, Turkey	Bolu	7.14	0.96
28	1605	Duzce, Turkey	Duzce	7.14	0.89
29	126	Gazli, USSR	Karakyr	6.80	1.15
30	165	Imperial Valley-06	Chihuahua	6.53	1.31
31	727	Superstition Hills-02	Superstition Mtn Camera	6.54	1.02
32	741	Loma Prieta	BRAN	6.93	0.91
33	864	Landers	Joshua Tree	7.28	1.21
34	959	Northridge-01	Canoga Park-Topanga Can	6.69	1.39
35	960	Northridge-01	Canyon Country-W Lost Cany	6.69	0.99
36	1004	Northridge-01	LA-Sepulveda VA Hospital	6.69	0.68
37	1048	Northridge-01	Northridge-17645 Saticoy St	6.69	1.45
38	1052	Northridge-01	Pacoima Kagel Canyon	6.69	1.19
39	1080	Northridge-01	Simi Valley-Katherine Rd	6.69	0.90
40	1111	Kobe, Japan	Nishi-Akashi	6.90	1.02

Table F.3 Documentation of 40 GMs of $S_a(T_1)_P$ procedure for Bridge A with Type I abutment modeling.

Record Number	NGA Record Sequence Number	Earthquake Name	Station	Magnitude	Scaling Factor
1	173	Imperial Valley-06	El Centro Array #10	6.53	4.42
2	174	Imperial Valley-06	El Centro Array #11	6.53	2.50
3	179	Imperial Valley-06	El Centro Array #4	6.53	1.94
4	185	Imperial Valley-06	Holtville Post Office	6.53	2.72
5	292	Irpinia, Italy-01	Sturno	6.90	2.41
6	763	Loma Prieta	Gilroy - Gavilan Coll.	6.93	3.30
7	764	Loma Prieta	Gilroy - Historic Bldg.	6.93	3.59
8	765	Loma Prieta	Gilroy Array #1	6.93	3.31
9	170	Imperial Valley-06	EC County Center FF	6.53	1.94
10	184	Imperial Valley-06	El Centro Differential Array	6.53	1.43
11	766	Loma Prieta	Gilroy Array #2	6.93	1.64
12	767	Loma Prieta	Gilroy Array #3	6.93	2.13
13	802	Loma Prieta	Saratoga-Aloha Ave	6.93	2.28
14	803	Loma Prieta	Saratoga-W Valley Coll.	6.93	1.75
15	825	Cape Mendocino	Cape Mendocino	7.01	1.75
16	828	Cape Mendocino	Petrolia	7.01	0.61
17	983	Northridge-01	Jensen Filter Plant Generator	6.69	0.89
18	1013	Northridge-01	LA Dam	6.69	1.42
19	1044	Northridge-01	Newhall-Fire Sta	6.69	0.74
20	1045	Northridge-01	Newhall-W Pico Canyon Rd.	6.69	1.62
21	1050	Northridge-01	Pacoima Dam (downstr)	6.69	1.99
22	1051	Northridge-01	Pacoima Dam (upper left)	6.69	0.67
23	1063	Northridge-01	Rinaldi Receiving Sta	6.69	0.71
24	1084	Northridge-01	Sylmar-Converter Sta	6.69	0.78
25	1085	Northridge-01	Sylmar-Converter Sta East	6.69	1.00
26	1086	Northridge-01	Sylmar-Olive View Med FF	6.69	0.96
27	1602	Duzce, Turkey	Bolu	7.14	0.96
28	1605	Duzce, Turkey	Duzce	7.14	0.89
29	126	Gazli, USSR	Karakyr	6.80	1.15
30	165	Imperial Valley-06	Chihuahua	6.53	1.31
31	727	Superstition Hills-02	Superstition Mtn Camera	6.54	1.02
32	741	Loma Prieta	BRAN	6.93	0.91
33	864	Landers	Joshua Tree	7.28	1.21
34	959	Northridge-01	Canoga Park-Topanga Can	6.69	1.39
35	960	Northridge-01	Canyon Country-W Lost Cany	6.69	0.99
36	1004	Northridge-01	LA-Sepulveda VA Hospital	6.69	0.68
37	1048	Northridge-01	Northridge-17645 Saticoy St	6.69	1.45
38	1052	Northridge-01	Pacoima Kagel Canyon	6.69	1.19
39	1080	Northridge-01	Simi Valley-Katherine Rd	6.69	0.90
40	1111	Kobe, Japan	Nishi-Akashi	6.90	1.02

Table F.4 Documentation of 40 GMs of $S_a(T_1)$ procedure for Bridge A with Type II abutment modeling.

Record Number	NGA Record Sequence Number	Earthquake Name	Station	Magnitude	Scaling Factor
1	139	Tabas, Iran	Dayhook	7.35	2.02
2	768	Loma Prieta	Gilroy Array #4	6.93	1.75
3	829	Cape Mendocino	Rio Dell Overpass-FF	7.01	1.10
4	189	Imperial Valley-06	SAHOP Casa Flores	6.53	2.01
5	495	Nahanni, Canada	Site 1	6.76	1.63
6	725	Superstition Hills-02	Poe Road (temp)	6.54	1.90
7	949	Northridge-01	Arleta-Nordhoff Fire Sta	6.69	1.61
8	1082	Northridge-01	Sun Valley-Roscoe Blvd	6.69	1.48
9	170	Imperial Valley-06	EC County Center FF	6.53	1.70
10	184	Imperial Valley-06	El Centro Differential Array	6.53	1.47
11	766	Loma Prieta	Gilroy Array #2	6.93	1.84
12	767	Loma Prieta	Gilroy Array #3	6.93	1.73
13	802	Loma Prieta	Saratoga-Aloha Ave	6.93	1.93
14	803	Loma Prieta	Saratoga-W Valley Coll.	6.93	1.96
15	825	Cape Mendocino	Cape Mendocino	7.01	1.55
16	828	Cape Mendocino	Petrolia	7.01	0.64
17	983	Northridge-01	Jensen Filter Plant Generator	6.69	1.11
18	1013	Northridge-01	LA Dam	6.69	1.58
19	1044	Northridge-01	Newhall-Fire Sta	6.69	0.66
20	1045	Northridge-01	Newhall-W Pico Canyon Rd.	6.69	1.58
21	1050	Northridge-01	Pacoima Dam (downstr)	6.69	1.56
22	1051	Northridge-01	Pacoima Dam (upper left)	6.69	0.57
23	1063	Northridge-01	Rinaldi Receiving Sta	6.69	0.78
24	1084	Northridge-01	Sylmar-Converter Sta	6.69	0.69
25	1085	Northridge-01	Sylmar-Converter Sta East	6.69	1.09
26	1086	Northridge-01	Sylmar-Olive View Med FF	6.69	0.80
27	1602	Duzce, Turkey	Bolu	7.14	0.79
28	1605	Duzce, Turkey	Duzce	7.14	1.12
29	126	Gazli, USSR	Karakyr	6.80	0.98
30	165	Imperial Valley-06	Chihuahua	6.53	1.42
31	727	Superstition Hills-02	Superstition Mtn Camera	6.54	1.00
32	741	Loma Prieta	BRAN	6.93	0.86
33	864	Landers	Joshua Tree	7.28	1.77
34	959	Northridge-01	Canoga Park-Topanga Can	6.69	0.85
35	960	Northridge-01	Canyon Country-W Lost Cany	6.69	0.88
36	1004	Northridge-01	LA-Sepulveda VA Hospital	6.69	0.74
37	1048	Northridge-01	Northridge-17645 Saticoy St	6.69	1.26
38	1052	Northridge-01	Pacoima Kagel Canyon	6.69	1.13
39	1080	Northridge-01	Simi Valley-Katherine Rd	6.69	0.72
40	1111	Kobe, Japan	Nishi-Akashi	6.90	1.31

Table F.5 Documentation of 40 GMs of $S_a(T_1)_P$ procedure for Bridge A with Type II abutment modeling.

Record Number	NGA Record Sequence Number	Earthquake Name	Station	Magnitude	Scaling Factor
1	173	Imperial Valley-06	El Centro Array #10	6.53	3.51
2	174	Imperial Valley-06	El Centro Array #11	6.53	2.07
3	179	Imperial Valley-06	El Centro Array #4	6.53	2.04
4	185	Imperial Valley-06	Holtville Post Office	6.53	2.90
5	292	Irpinia, Italy-01	Sturno	6.90	2.25
6	763	Loma Prieta	Gilroy-Gavilan Coll.	6.93	2.53
7	764	Loma Prieta	Gilroy-Historic Bldg.	6.93	2.56
8	765	Loma Prieta	Gilroy Array #1	6.93	2.41
9	170	Imperial Valley-06	EC County Center FF	6.53	1.70
10	184	Imperial Valley-06	El Centro Differential Array	6.53	1.47
11	766	Loma Prieta	Gilroy Array #2	6.93	1.84
12	767	Loma Prieta	Gilroy Array #3	6.93	1.73
13	802	Loma Prieta	Saratoga-Aloha Ave	6.93	1.93
14	803	Loma Prieta	Saratoga-W Valley Coll.	6.93	1.96
15	825	Cape Mendocino	Cape Mendocino	7.01	1.55
16	828	Cape Mendocino	Petrolia	7.01	0.64
17	983	Northridge-01	Jensen Filter Plant Generator	6.69	1.11
18	1013	Northridge-01	LA Dam	6.69	1.58
19	1044	Northridge-01	Newhall-Fire Sta	6.69	0.66
20	1045	Northridge-01	Newhall-W Pico Canyon Rd.	6.69	1.58
21	1050	Northridge-01	Pacoima Dam (downstr)	6.69	1.56
22	1051	Northridge-01	Pacoima Dam (upper left)	6.69	0.57
23	1063	Northridge-01	Rinaldi Receiving Sta	6.69	0.78
24	1084	Northridge-01	Sylmar-Converter Sta	6.69	0.69
25	1085	Northridge-01	Sylmar-Converter Sta East	6.69	1.09
26	1086	Northridge-01	Sylmar-Olive View Med FF	6.69	0.80
27	1602	Duzce, Turkey	Bolu	7.14	0.79
28	1605	Duzce, Turkey	Duzce	7.14	1.12
29	126	Gazli, USSR	Karakyr	6.80	0.98
30	165	Imperial Valley-06	Chihuahua	6.53	1.42
31	727	Superstition Hills-02	Superstition Mtn Camera	6.54	1.00
32	741	Loma Prieta	BRAN	6.93	0.86
33	864	Landers	Joshua Tree	7.28	1.10
34	959	Northridge-01	Canoga Park-Topanga Can	6.69	0.85
35	960	Northridge-01	Canyon Country-W Lost Cany	6.69	0.88
36	1004	Northridge-01	LA-Sepulveda VA Hospital	6.69	0.74
37	1048	Northridge-01	Northridge-17645 Saticoy St	6.69	1.26
38	1052	Northridge-01	Pacoima Kagel Canyon	6.69	1.13
39	1080	Northridge-01	Simi Valley-Katherine Rd	6.69	0.72
40	1111	Kobe, Japan	Nishi-Akashi	6.90	1.31

Table F.6 Documentation of 40 GMs of *CMS* procedure for Bridge A with Type I abutment modeling.

Record Number	NGA Record Sequence Number	Earthquake Name	Station	Magnitude	Scaling Factor
1	1111	Kobe, Japan	Nishi-Akashi	6.90	1.02
2	1350	Chi-Chi, Taiwan	ILA067	7.62	2.94
3	1425	Chi-Chi, Taiwan	TAP032	7.62	2.16
4	739	Loma Prieta	Anderson Dam (Downstream)	6.93	2.01
5	1317	Chi-Chi, Taiwan	ILA013	7.62	2.06
6	757	Loma Prieta	Dumbarton Bridge West End	6.93	2.60
7	776	Loma Prieta	Hollister-South & Pine	6.93	1.58
8	829	Cape Mendocino	Rio Dell Overpass-FF	7.01	1.53
9	721	Superstition Hills-02	El Centro Imp. Co. Cent	6.54	2.45
10	900	Landers	Yermo Fire Station	7.28	2.58
11	881	Landers	Morongo Valley	7.28	2.20
12	169	Imperial Valley-06	Delta	6.53	1.72
13	1084	Northridge-01	Sylmar-Converter Sta	6.69	0.78
14	1508	Chi-Chi, Taiwan	TCU072	7.62	0.78
15	778	Loma Prieta	Hollister Diff. Array	6.93	1.35
16	527	N. Palm Springs	Morongo Valley	6.06	1.94
17	1490	Chi-Chi, Taiwan	TCU050	7.62	2.73
18	1521	Chi-Chi, Taiwan	TCU089	7.62	2.31
19	1155	Kocaeli, Turkey	Bursa Tofas	7.51	2.92
20	1202	Chi-Chi, Taiwan	CHY035	7.62	1.53
21	1504	Chi-Chi, Taiwan	TCU067	7.62	1.25
22	1529	Chi-Chi, Taiwan	TCU102	7.62	1.51
23	1234	Chi-Chi, Taiwan	CHY086	7.62	2.49
24	1187	Chi-Chi, Taiwan	CHY015	7.62	2.71
25	1198	Chi-Chi, Taiwan	CHY029	7.62	1.40
26	1506	Chi-Chi, Taiwan	TCU070	7.62	1.55
27	1493	Chi-Chi, Taiwan	TCU053	7.62	2.33
28	343	Coalinga-01	Parkfield-Fault Zone 4	6.36	2.94
29	1227	Chi-Chi, Taiwan	CHY074	7.62	2.64
30	171	Imperial Valley-06	EC Meloland Overpass FF	6.53	1.49
31	983	Northridge-01	Jensen Filter Plant Generator	6.69	0.90
32	729	Superstition Hills-02	Wildlife Liquef. Array	6.54	2.70
33	808	Loma Prieta	Treasure Island	6.93	2.40
34	1550	Chi-Chi, Taiwan	TCU136	7.62	2.68
35	1203	Chi-Chi, Taiwan	CHY036	7.62	1.22
36	1045	Northridge-01	Newhall-W Pico Canyon Rd.	6.69	1.64
37	170	Imperial Valley-06	EC County Center FF	6.53	1.95
38	1500	Chi-Chi, Taiwan	TCU061	7.62	2.83
39	159	Imperial Valley-06	Agrarias	6.53	2.29
40	1456	Chi-Chi, Taiwan	TAP095	7.62	2.24

Table F.7 Documentation of 40 GMs of *CMS* procedure for Bridge A with Type II abutment modeling.

Record Number	NGA Record Sequence Number	Earthquake Name	Station	Magnitude	Scaling Factor
1	337	Coalinga-01	Parkfield-Fault Zone 12	6.36	2.88
2	1087	Northridge-01	Tarzana-Cedar Hill A	6.69	0.43
3	1184	Chi-Chi, Taiwan	CHY010	7.62	2.52
4	1317	Chi-Chi, Taiwan	ILA013	7.62	1.76
5	1221	Chi-Chi, Taiwan	CHY065	7.62	2.40
6	1234	Chi-Chi, Taiwan	CHY086	7.62	2.50
7	864	Landers	Joshua Tree	7.28	1.82
8	721	Superstition Hills-02	El Centro Imp. Co. Cent	6.54	2.26
9	808	Loma Prieta	Treasure Island	6.93	2.24
10	776	Loma Prieta	Hollister-South & Pine	6.93	1.65
11	1787	Hector Mine	Hector	7.13	2.21
12	778	Loma Prieta	Hollister Diff. Array	6.93	1.51
13	184	Imperial Valley-06	El Centro Differential Array	6.53	1.50
14	1227	Chi-Chi, Taiwan	CHY074	7.62	2.21
15	1456	Chi-Chi, Taiwan	TAP095	7.62	2.48
16	342	Coalinga-01	Parkfield-Fault Zone 3	6.36	2.50
17	1515	Chi-Chi, Taiwan	TCU082	7.62	2.02
18	1509	Chi-Chi, Taiwan	TCU074	7.62	0.90
19	1160	Kocaeli, Turkey	Fatih	7.51	1.96
20	316	Westmorland	Parachute Test Site	5.90	2.33
21	1493	Chi-Chi, Taiwan	TCU053	7.62	2.50
22	779	Loma Prieta	LGPC	6.93	0.73
23	1063	Northridge-01	Rinaldi Receiving Sta	6.69	0.79
24	1519	Chi-Chi, Taiwan	TCU087	7.62	2.88
25	1158	Kocaeli, Turkey	Duzce	7.51	1.51
26	1491	Chi-Chi, Taiwan	TCU051	7.62	2.73
27	1506	Chi-Chi, Taiwan	TCU070	7.62	1.14
28	1187	Chi-Chi, Taiwan	CHY015	7.62	2.77
29	1536	Chi-Chi, Taiwan	TCU110	7.62	2.18
30	1198	Chi-Chi, Taiwan	CHY029	7.62	1.38
31	1202	Chi-Chi, Taiwan	CHY035	7.62	1.16
32	1504	Chi-Chi, Taiwan	TCU067	7.62	1.31
33	169	Imperial Valley-06	Delta	6.53	1.69
34	1770	Hector Mine	Big Bear Lake-Fire Station	7.13	2.68
35	1508	Chi-Chi, Taiwan	TCU072	7.62	0.99
36	183	Imperial Valley-06	El Centro Array #8	6.53	1.42
37	527	N. Palm Springs	Morongo Valley	6.06	2.30
38	1484	Chi-Chi, Taiwan	TCU042	7.62	2.27
39	170	Imperial Valley-06	EC County Center FF	6.53	1.74
40	1541	Chi-Chi, Taiwan	TCU116	7.62	2.65

Table F.8 Documentation of 40 GMs of *US* procedure for Bridge A.

Record Number	NGA Record Sequence Number	Earthquake Name	Station	Magnitude	Scaling Factor
1	1518	Chi-Chi, Taiwan	TCU085	7.62	2.00
2	1515	Chi-Chi, Taiwan	TCU082	7.62	2.60
3	1491	Chi-Chi, Taiwan	TCU051	7.62	2.80
4	1537	Chi-Chi, Taiwan	TCU111	7.62	3.00
5	1502	Chi-Chi, Taiwan	TCU064	7.62	3.00
6	1529	Chi-Chi, Taiwan	TCU102	7.62	3.00
7	187	Imperial Valley-06	Parachute Test Site	6.53	1.80
8	1494	Chi-Chi, Taiwan	TCU054	7.62	3.00
9	1476	Chi-Chi, Taiwan	TCU029	7.62	3.00
10	180	Imperial Valley-06	El Centro Array #5	6.53	2.00
11	1496	Chi-Chi, Taiwan	TCU056	7.62	3.00
12	1492	Chi-Chi, Taiwan	TCU052	7.62	1.70
13	1086	Northridge-01	Sylmar-Olive View Med FF	6.69	2.90
14	1148	Kocaeli, Turkey	Arcelik	7.51	3.00
15	1508	Chi-Chi, Taiwan	TCU072	7.62	2.10
16	1493	Chi-Chi, Taiwan	TCU053	7.62	2.80
17	1489	Chi-Chi, Taiwan	TCU049	7.62	2.60
18	169	Imperial Valley-06	Delta	6.53	3.00
19	1488	Chi-Chi, Taiwan	TCU048	7.62	3.00
20	729	Superstition Hills-02	Wildlife Liquef. Array	6.54	3.00
21	1504	Chi-Chi, Taiwan	TCU067	7.62	2.80
22	721	Superstition Hills-02	El Centro Imp. Co. Cent	6.54	2.00
23	1490	Chi-Chi, Taiwan	TCU050	7.62	2.90
24	1787	Hector Mine	Hector	7.13	2.90
25	728	Superstition Hills-02	Westmorland Fire Sta	6.54	2.90
26	172	Imperial Valley-06	El Centro Array #1	6.53	2.80
27	285	Irpinia, Italy-01	Bagnoli Irpinio	6.90	3.00
28	900	Landers	Yermo Fire Station	7.28	3.00
29	1505	Chi-Chi, Taiwan	TCU068	7.62	1.30
30	1472	Chi-Chi, Taiwan	TCU017	7.62	3.00
31	1526	Chi-Chi, Taiwan	TCU098	7.62	2.60
32	1546	Chi-Chi, Taiwan	TCU122	7.62	2.00
33	1527	Chi-Chi, Taiwan	TCU100	7.62	3.00
34	182	Imperial Valley-06	El Centro Array #7	6.53	2.40
35	832	Landers	Amboy	7.28	3.00
36	1528	Chi-Chi, Taiwan	TCU101	7.62	2.40
37	179	Imperial Valley-06	El Centro Array #4	6.53	1.70
38	1202	Chi-Chi, Taiwan	CHY035	7.62	2.90
39	1231	Chi-Chi, Taiwan	CHY080	7.62	1.00
40	1521	Chi-Chi, Taiwan	TCU089	7.62	2.00

Table F.9 Documentation of 40 GMs of $S_a(T_1)$ procedure for Bridge B.

Record Number	NGA Record Sequence Number	Earthquake Name	Station	Magnitude	Scaling Factor
1	1084	Northridge-01	Sylmar-Converter Sta	6.69	0.53
2	1063	Northridge-01	Rinaldi Receiving Sta	6.69	0.73
3	1085	Northridge-01	Sylmar-Converter Sta East	6.69	0.86
4	1044	Northridge-01	Newhall-Fire Sta	6.69	0.89
5	983	Northridge-01	Jensen Filter Plant Generator	6.69	1.07
6	1602	Duzce, Turkey	Bolu	7.14	1.11
7	1051	Northridge-01	Pacoima Dam (upper left)	6.69	1.11
8	1045	Northridge-01	Newhall-W Pico Canyon Rd.	6.69	1.20
9	803	Loma Prieta	Saratoga-W Valley Coll.	6.93	1.26
10	1086	Northridge-01	Sylmar-Olive View Med FF	6.69	1.28
11	828	Cape Mendocino	Petrolia	7.01	1.28
12	1013	Northridge-01	LA Dam	6.69	1.35
13	179	Imperial Valley-06	El Centro Array #4	6.53	1.60
14	1605	Duzce, Turkey	Duzce	7.14	1.78
15	825	Cape Mendocino	Cape Mendocino	7.01	1.80
16	766	Loma Prieta	Gilroy Array #2	6.93	2.04
17	802	Loma Prieta	Saratoga-Aloha Ave	6.93	2.12
18	764	Loma Prieta	Gilroy-Historic Bldg.	6.93	2.16
19	184	Imperial Valley-06	El Centro Differential Array	6.53	2.23
20	170	Imperial Valley-06	EC County Center FF	6.53	2.25
21	185	Imperial Valley-06	Holtville Post Office	6.53	2.46
22	292	Irpinia, Italy-01	Sturno	6.90	2.51
23	1004	Northridge-01	LA-Sepulveda VA Hospital	6.69	1.11
24	126	Gazli, USSR	Karakyr	6.80	1.41
25	864	Landers	Joshua Tree	7.28	1.46
26	1080	Northridge-01	Simi Valley-Katherine Rd	6.69	1.47
27	1048	Northridge-01	Northridge-17645 Saticoy St	6.69	1.58
28	1787	Hector Mine	Hector	7.13	1.74
29	1082	Northridge-01	Sun Valley-Roscoe Blvd	6.69	1.74
30	829	Cape Mendocino	Rio Dell Overpass-FF	7.01	1.80
31	741	Loma Prieta	BRAN	6.93	1.87
32	727	Superstition Hills-02	Superstition Mtn Camera	6.54	1.91
33	960	Northridge-01	Canyon Country-W Lost Cany	6.69	2.09
34	728	Superstition Hills-02	Westmorland Fire Sta	6.54	2.27
35	1052	Northridge-01	Pacoima Kagel Canyon	6.69	2.31
36	725	Superstition Hills-02	Poe Road (temp)	6.54	2.36
37	768	Loma Prieta	Gilroy Array #4	6.93	2.37
38	949	Northridge-01	Arleta-Nordhoff Fire Sta	6.69	2.47
39	1042	Northridge-01	N Hollywood-Coldwater Can	6.69	2.47
40	495	Nahanni, Canada	Site 1	6.76	2.59

Table F.10 Documentation of 40 GMs of $S_a(T_1)_P$ procedure for Bridge B.

Record Number	NGA Record Sequence Number	Earthquake Name	Station	Magnitude	Scaling Factor
1	1084	Northridge-01	Sylmar-Converter Sta	6.69	0.53
2	1063	Northridge-01	Rinaldi Receiving Sta	6.69	0.73
3	1085	Northridge-01	Sylmar-Converter Sta East	6.69	0.86
4	1044	Northridge-01	Newhall-Fire Sta	6.69	0.89
5	983	Northridge-01	Jensen Filter Plant Generator	6.69	1.07
6	1602	Duzce, Turkey	Bolu	7.14	1.11
7	1051	Northridge-01	Pacoima Dam (upper left)	6.69	1.11
8	1045	Northridge-01	Newhall-W Pico Canyon Rd.	6.69	1.20
9	803	Loma Prieta	Saratoga-W Valley Coll.	6.93	1.26
10	1086	Northridge-01	Sylmar-Olive View Med FF	6.69	1.28
11	828	Cape Mendocino	Petrolia	7.01	1.28
12	1013	Northridge-01	LA Dam	6.69	1.35
13	179	Imperial Valley-06	El Centro Array #4	6.53	1.60
14	1605	Duzce, Turkey	Duzce	7.14	1.78
15	825	Cape Mendocino	Cape Mendocino	7.01	1.80
16	766	Loma Prieta	Gilroy Array #2	6.93	2.04
17	802	Loma Prieta	Saratoga-Aloha Ave	6.93	2.12
18	764	Loma Prieta	Gilroy-Historic Bldg.	6.93	2.16
19	184	Imperial Valley-06	El Centro Differential Array	6.53	2.23
20	170	Imperial Valley-06	EC County Center FF	6.53	2.25
21	185	Imperial Valley-06	Holtville Post Office	6.53	2.46
22	292	Irpinia, Italy-01	Sturno	6.90	2.51
23	1004	Northridge-01	LA-Sepulveda VA Hospital	6.69	1.11
24	126	Gazli, USSR	Karakyr	6.80	1.41
25	864	Landers	Joshua Tree	7.28	1.46
26	1080	Northridge-01	Simi Valley-Katherine Rd	6.69	1.47
27	1048	Northridge-01	Northridge-17645 Saticoy St	6.69	1.58
28	1787	Hector Mine	Hector	7.13	1.74
29	1082	Northridge-01	Sun Valley-Roscoe Blvd	6.69	1.74
30	829	Cape Mendocino	Rio Dell Overpass-FF	7.01	1.80
31	741	Loma Prieta	BRAN	6.93	1.87
32	727	Superstition Hills-02	Superstition Mtn Camera	6.54	1.91
33	960	Northridge-01	Canyon Country-W Lost Cany	6.69	2.09
34	728	Superstition Hills-02	Westmorland Fire Sta	6.54	2.27
35	173	Imperial Valley-06	El Centro Array #10	6.53	2.94
36	767	Loma Prieta	Gilroy Array #3	6.93	2.96
37	1050	Northridge-01	Pacoima Dam (downstr)	6.69	3.06
38	174	Imperial Valley-06	El Centro Array #11	6.53	3.08
39	161	Imperial Valley-06	Brawley Airport	6.53	3.35
40	765	Loma Prieta	Gilroy Array #1	6.93	4.87

Table F.11 Documentation of 40 GMs of *CMS* procedure for Bridge B.

Record Number	NGA Record Sequence Number	Earthquake Name	Station	Magnitude	Scaling Factor
1	959	Northridge-01	Canoga Park-Topanga Can	6.69	2.61
2	1457	Chi-Chi, Taiwan	TAP097	7.62	2.57
3	729	Superstition Hills-02	Wildlife Liquef. Array	6.54	2.70
4	1410	Chi-Chi, Taiwan	TAP003	7.62	2.23
5	1045	Northridge-01	Newhall-W Pico Canyon Rd.	6.69	1.20
6	776	Loma Prieta	Hollister-South & Pine	6.93	1.29
7	1454	Chi-Chi, Taiwan	TAP090	7.62	2.87
8	1198	Chi-Chi, Taiwan	CHY029	7.62	2.17
9	1555	Chi-Chi, Taiwan	TCU147	7.62	2.91
10	285	Irpinia, Italy-01	Bagnoli Irpinio	6.90	2.91
11	1425	Chi-Chi, Taiwan	TAP032	7.62	2.82
12	1334	Chi-Chi, Taiwan	ILA044	7.62	2.91
13	182	Imperial Valley-06	El Centro Array #7	6.53	1.31
14	723	Superstition Hills-02	Parachute Test Site	6.54	1.11
15	1418	Chi-Chi, Taiwan	TAP014	7.62	2.87
16	771	Loma Prieta	Golden Gate Bridge	6.93	2.41
17	1515	Chi-Chi, Taiwan	TCU082	7.62	2.51
18	1530	Chi-Chi, Taiwan	TCU103	7.62	2.93
19	1286	Chi-Chi, Taiwan	HWA037	7.62	2.84
20	1541	Chi-Chi, Taiwan	TCU116	7.62	2.10
21	1494	Chi-Chi, Taiwan	TCU054	7.62	2.52
22	1504	Chi-Chi, Taiwan	TCU067	7.62	1.10
23	1264	Chi-Chi, Taiwan	HWA013	7.62	2.51
24	1529	Chi-Chi, Taiwan	TCU102	7.62	1.29
25	1503	Chi-Chi, Taiwan	TCU065	7.62	0.70
26	1537	Chi-Chi, Taiwan	TCU111	7.62	2.97
27	1547	Chi-Chi, Taiwan	TCU123	7.62	1.97
28	1492	Chi-Chi, Taiwan	TCU052	7.62	0.75
29	1536	Chi-Chi, Taiwan	TCU110	7.62	1.90
30	1147	Kocaeli, Turkey	Ambarli	7.51	1.82
31	527	N. Palm Springs	Morongo Valley	6.06	2.09
32	900	Landers	Yermo Fire Station	7.28	2.23
33	1550	Chi-Chi, Taiwan	TCU136	7.62	1.94
34	864	Landers	Joshua Tree	7.28	1.46
35	1456	Chi-Chi, Taiwan	TAP095	7.62	2.86
36	721	Superstition Hills-02	El Centro Imp. Co. Cent	6.54	2.38
37	2461	Chi-Chi, Taiwan-03	CHY028	6.20	2.77
38	1551	Chi-Chi, Taiwan	TCU138	7.62	2.34
39	1534	Chi-Chi, Taiwan	TCU107	7.62	2.45
40	1265	Chi-Chi, Taiwan	HWA014	7.62	2.98

Table F.12 Documentation of 40 GMs of *US* procedure for Bridge B.

Record Number	NGA Record Sequence Number	Earthquake Name	Station	Magnitude	Scaling Factor
1	2492	Chi-Chi, Taiwan-03	CHY076	6.20	2.90
2	1534	Chi-Chi, Taiwan	TCU107	7.62	3.00
3	1498	Chi-Chi, Taiwan	TCU059	7.62	3.00
4	1537	Chi-Chi, Taiwan	TCU111	7.62	3.00
5	1506	Chi-Chi, Taiwan	TCU070	7.62	3.00
6	1515	Chi-Chi, Taiwan	TCU082	7.62	3.00
7	1538	Chi-Chi, Taiwan	TCU112	7.62	3.00
8	1491	Chi-Chi, Taiwan	TCU051	7.62	2.10
9	1492	Chi-Chi, Taiwan	TCU052	7.62	3.00
10	1475	Chi-Chi, Taiwan	TCU026	7.62	3.00
11	1504	Chi-Chi, Taiwan	TCU067	7.62	2.60
12	1496	Chi-Chi, Taiwan	TCU056	7.62	3.00
13	1489	Chi-Chi, Taiwan	TCU049	7.62	1.80
14	1529	Chi-Chi, Taiwan	TCU102	7.62	3.00
15	721	Superstition Hills-02	El Centro Imp. Co. Cent	6.54	2.90
16	1490	Chi-Chi, Taiwan	TCU050	7.62	3.00
17	1546	Chi-Chi, Taiwan	TCU122	7.62	2.10
18	729	Superstition Hills-02	Wildlife Liquef. Array	6.54	2.70
19	1494	Chi-Chi, Taiwan	TCU054	7.62	2.70
20	1527	Chi-Chi, Taiwan	TCU100	7.62	3.00
21	832	Landers	Amboy	7.28	2.90
22	1158	Kocaeli, Turkey	Duzce	7.51	3.00
23	1202	Chi-Chi, Taiwan	CHY035	7.62	2.30
24	1508	Chi-Chi, Taiwan	TCU072	7.62	1.40
25	1501	Chi-Chi, Taiwan	TCU063	7.62	2.80
26	1493	Chi-Chi, Taiwan	TCU053	7.62	2.70
27	1482	Chi-Chi, Taiwan	TCU039	7.62	2.60
28	1505	Chi-Chi, Taiwan	TCU068	7.62	1.20
29	169	Imperial Valley-06	Delta	6.53	1.40
30	1528	Chi-Chi, Taiwan	TCU101	7.62	3.00
31	1176	Kocaeli, Turkey	Yarimca	7.51	3.00
32	1148	Kocaeli, Turkey	Arcelik	7.51	2.40
33	1084	Northridge-01	Sylmar-Converter Sta	6.69	2.20
34	179	Imperial Valley-06	El Centro Array #4	6.53	2.10
35	1555	Chi-Chi, Taiwan	TCU147	7.62	2.90
36	285	Irpinia, Italy-01	Bagnoli Irpinio	6.90	2.20
37	1436	Chi-Chi, Taiwan	TAP052	7.62	3.00
38	811	Loma Prieta	WAHO	6.93	2.00
39	1536	Chi-Chi, Taiwan	TCU110	7.62	2.70
40	1488	Chi-Chi, Taiwan	TCU048	7.62	2.80

Table F.13 Documentation of 40 GMs of $S_a(T_1)$ procedure for Bridge C.

Record Number	NGA Record Sequence Number	Earthquake Name	Station	Magnitude	Scaling Factor
1	1084	Northridge-01	Sylmar-Converter Sta	6.69	0.70
2	1063	Northridge-01	Rinaldi Receiving Sta	6.69	0.89
3	1085	Northridge-01	Sylmar-Converter Sta East	6.69	0.94
4	1045	Northridge-01	Newhall-W Pico Canyon Rd.	6.69	0.95
5	1086	Northridge-01	Sylmar-Olive View Med FF	6.69	1.03
6	1044	Northridge-01	Newhall-Fire Sta	6.69	1.13
7	983	Northridge-01	Jensen Filter Plant Generator	6.69	1.16
8	1605	Duzce, Turkey	Duzce	7.14	1.53
9	803	Loma Prieta	Saratoga-W Valley Coll.	6.93	1.59
10	1013	Northridge-01	LA Dam	6.69	1.60
11	766	Loma Prieta	Gilroy Array #2	6.93	1.65
12	179	Imperial Valley-06	El Centro Array #4	6.53	1.73
13	802	Loma Prieta	Saratoga-Aloha Ave	6.93	1.82
14	170	Imperial Valley-06	EC County Center FF	6.53	1.90
15	825	Cape Mendocino	Cape Mendocino	7.01	1.91
16	184	Imperial Valley-06	El Centro Differential Array	6.53	1.94
17	828	Cape Mendocino	Petrolia	7.01	1.96
18	1602	Duzce, Turkey	Bolu	7.14	1.98
19	292	Irpinia, Italy-01	Sturno	6.90	2.04
20	1051	Northridge-01	Pacoima Dam (upper left)	6.69	2.09
21	173	Imperial Valley-06	EC Meloland Overpass FF	6.53	2.13
22	767	Loma Prieta	Gilroy Array #3	6.93	2.55
23	764	Loma Prieta	Gilroy-Historic Bldg.	6.93	2.62
24	174	Imperial Valley-06	El Centro Array #11	6.53	2.69
25	161	Imperial Valley-06	Brawley Airport	6.53	3.02
26	126	Gazli, USSR	Karakyr	6.80	1.19
27	1048	Northridge-01	Northridge-17645 Saticoy St	6.69	1.71
28	1004	Northridge-01	LA-Sepulveda VA Hospital	6.69	1.90
29	960	Northridge-01	Canyon Country-W Lost Cany	6.69	2.06
30	768	Loma Prieta	Gilroy Array #4	6.93	2.15
31	1787	Hector Mine	Hector	7.13	2.16
32	959	Northridge-01	Canoga Park-Topanga Can	6.69	2.20
33	864	Landers	Joshua Tree	7.28	2.20
34	1111	Kobe, Japan	Nishi-Akashi	6.90	2.58
35	1080	Northridge-01	Simi Valley-Katherine Rd	6.69	2.64
36	285	Irpinia, Italy-01	Bagnoli Irpinio	6.90	2.68
37	1052	Northridge-01	Pacoima Kagel Canyon	6.69	2.78
38	728	Superstition Hills-02	Westmorland Fire Sta	6.54	2.87
39	829	Cape Mendocino	Rio Dell Overpass-FF	7.01	2.88
40	1082	Northridge-01	Sun Valley-Roscoe Blvd	6.69	2.89

Table F.14 Documentation of 40 GMs of $S_a(T_1)_P$ procedure for Bridge C.

Record Number	NGA Record Sequence Number	Earthquake Name	Station	Magnitude	Scaling Factor
1	1084	Northridge-01	Sylmar-Converter Sta	6.69	0.70
2	1063	Northridge-01	Rinaldi Receiving Sta	6.69	0.89
3	1085	Northridge-01	Sylmar-Converter Sta East	6.69	0.94
4	1045	Northridge-01	Newhall-W Pico Canyon Rd.	6.69	0.95
5	1086	Northridge-01	Sylmar-Olive View Med FF	6.69	1.03
6	1044	Northridge-01	Newhall-Fire Sta	6.69	1.13
7	983	Northridge-01	Jensen Filter Plant Generator	6.69	1.16
8	1605	Duzce, Turkey	Duzce	7.14	1.53
9	803	Loma Prieta	Saratoga-W Valley Coll.	6.93	1.59
10	1013	Northridge-01	LA Dam	6.69	1.60
11	766	Loma Prieta	Gilroy Array #2	6.93	1.65
12	179	Imperial Valley-06	El Centro Array #4	6.53	1.73
13	802	Loma Prieta	Saratoga-Aloha Ave	6.93	1.82
14	170	Imperial Valley-06	EC County Center FF	6.53	1.90
15	825	Cape Mendocino	Cape Mendocino	7.01	1.91
16	184	Imperial Valley-06	El Centro Differential Array	6.53	1.94
17	828	Cape Mendocino	Petrolia	7.01	1.96
18	1602	Duzce, Turkey	Bolu	7.14	1.98
19	292	Irpinia, Italy-01	Sturno	6.90	2.04
20	1051	Northridge-01	Pacoima Dam (upper left)	6.69	2.09
21	173	Imperial Valley-06	EC Meloland Overpass FF	6.53	2.13
22	767	Loma Prieta	Gilroy Array #3	6.93	2.55
23	764	Loma Prieta	Gilroy-Historic Bldg.	6.93	2.62
24	174	Imperial Valley-06	El Centro Array #11	6.53	2.69
25	161	Imperial Valley-06	Brawley Airport	6.53	3.02
26	126	Gazli, USSR	Karakyr	6.80	1.19
27	1048	Northridge-01	Northridge-17645 Saticoy St	6.69	1.71
28	1004	Northridge-01	LA-Sepulveda VA Hospital	6.69	1.90
29	960	Northridge-01	Canyon Country-W Lost Cany	6.69	2.06
30	768	Loma Prieta	Gilroy Array #4	6.93	2.15
31	1787	Hector Mine	Hector	7.13	2.16
32	959	Northridge-01	Canoga Park-Topanga Can	6.69	2.20
33	864	Landers	Joshua Tree	7.28	2.20
34	1111	Kobe, Japan	Nishi-Akashi	6.90	2.58
35	1080	Northridge-01	Simi Valley-Katherine Rd	6.69	2.64
36	285	Irpinia, Italy-01	Bagnoli Irpinio	6.90	2.68
37	1052	Northridge-01	Pacoima Kagel Canyon	6.69	2.78
38	185	Imperial Valley-06	Holtville Post Office	6.53	2.72
39	1050	Northridge-01	Pacoima Dam (downstr)	6.69	3.98
40	765	Loma Prieta	Gilroy Array #1	6.93	4.84

Table F.15 Documentation of 40 GMs of *CMS* procedure for Bridge C.

Record Number	NGA Record Sequence Number	Earthquake Name	Station	Magnitude	Scaling Factor
1	1537	Chi-Chi, Taiwan	TCU111	7.62	2.55
2	1547	Chi-Chi, Taiwan	TCU123	7.62	1.58
3	1147	Kocaeli, Turkey	Ambarli	7.51	2.55
4	1329	Chi-Chi, Taiwan	ILA037	7.62	2.50
5	1262	Chi-Chi, Taiwan	HWA011	7.62	2.99
6	1492	Chi-Chi, Taiwan	TCU052	7.62	0.65
7	1203	Chi-Chi, Taiwan	CHY036	7.62	1.96
8	1553	Chi-Chi, Taiwan	TCU141	7.62	2.79
9	1536	Chi-Chi, Taiwan	TCU110	7.62	1.17
10	1472	Chi-Chi, Taiwan	TCU017	7.62	2.64
11	316	Westmorland	Parachute Test Site	5.90	2.72
12	1182	Chi-Chi, Taiwan	CHY006	7.62	1.80
13	721	Superstition Hills-02	El Centro Imp. Co. Cent	6.54	2.23
14	1317	Chi-Chi, Taiwan	ILA013	7.62	2.75
15	173	Imperial Valley-06	El Centro Array #10	6.53	2.13
16	1187	Chi-Chi, Taiwan	CHY015	7.62	2.72
17	1503	Chi-Chi, Taiwan	TCU065	7.62	0.80
18	1166	Kocaeli, Turkey	Iznik	7.51	2.28
19	1264	Chi-Chi, Taiwan	HWA013	7.62	2.71
20	2509	Chi-Chi, Taiwan-03	CHY104	6.20	2.47
21	285	Irpinia, Italy-01	Bagnoli Irpinio	6.90	2.68
22	1504	Chi-Chi, Taiwan	TCU067	7.62	1.01
23	1534	Chi-Chi, Taiwan	TCU107	7.62	2.13
24	1509	Chi-Chi, Taiwan	TCU074	7.62	0.90
25	1084	Northridge-01	Sylmar-Converter Sta	6.69	0.70
26	1494	Chi-Chi, Taiwan	TCU054	7.62	2.13
27	1419	Chi-Chi, Taiwan	TAP017	7.62	2.76
28	1529	Chi-Chi, Taiwan	TCU102	7.62	1.34
29	1515	Chi-Chi, Taiwan	TCU082	7.62	2.20
30	900	Landers	Yermo Fire Station	7.28	2.13
31	1045	Northridge-01	Newhall-W Pico Canyon Rd.	6.69	0.95
32	1787	Hector Mine	Hector	7.13	2.16
33	1410	Chi-Chi, Taiwan	TAP003	7.62	1.78
34	1316	Chi-Chi, Taiwan	ILA012	7.62	2.97
35	808	Loma Prieta	Treasure Island	6.93	2.43
36	169	Imperial Valley-06	Delta	6.53	1.73
37	289	Irpinia, Italy-01	Calitri	6.90	2.71
38	1491	Chi-Chi, Taiwan	TCU051	7.62	2.52
39	3317	Chi-Chi, Taiwan-06	CHY101	6.30	2.78
40	864	Landers	Joshua Tree	7.28	2.20

Table F.16 Documentation of 40 GMs of *US* procedure for Bridge C.

Record Number	NGA Record Sequence Number	Earthquake Name	Station	Magnitude	Scaling Factor
1	2115	Denali, Alaska	TAPS Pump Station #11	7.90	1.80
2	1436	Chi-Chi, Taiwan	TAP052	7.62	2.60
3	729	Superstition Hills-02	Wildlife Liquef. Array	6.54	1.40
4	1489	Chi-Chi, Taiwan	TCU049	7.62	1.50
5	1505	Chi-Chi, Taiwan	TCU068	7.62	1.00
6	732	Loma Prieta	APEEL 2-Redwood City	6.93	3.00
7	1491	Chi-Chi, Taiwan	TCU051	7.62	2.60
8	1490	Chi-Chi, Taiwan	TCU050	7.62	2.60
9	285	Irpinia, Italy-01	Bagnoli Irpinio	6.90	2.80
10	1787	Hector Mine	Hector	7.13	2.70
11	1494	Chi-Chi, Taiwan	TCU054	7.62	2.40
12	1492	Chi-Chi, Taiwan	TCU052	7.62	2.30
13	1504	Chi-Chi, Taiwan	TCU067	7.62	2.60
14	1527	Chi-Chi, Taiwan	TCU100	7.62	3.00
15	1526	Chi-Chi, Taiwan	TCU098	7.62	2.80
16	1488	Chi-Chi, Taiwan	TCU048	7.62	3.00
17	1048	Northridge-01	Northridge-17645 Saticoy St	6.69	2.80
18	801	Loma Prieta	San Jose-Santa Teresa Hills	6.93	3.00
19	1475	Chi-Chi, Taiwan	TCU026	7.62	3.00
20	1478	Chi-Chi, Taiwan	TCU033	7.62	2.80
21	1496	Chi-Chi, Taiwan	TCU056	7.62	2.80
22	832	Landers	Amboy	7.28	3.00
23	1472	Chi-Chi, Taiwan	TCU017	7.62	3.00
24	1515	Chi-Chi, Taiwan	TCU082	7.62	2.20
25	1503	Chi-Chi, Taiwan	TCU065	7.62	2.00
26	169	Imperial Valley-06	Delta	6.53	1.90
27	1546	Chi-Chi, Taiwan	TCU122	7.62	3.00
28	1482	Chi-Chi, Taiwan	TCU039	7.62	2.90
29	1529	Chi-Chi, Taiwan	TCU102	7.62	3.00
30	1045	Northridge-01	Newhall-W Pico Canyon Rd.	6.69	3.00
31	1176	Kocaeli, Turkey	Yarimca	7.51	3.00
32	1508	Chi-Chi, Taiwan	TCU072	7.62	2.50
33	1493	Chi-Chi, Taiwan	TCU053	7.62	3.00
34	1476	Chi-Chi, Taiwan	TCU029	7.62	2.80
35	1528	Chi-Chi, Taiwan	TCU101	7.62	1.90
36	180	Imperial Valley-06	El Centro Array #5	6.53	2.00
37	829	Cape Mendocino	Rio Dell Overpass-FF	7.01	2.10
38	1499	Chi-Chi, Taiwan	TCU060	7.62	2.80
39	179	Imperial Valley-06	El Centro Array #4	6.53	2.70
40	139	Tabas, Iran	Dayhook	7.35	1.80